NMR Crystallographic Investigations of Group 14 σ-hole Interactions: Tetrel Bonds

Scott Alexander Southern

A thesis submitted in partial fulfillment of the requirements for the Doctorate in Philosophy degree in Chemistry

Department of Chemistry and Biomolecular Sciences
Faculty of Science
University of Ottawa

This thesis was defended successfully before the members of the thesis evaluation committee on March 8th, 2021 in Ottawa, Ontario.

Committee Members:	Dr. Natalie Goto
	Dr. Alain St-Amant
	Dr. Jeffrey Smith (Carleton University)
	Dr. Vladimir Michaelis (University of Alberta)
Thesis Supervisor:	Dr. David L. Bryce
Defence Chairperson:	Dr. Pieter Hofstra

I Table of Contents

II List of Figures

III List of Tables

IV Abbreviations

a.u.	Atomic units
ADF	Amsterdam Density Functional
CASTEP	Cambridge Serial Total Energy Package
CCDC	Cambridge Crystallographic Data Centre
ChB	Chalcogen Bond
CP	Cross-polarization
CP/MAS	Cross-polarization magic angle spinning
CPMG	Carr-Purcell-Meiboom-Gill
CS	Chemical Shift
CSA	Chemical Shift Anisotropy
CSD	Crystal Structure Database
DFT	Density functional theory
EFG	Electric field gradient
FID	Free induction decay
FT	Fourier transform
GGA	Generalized gradient approximation
GIPAW	Gauge-including projector-augmented wave
HB	Hydrogen bond
HBA	*Herzfeld-Berger* Analysis
HOMO	Highest Occupied Molecular Orbital
Hz	Hertz
IUPAC	International Union of Pure and Applied Chemistry
kHz	Kilohertz
LUMO	Lowest Unoccupied Molecular Orbital
MAS	Magic angle spinning
MHz	Megahertz
n.a.	Natural abundance
MEPS	Molecular Electrostatic Potential Surface
NBO	Natural Bond Orbital
NLMO	Natural Localized Molecular Orbital
NMR	Nuclear Magnetic Resonance
NQR	Nuclear Quadrupole Resonance
PBE	Perdew Burke Ernzerhof
PnB	Pnictogen Bond
ppm	Parts per million
PXRD	Powder X-ray diffraction
revPBE	Revised PBE
RF	Radiofrequency
RMSD	Root-mean-square deviation
SCXRD	Single Crystal X-ray Diffraction
TB	Tetrel bond
TPPM	Two-pulse phase modulation
TZP	Triple-zeta with polarization functions
VOCS	Variable offset cumulative spectrum
XB	Halogen Bond
XRD	X-ray Diffraction
ZORA	Zeroth-order regular approximation

V Abstract

The concept of noncovalent bonding has evolved over the last number of years to include a very interesting class of interactions that is analogous to hydrogen bonding, called σ-hole interactions. These result from the depletion of electrostatic charge on the opposite end of a covalent bond between an electron-withdrawing substituent and a bond donor atom, which resides in groups 14-17 of the periodic table. One of these interactions is the tetrel bond (TB), whereby the bond donor is a group 14 element (T=C, Si, Ge, Sn, Pb). This thesis's primary goal is to explore the solid-state NMR parameters arising from the formation of tetrel bonds. To this end, combined density functional theory (DFT) and experimental multinuclear solid-state NMR spectroscopic investigations are carried out on complexes featuring carbon, Pb(II) and tin tetrel bonds.

Firstly, solid-state NMR and computational approaches are used to examine a series of cocrystals formed from either caffeine or theophylline and several other small organic acceptor molecules. It is shown that the NMR response due to tetrel bond formation is detectible, but it can be hidden by other effects, including those of crystal packing. Careful analysis of NMR data alongside DFT calculations can reveal that the weak tetrel bond in these sorts of complexes increases the ^{13}C chemical shift by 3-5 ppm.

Next, a study of five Pb(II) centres hemidirectionally coordinated by isonicotinoyl hydrazone ligands demonstrates that the ^{207}Pb NMR response is highly sensitive to the Pb(II) coordination environment. The NMR data indicate that a tetrel bond can induce an NMR response corresponding to a coordination environment between hemidirectional and holodirectional character.

Finally, a series of organotin chloride donor molecules complexed with *N*-oxides and carboxylates, which feature short and linear tetrel bonds, are subjected to magic angle spinning (MAS) NMR experiments. The recorded data gives rise to a correlation between the tetrel bond length and both the experimental chemical shift and the $^{1}J(^{119}\text{Sn}\text{-}^{35}\text{Cl})$ coupling.

Throughout this thesis, it is demonstrated that the isotropic chemical shift, the principal components of the chemical shift tensor, and indirect spin-spin coupling can be used to probe and gain insights into the electronic environment at the tetrel bond. More importantly, this work is fundamental to rationalize NMR data while refining crystal structure data in NMR crystallographic approaches for compounds featuring tetrel bonds.

VI Acknowledgements

I would like to begin by thanking my supervisor and mentor, Dr. David Bryce. I first met Dr. Bryce when joining the University of Ottawa's Department of Chemistry as a graduate student in 2014. At the time, I had finished my second undergraduate degree, and I was visiting with my parents overseas for an extended stay, wondering what I would do next. He was gracious to invite me to join his lab as a master's candidate, where I began this incredible journey. After two years, he encouraged me to stay in his lab to complete my doctorate, and I cannot thank him enough for believing in me. I will be forever grateful for his leadership and the knowledge and wisdom he has passed along to me during my time as his student. He taught me the fundamental concepts of solid-state NMR spectroscopy. He made sure I knew how to write scientific literature correctly. He made me realize the importance of paying attention to details. I would not be where I am today without him. For Dave, I raise a good craft ale!

I would also like to thank my thesis advisory committee, Dr. Goto, Dr. St-Amant and Dr. Smith. I am grateful for everything I have learned from them over the years, whether in their courses or through the valuable feedback I have received at my comprehensive examination, research proposal defence and seminar presentation. I hope to follow their example as I carry down my career path.

I also had the opportunity to work at the National Research Council Canada (NRCC) for about a year. I want to thank Dr. Andreas Brinkmann for teaching me to be methodical and thorough in analyzing my data. I also thank him for showing me many of the spectrometer's ins and outs and showing me how it truly works from a technical perspective.

I also had the pleasure of working with Dr. Victor Terskikh, whom I can say with certainty is a legend in the field of solid-state NMR. While I appreciate all of the light-hearted conversations we had about Twitter, politics and other things (I hope the O-train finally works for him one day!), I honestly did learn a lot from Victor. He made me feel comfortable and at ease using the 900 MHz spectrometer, and we had many valuable discussions about the experiments that could be used for my research.

As a Bryce Lab member, I enjoyed meeting and working with many colleagues over the years. I still remember the first day I came to the University, having returned from Africa the day before and severely jet-lagged (I showed up at 6:30 in the morning thanks to the time change!). I remember being welcomed to the lab with open arms by Drs. Fred Perras, Jasmine Viger-Gravel and Kevin Burgess. These three people would have a significant impact on my way forward. They were mentors to me and taught me much of what I know about NMR. The first day in my lab, Fred took me to the magnets and gave me a crash course on magic-angle spinning – from then on, hooking me to solid-state NMR! I will fondly remember the many lab discussions between the three of them, with us newcomers at the periphery, from in-depth discussions about religion to politics, lighter subjects such as the Bryce Lab history, stories about previous lab outings and conference trips, and tales of the great floods. There was never a dull moment! I thank Fred for passing on his in-depth knowledge and wisdom (as much as I could absorb). I also want to thank Jasmine for showing me how to be methodical and thoughtful in my approach to science. Finally, I thank Kevin for being a positive influence and reminding me of the importance of taking the time for self-reflection.

Of course, a few individuals were there from the start of this adventure until the end. I want to thank Dr. Patrick Szell and Yixue Xu (Colette) for their friendship over the years. I

am amazed by Pat's achievements throughout his Ph.D. I admire his creativity and experimental design, and I am grateful for everything I learned from him. I also thoroughly enjoyed sharing jokes and stories with him. Thank you, Colette, for being someone I could bounce ideas and thoughts off and vent when I needed to. I wish both the best of success in their academic careers.

I would also like to acknowledge some of the other Bryce Lab postdocs I've had the opportunity to work directly with on various projects. Thank you to Dr. Libor Kobera for teaching me the multitude of tips and tricks helpful in working with the NMR instruments. Libor also patiently took much time and effort to show me how to carry out advanced experiments such as MQMAS, DUMBO, and others. And I will also always remember his' less serious' side… you were undoubtedly a hoot! I also acknowledge Dr. Jamie Frost, whom I learned much from about chemical synthesis. I am also incredibly appreciative of Dr. Cesar Leroy for being a positive influence in the lab and for the many great ideas for advancing my research. Finally, a big thank you goes to Dr. Vijith Kumar, whom I had the pleasure to work with for a long time and learned much from his experiences. It was humbling to discuss his prior work and experiences in different labs around the world.

I also thank the other Bryce Lab members, who have made incredible colleagues over the years. I want to acknowledge Vincent, Tamali, Shubha and Christelle and wish them many successes as they navigate their chemistry careers. I also want to specifically thank the undergraduate students who have worked on my projects, namely Michael West, Maressa Bradshaw and Dan Ni Zheng. Michael was an asset to my projects and was incredibly hard working. I thank him for the hours he spent working on synthesis and NMR. Maressa was also diligent as a student. I acknowledge the hard work she spent making countless samples in the

ball-mill and by recrystallization. Work that might have been mundane but essential nonetheless. Finally, I thank Dan for her hard work and eagerness to learn. I know all three will make great chemists one day! Finally, I thank all of the other students who have come through the lab over the years from Canada, France and other places, and I thank them for their friendship and acquaintance.

I also want to acknowledge the many people who work at the University of Ottawa and who have made my time an enriching experience. Notably, the NMR staff, Dr Glenn Facey, Dr. Peter Pallister and Dr. Eric Ye. Thank you all for the many enlightening conversations about NMR. In particular, I would like to thank Glenn for passing on his incredible experience to me. I can't tell you how many times the uOttawa NMR Blog has saved me. I hope it remains a valuable source of NMR wisdom to the world's NMR spectroscopists for many years to come. I hope that retirement is treating you well. I would also like to thank Dr. Wendy Pell for being a positive influence on me and making those physical chemistry labs really enjoyable to teach. And Josée Rouleau, our esteemed administrative assistant who made every day better because she always greeted me in the morning with a smile.

My time in the Bryce Lab would not have been made possible without the incredible support system I had at home and my workplace in the reserves. I first want to thank my colleagues at 632 RCACS, 706 RCACS, RCSU(E) and CJCR – all of whom have the shared love of working for Canada's youth. I thank my chain of command for having confidence in me as a youth leader and acting as the Commanding Officer at Major's rank for all these years. And I am incredibly grateful for their understanding and support throughout the last six years. I am also thankful for the many friendships made.

I want to thank my parents, Barry and Gisele, for their incredible support over the years on the home front. They have always been there for me near and far, and I am deeply thankful to them for giving me the opportunities to get away and relax in fascinating and unique locations around abroad. I thank them for always encouraging me and pushing me to be the best I can be, and I will forever be grateful to them.

I also want to thank my mother and father-in-law, Jane and Doug. From the time that we first met, they have always been caring and supportive of me. While my parents were living overseas, they welcomed me into their home as much as possible. I have fond memories of dinners and discussions, and I will always cherish the time spent with them.

I could not possibly imagine my life during the last few years without the twisted humour of my brother, Evan. He brought me many laughs, but he also allowed me to escape and dream now and then when he would send me beautiful pictures of the BC coast and Rockies from the cockpit of a CH-149 Cormorant. Equally so, one of my most incredible escapes has been to spend time with my niece and nephew, Claire and Ben. I cannot express enough how much joy their little smiles bring to me. I am grateful that Joel and Eve have been so close to allowing this to happen.

I would finally like to acknowledge the people who have had the most influence in my life as I have navigated my way through my doctorate. Firstly, I recognize my grandfather, Dr. Julius S. Etele, who has been one of the primary motivation sources, even over time since he left this world. He taught me to have high expectations of myself, dream, and work hard to accomplish my goals. I know that he would be proud of me now. I would like to thank him, my grandmothers, Margo and Marjorie, and my adopted grandmother Yvonne for all of their love and support while I have been undertaking my studies.

This last year has been challenging. With the COVID-19 pandemic all but shutting down our city for months at a time during the final year of my research, I cannot imagine how I could have gotten through it without my puppy, Persephone. Since March 2020, she has kept me active and entertained while it was often tricky otherwise. In the times we were distant from family, Persephone brought me great joy and happiness.

Beyond everyone else, my deepest gratitude goes to my wife, Alison. I thank her for always being there to encourage me and to support me. We have certainly been through a lot together since the beginning of our adventure. On all those late nights, she has stood by me while I accomplished that last bit of work on those weekends while I had to grade reports and those trips that she mostly enjoyed alone while I was in conferences. I know that these years have been difficult and that I had to devote much of my time and attention to my research. I also know that this experience has brought us much closer together in many ways. I am deeply thankful for Alison's friendship and companionship through all of this, and I look forward to embarking on the next chapter of my journey with her. I love you very much, Alison.

To my high school science teacher, who told me I did not have the capability to succeed in science – thank you for pointing me down this path towards success!

VII Statement of Originality

I certify that the results presented in this thesis result from my own work, and if others carried out any work, it is fully acknowledged. For all my works, I acknowledge my supervisor and mentor, Dr. David L. Bryce and I acknowledge the many coworkers I have had the pleasure to share my work with over the years. Permissions have been granted by the publishers to reproduce my original work in this thesis.

VII.1 Acknowledgements

Chapter 1 is adapted from the following publication:

Southern, S. A.; Bryce, D. L. Recent Advances in NMR Crystallography and Polymorphism, *Ann. Rep. Nucl. Magn. Reson. Spectrosc.*, **2020**, *102*, 1-80.

Chapter 2 is adapted from the following publication:

Southern, S. A.; West, M. S.; Bradshaw, M. J. Z.; Bryce, D. L. The Experimental ^{13}C and ^{1}H Solid-State NMR Response in Weakly Tetrel-Bonded Methyl Groups, *J. Phys. Chem C.*, **2020**, *In Press*.

I thank M. S. West, M. J. Z. Bradshaw and D. Ni Zheng for preparing the samples and M. J. Z. West for carrying out some of the NMR experiments.

Chapter 3 is adapted from the following publication:

Southern, S. A.; Errulat, D.; Frost, J. M.; Gabidullin B.; Bryce, D. L. Prospects for ^{207}Pb Solid-State NMR Studies of Lead Tetrel Bonds, *Faraday Discuss.*, **2017**, *203*, 165-186.

I acknowledge D. Errulat, who prepared some of the samples with Dr. J. M Frost and Dr. B. Gabidullin's help for solving the crystal structures of the compounds using single-crystal X-ray diffraction.

Chapter 4 is based on new research that is being prepared for publication.
I acknowledge C. Rodrigue, who prepared the samples, and Dr. V. Kumar, who solved the crystal structures using single-crystal X-ray diffraction structures for a prior manuscript and carried out some of the NMR experiments.

Appendices containing supporting information have been reproduced from the corresponding publications, except for Appendix 3, where the appropriate attribution has been made in-text.

VII.2 List of Other Works

Further to the publications listed above, I have co-authored the following published works that do not appear in this thesis.

Kobera, L.; Southern, S. A.; Kumar Rao, G.; Richeson, D.; Bryce, D. L. New Experimental Insight into the Nature of Metal-Metal Bonds in Digallium Compounds: J Coupling between Quadrupolar Nuclei, *Chem. Eur. J.*, **2016**, *22*, 1-10.

Xu, Y.; Southern, S. A.; Szell, P. M. J.; Bryce, D. L. The Role of Solid-State Nuclear Magnetic Resonance in Crystal Engineering, *CrystEngComm*, **2016**, *22*, 5236-5252.

Frost, J. M.; Kobera, L.; Pialat, A.; Zhang, Y.; Southern, S. A.; Gabidullin, B.; Bryce, D. L.; Murugesu, M. From Discrete Molecule to Polymer, to MOF: Mapping the Coordination Chemistry of Cd II using ^{113}Cd Solid-State NMR, *Chem. Commun.*, **2016**, *52*, 10680-10683.

Kobera, L.; Southern, S. A.; Frost, J. M.; Bryce, D. L. Multinuclear Solid-State Magnetic Resonance Study of Oxo-bridged Diniobium and Quadruply-bonded Dimolybdenum Carboxylate Clusters, *Solid State Nucl. Magnet. Reson.*, **2017**, *84*, 20-27.

Deshkar, A.; Marcial, J.; Southern, S. A.; Kobera, L.; Bryce, D. L.; McCloy, J. S.; Goel, A. Understanding the Structural Origin of Crystalline Phase Transformations in Nepheline ($NaAlSiO_4$)-based Glass-ceramics, *J. Am. Ceram. Soc.*, **2017**, *100*, 2859-2878.

Chapter 1 Introduction

Solid-state nuclear magnetic resonance (NMR) spectroscopy can provide information about chemical bonds or characterize the chemical structure of a molecule or a complex system such as a protein. It may also provide new insights into the mechanisms of catalysis and biochemical reactions[1-4] or the formation of supramolecular structures such as zeolites or metal-organic frameworks (MOFs).[5]

However, NMR alone is not necessarily sufficient for studying such systems. The field of NMR crystallography employs various approaches to study crystal structures to either determine, validate, or select crystal structures and their polymorphs. Examples of this are crystal structure prediction or determination of structural properties validation based on NMR data. In this context, NMR crystallography usually relies on the complementary use of *ab initio* calculations (usually density functional theory (DFT)) and X-ray diffraction methods to create a complete picture of the problem at hand. However, it should be stressed that while helpful, these data are not always required. For example, protein structure refinements regularly use two- or three-dimensional NMR data without recourse to diffraction-based models.[6] Alternatively, NMR data can often validate structural features seen in diffraction-based crystal structures without DFT calculations. Other analytical methods fall under the umbrella of NMR crystallography[7], such as powder X-ray diffraction, single-crystal X-ray diffraction, infrared spectroscopy, thermal analysis, and scanning electron microscopy.

The goal of this chapter is to provide the basic concepts required to understand fully the experimentation that is presented within this thesis. The chapter discusses some of the fundamental theories of chemical bonding, solid-state NMR, and computational chemistry in

brief detail. Afterwards, NMR spectroscopy's importance in NMR crystallography is discussed in the context of a literature survey of some of the most recent developments in the field. Finally, an introduction to σ-hole bonding is presented to set the stage for this thesis's primary focus. This chapter's aim is for the reader to become well acquainted with the field of solid-state NMR spectroscopy and NMR crystallography and become convinced of the importance of understanding the role that the NMR response to tetrel bonds has to play in both of these fields.

1.1 Chemical Bonding

Molecules are formed from bonds that occur between atoms. Atoms are composed of neutrons and positively charged protons that are surrounded by negatively charged electrons. The electrons in an atom can be described by a wavefunction, describing an electron's probability density at a particular spatial coordinate around the nucleus. This model is greatly simplified by describing the wavefunction using a linear combination of atomic orbitals (LCAO). From this model, chemists can easily describe bonding between atoms to form molecules through atomic orbitals' overlap.

At a basic level, bonding occurs when two atomic orbitals come together to share electron density. In a simple case of two spherical *s*-type orbitals with arbitrary but equal energies, mixing the atomic orbitals will form both a lower energy and stabilizing σ bonding orbital and a destabilizing, and higher energy σ^* antibonding orbital. Importantly, when these two bonding orbitals are formed, the Aufbau Principle dictates that the electrons from the two *s*-orbitals will occupy the lowest energy bonding orbital before occupying the higher-level bonding orbital. For two *s*-orbitals, each containing one electron participating in a σ-bond, the

electron will occupy the σ-bonding orbital as a pair, while the σ^* antibonding orbital remains empty, thus resulting in a stable covalent bond.

There are four major classes of chemical bonds, including covalent bonds, ionic bonds, dative bonds and noncovalent interactions. The former three classifications are considered strong bonds, involving either the sharing of electrons or the transfer of electrons from one atom to the other, and are typically associated with the formation of molecules or materials. The last type of bond, being noncovalent interactions, is considered weak, with energies far below those of the formal chemical bonds, but enough to form net attractive interactions based on the forces that arise between atoms' and molecules' distribution of electrons over their surfaces.

Noncovalent bonding can be described using a few models, the first being Coulomb's Law. A basic description of Coulomb's law involves the classic romantic moniker, "Opposites attract." In chemistry, this refers to the presence of point charges, which are either positive or negative. An example of this is the dipole interaction, whereby molecules with positively and negatively charged regions resulting from electron-rich or electron-poor regions interact with one another, aligning themselves according to the long-range interactions between opposite charges.

This thesis's subject is the spectroscopic investigation of a subclass of noncovalent interactions known as σ-hole bonds. In particular, the research presented here involves a close look at tetrel bonds (TB), which is a further subclassification of σ-hole bonds. To understand this thesis's work, a brief overview of the spectroscopic methods used is required before introducing the concept of tetrel bonding and its relationship with NMR crystallography. The

remainder of this chapter will solely address the experimental approaches used to study the tetrel bond, which will be introduced in detail in section 1.4 *NMR Crystallography*.

1.2 Basic Principles of Solid-State Nuclear Magnetic Resonance Spectroscopy

The fundamental properties of the magnetic resonance of spins have been applied to the technique of NMR spectroscopy to reveal many insights into the nature of materials.[8,9] Nuclides are subatomic particles that can be described as fermions and bosons. The "spin" of a nuclide is an intrinsic property, and all fermions possess half-integer spin, while bosons possess whole-integer spin. All nuclei with non-zero spin are important in NMR spectroscopy because they possess intrinsic angular momentum, I, which is also known as the spin quantum number. This angular momentum is related to the magnetic moment, m, fundamental to NMR spectroscopy because it can interact with an external magnetic field. There is a corresponding number $(2I + 1)$ of eigenvalues of m_l, or magnetic quantum numbers for any value of I. These eigenvalues refer to the degenerate energy states that lose their degeneracy when the nuclide is subjected to a magnetic field. For example, a spin-1/2 nucleus will have two degenerate energy states in the presence of a magnetic field, while a quadrupolar nucleus of $I = 3/2$ will have four. This phenomenon is known as the *Zeeman effect*, whereby the eigenstates possess energy described by:

$$E = -m_l \gamma \hbar B_0 \qquad \text{Eq. 1-1}$$

where the energy levels are separated by an energy corresponding to:

$$\Delta E = \gamma \hbar B_0 \qquad \text{Eq. 1-2}$$

where the gyromagnetic ratio is given by γ (rad s^{-1} T^{-1}), $\hbar$ is the reduced Planck constant in angular frequency units ($\hbar = \frac{h}{2\pi}; h = 6.626 \times 10^{-34} Js$ and the external magnetic field is given by B_0 (T). Thus, in increasing magnetic field strengths, the energy difference between the *Zeeman* levels becomes greater. In this thesis, experiments are conducted in external magnetic field strengths of 4.7, 9.4 and 14.1 T.

In pulsed NMR spectroscopy, the separation of energy states is exploited by subjecting the nuclide to electromagnetic radiation in the form of a radiofrequency (*rf*) pulse with a frequency that matches the *Larmor* frequency, or that which is required to induce an NMR transition from the lower energy state to the higher energy state. The *Larmor frequency* of a nuclide is related to its gyromagnetic ratio and the magnetic field strength by:

$$v_L = \frac{\gamma B_0}{2\pi} \qquad \text{Eq. 1-3}$$

In a simple experiment on a single non-zero spin in a vacuum, the *rf* pulse will induce an NMR transition, and the NMR spectrometer would detect the resulting precession of the spins magnetic field as it precesses through the detection coil. The induced current is recorded, and a Fourier transformation (FT) is applied to the resulting NMR signal, and a peak would appear at a frequency of v_L. Naturally, however, NMR experiments are customarily carried out on complex chemical samples, with many spins experiencing different magnetic shieldings due to differences in their local magnetic fields arising from factors such as their chemical environments. Also, mechanisms such as homonuclear and heteronuclear dipolar coupling, scalar coupling and quadrupolar interactions perturb the *Zeeman effect* resulting in a more complex NMR spectrum with many NMR signals.

While the *Zeeman effect* makes pulsed NMR spectroscopy possible, the major limitation is that it is inherently insensitive, even though it is powerful for probing chemical structures. The detection of an NMR signal depends on an inequivalent number of spins in the lower and higher energy states. This phenomenon is governed by *Boltzmann's distribution* (Eq. 1-4).

$$\frac{N_\alpha}{N_\beta} = e^{-\frac{\gamma \hbar B_0}{kT}} \qquad \text{Eq. 1-4}$$

where k is *Boltzmann's constant* (m^2 kg s^{-2} K^{-1}), T is the temperature (K), and the populations of spins in the lower (α) and higher (β) energy states are given by N. This formula describes the ratio of spins at each energy level and is dependent on both the temperature and the magnetic field strength. One can quickly notice that a substantially elevated magnetic field strength is needed to induce any notable population differences. Since the signal-to-noise of the NMR response is related to the spin population difference, it is often desirable to maximize the magnetic field strength and minimize the temperature. Strong magnetic fields such as 9.4 T are routinely used, while instruments using ultra-high magnetic fields (≥21.1 T) are becoming more prevalent.

1.2.1 NMR Interactions

It is worthwhile to provide a short overview of the nuclear spin interactions relevant to solid-state NMR and NMR crystallography. A more detailed discussion of NMR theory is provided in further chapters when necessary and relevant to the experimentation methods described. For an isolated spin-1/2 nucleus, a peak measured in an NMR spectrum is characterized by its chemical shift (δ_{iso}), which originates from the magnetic shielding (σ) interaction, given by the frequency:

$$\nu = (1-\sigma)\frac{\gamma B_0}{2\pi} \qquad \text{Eq. 1-5}$$

The magnetic shielding tensor may be expressed in the diagonal form such that the interaction is represented in its principal axis system (PAS) where:

$$\sigma_{11} \leq \sigma_{22} \leq \sigma_{33} \qquad \text{Eq. 1-6}$$

The shielding constant is manifested directly in the NMR spectrum in the form of a chemical shift δ. The chemical shift (CS) is related to the magnetic shielding constant by:

$$\delta = \frac{\sigma_{ref} - \sigma}{1 - \sigma_{ref}} \qquad \text{Eq. 1-7}$$

and the isotropic chemical shift, $\delta_{iso,}$ is given as the average of the three chemical shift tensor components:

$$\delta_{iso} = \frac{\delta_{11} + \delta_{22} + \delta_{33}}{3} \qquad \text{Eq. 1-8}$$

The CS is important because it can be related to structural features due to its sensitivity to the immediate chemical environment. The chemical shift (or shielding) anisotropy (CSA) refers to the chemical shielding's orientational dependence at an observed nucleus. There are multiple ways of expressing the CSA.[10] In the *Herzfeld-Berger* convention[11], the span (Ω) and skew (κ) of the tensor are given by Eq. 1-9 and Eq. 1-10, respectively.

$$\Omega = \delta_{11} - \delta_{33} \qquad \text{Eq. 1-9}$$

$$\kappa = \frac{3(\delta_{22} - \delta_{iso})}{\Omega} \qquad \text{Eq. 1-10}$$

The span is used to describe the NMR line shape's breadth and is usually reported in ppm units. On the other hand, the skew is reported as a unitless value between -1 and 1 (with both extremes indicating axial symmetry) and is related to the CS tensor's symmetry, which is related to the rotational symmetry of the observed nuclide. For example, a CS tensor is axially symmetric when the skew is -1 or 1.

In the *Haeberlen* convention[12], the chemical shift tensor is described in terms of its anisotropy and its asymmetry (Eq. 1-11 and Eq. 1-12).

$$\Delta\delta = \delta_{zz} - \frac{\delta_{xx} + \delta_{yy}}{2} \qquad \text{Eq. 1-11}$$

$$\eta = \frac{\delta_{yy} - \delta_{xx}}{\delta_{zz} - \delta_{iso}}; (0 \leq \eta \leq 1) \qquad \text{Eq. 1-12}$$

1.2.1.1 Quadrupolar Interaction (Spin > ½)

This thesis generally deals only with spin-1/2 nuclei, but nuclei with spin >1/2 are also important and discussed briefly. For spin-1/2 nuclei, NMR spectra are dominated by the CSA and dipolar coupling interactions. The situation changes for quadrupolar nuclei ($I \geq 1$), which possess a non-spherical charge distribution. Therefore, NMR spectra are affected by the quadrupolar interaction between the electric field gradient (EFG) at the nucleus and the nuclear electric quadrupole moment (Q). This interaction is described in terms of the quadrupolar coupling constant:

$$C_Q = \frac{eV_{ZZ}Q}{h} \qquad \text{Eq. 1-13}$$

where e is the charge of the electron and V_{ZZ} is the largest principal component of the EFG, and h is the Planck constant. The quadrupolar asymmetry parameter is calculated from the three principal components of the EFG:

$$\eta_Q = \frac{V_{XX} - V_{YY}}{V_{ZZ}} \qquad \text{Eq. 1-14}$$

A set of Euler angles relates the principal axis systems of the CS and EFG tensors, α, β, and γ, which can give rise to important information about local symmetry at a particular nucleus[13], and indeed about the overall crystallographic symmetry.

One must be cautious when interpreting solid-state NMR spectra of quadrupolar nuclei. These spectra are generally affected by second-order quadrupolar shifts, where the apparent isotropic shift is displaced from the real chemical shift by the second-order quadrupolar interaction. We direct the reader to a thorough account of this effect and how it can be modelled.[14] Besides second-order quadrupolar effects, some systems can be influenced by higher-order quadrupolar effects, which can manifest in the form of non-uniform frequency shifts of the spectrum and must be considered.[15-18]

1.2.1.2 Direct Dipolar and Indirect Spin-Spin Coupling

Dipolar coupling arises from the interaction of magnetic dipoles through space. The dipolar coupling constant is inversely related to the motionally-averaged inverse cube of the internuclear distance, r_{12}, between a pair of spins and is given by:

$$R_{DD} = \left(\frac{\mu_0}{4\pi}\right)\left(\frac{\gamma_1\gamma_2\hbar}{2\pi}\right)\left\langle r_{12}^{-3}\right\rangle \qquad \text{Eq. 1-15}$$

where μ_0 is the free-space permittivity constant, γ is the gyromagnetic ratio, which varies for each NMR active nuclide, and r is the distance between nuclei 1 and 2.

The dipolar coupling between a pair of spins can manifest in several ways depending on the spin system under study. The effects can be minimized using higher magnetic fields and fast magic angle spinning. There are also several advanced radiofrequency schemes available for minimizing the effects of homonuclear and heteronuclear decoupling.

The intervening electronic structure gives rise to *J*-coupling between nuclear spins. While these couplings can be taken advantage of to gain information about molecular structures, they may often be overshadowed by other more significant effects in the solid-state. Therefore, they are relatively rarely measured directly in NMR crystallographic approaches, but when measured, *J*-couplings can provide helpful information about the relative arrangement of NMR-active nuclei in the crystal structure. There are many recent examples of *J*-couplings that have been measured in solids.[19] $^1J(^{13}C, ^{17}O)$ couplings have been used to characterize O positions in napthaladaldehydic acid.[20] Also, (^1H, ^{17}O) *J*-couplings were measured and compared to theoretical calculations in a series of oxygen-containing crystal structures.[21] $^1J(^{77}Se, ^{31}P)$ couplings have also been in halogen bonded P=Se···I motif.[22] *J*-couplings between quadrupolar nuclei have been used to probe the electronic properties and dynamics of digallium[23] and diborane compounds.[24] Further details about the analysis of *J*-couplings in solid-state NMR experiments are provided in Chapter 4.

1.3 Methodology in NMR Crystallography

1.3.1 Experimental Techniques in Solid-State NMR

As described earlier in this chapter, the basic NMR experiment depends on applying an *rf* pulse to a sample of nuclear spins within the magnetic field, which induces an NMR transition and relaxation, the latter which can be observed as the spins process through the NMR coil and induce a current. The frequency of the precession gives rise to the chemical shift. Of course, most NMR experiments are more complicated than this simple description and involve a series of pulses and decoupling schemes to enhance the FID measurement. These combinations of pulses are referred to as *pulse sequences*, and the derivation of optimal pulse sequences for given problems forms the basis of very active research by many scientists in the field of NMR spectroscopy.

This section briefly discusses some of the experimental methodology relevant to this thesis and NMR crystallography, including some recent examples. A detailed account of the NMR methodology used to characterize organic crystals, and their polymorphs, is also available in the recent review by Hodgkinson.[25]

The homonuclear dipolar coupling has a broadening effect on the line shapes of ^{1}H NMR spectra of organic solids. Much effort has been put into improving ^{1}H solid-state NMR through the use of various pulse sequences and, because line narrowing is proportional to the spinning frequency, by using faster magic angle spinning (MAS). MAS is used to reduce or eliminate NMR interactions with an orientational dependence on the magnetic field, B_0. Each of these interactions, which include chemical shift anisotropy (CSA), homonuclear and heteronuclear dipolar coupling, quadrupolar coupling and other second-order effects, are

described, in part, by a 2nd order Legendre polynomial representing the angle, θ, between the interaction tensor and B_0 (Eq. 1-16).

$$3\cos^2\theta - 1 \qquad \text{Eq. 1-16}$$

The magic angle, θ_m is mathematically represented by the angle between a cube's diagonal and any connected corner (**Figure 1-1**). If $\theta_m = 54.74$, then $3\cos^2\theta - 1 = 0$ and the orientational dependence of the tensor vanishes. The average orientational dependence of a bulk powder spinning around an axis oriented with respect to B_0 goes to zero when $\theta_r = \theta_m = 54.74$ and is given by:

$$\langle 3\cos^2\theta - 1\rangle = \frac{1}{2}(3\cos^2\theta_r - 1)(3\cos^2\beta - 1) \qquad \text{Eq. 1-17}$$

where θ is the angle between the interaction tensor and B_0, and β is the angle between the axis of rotation and the principle axis of the interaction tensor.

In principle, all NMR interaction tensors with this orientational dependence should be eliminated, but it can be shown that this is not always the case for all interactions. While, for the most part, they are significantly reduced, some are not entirely averaged at slower spinning speeds. CSA, for example, has a part of its orientational dependence that is modulated by the rotational frequency. Therefore, experiments employing slower spinning speeds will still result in NMR lineshapes that resemble the static powder pattern, but where the outline of the pattern is now formed by a series of spinning sidebands spaced equally at multiples of the rotational frequency on either side of the isotropic resonance. When the rotational frequency is greater than the CSA's magnitude (in Hz), only the isotropic peak is visible. Thus, higher spinning speeds are desirable, especially for nuclei showing large CSAs. At the time of writing

this thesis, to our knowledge, the fastest achieved magic angle spinning frequencies were 130[26], 140[27], 150[28], and 200[29] kHz MAS.

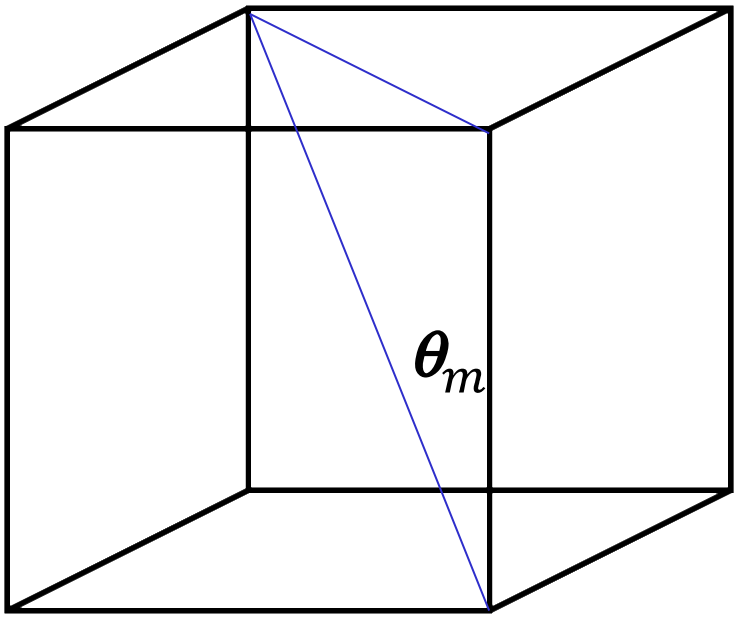

Figure 1-1. Mathematical representation of the magic angle, θ_m in a cube.

Combining MAS with sophisticated homonuclear dipolar decoupling sequences, such as ^{1}H CRAMPS (combined rotation and multiple-pulse spectroscopy), amplifies the possibility of recording high-resolution ^{1}H solid-state NMR spectra because of the line narrowing resulting from the averaging of chemical shift anisotropy and the reduction of dipolar couplings. Examples of decoupling mechanisms are the Lee-Goldberg techniques[30-33], WAHUHA[34], MREV-8[35,36], BR-24[37], or the family of DUMBO sequences[38-40], which has become increasingly used in recent years.

High-resolution proton NMR is used alongside a variety of methods for NMR crystallography, including crystal structure prediction.[41,42] Experimental ^{1}H NMR schemes

routinely use a combination of ultrafast magic angle spinning, sophisticated pulse sequences, and homonuclear decoupling routines to average out dipolar couplings and thus enhance the resolution and sensitivity of ^{1}H line shapes.[43-45]

The use of the dipolar interaction has been critical in NMR crystallography. Often, long-range interactions can be explored using NMR data, and the dipolar coupling can provide information about the internuclear distance between two nuclear spins. Under MAS conditions, van Rossum *et al.* initially proposed a method of determining long-range heteronuclear ^{1}H-^{13}C distances using Lee-Goldburg (LG) cross-polarization and LG decoupling.[46] In this experiment, ^{1}H-^{1}H dipolar couplings are suppressed by tilting the magnetization to the LG-CP condition, allowing for the observation of weaker ^{1}H-^{13}C couplings absent of any effects because of homonuclear dipolar coupling. Here, a COOH···O(H)C hydrogen bond in tyrosine hydrochloride was measured to be 2.47 Å, in close agreement with previous neutron diffraction studies (2.521 Å), thereby confirming the robustness of this experiment.

Cross-polarization (CP) techniques, including the well-known CP/MAS experiment, are used extensively for structural studies. ^{1}H-^{13}C CP is more broadly applied to two-dimensional heteronuclear methods via through-space correlation (heteronuclear correlation - HETCOR). For example, the ^{1}H-^{13}C frequency swept LG heteronuclear correlation experiment (FSLG-HETCOR)[46] has been used to characterize solids from small organic molecules to complex pharmaceuticals. An extension to one-dimensional CRAMPS, two-dimensional double-quantum-single-quantum (DQ/SQ) experiments under magic angle spinning can provide valuable information about the proximities between hydrogen atoms *via* strong homonuclear dipolar couplings.[47] These correlations may be paired with ^{1}H-^{13}C

HETCOR experiments to provide a complete description of the bonding within a chemical structure.

1.3.2 Theoretical Calculations

Here, a brief overview of the theory behind theoretical calculations as it applies to this thesis is discussed. A more detailed perspective description of some of the fundamental principles of quantum chemical calculations has been discussed before this work[48], but the focus here will be to describe density functional theory (DFT).

Theoretical calculations are often employed alongside solid-state NMR experiments[49] [68] to rationalize the results obtained, for example, either for peak assignment or line shape analysis and are applied frequently towards structural refinement in crystals.[50-53] Theoretical studies are often performed on their own to generate general understandings of the NMR response to various structural and crystal packing effects. Programs such as CASTEP[54-60], Quantum-Espresso[61,62], ADF[63-67] (which can account for relativistic effects[68-70]), ABINIT[71], and others have played essential roles in calculating energy minimized gas-phase or crystal structures and their corresponding NMR parameters.

DFT is a computational method that is most often used to calculate NMR parameters. As opposed to *ab initio* methods, the main goal of DFT is to calculate the energy of a system using the electronic density of the system rather than solving the wavefunction *via* the Schrödinger equation. This is achieved by functionalizing the electronic density, $\rho(\vec{r})$, to form the *density functional*, such that:

$$E_{DFT} = E[\rho(\vec{r})] \qquad \text{Eq. 1-18}$$

While the exact density functional is not known, it can be approximated by breaking it down into four terms that can be approximated[72]:

$$E[\rho] = T_s[\rho] + E_{Ne}[\rho] + J[\rho] + E_{XC}[\rho] \qquad \text{Eq. 1-19}$$

including the kinetic energy term, $T_s[\rho]$, the electron-nucleus attraction potential, $E_{Ne}[\rho]$, the Coulombic interaction between electrons, $J[\rho]$, and the exchange-correlation, $E_{XC}[\rho]$.

In DFT, it is the modification of the $E_{XC}[\rho]$ term that is most often studied to produce different "flavours" of DFT, or *functionals*, that most accurately describe a system's total energy for a given problem. Density functionals such as LDA, GGA PBE[73], B3LYP[74,75] and others are widely used to compute NMR parameters, with GGA PBE having been designed for period calculations and B3LYP designed to be applied to gas-phase cluster models.[76,77]

These functionals are often applied to model clusters in gas phase calculations. It is important to simulate a solid crystal lattice's long-range effects in NMR crystallography by carrying out calculations on an entire crystal structure. On an atomic scale, this is problematic because the computational cost increases exponentially with an increasing number of electrons. The problem is solved by imposing periodic boundary conditions on a crystalline system (0 K) with repeating unit cells in the GIPAW DFT method, limiting the computational resources required to calculate and reproduce accurate results.[78,79]

Relativistic effects are of particular concern for quantum chemical calculations.[80] In general, heavier atoms must be subjected to relativistic perturbations to the electronic energy. Normally, calculations are carried out under the non-relativistic approximation, but as a nucleus gets larger, electrons must travel faster around the nucleus in order to maintain a sufficient amount of kinetic energy to overcome the attraction to the nucleus. Consequently,

the electrons travel faster, compared to the speed of light. Relativistic effects take this into account, and affect atoms differently depending on the speed that their electrons travel.

1.3.3 Mechanochemistry

Mechanochemistry is the study of solid-state chemical changes resulting from energy input derived from mechanical processes. The benefit of mechanochemistry is that often chemical reactions can proceed in the absence of excess solvents or heating, making this a key component in the recent uptick of interest in green chemistry. Solid-state NMR studies of mechanochemically formed cocrystals have been popular in the last number of years. The formation of a bulk powder of racemic praziquantel hemihydrate in a vibrational mill was investigated in a detailed study by Zanolla *et al.*[81], showing how mechanochemistry can be practical and sometimes the only way to access new polymorphs. For example, Xu *et al.* observed the formation of mechanochemically induced halogen bonded solids featuring P=O---I-C motifs by observing ^{31}P-^{17}O *J*-coupling.[82] In another example by Peach *et al.*[83], cocrystals of fluoxetine hydrochloride and benzoic acid, fumaric acid and succinic acid were prepared by liquid-assisted and neat grinding and analyzed by ^{35}Cl solid-state NMR. Their study showed that grinding can yield active pharmaceutical ingredient (API) cocrystals with higher purity and that ^{35}Cl is particularly well suited for detecting the differences between the cocrystals and the respective starting materials due to the high sensitivity of ^{35}Cl to the hydrogen bonding environment surrounding the chloride ion. Mechanochemistry was also used to prepare anion coordinated architectures based on 3-iodoethynyl pyridine and 3-iodoethynylbenzoic acid and subsequently studied by solid-state NMR to characterize their presence.[84]

An exciting example of the use of mechanochemistry in NMR crystallography is the isotopic labelling of compounds. Laurencin and colleagues have been active in this area, having demonstrated the feasibility of ^{17}O labelling by mechanochemical methods.[85,86] For example, ibuprofen was ^{17}O-enriched for the first time in the presence of only 1.5 equivalents of $H_2{}^{17}O$ and 1,1'-carbonyl-diimidazole under ball milling for 5 minutes, resulting in approximately 8% enrichment per carboxylic acid oxygen. The ^{17}O MAS spectrum was obtained in less than two hours of acquisition. This work's impact is that ^{17}O NMR becomes more accessible for just about any organic or inorganic compound of interest, including potentially many of the compounds studied in this work, due to the low cost of enrichment.

1.4 NMR Crystallography

Solid-state NMR spectroscopy has long played a vital role in the characterization of solid materials. Solid-state NMR is suitable for many systems because it is non-invasive, and the required equipment is widely available. It can probe nuclei of interest, whose spectral responses are sensitive to even the most subtle changes in their local electronic environments. The purpose of this chapter is to provide an overview of how solid-state NMR spectroscopy is used in conjunction with other experimental techniques to provide valuable insights into the structure of organic crystals. A short literature review of recent developments in NMR crystallography focusing on solid-state NMR study of crystal polymorphs is provided to illustrate the importance of NMR crystallography. The scope is then narrowed down to the use of NMR crystallography to probe noncovalent interactions, specifically tetrel bonds that form this thesis's basis.

There are many reasons to study crystal structures. There are many examples where crystal structures may adopt different phases, called polymorphs, because of the unique crystal

growth medium or method used. Noncovalent interactions play a vital role in the formation of crystal structures, and solid-state NMR is used extensively to understand the nature of such interactions, including hydrogen bonds and σ-hole interactions, and how they play a role in guiding crystallization. Crystal structures may convert into other forms because of external effects (e.g., temperature, pressure) or, in the case of pharmaceuticals, the presence of excipients and other ingredients in a pharmaceutical formulation. Polymorphs are especially crucial in pharmaceutical sciences because each polymorph of an active pharmaceutical ingredient (API) generally exhibits unique bioavailability properties and because each polymorph can be subject to a patent.

1.4.1 Polymorphism

Polymorphism is the ability of a substance to crystallize in more than one distinct crystal structure and forms the basis of many questions in NMR crystallography. Understanding polymorphism extant in solids of interest is essential because the arrangement of a crystal structure can affect how it dissolves or, in the case of pharmaceuticals, their bioavailability. For example, a crystallization process can yield a kinetic or thermodynamic product, or multiple forms thereof, depending on the imposed conditions. Packing polymorphism occurs when the arrangement of molecules changes in forming a crystal structure, depending on the external conditions such as the crystallization solvent used, ambient temperatures or pressures.

The use of solid-state NMR for characterizing organic solids and APIs is well established. Solid-state NMR methods are used extensively to describe the structures and noncovalent bonding networks present in pharmaceutical solids. However, one of the biggest challenges to drug manufacturers is polymorphism, the possibility that a particular crystal

structure alters its phase spontaneously or during manufacturing processes. Polymorphism can impact the function of an API's solvation properties or bioavailability.[87] Much effort has been put into establishing protocols whereby polymorphs can be identified either in pure phases or pharmaceutical mixtures (including excipients and other ingredients).

One-dimensional solid-state NMR often suffices for detecting polymorphism. For example, one-dimensional ^{13}C solid-state NMR is usually suitable for studying the significant differences from one polymorph to another. ^{13}C CP/MAS has been used to study polymorphism in piracetam[88], an API related to Alzheimer's and dementia treatment. It exists in three stable forms at normal pressures obtained by recrystallization in different solvents or by heating (form II and form III; and form I, respectively). The unambiguous assignment of carbon peaks in ^{13}C CP/MAS spectra was used to study the differences between the three polymorphs, which can be done at moderate magnetic field strengths. However, molecules like piracetam feature many nitrogen atoms. It is crucial to consider the broadening and splitting of the ^{13}C signal due to dipolar coupling to ^{14}N. The splitting should not be mistaken as overlapping ^{13}C signals or *J*-coupling. This issue can often be resolved by running the experiments at higher magnetic field strengths. One goal of identifying polymorphs is to determine the constitution of pharmaceutical formulations. Comparing the pure form of piracetam to a series of commercial formulations, including excipients and other ingredients, shows that the form III polymorph is most often used in pharmaceutical formulations. DFT was further used in this paper to study the effects of temperature on the stability of the polymorph's unique forms, giving insights into the processes by which the three forms can interconvert at different temperatures.

One-dimensional solid-state NMR may not be sufficient for characterizing polymorphs in a more complex pharmaceutical sample. Often, drug molecules are complex and exhibit overlapping chemical shifts. Two-dimensional methods such as HETCOR are beneficial in these circumstances because they allow for identifying a species through 'fingerprinting' and structural elucidation based on heteronuclear through-space correlations. An example of this is the case of cefazolin sodium[89], a cephalosporin antibiotic that forms four distinct phases depending on the preparation method: the α-form (pentahydrate), β-form (sesquihydrate), γ-form (methanol solvate) and the amorphous phase. ^{13}C CP/MAS clearly showed that, in fact, among a series of commercial formulations prepared by different vendors, the α-form is usually used.

Nevertheless, between different pharmaceutical manufacturers, subtle differences between preparations, likely resulting from the manufacturing process, can even be probed. Solid-state NMR provides a clear picture of the differences between the cefazolin formulations prepared by three different vendors and reveals subtle differences in formulations containing the α-form, specifically at the C19 and C14 sites. This conclusion was confirmed by two-dimensional ^{1}H-^{13}C HETCOR spectra and attributed to a phenomenon related to the molecules' unique arrangements within the unit cell. Theoretical calculations exploring the change in the shape of the C19 signal from one formulation to the next show that this is related to forming a hydrogen bond in conformation 2, while the signal at C14 is affected by the degree to which conformation 2 is present in the formulation. This study showed the power of solid-state NMR for detecting very subtle changes in the arrangements of atoms or side chains in a crystal structure, despite the unit cell parameters remaining essentially the same.

An unusual case of polymorphism involves the interconversion of some substances between a salt and a cocrystal.[90] These situations are rare: there are only a few known cases where the same chemical species can crystallize as one or the other at the same temperature, and only in the last couple of years has there been an increase in interest in these peculiar compounds.[91-94] Bernasconi *et al*. recently discussed one of these examples comprising an adduct of ethionamide and salicylic acid[95] where either liquid-assisted grinding or rapid evaporation selectively produced the salt or cocrystal, respectively. X-ray diffraction results showed that the salt crystallized in a $P2_1/c$ space group, with one unit each of the cation and anion in the asymmetric unit, whereas the cocrystal crystallized in the $P2_1/n$ space group with one unit of both molecules present in the asymmetric unit. ^{15}N CP/MAS provides evidence as to the ionic or neutral charge nature of the compounds. For the salt, N1 exhibited a shift of 211.9 ppm compared to 309.0 ppm for pure ethionamide, versus a shift to only 273.4 ppm for the cocrystal. The authors noted that these results are consistent with proton transfer and neutral hydrogen bonding based on prior studies. Bridging N-H distances were extracted from $^{1}H\{^{14}N\}$ PM-S-RESPDOR experiments, resulting in values of 1.07 Å for the salt and 1.50 Å for the cocrystal, in excellent agreement with a CSD survey of various pyridine-carboxylic acid interactions. The results were supported by DFT calculations, thermal analysis and dissolution kinetic tests, where the thermodynamic phase is the salt, and the kinetic phase is the cocrystal. This study successfully demonstrated that solid-state NMR is useful alongside X-ray diffractions and several other techniques to detect salt-cocrystal polymorphism easily.

1.5 Probing noncovalent bonding in solids

A key aspect of NMR crystallography is the study of noncovalent interactions. Understanding inter- and intramolecular interactions is a fundamental practice of NMR

crystallography because they influence the formation of a periodic crystal structure to varying degrees depending on their bond strengths. Conversely, understanding bonding is equally vital as it contributes directly to the understanding of conformational polymorphism and dynamics. Solid-state NMR provides observables related to the electronic properties of nuclei as they interact with other atoms. The chemical shift, the quadrupolar interaction, dipolar coupling, and *J*-coupling may be used to understand the nature of bonding and noncovalent interactions. For example, an effort will be made to summarize the relationship between NMR crystallography and noncovalent interactions, but the reader is directed to other manuscripts that discuss this subject at length.[96,97]

Noncovalent interactions are prevalent in chemistry and arise due to the interaction between anisotropic electronic charge distributions over molecules' surfaces. While noncovalent interactions are classified based on their electrostatic properties, one of the most significant examples is the hydrogen bond.

Hydrogen bonds[98-100] are likely the most studied of the noncovalent interactions by NMR spectroscopy as they are one of the most well-known and are significant in many applications, including crystal engineering, biological process, catalysis and materials science. Interactions such as π-π, cation-π and anion-π play an essential role in guiding crystallization (for an exciting look at the role of π-π stacking in crystal engineering, see a recent virtual issue of Crystal Growth and Design[101]). Beyond that, an effort has been made to understand the hydrogen bond and its effect on NMR chemical shifts.[102-105] X-ray crystallography can play an essential role in identifying hydrogen bonds and their geometries but cannot always determine hydrogen atom positions with high accuracy. Solid-state NMR alongside GIPAW DFT methods can confirm hydrogen bond lengths using dipolar coupling measurements.

1.6 σ-hole Interactions and Tetrel Bonds

Analogous to hydrogen bonds are σ-hole interactions. These involve the attractive interaction between the electrophilic region of a donor atom (σ-hole) and an electron-rich acceptor.[106-108] This naming convention originates from hydrogen bonding, where the donor atom is the one that provides the hydrogen to the hydrogen bond. In this case, however, the electropositive atom is considered the donor, but it behaves somewhat differently from a hydrogen bond.

These sorts of interactions are named after the group in the periodic table (groups 14-17) to which the electrophilic atom belongs.[109] Examples of σ-hole interactions include halogen (XB)[110], chalcogen (ChB)[111], pnictogen (PnB)[112], and tetrel (TB)[113] bonds. Even the term "aerogen bond" [114] has been coined for the noble gases.

A σ-hole is an area of reduced electron density that forms over an atom bonded to an electronegative substituent. The electrostatic potential, $V(r)$, over the surface of an atom is related to electron density, $\rho(r)$, and the nuclear charge, Z_A, at any point, r, on its surface and is described by[115]:

$$V(r) = \sum_A \frac{Z_A}{|R_A - r|} - \int \frac{\rho(r')dr'}{|r' - r|} \qquad \text{Eq. 1-20}$$

where R_A is the point which describes the nucleus. When the electron density is removed from the pole opposite the covalent bond, an electrophilic area of increased electrostatic potential forms. Because the σ-hole generally forms directly opposite of the covalent bond, and there can be as many σ-holes as there are covalent bonds, provided the substituents are each electronegative enough to form the σ-hole. The σ-hole is a highly directional and tunable

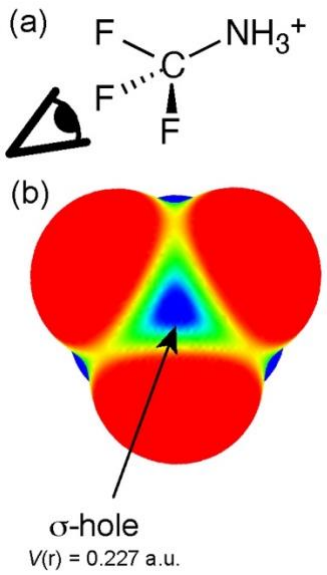

Figure 1-2. Molecular electrostatic potential (b) (MESP) diagram of $CF_3NH_3^+$ depicting a σ-hole on carbon, as observed from the opposite end of the C-N covalent bond. Shown in (a) is the chemical structure, where the eye corresponds to the perspective from which (b) is shown. The MESP was calculated using Gaussian 09 using the B3LYP functional with a 6-31G* basis set. The molecular electrostatic potential, $V(r)$ of the centre of the σ-hole, in units of a.u., taken at the 0.001 electrons $Bohr^{-3}$ isodensity surface, is indicated by the black arrow. The colour red corresponds to values ≤ 0.170 a.u., while blue areas correspond to values ≥ 0.217 a.u.

interaction.[116-120] σ-hole interactions may therefore be described schematically as R—X···Y bonds, where R is the electron-withdrawing substituent, X is the bond donor atom, and Y is the Lewis base acceptor atom (**Figure 1-3**).

It is important to note that while the σ-hole is an electrostatic description that provides an excellent and intuitive model to describe these interactions, there is a debate in the literature about the exact mechanism by which this form of noncovalent bonding occurs. Evidence suggests that charge transfer[121-125] mechanisms occurring between molecular orbitals are essential for considering the accurate description of the σ-hole interaction. In this model, the

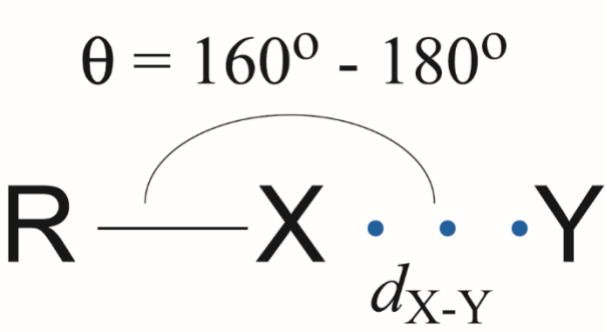

Figure 1-3. Generalized example of a σ-hole interaction, where X is the interaction donor atom and may be an element within the halogen, chalcogen, pnictogen and tetrel groups of the periodic table.

bonding process is mediated in part by an electron charge transfer from a nonbonding orbital on the Lewis base to the antibonding orbital in the donor atom's covalent bond. Experimentally, halogen bonds' strength, for example, correlates well with the amount of charge transfer between the donor and acceptor atoms. Fundamentally, electrostatics and charge transfer can be considered equally important in describing the bonding mechanisms in σ-hole interaction.[126] However, from an NMR crystallographic point of view, the interaction's exact mechanism is not a matter of great importance for relating NMR observables to the crystallographic structure of solids.

Many works have been undertaken to understand the experimental observables related to the formation of σ-holes. In a computational study, Lu and Scheiner[127] suggested that the NMR signal for donor nuclei involved in noncovalent interactions exhibit consistent spectroscopic changes: first, the covalent bond is weakened and shows an IR redshift because of the bond stretching; second, the magnetic shielding of the electrophile increases while that

of the electron donor decreases; third, the relative magnitude of the changes follow periodic trends. In a recent advance on the understanding of chalcogen bonding, Kumar *et al.* showed the utility of solid-state NMR and vibrational spectroscopy for studying chalcogen bonds.[128] In their work, ^{77}Se CP/MAS spectroscopy was performed at 9.4 T ($\nu_L(^{77}Se)$ = 76.311 MHz). They showed the ^{77}Se chemical shift tensor correlates to the geometry at the site of the chalcogen bond. On cocrystal formation, they found the isotropic chemical shift to generally decrease. In particular, δ_{11} of ^{77}Se increases for nitrogen-based donors (increase in the span) but decreases when the donor is a halide ion (reduction in span). δ_{33} was found to decrease generally. Notably, the authors also reported some ^{125}Te CP/MAS data; however, the NMR data could not be obtained for all the cocrystals because of the complexes' stability. Kumar *et al.* probed double chalcogen bonds present in a series of 12 cocrystals in a related study.[129] ^{77}Se and ^{125}Te NMR confirmed the correlation between chalcogen bond geometry and chemical shift tensor data. The change in the measured span provides insights into the ChB geometry and results from the Ch-N bonding orbitals' contribution to the chemical shift tensor. Along with chalcogen bonding, solid-state NMR has provided valuable contributions to understanding pnictogen bonding via ^{209}Bi-^{31}P *J*-coupling.[130]

Single-crystal solid-state NMR studies have been useful but under-used in providing critical insights into noncovalent bonding. For these studies, suitably sized crystals are grown and mounted on a goniometer fixed in a solid-state NMR probe. Throughout the NMR analysis, the sample is rotated stepwise to record the magnitude of the NMR interaction tensors and their orientation with respect to the molecular frame. The information obtained from these experiments can give rise to a greater understanding of noncovalent interactions' nature, translating to a greater appreciation of the guiding forces in crystallization processes.

Past single-crystal NMR studies have looked at hydrogen bonding, both directly[131-133] and indirectly.[134-136] Recently, the method was used to study halogen bonds[137] by ^{31}P and ^{17}O NMR at 9.4 T ($\nu_L(^{31}P)$ = 161.976 MHz, ($\nu_L(^{17}O)$ = 54.243 MHz). Three cocrystals that feature halogen bonds involving ^{17}O-enriched $Ph_3P^{17}O$ acceptors were studied. The single-crystal NMR data were used to obtain exact measurements of the ^{17}O and ^{31}P chemical shift and EFG tensors related to structural features across the halogen bond. It was found that the direction of both the unique components of the ^{31}P and ^{17}O CS tensors and the ^{17}O quadrupolar coupling tensor were dependent on the linearity of the halogen bond, while the magnitude of these interactions is also sensitive to the halogen bond formation. The spectra further revealed that upon halogen bond formation, $\mathbf{J}(^{31}P, ^{17}O)$ tensor asymmetry increases from 0.43 to 0.47, while the magnitude of anisotropy of **J** decreases from -512 to -281 Hz. The study provides insights into the NMR response upon halogen-bond-induced crystallization.

This thesis focuses on the study of tetrel bonding by solid-state NMR. Presented within the introduction to each chapter of this thesis is a literature review of tetrel bonds, which collectively form a comprehensive description of the tetrel bond. A more recent look at the tetrel bond is presented to allow the reader to understand what it is and why it is important.

Noncovalent interactions have been identified for most groups in the periodic table.[138] Having been identified long before they were named[139], tetrel bonds are known as such based on where the donor atom resides on the periodic table: in this case, group 14 or the *Tetrel* elements (**Figure 1-4**).[140] Today, tetrel bonds are well known. Recent crystal structure database surveys have revealed numerous examples of tetrel bonds occurring with carbon, silicon, lead, tin and germanium centres, leading to numerous studies into the utility of tetrel bonds in crystal engineering. [141-145]

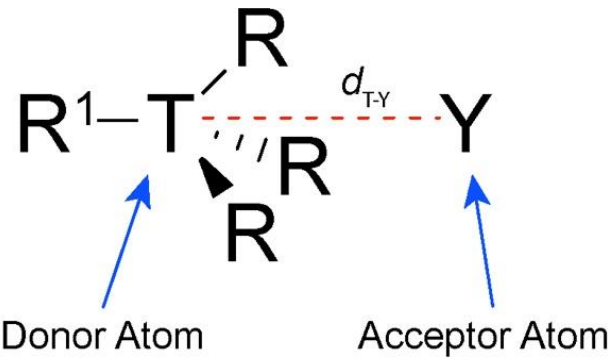

Figure 1-4. The general structure of a tetrel bond. The bond features a group 14 "tetrel" donor atom, T, with tetrahedral geometry and a nucleophilic acceptor atom. R^1 refers to the electron-withdrawing substituent to which the tetrel atom is covalently bonded, while R can be any other neutrally charged substituent, often H, such as in the case of a methyl group.

ike other σ-hole interactions, tetrel bonds tend to be short and linear. They are tunable, with the strength and the size of a σ-hole on a tetrel atom increasing as its polarizability increases and as the strength of the electron-withdrawing substituent increases. **Figure 1-5** depicts the phenomenon whereby the size and strength of the σ-hole increases as the atomic number of the tetrahedral tetrel donor atom increases (C < Si < Ge < Sn < Pb). $V(r)$ values taken from the centre of the σ-hole are shown to systematically increase from carbon down to lead (**Table 1-1**). Interestingly, however, the MESP diagram for carbon shows that while a σ-hole is present, it is very weak compared to the other molecules. This is not surprising, as carbon is the least polarizable element in group 14. The calculated electrostatic potential is very similar to the surrounding hydrogen atoms, making it possible for weak CH···X hydrogen bonds to form in competition with the σ-hole. The inherent weakness of a carbon σ-hole is unavoidable, but its relative strength can be improved by adding stronger electron-withdrawing substituents, such as depicted in **Figure 1-5**, where the hydrogen atoms are replaced with fluorines.

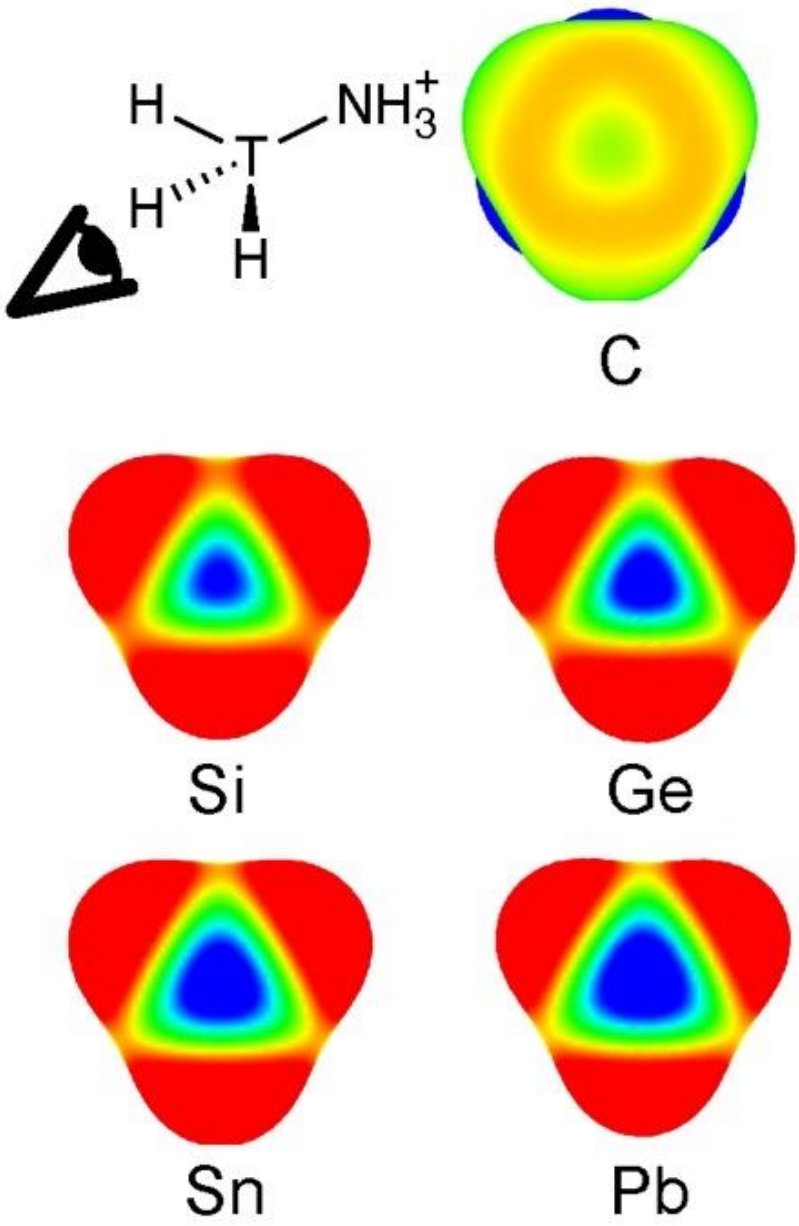

Figure 1-5. MESP diagrams of $TH_3NH_3^+$ (T = C, Si, Ge, Sn and Pb) depicting a σ-hole on tetrahedral tetrel bond donor atoms, as observed from the opposite end of the C-N covalent bond. The MESP diagrams were generated from calculations using Gaussian 09 using the B3LYP functional with a 6-31G* basis set for molecules containing C, Si and Ge, and the LANL2DZ basis set for the heavier elements Sn and Pb. The molecular electrostatic potential, $V(r)$ of the centre of the σ-hole, in units of a.u., taken at the 0.001 electrons Bohr^{-3} isodensity surface, are shown in **Table 1-1**. The colour red corresponds to values ≤ 0.170 a.u., while blue areas correspond to values ≥ 0.217 a.u.

Table 1-1. Values of $V(\mathbf{r})$ taken at the centre of the σ-holes for the molecules depicted in **Figure 1-5**.

Donor Atom	$V(\mathbf{r})$ at σ-hole / a.u.
C	0.186
Si	0.220
Ge	0.228
Sn	0.231
Pb	0.235

An MESP map over 1,3-dimethyluracil, a structural analogue to caffeine and theophylline (to be discussed in Chapter 2), was generated to demonstrate that σ-holes are relevant to structures more complex than simple gas-phase molecules. **Figure 1-6** depicts the MESP generated at the 0.001 electron Bohr^{-3} isosurface of 1,3-dimethyluracil, in which it is clear that a σ-hole is positioned on the extension of an N-CH_3 covalent bond. While the σ-hole itself is somewhat delocalized with the hydrogen atoms bonded to carbon, it demonstrates the possibility for a Lewis base acceptor atom to engage carbon at this site.

In the last decade over which the concept of sigma-hole bonding has piqued many chemists' curiosity, there have been numerous studies, primarily computational on simple model systems, investigating the ability for tetrel centres to interact electrophilically with anions. Over the years, there have been numerous reviews written to discuss the subject. [146-148] More recently, for example, the idea of tetrel bonding has been explained using other examples. For example, tetrel bonding from π-electrons on aromatic rings is known to occur.[149]

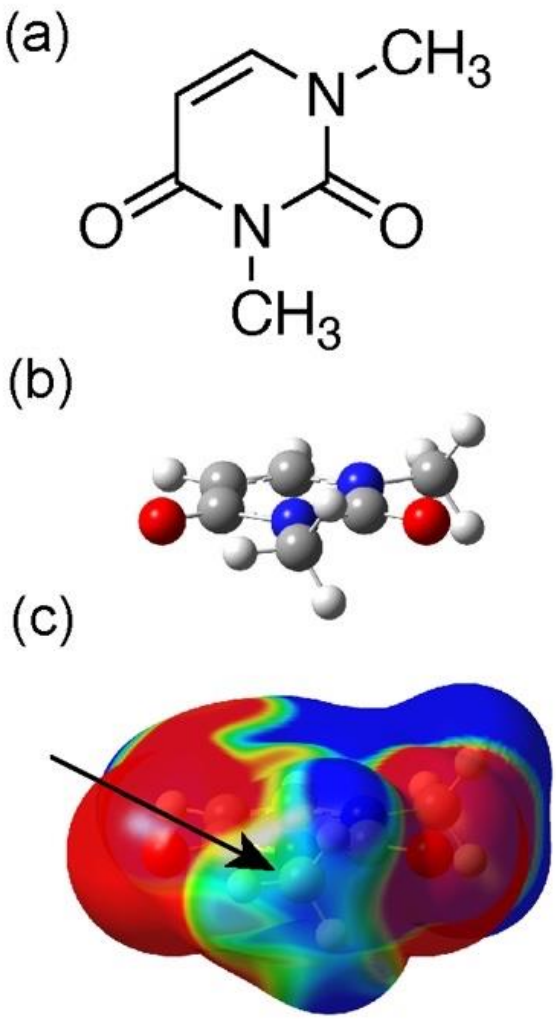

Figure 1-6. (a) Chemical structure of 1,3-dimethyluracil (b) Geometry optimized structure of 1,3-dimethyluracil with the corresponding (c) MESP diagram depicting a weak σ-hole at the centre of the N-CH_3 methyl carbon (indicated by the arrow). The MESP diagrams were generated from calculations using Gaussian 09 using the B3LYP functional with a 6-31G* The MESP map was generated at the 0.001 electrons $Bohr^{-3}$ isodensity surface. The colour red corresponds to $V(r)$ values ≤ 0.01 a.u., while blue areas correspond to values ≥ 0.013 a.u.

Not surprisingly, lead has been studied extensively in recent years due to the apparent ease with which it readily forms tetrel bonds. Pb(II) based tetrel bonds are vital in stabilizing various supramolecular complexes in hemidirectionally coordinated complexes.[150-156] Pb(II), as opposed to Pb(IV) has the unique characteristic of adopting either hemidirected or

holodirected geometry, based on the stereoactivity of the $6s^2$ lone pair of electrons. The stereochemical activity of this lone pair is related to the coordination environment around Pb(II), with the lone pair becoming inactive, or *holotropic*, when the coordination number exceeds 5.[157,158] Of course, as seen in Chapter 3, Pb(II) ligands can be chosen in such a way that the geometry of the Pb(II) ion is forced to be hemidirectional. The tetrel bonds to lead centres are relatively easily studied by computational techniques such as quantum chemical computational techniques, including Hirshfeld surface analysis and quantum theory of atoms-in-molecules (QTAIM) calculations. Such calculations can confirm the presence of Pb···X tetrel bonds in the aforementioned Pb(II) complexes.[150] Pb(IV), which forms tetrahedral geometry, is also shown to form tetrel bonds in several examples.[159]

Tetrel bonding is important in both organic chemical and biological reactions. One of the easiest ways to demonstrate the importance of a tetrel bond in chemistry is by indicating its role as the precursor to S_N2 displacement reactions.[160,161] In biochemical applications, the tetrel bond has been observed to induce the conversion of amino acids into zwitterions via proton transfer.[162] There is also evidence that the tetrel bond plays a vital role in some biological processes.[163] A survey of AdoMet-bound methyltransferase structures resulted in geometries that suggest methyl tetrel bonding to electronegative atoms in small molecule inhibitors, solvent molecules, and ions may have an important role in catabolism and other processes.[164] In another study, carbon tetrel bonds in proteins contribute enthalpically to the protein structure's overall hydrophobic interaction and play a role in other metabolic processes.[165]

It has become evident that the tetrel bond is an imperative class of noncovalent interaction. From investigating the nature of the interaction to understanding what can affect

a tetrel bond's strength, much work has collectively gone into developing a general picture of what is going on with tetrel bonds. Models such as valence shell electron pair repulsion (VSEPR) theory[166] and valence bond theory[167] have helped describe tetrel bonds. At the basic level, there is some debate about the degree to which electrostatics *versus* charge transfer plays a role in the tetrel bond. Many works argue that charge transfer at least partially[168] explains the tetrel bond. For example, in tetrahedral carbons[169], complexation results in charge transfer from the Lewis base to the tetrel bond donor.

Furthermore, a stronger interaction results in a shorter interaction length, which results from covalent character.[170,171] The addition of electron-withdrawing substituents on pyridine rings affects tetrel bond strength in tetrel bonds from nitrogen. [172] In that work, Laplacian and energy densities are calculated to be positive in complexes with CH_3F, which indicates that the interaction features closed-shell atoms and that the interaction is purely electrostatic. However, when the tetrel element is either Si or Ge, the calculated Laplacian remains positive, but the electron density is negative, suggesting some covalency in the bond. Charge transfer, calculated as the sum of all atomic natural bond orbital charges, is observed for all of the studied species, and the amount of charge transfer that occurs correlates with interaction energy, which depends on the nature of the electron-withdrawing substituent. The correlation of charge transfer with the interaction energy is supported by other work.[173] While the electrostatic model is often associated with inconsistencies regarding the bonding energy, it is still viewed as the dominant effect.[169] In one particular study, an analysis of the bond energy decomposition revealed that electrostatic contribution plays a significant role in the studied tetrel bonded complexes.[174] In another example[175], tetrel bonds involving tetrel anions as acceptors are shown to form strong interactions with bonding energies as large as 90 kcal/mol,

with the strength increasing as the acceptor tetrel anion becomes smaller in size or as the donor tetrel atom becomes larger. Calculations showed that the electrostatic component is dominant and calculated to comprise up to 55-70% of the total interaction energy.

This thesis does not attempt to determine the precise nature of a tetrel bond. Nor is it written to argue one descriptive model over the other. Generally speaking, the tetrel bond, like the other σ-hole interactions to which it is related, can be explained by both electrostatic effects and charge transfer, which are not mutually exclusive. Instead, this thesis attempts to describe the NMR response to tetrel bonding to be applied to the broad field of NMR crystallography. Before writing this work, both computational and experimental techniques have been used to study the spectroscopic properties of the tetrel bond. In recent studies, the tetrel bond formation has been related to responses in vibrational, rotational and NMR spectroscopic methods.[176-181] In one notable example, computational vibrational spectroscopic data has provided a means to calculate tetrel bond strengths directly.[182] In the study, bond strengths over a series of complexes were calculated to be between -1.4 to -26 kcal/mol, with the more robust bonds resulting from the addition of electron-withdrawing substituents to the tetrel bond donor molecule. This, in turn, affects the tetrel bond's partial covalency and the degree to which the electrons delocalize from the HOMO of the acceptor molecule to the LUMO of the tetrel bond donor.

Before embarking on this thesis's work, this author had written the only previous solid-state NMR study that had been performed to understand the NMR response resulting from tetrel bond formation.[183] In that work, there was a clear trend observed between the ^{13}C chemical shift and the formation of a C···O tetrel bond in two cocrystals featuring small organic molecules. This work is, therefore, a continuation of that initial investigation and

presents a systematic study of the NMR response to three different NMR-active tetrel bond donors with the primary goal of understanding how, and under what circumstances, must a tetrel bond be considered when applying solid-state NMR to understanding the crystal structure of compounds featuring tetrel bonds.

1.7 References

[1] Burgess, K. M. N.; Widdifield, C. M.; Xu, Y.; Leroy, C.; Bryce, D. L. Structural Insights from ^{59}Co Solid-State NMR Experiments on Organocobalt(I) Catalysts. *ChemPhysChem* **2018**, *19*, 227-236.

[2] Crewdson, P.; Bryce, D. L.; Rominger, F.; Hofmann, P. Application of Ultrahigh-Field ^{59}Co Solid-State NMR Spectroscopy in the Investigation of the 1,2-Polybutadiene Catalyst [Co(C_8H_{13})(C_4H_6)]. *Angew. Chem. Int. Ed.* **2008**, *47*, 3454-3457.

[3] Szell, P. M. J.; Zablotny, S.; Bryce, D. L. Halogen Bonding as a Supramolecular Dynamics Catalyst. *Nat. Commun.* **2019**, *10*, 916.

[4] Lummiss, J. A. M.; Perras, F. A.; McDonald, R.; Bryce, D. L.; Fogg, D. E. Sterically Driven Olefin Metathesis: The Impact of Alkylidene Substitution on Catalyst Activity. *Organometallics*, **2016**, *35*, 691-698.

[5] Sutrisno, A.; Huang, Y. Solid-state NMR: A powerful tool for characterization of metal-organic frameworks. *Solid State Nucl. Magn. Reson.* **2013**, *49-50*, 1-11.

[6] Cavalli, A.; Salvatella, X.; Dobson, C. M.; Vendruscolo, M. Protein structure determination from NMR chemical shifts. *Proc. Natl. Academ. Sci.* **2007**, *104*, 9615-9620.

[7] Zanolla, D.; Hasa, D.; Arhangelskis, M.; Schneider-Rauber, G.; Chierotti, M. R.; Keiser, J.; Voinovich, D.; Jones, W.; Perissutti, B. Mechanochemical Formation of Racemic Praziquantel Hemihydrate with Improved Biopharmaceutical Properties. *Pharmaceutics*, **2020**, *12*, 289.

[8] Slichter, C. P. *Principles of Magnetic Resonance*. Springer-Verlag Berlin Heidelberg: Harper & Row Publishers, New York, 1963.

[9] Abragam, A. *The Principles of Nuclear Magnetism.* Clarendon Press: Oxford University Press, London, 1961.

[10] Harris, R. K.; Becker, E. D.; Menezes, S. M. C. D.; Granger, P.; Hoffman, R. E.; Zilm, K. W. Further Conventions for NMR Shielding and Chemical Shifts: (IUPAC Recommendations 2008), *Pure Appl. Chem.* **2008**, *80*, 59-84.

[11] Herzfeld, J.; Berger, A. E. Sideband intensities in NMR spectra of samples spinning at the magic angle, *J. Chem. Phys.* **1980**, *73*, 6021-6030.

[12] Haeberlen, U. High Resolution NMR in Solids Selective Averaging, Supplement to Advances in Magnetic Resonance, Academic Press, Inc. New York, **1976**.

[13] Young, R. P.; Lewis, C. R.; Yang, C.; Wang, L.; Harper, J. K.; Mueller, L. J. TensorView: A software tool for displaying NMR tensors, *Magn. Reson. Chem.* 2019, *57*, 211-223.

[14] Samoson, A. Satellite Transition High-Resolution NMR of Quadrupolar Nuclei in Powders, *Chem. Phys. Lett.* **1985**, *119*, 29-32.

[15] Widdifield, C. M.; Bryce, D. L.; Solid-State ^{127}I NMR and GIPAW DFT Study of Metal Iodides and Their Hydrates: Structure, Symmetry, and Higher-Order Quadrupole-Induced Effects, *J. Phys. Chem. A*, **2010**, *114*, 10810-10823.

[16] Widdifield, C. M.; Bain, A. D.; Bryce, D. L. Definitive solid-state $^{185/187}$Re NMR spectral evidence for and analysis of the origin of high-order quadrupole-induced effects for *I* = 5/2, *Phys. Chem. Chem. Phys.* **2011**, *13*, 12413-12420.

[17] Bain, A. D. Exact calculation, using angular momentum, of combined Zeeman and quadrupolar interactions in NMR, *Mol. Phys.* **2003**, *101*, 3163-3175.

[18] Perras, F. A.; Widdifield, C. M.; Bryce, D. L. QUEST—QUadrupolar Exact SofTware: A fast graphical program for the exact simulation of NMR and NQR spectra for quadrupolar nuclei, *Solid State Nucl. Magn. Reson.* **2012**, *45-46*, 36-44.

[19] Massiot, D.; Fayon, F.; Deschamps, M.; Cadars, S.; Florian, P.; Montouillout, V.; Pellerin, N.; Hiet, J.; Rakhmatullin, A.; Besseda, C. Detection and use of small *J* couplings in solid state NMR experiments, *Comptes Rendus Chim.* **2010**, *13*, 117-129.

[20] Rees, G. J.; Day, S. P.; Barnsley, K. E.; Iuga, D.; Yates, J. R.; Wallis, J. D.; Hanna, J. V. Measuring multiple ^{17}O-^{13}C *J*-couplings in naphthalaldehydic acid: a combined solid state NMR and density functional theory approach, *Phys. Chem. Chem. Phys.* **2020**, *22*, 3400-3413.

[21] Carnahan, S. L.; Lampkin, B. J.; Naik, P.; Hanrahan, M. P.; Slowing, I. I.; Van Veller, B.; Wu, G.; Rossini, RA. J. Probing O-H Bonding through Proton Detected ^{1}H-^{17}O Double Resonance Solid-State NMR Spectroscopy, *J. Am. Chem. Soc.* **2019**, *141*, 441-450.

[22] Viger-Gravel, J.; Meyer, J. E.; Korobkov, I.; Bryce, D. L. Probing halogen bonds with solid-state NMR spectroscopy: observation and interpretation of $J(^{77}\text{Se},^{31}\text{P})$ coupling in halogen-bonded P=Se···I motifs. *CrystEngComm*, **2014**, *16*, 7285-7297.

[23] Kobera, L.; Southern, S. A.; Rao, G. K.; Richeson, D. S.; Bryce, D. L. New Experimental Insight into the Nature of Metal−Metal Bonds in Digallium Compounds: *J* Coupling between Quadrupolar Nuclei. *Chem. -Eur. J.* **2016**, *22*, 9565-9573.

[24] Wong, Y. T. A.; Landmann, J.; Finze, M.; Bryce, D. L. Disorder and Electronic Structures of Electron-Precise Dianionic Diboranes: Insights from Solid-State Multinuclear Magnetic Resonance Spectroscopy. *J. Am. Chem. Soc.* **2017**, *139,* 8200-8211.

[25] Hodgekinson, P. NMR crystallography of molecular organics. *Prog. Nucl. Magn. Reson. Spectropsc.* **2020**, *118-119*, 10-53.

[26] Penzel, S.; Oss, A.; Org, M. -L.; Samoson, A. Böckmann, A.; Ernst, M.; Meier, B. H.; Spinning faster: protein NMR at MAS frequencies up to 126 kHz. *J. Biomol. NMR*, **2019**, *73*, 19-29.

[27] Lin, Y. -L.; Cheng, Y. -S.; Ho, C. -I.; Guo, Z. -H.; Huang, S. -J.; Org, M. -L.; Oss, A.; Samoson, A.; Chan, J. C. C. Preparation of fibril nuclei of beta-amyloid peptides in reverse micelles. *Chem. Commun.* **2018**, *54*, 10459-10462.

[28] Schledorn, M.; Malär, A.A.; Torosyan, A.; Penzel, S.; Klose, D.; A. Oss, A.; Org, M.-L; Wang, S.; Lecoq, L.; Cadalbert, R.; Samoson, A.; Böckmann, A.; Meier, B.H. Protein NMR Spectroscopy at 150 kHz Magic-Angle Spinning Continues to Improve Resolution and Mass Sensitivity, *ChemBioChem*. **2020**.

[29] Samoson, A. 0.2 MHz MAS. In *Experimental Nuclear Magnetic Resonance Conference,* Virtual Online Conference, March 29-31, **2021**.

[30] Goldburg, W. I.; Lee, M.; Nuclear Magnetic Resonance Line Narrowing by a Rotating rf Field, *Phys. Rev. Lett*. **1963**, *11*, 255-258.

[31] Lee, M.; Goldburg, W. I.; Nuclear-Magnetic-Resonance Line Narrowing by a Rotating rf Field, *Phys. Rev*. **1965**, *140*, A1261-A1271.

[32] Vinogradov, E.; Madhu, P. K.; Vega, S. High-Resolution Proton Solid-State NMR Spectroscopy by Phase-Modulated Lee-Goldburg Experiment. *Chem. Phys. Lett.* **1999**, *314*, 443-450.

[33] Bielecki, A.; Kolbert, A. C.; Levitt, M. H. Frequency-Switched Pulse Sequences: Homonuclear Decoupling and Dilute Spin NMR in Solids. *Chem. Phys. Lett.* **1989**, *155*, 341-346.

[34] Waugh, J. S.; Huber, L. M.; Haeberlen, U. Approach to High-Resolution Nmr in Solids. *Phys. Rev. Lett.* **1968**, *20*, 180-182

[35] Mansfield, P. Symmetrized Pulse Sequences in High Resolution NMR in Solids. *J. Phys. C Solid State Phys.* **1971**, *4*, 1444-1452.

[36] Rhim, W. -K.; Elleman, D. D.; Vaughan, R. W. Analysis of Multiple Pulse NMR in Solids. *J. Chem. Phys.* **1973**, *59*, 3740-3749.

[37] Burum, D. P.; Rhim, W.-K. Analysis of Multiple Pulse NMR in Solids. III. *J. Chem. Phys.* **1979**, *71*, 944-956.

[38] Sakellariou, D.; Lesage, A.; Hodgkinson, P.; Emsley, L. Homonuclear Dipolar Decoupling in Solid-State NMR Using Continuous Phase Modulation. *Chem. Phys. Lett.* **2000**, *319*, 253-260.

[39] Elena, B.; de Paëpe, G.; Emsley, L. Direct Spectral Optimisation of Proton-Proton Homonuclear Dipolar Decoupling in Solid-State NMR. *Chem. Phys. Lett.* **2004**, *398*, 532-538.

[40] Paruzzo, F. M.; Emsley, L. High-Resolution ^{1}H NMR of Powdered Solids by Homonuclear Dipolar Decoupling. *J. Magn. Reson.* **2019**, *309*, 106598.

[41] Salager, E.; Day, G. M.; Stein, R. S.; Pickard, C. J.; Elena, B.; Emsley, L. Powder Crystallography by Combined Crystal Structure Prediction and High-Resolution ^{1}H Solid-State NMR Spectroscopy. *J. Am. Chem. Soc.* **2010**, *132*, 2564-2566.

[42] Baias, M.; Widdifield, C. M.; Dumez, J.-N.; Thompson, H. P. G.; Cooper, T. G.; Salager, E.; Bassil, S.; Stein, R. S.; Lesage, A.; Day, G. M.; Emsley, L. Powder Crystallography of Pharmaceutical Materials by Combined Crystal Structure Prediction and Solid-State ^{1}H NMR Spectroscopy. *Phys. Chem. Chem. Phys.* **2013**, *15*, 8069-8080.

[43] Andreas, L. B.; Jaudzems, K.; Stanek, J.; Lalli, D.; Bertarello, A.; Marchand, T. L.; Paepe, D. C.-D.; Kotelovica, S.; Akopjana, I.; Knott, B.; Wegner, S.; Engelke, F.; Lesage, A.; Emsley, L.; Tars, K.; Herrmann, T.; Pintacuda, G. Structure of Fully Protonated Proteins by Proton-Detected Magic-Angle Spinning NMR. *Proc. Natl. Acad. Sci.* **2016**, *113*, 9187-9192.

[44] Zhang, R.; Mroue, K. H.; Ramamoorthy, A. Proton-Based Ultrafast Magic Angle Spinning Solid-State NMR Spectroscopy. *Acc. Chem. Res.* **2017**, *50*, 1105-1113.

[45] Struppe, J.; Quinn, C. M.; Lu, M.; Wang, M.; Hou, G.; Lu, X.; Kraus, J.; Andreas, L. B.; Stanek, J.; Lalli, D.; Lesage, A.; Pintacuda, G.; Maas, W.; Gronenborn, A. M.; Polenova, T. Expanding the Horizons for Structural Analysis of Fully Protonated Protein Assemblies by NMR Spectroscopy at MAS Frequencies above 100 KHz. *Solid State Nucl. Magn. Reson.* **2017**, *87*, 117-125.

[46] van Rossum, B.-J.; de Groot, C. P.; Ladizhansky, V.; Vega, S.; de Groot, H. J. M. A Method for Measuring Heteronuclear (^{1}H–^{13}C) Distances in High Speed MAS NMR. *J. Am. Chem. Soc.* **2000**, *122*, 3465-3472.

[47] Griffin, J. M.; Martin, D. R.; Brown, S. P. Distinguishing Anhydrous and Hydrous Forms of an Active Pharmaceutical Ingredient in a Tablet Formulation Using Solid-State NMR Spectroscopy. *Angew. Chem. Int. Ed.* **2007**, *46*, 8036-8038.

[48] Southern, S. A. 2015, Investigations of Non-Covalent Carbon Tetrel Bonds by Computational Chemistry and Solid Stat NMR Spectroscopy, M. Sc. Thesis, University of Ottawa, Ottawa, Ontario.

[49] Ashbrook, S. E.; McKay, D. Combining solid-state NMR spectroscopy with first-principles calculations - a guide to NMR crystallography, *Chem. Commun.* **2016**, *52*, 7186-7204.

[50] Bryce, D. L.; Sward, G. D. Chlorine-35/37 NMR Spectroscopy of Solid Amino Acid Hydrochlorides: Refinement of Hydrogen-Bonded Proton Positions Using Experiment and Theory. *J. Phys. Chem. B* **2006**, *110*, 26461-26470.

[51] Cui, J.; Olmsted, D. L.; Mehta, A. K.; Asta, M.; Hayes, S. E. NMR Crystallography: Evaluation of Hydrogen Positions in Hydromagnesite by $^{13}C\{^{1}H\}$ REDOR Solid-State NMR and Density Functional Theory Calculation of Chemical Shielding Tensors. *Angew. Chem. Int. Ed.* **2019**, *58*, 4210-4216.

[52] Harris, R. K.; Ghi, P. Y.; Hammond, R. B.; Ma, C.-Y.; Roberts, K. J. Refinement of Hydrogen Atomic Position in a Hydrogen Bond Using a Combination of Solid-State NMR and Computation. *Chem. Commun.* **2003**, *22*, 2834-2835.

[53] Widdifield, C. M.; Bryce, D. L. Crystallographic Structure Refinement with Quadrupolar Nuclei: A Combined Solid-State NMR and GIPAW DFT Example Using $MgBr_2$. *Phys. Chem. Chem. Phys.* **2009**, *11*, 7120-7122.

[54] Joyce, S. A.; Yates, J. R.; Pickard, C. J.; Mauri, F. A First Principles Theory of Nuclear Magnetic Resonance *J*-Coupling in Solid-State Systems. *J. Chem. Phys.* **2007**, *127*, 204107.

[55] Profeta, M.; Mauri, F.; Pickard, C. J. Accurate First Principles Prediction of ^{17}O NMR Parameters in SiO_2: Assignment of the Zeolite Ferrierite Spectrum. *J. Am. Chem. Soc.* **2003**, *125*, 541-548.

[56] Pickard, C. J.; Mauri, F. All-Electron Magnetic Response with Pseudopotentials: NMR Chemical Shifts. *Phys. Rev. B* **2001**, *63*, 245101.

[57] Yates, J. R.; Pickard, C. J.; Mauri, F. Calculation of NMR Chemical Shifts for Extended Systems Using Ultrasoft Pseudopotentials. *Phys. Rev. B* **2007**, *76*, 024401.

[58] Clark, S. J.; Segall, M. D.; Pickard, C. J.; Hasnip, P. J.; Probert, M. I. J.; Refson, K.; Payne, M. C. First Principles Methods Using CASTEP. *Z. Für Krist. - Cryst. Mater.* **2005**, *220*, 567-570.

[59] Green, T. F. G.; Yates, J. R. Relativistic Nuclear Magnetic Resonance J-Coupling with Ultrasoft Pseudopotentials and the Zeroth-Order Regular Approximation. *J. Chem. Phys.* **2014**, *140*, 234106.

[60] Refson, K.; Tulip, P. R.; Clark, S. J. Variational Density-Functional Perturbation Theory for Dielectrics and Lattice Dynamics. *Phys. Rev. B* **2006**, *73*, 155114.

[61] Giannozzi, P.; Baroni, S.; Bonini, N.; Calandra, M.; Car, R.; Cavazzoni, C.; Ceresoli, D.; Chiarotti, G. L.; Cococcioni, M.; Dabo, I.; Corso, A. D.; Gironcoli, S. de; Fabris, S.; Fratesi, G.; Gebauer, R.; Gerstmann, U.; Gougoussis, C.; Kokalj, A.; Lazzeri, M.; Martin-Samos, L.; Marzari, N.; Mauri, F.; Mazzarello, R.; Paolini, S.; Pasquarello, A.; Paulatto, L.; Sbraccia, C.; Scandolo, S.; Sclauzero, G.; Seitsonen, A. P.; Smogunov, A.; Umari, P.; Wentzcovitch, R. M. QUANTUM ESPRESSO: A Modular and Open-

Source Software Project for Quantum Simulations of Materials. *J. Phys. Condens. Matter* **2009**, *21*, 395502.

[62] Giannozzi, P.; Andreussi, O.; Brumme, T.; Bunau, O.; Buongiorno Nardelli, M.; Calandra, M.; Car, R.; Cavazzoni, C.; Ceresoli, D.; Cococcioni, M.; Colonna, N.; Carnimeo, I.; Dal Corso, A.; de Gironcoli, S.; Delugas, P.; DiStasio, R. A.; Ferretti, A.; Floris, A.; Fratesi, G.; Fugallo, G.; Gebauer, R.; Gerstmann, U.; Giustino, F.; Gorni, T.; Jia, J.; Kawamura, M.; Ko, H.-Y.; Kokalj, A.; Küçükbenli, E.; Lazzeri, M.; Marsili, M.; Marzari, N.; Mauri, F.; Nguyen, N. L.; Nguyen, H.-V.; Otero-de-la-Roza, A.; Paulatto, L.; Poncé, S.; Rocca, D.; Sabatini, R.; Santra, B.; Schlipf, M.; Seitsonen, A. P.; Smogunov, A.; Timrov, I.; Thonhauser, T.; Umari, P.; Vast, N.; Wu, X.; Baroni, S. Advanced Capabilities for Materials Modelling with Quantum ESPRESSO. *J. Phys. Condens. Matter* **2017**, *29*, 465901.

[63] te Velde, G.; Bickelhaupt, F. M.; Baerends, E. J.; Fonseca Guerra, C.; van Gisbergen, S. J. A.; Snijders, J. G.; Ziegler, T. Chemistry with ADF. *J Comput Chem* **2001**, *22*, 931967.

[64] Autschbach, J. Analyzing NMR Shielding Tensors Calculated with Two-Component Relativistic Methods Using Spin-Free Localized Molecular Orbitals. *J. Chem. Phys.* **2008**, *128*, 164112.

[65] Autschbach, J.; Zheng, S. Analyzing Pt Chemical Shifts Calculated from Relativistic Density Functional Theory Using Localized Orbitals: The Role of Pt 5d Lone Pairs. *Magn. Reson. Chem.* **2008**, *46*, S45-S55.

[66] Autschbach, J.; Ziegler, T. Nuclear Spin-Spin Coupling Constants from Regular Approximate Relativistic Density Functional Calculations. I. Formalism and Scalar Relativistic Results for Heavy Metal Compounds. *J. Chem. Phys.* **2000**, *113*, 936-947.

[67] Autschbach, J.; Ziegler, T. Nuclear Spin-Spin Coupling Constants from Regular Approximate Relativistic Density Functional Calculations. II. Spin-Orbit Coupling Effects and Anisotropies. *J. Chem. Phys.* **2000**, *113*, 9410-9418.

[68] van Lenthe, E.; Ehlers, A.; Baerends, E.-J. Geometry Optimizations in the Zero Order Regular Approximation for Relativistic Effects. *J. Chem. Phys.* **1999**, *110*, 8943-8953.

[69] van Lenthe, E.; Baerends, E. J.; Snijders, J. G. Relativistic Total Energy Using Regular Approximations. *J. Chem. Phys.* **1994**, *101*, 9783-9792.

[70] Lenthe, E. van; Baerends, E. J.; Snijders, J. G. Relativistic Regular Two-component Hamiltonians. *J. Chem. Phys.* **1993**, *99*, 4597-4610.

[71] Gonze, X.; Amadon, B.; Antonius, G.; Arnardi, F.; Baguet, L.; Beuken, J.-M.; Bieder, J.; Bottin, F.; Bouchet, J.; Bousquet, E.; Brouwer, N.; Bruneval, F.; Brunin, G.; Cavignac, T.; Charraud, J.-B.; Chen, W.; Côté, M.; Cottenier, S.; Denier, J.; Geneste, G.; Ghosez, P.; Giantomassi, M.; Gillet, Y.; Gingras, O.; Hamann, D. R.; Hautier, G.; He, X.; Helbig, N.; Holzwarth, N.; Jia, Y.; Jollet, F.; Lafargue-Dit-Hauret, W.; Lejaeghere, K.; Marques, M. A. L.; Martin, A.; Martins, C.; Miranda, H. P. C.; Naccarato, F.; Persson, K.; Petretto, G.; Planes, V.; Pouillon, Y.; Prokhorenko, S.; Ricci, F.; Rignanese, G.-M.; Romero, A. H.; Schmitt, M. M.; Torrent, M.; van Setten, M. J.; Van Troeye, B.; Verstraete, M. J.; Zérah, G.; Zwanziger, J. W. The Abinitproject: Impact, Environment and Recent Developments. *Comput. Phys. Commun.* **2020**, *248*, 107042.

[72] Jensen, F. Introduction to Computational Chemistry, 2nd ed.; John Wiley & Sons Ltd.: New York, 2006

[73] Perdew, J. P.; Burke, K.; Ernzerhof, M. Generalized Gradient Approximation Made Simple. *Phys. Rev. Lett.* **1996**, *77*, 3865-3868.

[74] Becke, A. D. Density-functional exchange-energy approximation with correct asymptotic behaviour. *Phys. Rev. A*, **1988**, *38*, 3098-3100.

[75] Lee, C.; Yang, W.; Parr, R. G. Development of the Colle-Salvetti correlation-energy formula into a functiuonal of the electron density. *Phys. Rev. B*, **1988**, *37*, 785-789.

[76] Helgaker, T.; Jaszuński, M.; Ruud, K. Ab Initio Methods for the Calculation of NMR Shielding and Indirect Spin−Spin Coupling Constants. *Chem. Rev.* **1999**, *99*, 293-352.

[77] Gregor, T.; Mauri, F.; Car, R. A comparison of methods for the calculation of NMR chemical shifts. *J. Chem. Phys*. **1999**, *111*, 1815-1822.

[78] Bonhomme, C.; Gervais, C.; Babonneau, F.; Coelho, C.; Pourpoint, F.; Azaïs, T.; Ashbrook, S. E.; Griffin, J. M.; Yates, J. R.; Mauri, F.; Pickard, C. J. First-principles calculation of NMR parameters using the gauge including projector augmented wave method: a chemist′s point of view. *Chem. Rev.* **2012**, *112*, 5733-5779.

[79] Pickard, C. J.; Mauri, F. All-electron magnetic response with pseudopotentials: NMR chemical shifts. *Phys. Rev. B*, **2001**, *63*, 245101.

[80] Autschbach, J. Perspective: Relativistic effects. *J. Chem. Phys.* **2012**, *136*, 150902.

[81] Zanolla, D.; Hasa, D.; Arhangelskis, M.; Schneider-Rauber, G.; Chierotti, M. R.; Keiser, J.; Voinovich, D.; Jones, W.; Perissutti, B. Mechanochemical Formation of Racemic

Praziquantel Hemihydrate with Improved Biopharmaceutical Properties. *Pharmaceutics* **2020**, *12*, 289.

[82] Xu, Y.; Viger-Gravel, J.; Korobkov, I.; Bryce, D. L. Mechanochemical Production of Halogen-Bonded Solids Featuring P═O···I-C Motifs and Characterization via X-Ray Diffraction, Solid-State Multinuclear Magnetic Resonance, and Density Functional Theory. *J. Phys. Chem. C* **2015**, *119*, 27104-27117.

[83] Peach, A. A.; Hirsh, D. A.; Holmes, S. T.; Schurko, R. W. Mechanochemical Syntheses and ^{35}Cl Solid-State NMR Characterization of Fluoxetine HCl Cocrystals. *CrystEngComm* **2018**, *20*, 2780-2792.

[84] Stolar, T.; Batzdorf, L.; Lukin, S.; Žilić, D.; Motillo, C.; Friščić, T.; Emmerling, F.; Halasz, I.; Užarević, K. In Situ Monitoring of the Mechanosynthesis of the Archetypal Metal-Organic Framework HKUST-1: Effect of Liquid Additives on the Milling Reactivity. *Inorg. Chem.* **2017**, *56*, 6599-6608.

[85] Métro, T.-X.; Gervais, C.; Martinez, A.; Bonhomme, C.; Laurencin, D. Unleashing the Potential of ^{17}O NMR Spectroscopy Using Mechanochemistry. *Angew. Chem. Int. Ed.* **2017**, *56*, 6803-6807.

[86] Chen, C.-H.; Gaillard, E.; Mentink-Vigier, F.; Chen, K.; Gan, Z.; Gaveau, P.; Rebière, B.; Berthelot, R.; Florian, P.; Bonhomme, C.; Smith, M. E.; Métro, T.-X.; Alonso, B.; Laurencin, D. Direct ^{17}O Isotopic Labeling of Oxides Using Mechanochemistry. *Inorg. Chem.* **2020**. *59*, 13050-13066.

[87] Censi, R.; Di Martino, P. Polymorph Impact on the Bioavailability and Stability of Poorly Soluble Drugs. *Molecules* **2015**, *20*, 18759-18776.

[88] Szeleszczuk, Ł.; Pisklak, D. M.; Gubica, T.; Matjakowska, K.; Kaźmierski, S.; Zielińska-Pisklak, M. Application of Combined Solid-State NMR and DFT Calculations for the Study of Piracetam Polymorphism. *Solid State Nucl. Magn. Reson.* **2019**, *97*, 17-24.

[89] Tian, Y.; Wang, W. D.; Zou, W.-B.; Qian, J.-Q.; Hu, C.-Q. Application of Solid-State NMR to Reveal Structural Differences in Cefazolin Sodium Pentahydrate From Different Manufacturing Processes. *Front. Chem.* **2018**, *6*, 113.

[90] Rajput, L.; Banik, M.; Yarava, J. R.; Joseph, S.; Pandey, M. K.; Nishiyama, Y.; Desiraju, G. R. Exploring the Salt-Cocrystal Continuum with Solid-State NMR Using Natural-Abundance Samples: Implications for Crystal Engineering. *IUCrJ* **2017**, *4*, 466-475.

[91] Losev, E. A.; Boldyreva, E. V. A Salt or a Co-Crystal - When Crystallization Protocol Matters. *CrystEngComm* **2018**, *20*, 2299-2305.

[92] Stainton, P.; Grecu, T.; McCabe, J.; Munshi, T.; Nauha, E.; Scowen, I. J.; Blagden, N. First Comparative Study of the Three Polymorphs of Bis(Isonicotinamide) Citric Acid Cocrystals and the Concomitant Salt 4-Carbamoylpyridinium Citrate Isonicotinamide. *Cryst. Growth Des.* **2018**, *18*, 4150-4159.

[93] Jones, C. L.; Skelton, J. M.; Parker, S. C.; Raithby, P. R.; Walsh, A.; Wilson, C. C.; Thomas, L. H. Living in the Salt-Cocrystal Continuum: Indecisive Organic Complexes with Thermochromic Behaviour. *CrystEngComm* **2019**, *21*, 1626-1634.

[94] Perumalla, S. R.; Wang, C.; Guo, Y.; Shi, L.; Sun, C. C. Robust Bulk Preparation and Characterization of Sulfamethazine and Saccharine Salt and Cocrystal Polymorphs. *CrystEngComm* **2019**, *21*, 2089-2096.

[95] Bernasconi, D.; Bordignon, S.; Rossi, F.; Priola, E.; Nervi, C.; Gobetto, R.; Voinovich, D.; Hasa, D.; Duong, N. T.; Nishiyama, Y.; Chierotti, M. R. Selective Synthesis of a Salt and a Cocrystal of the Ethionamide-Salicylic Acid System. *Cryst. Growth Des.* **2020**, *20*, 906-915.

[96] Xu, Y.; Southern, S. A.; Szell, P. M. J.; Bryce, D. L. The Role of Solid-State Nuclear Magnetic Resonance in Crystal Engineering. *CrystEngComm* **2016**, *18*, 5236-5252.

[97] Xu, Y.; Szell, P. M. J.; Kumar, V.; Bryce, D. L. Solid-State NMR Spectroscopy for the Analysis of Element-Based Non-Covalent Interactions. *Coord. Chem. Rev.* **2020**, *411*, 213237.

[98] Arunan, E.; Desiraju, G. R.; Klein, R. A.; Sadlej, J.; Scheiner, S.; Alkorta, I.; Clary, D. C.; Crabtree, R. H.; Dannenberg, J. J.; Hobza, P.; Kjaergaard, H. G.; Legon, A. C.; Mennucci, B.; Nesbitt, D. J. Definition of the Hydrogen Bond (IUPAC Recommendations 2011). *Pure Appl. Chem.* **2011**, *83*, 1637-1641.

[99] Scheiner, S. Forty years of progress in the study of the hydrogen bond. *Struct. Chem.* **2019**, *30*, 1119-1128.

[100] Scheiner, S. The Hydrogen Bond: A Hundred Years and Counting. *J. Indian Inst. Sci.* **2020**, *100*, 61-76.

[101] π-π Stacking in Crystal Engineering: Fundamentals and Applications. *Cryst. Growth Des.* **2019**, *18-19*.

[102] Grzesiek, S.; Cordier, F.; Dingley, A. J. Hydrogen Bond Scalar Couplings — A New Tool in Biomolecular NMR. In *Protein NMR for the Millennium*; Krishna, N. R. Berliner, L. J. Eds.; Biological Magnetic Resonance; Springer: Boston, MA, **2002**, 255-283.

[103] Grzesiek, S.; Becker, E. D. Hydrogen Bonding. In *eMagRes*; Harris, R. K. Wasylishen, R. E. Eds.; **2011**.

[104] Korinek, G. J.; Schneider, W. G. On the Proton Magnetic Resonance Shift Due to Hydrogen Bonding. *Can. J. Chem.* **1957**, *35*, 1157-1163. https://doi.org/10.1139/v57-156.

[105] Brown, S. P. Hydrogen Bonding in Crystalline Organic Solids. In *eMagRes*; Harris, R. K. Wasylishen, R. E. Eds.; 2008.

[106] Clark, T.; Hennemann, M.; Murray, J. S.; Politzer, P. Halogen Bonding: The σ-Hole. *J. Mol. Model.* **2007**, *13*, 291-296.

[107] Xu, Y.; Szell, P. M. J.; Kumar, V.; Bryce, D. L. Solid-state NMR spectroscopy for the analysis of element-based non-covalent interactions. *Coord. Chem. Rev.* **2020**, *411*, 213237.

[108] Scheiner, S. Understanding noncovalent bonds and their controlling forces. *J. Chem. Phys.* **2020**, *153*, 140901.

[109] Cavallo, G.; Metrangolo, P.; Pilati, T.; Resnati, G.; Terraneo, G. Naming Interactions from the Electrophilic Site. *Cryst. Growth Des.* **2014**, *14*, 2697-2702.

[110] Desiraju, G. R.; Ho, P. S.; Kloo, L.; Legon, A. C.; Marquardt, R.; Metrangolo, P.; Politzer, P.; Resnati, G.; Rissanen, K. Definition of the Halogen Bond (IUPAC Recommendations 2013). *Pure Appl. Chem.* **2013**, *85*, 1711-1713.

[111] Aakeroy, C. B.; Bryce, D. L.; Desiraju, G. R.; Frontera, A.; Legon, A. C.; Nicotra, F.; Rissanen, K.; Scheiner, S.; Terraneo, G.; Metrangolo, P.; Resnati, G. Definition of the

Chalcogen Bond (IUPAC Recommendations 2019). *Pure Appl. Chem.* **2019**, *91*, 1889-1892.

[112] Zahn, S.; Frank, R.; Hey-Hawkins, E.; Kirchner, B. Pnicogen Bonds: A New Molecular Linker? *Chem. - Eur. J.* **2011**, *17*, 6034-6038.

[113] Bauzá, A.; Mooibroek, T. J.; Frontera, A. Tetrel-Bonding Interaction: Rediscovered Supramolecular Force? *Angew. Chem. Int. Ed.* **2013**, *52*, 12317-12321.

[114] Bauzá, A.; Frontera, A. Aerogen Bonding Interaction: A New Supramolecular Force? *Angew. Chem. Int. Ed.* **2015**, *54*, 7340-7343.

[115] Politzer, P.; Murray, J. S. The fundamental nature and role of the electrostatic potential in atoms and molecule. *Theor. Chem. Acc.* **2002**, *108*, 134-142.

[116] Del Bene, J. E.; Alkorta, J.; Elguero, J. Influence of Substituent Effects on the Formation of P···Cl Pnicogen Bonds or Halogen Bonds. *J. Phys. Chem. A* **2014**, *118*, 2360-2366.

[117] Li, Q.; Guo, X.; Yang, X.; Li, W.; Cheng, J.; Li, H.-B. A σ-Hole Interaction with radical species as Electron Donors: Does Single-Electron Tetrel Bonding Exist? *Phys. Chem. Chem. Phys*. **2014**, *16*, 11617-11625.

[118] Clark, T. Hennemann, M.; Murrary, J. S.; Politzer, P. Halogen Bonding:The σ-Hole. *J. Mol. Model.* **2007**, *13*, 291-296.

[119] Mani, D.; Arunan, E. The X-C···Y (X = O/F, Y = O/S/F/Cl/Br/N/P) 'Carbon Bond' and Hydrophobic Interactions. *Phys. Chem. Chem. Phys.* **2013**, *15*, 14377-14383.

[120] Murray, J. S.; Lane, P.; Politzer, P. Expansion of the σ-Hole *Concept. J. Mol. Model*. **2009**, *15*, 723-729.

[121] Huber, S. M.; Jimenez-Izal, E.; Ugalde J. M.; Infante, I. Unexpected trends in halogen - bond based noncovalent adducts, *Chem Commun*, **2012**, *48*, 7708-7710.

[122] Řezáč, J.; de la Lande, A. On the role of charge transfer in halogen bonding, *Phys. Chem. Chem. Phys.* **2016**, *19*, 791-803.

[123] Wang, C.; Danovich, D.; Mo Y.; Shaik, S. On The Nature of the Halogen Bond, *J. Chem. Theory Comput.* **2014**, *10*, 3726-3737.

[124] Wolters L. P.; Bickelhaupt, F. M. Halogen Bonding versus Hydrogen Bonding: A Molecular Orbital Perspective, *Chemistry Open*, **2012**, *1*, 96-105.

[125] Thirman, J.; Engelage, E.; Huber, S. M.; Head-Gordon, M. Characterizing the interplay of Pauli repulsion, electrostatics, dispersion and charge transfer in halogen bonding with energy decomposition analysis, *Phys. Chem. Chem. Phys.* **2017**, *20*, 905-915.

[126] Berger, G.; Grangville, P.; Meyer, F. Halogen bonding for molecular recognition: new developments in materials and biological sciences. *Chem. Commun.* **2020**, *56*, 4970-4981.

[127] Lu, J.; Scheiner, S. Effects of Halogen, Chalcogen, Pnicogen, and Tetrel Bonds on IR and NMR Spectra. *Molecules* **2019**, *24*, 2822.

[128] Kumar, V.; Xu, Y.; Leroy, C.; Bryce, D. L. Direct Investigation of Chalcogen Bonds by Multinuclear Solid-State Magnetic Resonance and Vibrational Spectroscopy. *Phys. Chem. Chem. Phys.* **2020**, *22* (7), 3817-3824.

[129] Kumar, V.; Xu, Y.; Bryce, D. L. Double Chalcogen Bonds: Crystal Engineering Stratagems via Diffraction and Multinuclear Solid-State Magnetic Resonance Spectroscopy. *Chem. -Eur. J.* **2020**, *26*, 3275-3286.

[130] Mokrai, R.; Barrett, J.; Apperley, D. C.; Batsanov, A. S.; Benkő, Z.; Heift, D. Weak Pnictogen Bond with Bismuth: Experimental Evidence Based on Bi−P Through-Space Coupling. *Chem. -Eur. J.* **2019**, *25*, 4017-4024.

[131] Horsewill, A. J.; Ikram, A. Experimental Investigations of the Quantum Dynamics of the Hydrogen Bond Using Single Crystal NMR. *Phys. B Condens. Matter* **1996**, *226*, 202-206.

[132] Detken, A.; Zimmermann, H.; Haeberlen, U.; Luz, Z. Dynamic Hydrogen Disorder in Solid Tropolone. A Single-Crystal NMR Study of the Hydroxyl Deuterons. *J. Magn. Reson.* **1997**, *126*, 95-102.

[133] Gerald II, R.; Bernhard, T.; Haeberlen, U.; Rendell, J.; Opella, S. Chemical Shift and Electric Field Gradient Tensors for the Amide and Carboxyl Hydrogens in the Model Peptide N-Acetyl-D,L-Valine. Single-Crystal Deuterium NMR Study. *J. Am. Chem. Soc.* **1993**, *115*, 777-782.

[134] Takeda, N.; Kuroki, S.; Kurosu, H.; Ando, I. ^{13}C-NMR Chemical Shift Tensor and Hydrogen-Bonded Structure of Glycine-Containing Peptides in a Single Crystal. *Biopolymers* **1999**, *50*, 61-69.

[135] Takegoshi, K.; Naito, A.; McDowell, C. A. Intermolecular Hydrogen-Bonding Effects on the ^{13}C NMR Shielding Tensor of the Carbonyl Carbon Nucleus in a Single Crystal of Dimedone. *J. Magn. Reson. 1969* **1985**, *65*, 34-42.

[136] Harbison, G. S.; Jelinsiu, L. W.; Stark, R. E.; Torchia, D. A.; Herzfeld, J.; Griffin, R. G. ^{15}N Chemical Shift and ^{15}N-^{13}C Dipolar Tensors for the Peptide Bond in [l-

^{13}C]Glycyl[^{15}N]Glycine Hydrochloride Monohydrate. *J. Magn. Reson.* **1984**, *60*, 79-82.

[137] Xu, Y.; Gabidullin, B.; Bryce, D. L. Single-Crystal NMR Characterization of Halogen Bonds. *J. Phys. Chem. A* **2019**, *123*, 6194-6209.

[138] Alkorta, I.; Elguero, J.; Frontera, A. Not Only Hydrogen Bonds: Other Noncovalent Interactions. *Crystals*, **2020**, *10*, 180.

[139] Legon, A. C. Tetrel, pnictogen and chalcogen bonds identified in the gas phase before they had names: a systematic look at non-covalent interactions. *Phys. Chem. Chem. Phys.* **2017**, *19*, 14884-14896.

[140] Cavallo, G.; Metrangolo, P.; Pilati, T.; Resnati, G.; Terraneo, G. Naming Interactions from the Electrophilic Site. *Cryst. Growth Des*. **2014**, *14*, 2697-2702.

[141] Scilabra, P.; Kumar, V.; Ursini, M.; Resnati, G. Close contacts involving germanium and tin in crystal structures: experimental evidence of tetrel bonds. *J. Molec. Model.* **2018**, *24*, 37.

[142] Bauzá, A.; Seth, S. K.; Frontera, A. Tetrel bonding interactions at work: Impact on tin and lead coordination compounds. *Coord. Chem. Rev.* **2019**, *384*, 107-125.

[143] Daolio, A.; Scilabra, P.; Terraneo, G.; Resnati, G. C(sp^3) atoms as tetrel bond donors: A crystallographic survey. *Coord. Chem. Rev.* **2020**, *413*, 213265.

[144] Roeleveld, J. J.; Lekanne Deprez, S. J.; Verhoofstad, A.; Frontera, A.; van der Vlugt, J. I.; Mooibroek, T. J. Engineering Crystals Using sp^3-C Centred Tetrel Bonding Interactions. *Chem. -Eur. J.* **2020**, *26,* 10126-10132.

[145] Kumar, V.; Rodrigue, C.; Bryce, D. L.; Short and Linear Intermolecular Tetrel Bonds to Tin. Cocrystal Engineering with Triphenyltin Chloride. *Cryst. Growth. Des.* **2020**, *20*, 2027-2034.

[146] Lim, J. Y. C.; Beer, P. D. Sigma-Hole Interactions in Anion Recognition. *Chem*, **2018**, *4*, 731-783.

[147] Taylor, M. S. Anion recognition based on halogen, chalcogen, pnictogen and tetrel bonding. *Coord. Chem. Rev.* **2020**, *413*, 213270.

[148] Scheiner, S.; Michalczyk, M.; Zierkiewicz, W. Coordination of anions by noncovalently bonded σ-hole ligands, *Coord. Chem. Rev.* **2020**, *405*, 213136.

[149] Grabowski, S. J. Tetrel Bonds with π-Electrons Acting as Lewis Bases—Theoretical Results and Experimental Evidences. *Molecules* **2018**, *23*, 1183.

[150] Grabowski, S. J. Tetrel bonds, penta- and hexa-coordinated tin and lead centres. *Appl. Organomet. Chem.* **2017**, *31*, e3727.

[151] Mahmoudi, G.; Zangrando, E.; Mitoraj, M. P.; Gurbanov, A. V.; Zubkov, F. I.; Moosavifar, M.; Konyaeva, I. A.; Kirilov, A. M.; Safin, D. A. Extended lead(II) architectures engineered via tetrel bonding interactions. *New J. Chem.* **2018**, *42*, 4959-4971.

[152] Dutta, A.; Trivedi, M.; Alarfi, A.; Kumar, A.; Muddassir, M. A new 1D coordination polymer of triphenyl lead hydrosulfide: Synthesis and insights into crystal architecture and Hirshfeld surface analyses. *J. Molec. Struct.* **2020**, *1207*, 127801.

[153] Afkhami, F. A.; Mahmoudi, G.; Qu, F.; Gupta, A.; Köse, M.; Zangrando, E.; Zubkov, F. I.; Alkorta, I.; Safin, D. A. Supramolecular lead(II) architectures engineered by tetrel bonds. *CrystEngComm* **2020**, *22*, 2389-2396.

[154] Afkhami, F. A.; Mahmoudi, G.; Qu, F.; Gupta, A.; Zangrando, E.; Frontera, A.; Dafin, D. A. Supramolecular architecture constructed from the hemidirected lead(II) complex with *N*'-(4-hydroxybenzylidene)isonicotinohydrazide. *Inorg. Chim. Acta* **2020**, *502*, 119350.

[155] Mahmoudi, G.; Abedi, M.; Lawrence, S. E.; Zangrando, E.; Babashkina, M. G.; Klein, A.; Frontera, A.; Safin, D. Tetrel Bonding and Other Non-Covalent Interactions Assisted Supramolecular Aggregation in a New Pb(II) Complex of an Isonicotinohydrazide. *Molecules* **2020**, *25*, 4506.

[156] Singh, P.; Singh, A.; Kociok-Köhn, G.; Kumar, A.; Muddassir, M. New lead(II) coordination polymer derived from second generation O-methylpyridylxanthate: Crystallographic and computational studies, *Inorg. Chim. Acta*, **2021**, *514*, 120032.

[157] Shimoni-Levy, L; Glusker, J. P.; Bock, C. W. Lone Pair Functionality in Divalent Lead Compounds. *Inorg. Chem.* **1998**, *37*, 1853-1867.

[158] Bauzá, A.; Seth, S. K.; Frontera, A. Tetrel bonding interactions at work: Impact on tin and lead coordination compounds. *Coord. Chem. Rev.* **2019**, *384*, 107-125.

[159] Franconetti, A.; Frontera, A. Theoretical and Crystallographic Study of Lead(IV) Tetrel Bonding Interactions. *Chem. -Eur. J.* **2019**, *25*, 6007-6013.

[160] Grabowski, S. J. Hydrogen Bond and Other Lewis Acid-Lewis Base Interactions as Preliminary Stages of Chemical Reactions. *Molecules*, **2020**, *25*, 4668.

[161] Grabowski, S. J. Tetrel bond-σ-hole bond as a preliminary stage of the S_N2 reaction. *Phys. Chem. Chem. Phys.* **2014**, *16*, 1824-1834.

[162] Hou, M.; Li, Q.; Scheiner, S. The ability of a tetrel bond to transition a neutral amino acid into a zwitterion. *Chem. Phys. Lett.* **2019**, *731,* 136584.

[163] Michalczyk, M.; Zierkiewicz, W.; Wysokiński, R.; Scheiner, S. Theoretical Studies of IR and NMR Spectral Changes Induced by Sigma-Hole Hydrogen, Halogen, Chalcogen, Pnicogen, and Tetrel Bonds in a Model Protein Environment. *Molecules*, **2019**, *24*, 3329.

[164] Trievel, R. C.; Scheiner, S. Crystallographic and Computational Characterization of Methyl Tetrel Bonding in S-Adenosylmethionine-Dependent Methyltransferases. *Molecules* **2018**, *23*, 2965.

[165] Mundlapati, V. R.; Sahoo, D. K.; Bhaumik, S.; Jena, S.; Chandrakar, A.; Biswal, H. S. Noncovalent Carbon-Bonding Interactions in Proteins. *Angew. Chem. Int. Ed.* **2018**, *57*, 16496-16500.

[166] Silva, B.; Alikhani, E.; Ratajczak, H. Towards an unified chemical model of secondary bonding. *J. Molec. Model.* **2020**, *26*, 62.

[167] Laconsay, C. J.; Gallbraith, J. M. A valence bond theory treatment of tetrel bonding interactions. *Comput. Theor. Chem.* **2017**, *116*, 202-206.

[168] Li, Y.; Wang, X.; Wang, H.; Lu, Y.; Zhu, Z.; Ni, Y. The differences and cooperativity between Ge (Sn)…O tetrel bonds and X (X = F, Cl, Br, and I) …O halogen bonds. *Chem. Phys.* **2020**, *534*, 110748.

[169] Heywood, V. L.; Alford, T. P. J.; Roeleveld, J. J.; Deprez, S. J. L.; Verhoofstad, A.; van der Vlugt, J. I.; Dominigos, S. R.; Schnell, M.; Davis, A. P.; Mooibroek, T. J.

Observations of tetrel bonding between sp^3-carbon and THF. *Chem. Sci.* **2020**, *11*, 5289-5293.

[170] Grabowski, S. J.; Sokalski, W. A. Are various σ-hole bonds steered by the same mechanisms? *ChemPhysChem* **2017**, *18*, 1569-1577.

[171] Grabowski, S. J. Pnicogen and tetrel bonds—tetrahedral Lewis acid centres. *Struct. Chem.* **2019**, *30*, 1141-1152.

[172] An, X.; Han, J. Influence of alkali substituents on the strength, properties, and nature of tetrel bond between TH_3F and pyridine. *J. Mol. Model.* **2020**, *26*, 224.

[173] Scheiner, S. The ditetrel bond: noncovalent bond between neutral tetrel atoms. *Phys. Chem. Chem. Phys.* **2020**, *22*, 16606-16614.

[174] Zhao, Q. Mutual influence of tetrel and halogen bonds between XCN (X=Cl, Br) and 4-TF_3-pyridine (T=C, Si, Ge), *J. Molec. Model.* **2020**, *26*, 329.

[175] Grabarz, A.; Michalczyk, M.; Zierkiewicz, W.; Scheiner, S. Noncovalent Bonds between Tetrel Atoms, *Chem. Eur.* **2020**, *21*, 1934-1944.

[176] Lu, J.; Scheiner, S. Relationships between Bond Strength and Spectroscopic Quantities in H-Bonds and Related Halogen, Chalcogen, and Pnicogen Bonds. *J. Phys. Chem. A.* **2020**, *124*, 7716-7725.

[177] Gao, S.; Obenchain, D. A.; Lei, J.; Feng, G.; Herbers, S.; Gou, Q.; Grabow, J. -U. Tetrel bonds and conformational equilibria in the formamide-CO_2 complex: a rotational study. *Phys. Chem. Chem. Phys.* **2019**, *21*, 7016-7020.

[178] Li, M.; Lei, J.; Feng, G.; Grabow, J. -U.; Gou, Q. The rotational spectrum of acetophenone-CO_2: Preferred non-covalent interactions. *Spectrochim. Acta A* **2020**, *238*, 118424.

[179] Scheiner, S. Dependence of NMR chemical shifts upon CH bond lengths of a methyl group involved in a tetrel bond. *Chem. Phys. Lett.* **2019**, *714*, 61-64.

[180] Lu, J.; Sheiner, S. Effects of Halogen, Chalcogen, Pnicogen, and Tetrel Bonds on IR and NMR Spectra. *Molecules* **2019**, *24*, 2822.

[181] Scheiner, S. Ability of IR and NMR Spectral Data to Distinguish between a Tetrel Bond and a Hydrogen Bond. *J. Phys. Chem. A* **2018**, *122*, 7852-7862.

[182] Sethio, D.; Oliveira, V.; Kraka, E. Quantitative Assessment of Tetrel Bonding Utilizing Vibrational Spectroscopy. *Molecules* **2018**, *23*, 2763.

[183] Southern, S. A.; Bryce, D. L. NMR Investigations of Noncovalent Carbon Tetrel Bonds. Computational Assessment and Initial Experimental Observation. *J. Phys. Chem. A* **2015**, *119*, 11891-11899.

Chapter 2 The Experimental ^{13}C and ^{1}H Solid-State NMR Response in Weakly Tetrel Bonded Methyl Groups

The study of tetrel bonding begins in period 2 of the periodic table. Like halogens, pnictogens, and chalcogens, group 14 tetrel atoms can exhibit areas of elevated electrostatic potential on their surfaces (σ-holes, **Figure 1-5**) which can engage in non-covalent interactions with electron donors. Evidence for tetrel bonds involving spin-1/2 nuclei, such as ^{13}C, may be found by careful observation of the isotropic chemical shift in solid-state NMR experiments.

Here, we study the ^{13}C and ^{1}H solid-state NMR spectroscopic responses to weak tetrel bond formation by examining a series of eight caffeine and theophylline cocrystals along with similar compounds not featuring tetrel bonds. Overall, we observe a moderate increase (<5 ppm) in the methyl ^{13}C chemical shift in cocrystals featuring tetrel bonds compared to their non-bonded counterparts. The value of $\delta(^{13}C)$ shows a weak inverse correlation with the tetrel bond length, while no strong correlation with the tetrel bond angle is observed experimentally. The presence of a tetrel bond also influences methyl proton chemical shifts, but no strong correlations with structural features are noted based on the experimental data.

With the aid of DFT calculations, we explore the relationship between the tetrel bond and the ^{13}C chemical shift tensor, furthering our understanding of how tetrel bonds and potentially competing weak CH···O hydrogen bonds affect the NMR response, which is a critical step towards the successful application of NMR crystallography. While computations generally show clear correlations between chemical shifts and structural features, this experimental work demonstrates that other interactions and crystal packing effects can weaken and even obscure the expected correlations.

2.1 Introduction

Over the last number of years, studies of non-covalent interactions involving elements of groups 14-18 as electrophilic sites have become numerous. Going beyond the well-known hydrogen bonds (HB), these noncovalent interactions are known by the name of the group in which the donor atom falls in the periodic table[1]: halogen bonds,[2,3] pnictogen bonds,[4-6] chalcogen bonds,[7,8] and tetrel bonds are now recognized as being part of an important category of non-covalent interactions.[9,10] Aerogen bonds have also been proposed.[11,12] A σ-hole is an area of depleted electron density and higher electrostatic potential that forms on an atom bonded to an electronegative substituent, which gives rise to a highly directional and tunable interaction.[13-17] σ-hole interactions may therefore be described schematically as R—X···Y bonds, where R is the electron-withdrawing substituent, X is the bond donor atom, and Y is the Lewis base acceptor atom. Generally, the bond's strength depends on the donor atom's polarizability, and consequently, carbon atoms will form the weakest bonds out of all the Group 14 elements.

The tetrel bond (TB) has become a popular subject of research due to the abundance of carbon in nature and chemistry. Of interest are sp^3 carbons, such as methyl carbons, because they are found in nearly every organic molecule, pharmaceutical compound, or biomolecule and may be a factor in molecular interactions' tunability.[18,19] Evidence for tetrel bonds involving Si and Sn goes back many years.[20-25] However, more recent works have contributed to furthering the understanding of tetrel bonds. For example, the tetrel bond was studied in its role as a coordinating precursor to S_N2 reactions.[10] There has also been a push to further the understanding of the impact of tetrel bonds on crystal engineering and catalysis.[26] For example, several organic cocrystals and supramolecular structures were identified featuring

tetrel bonds in the literature. Recently, Kumar and coworkers reported a series of tin-based tetrel bonds,[27] while others have reported lead-based metal-organic frameworks.[28,29] There is a significant amount of recent computational work that has contributed to our understanding of the physical aspects of tetrel bonds.[30-34] Given the low polarizability of carbon, the NMR spectroscopic effect resulting from carbon tetrel bond formation is expected to be small and could be easily overshadowed by other crystallographic effects in solids.

In a recent study, Scheiner described the calculated NMR shielding response due to TBs and HBs on methyl ^{13}C and ^{1}H nuclei in a series of simple model systems.[35] In short, it was shown that upon complexation, both the ^{1}H and ^{13}C chemical shifts increase. The extent to which this occurs depends on the angle and the length of the TB. Upon forming a linear TB, the ^{13}C chemical shift was predicted to increase by up to ~ 6 ppm, and the ^{1}H chemical shift was predicted to increase only slightly. On the other hand, the formation of a weak RCH···O hydrogen bond results in a more considerable increase of the ^{1}H chemical shift, whereas the ^{13}C chemical shift only slightly increases. Simultaneously, upon increasing the TB or HB bond length, the ^{13}C and ^{1}H chemical shifts were calculated to decrease. Upon deviation from the TB linearity towards HB geometry, the ^{13}C chemical shift decreases rapidly, while the ^{1}H chemical shift increases. Scheiner's results clearly demonstrate what happens to the NMR response when the geometry of TB at a methyl group changes, but the model assumes that there are no other competing factors in the crystal structure. What happens when there is a weak hydrogen bond in addition to the TB? Does the C-H bond length affect the carbon chemical shift?[36] What about other effects occurring over the crystal lattice as a result of cocrystallization? Some of these questions have been thoughtfully considered

computationally using model structures,[35-37] but these are problems that must also be addressed by studying tetrel bonds using experimental solid-state NMR methods.

Experimental evidence has shown that the presence of a tetrel bond can be detected by instrumental analysis, including microwave spectroscopy.[38] We previously showed that tetrel bonds are detectible using solid-state NMR spectroscopy in both carbon- and lead-based tetrel bonding systems.[39,40] The effect tetrel bond-induced cocrystallization has on the NMR response has an important impact on NMR crystallography applications. Understanding how tetrel bonds affect the various NMR parameters is key to applying NMR crystallography towards understanding the nature of solid-state crystal structures.

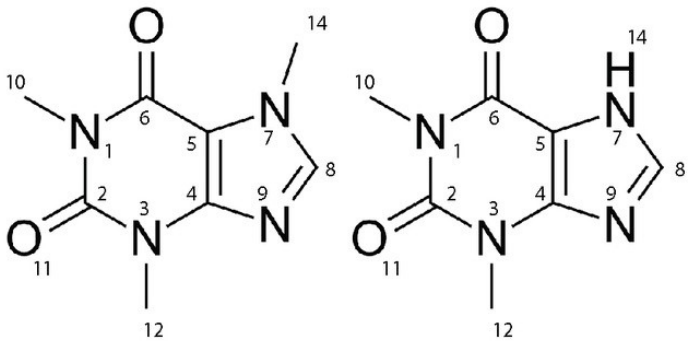

Scheme 1. Chemical structures of caffeine (left) and theophylline (right). Both structures are labelled with the numbering system used throughout this work.

Here, we report a solid-state NMR study on a series of caffeine and theophylline-based cocrystal structures featuring weak O···CH_3 tetrel bonds. Caffeine and theophylline **(Scheme 1)** make good candidates for this sort of study. It has been well documented that these compounds can easily form cocrystals with small organic molecules.[41,42] One of the standard features of many of these cocrystals is the tendency for contacts to form between the methyl carbons of caffeine or theophylline and oxygen atoms. These contacts are often linear ($\theta_{\text{N-C···O}}$

= 160°-180°), and the distance between the two atoms tends to be shorter than the sum of their van der Waals radii (3.22 Å) (**Figure 2-1**). A selection of a series of caffeine- and theophylline-based cocrystals allows for an easier comparison to be made between crystal structures featuring tetrel bonds. This work provides further understanding of the experimental NMR chemical shift response upon cocrystallization due to tetrel bonding and the competing effects of other phenomena such as hydrogen bonding.

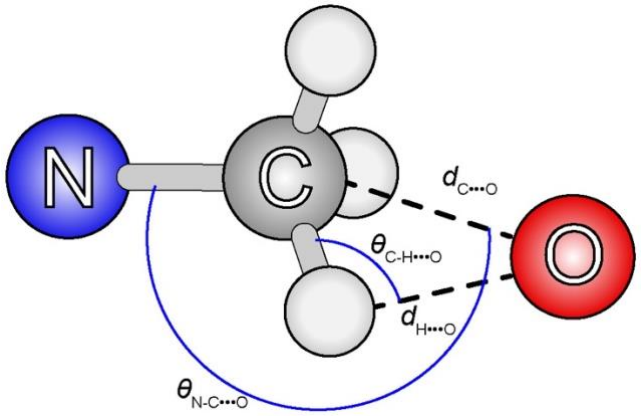

Figure 2-1. Schematic showing the general structure of an N-CH_3···O tetrel bond with all relevant angles and lengths discussed herein.

2.2 Experimental Methods

2.2.1 Cambridge Structural Database (CSD) Search

Cocrystals selected for recrystallization were identified from the Cambridge Structural Database (CSD) by searching for structural features using ConQuest.[43] Cocrystals featuring the linear (160-180 degrees) O···CH_3 motif with C···O TB lengths within the sum of their van der Waals radii (3.22 Å) were selected for further study. Structures were visualized using Mercury 4.1.3[44] or later.

2.2.2 Preparation of the tetrel bonded cocrystals

All precursors were obtained from Sigma Aldrich and used without further purification. Cocrystals were obtained using either slow evaporation or liquid-assisted grinding with a Retsch ball mill and minimal amounts (~10 mg) of organic solvent (See **Figure S1-1**).

2.2.3 Computational Methods

Periodic DFT calculations were performed using CASTEP v19.11.[45] In all cases, the revised Perdew-Burke-Ernzerhof (revPBE) functional was used with on-the-fly-generated scalar ZORA pseudopotentials (OTFG). The convergence of the computed parameters was tested such that 700 eV was determined to be an adequate cut-off energy for both geometry optimizations and magnetic resonance calculations, and the minimum *k*-point spacing of 0.07 $Å^{-1}$ over the Brillouin zone was observed to be sufficient for convergence in balance with our computational resource capabilities (see Appendix 1).[46] Geometry optimizations were carried out using the minimization approach of Broyden, Fletcher, Goldfarb, and Shanno (BFGS) with experimental unit cell dimensions fixed.[47] Dispersion was accounted for during geometry optimizations using the two-body force-field method of Grimme (D2). However, because the carbon atoms of interest in each of the crystal structures are involved in tetrel bonds with oxygen atoms and are directly bonded to nitrogen atoms, we re-parameterized the damping function using the approach of Holmes and Schurko (s_6=1.0; d=5.0).[48] Calculations of magnetic shielding tensors were carried out on the geometry-optimized crystal structures using the gauge including projector augmented wave (GIPAW) approach.

The calculated ^{1}H and ^{13}C isotropic magnetic shielding values were plotted against the experimentally determined isotropic chemical shifts to verify the quality of the calculated results. As shown in **Figure 2-2**, the correlation for ^{13}C is of higher quality than for ^{1}H. Part of the reason for this is that the HETCOR spectra were not resolved well enough in all cases to assign chemical shifts to each hydrogen atom in the spectrum. The distinct magnetic shielding constants are plotted against the average or the centre of the peak observed in the HETCOR spectrum if multiple ^{1}H resonances overlapped.

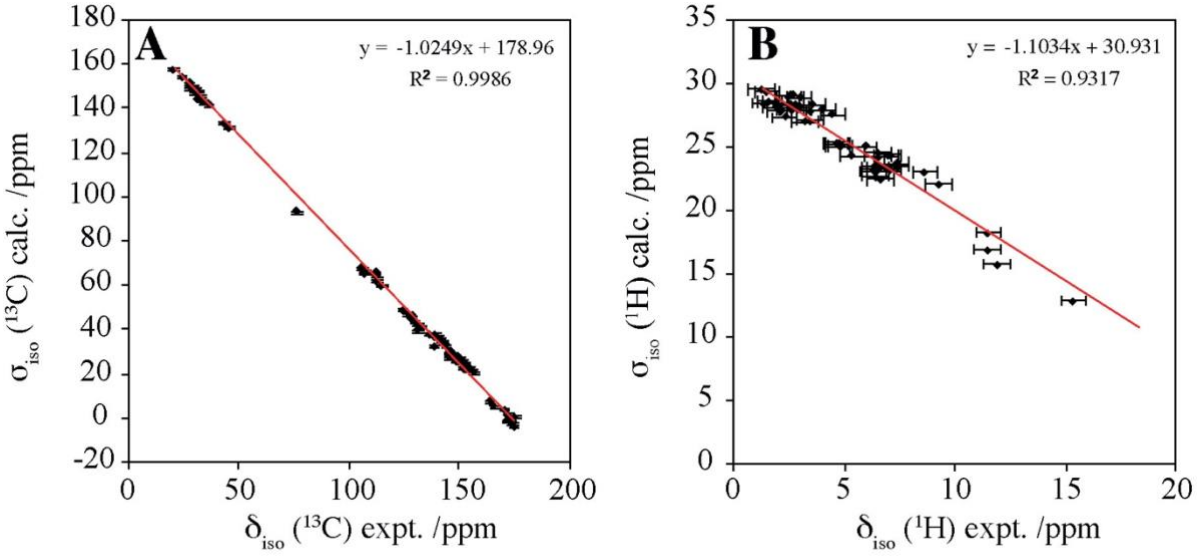

Figure 2-2. Comparison between the calculated isotropic shielding and the observed chemical shift corresponding to the compounds studied herein. Calculated values are obtained from periodic systems bearing geometry optimized hydrogen positions at the revPBE-D2 level. Magnetic resonance calculations were performed using the revPBE functional. ^{1}H magnetic shielding values are compared with the 'average' ^{1}H chemical shifts observed in the HETCOR experiment.

The computed isotropic magnetic shielding values were used to assign the ^{13}C and ^{1}H experimental isotropic chemical shifts of each compound. A comparison was made between the calculated shieldings and the experimental shifts and plotted, excluding the few ^{1}H chemical shifts that could not be assigned with confidence. The linear regression analysis is shown in **Figure 2-2** for both ^{13}C and ^{1}H. The equation of the line of best fit is in the form of:

$$\delta_{iso}(calc) = \sigma_{calc} - \frac{\sigma_{ref}}{m} \qquad \text{Eq. 2-1}$$

The calculated isotropic chemical shift is used to determine the root mean square (RMS) error. The RMS values for ^{13}C and ^{1}H are calculated using the expression:

$$RMS = \sqrt{\frac{\sum\left(\delta_{iso}(calc) - \delta_{iso}(expt)\right)^2}{n}} \qquad \text{Eq. 2-2}$$

where n is the number of observations made and are determined to be 0.197 and 0.067, respectively.

All calculated NMR data were extracted from CASTEP output files using EFGShield[49] v4.5 and visualized using the 2D plotting tool in Magresview v1.6.2.[50]

2.2.4 Solid-State NMR Spectroscopy

SSNMR experiments were conducted at 11.7 T ($\nu_0(^{1}H)$=500.35 MHz, $\nu_0(^{13}C)$=125.81 MHz); a Bruker Avance III console was used in combination with a Bruker 4 mm standard-bore triple resonance MAS probe, or at 9.4 T ($\nu_0(^{1}H)$=400.32 MHz, $\nu_0(^{13}C)$=100.67 MHz), where a Bruker Avance III console was used in combination with a Bruker 4 mm wide-bore

triple resonance MAS probe. All data sets were collected at ambient room temperature and pressure.

^{13}C NMR spectra of all compounds were obtained by employing magic-angle spinning $^{1}H \rightarrow {}^{13}C$ cross-polarization (CP/MAS) experiments. Samples were packed into 4 mm zirconia rotors and spun at rotational frequencies of 10.0 to 12.5 kHz to minimize as much as possible the overlap over the isotropic peaks with spinning sidebands resulting from chemical shift anisotropy at specific ^{13}C sites. Pulse powers and durations were optimized for each sample, resulting in ^{1}H $\pi/2$ pulses of around 3.0-3.5 μs, contact times of 2000 μs and ^{1}H decoupling frequencies of approximately 60 kHz. Caffeine and theophylline were found to require long relaxation delays, and in most cases, the recycle delay was set to a minimum of 30-60 s (see SI). All spectra were referenced to glycine (^{13}C=O) at 176.4 ppm with respect to adamantane ($^{13}CH_2$) at 38.48 ppm, relative to neat tetramethylsilane.[51]

^{1}H-^{13}C frequency-switched Lee-Goldburg (FSLG) heteronuclear correlation experiments (HETCOR)[52-55] were conducted at 11.7 T at spinning speeds of 10.0 kHz. The pulse sequence is shown in **Figure 2-3**. The sequence begins with a pulse on ^{1}H which rotates the magnetization to the magic angle (54.74°), followed by an incremented evolution time, t_1, during which the FSLG decoupling scheme, consisting of a series of 2π ^{1}H pulses, is applied to average all ^{1}H homonuclear dipolar couplings while allowing the ^{1}H chemical shift to evolve. The chemical shift encoded ^{1}H magnetization is then rotated to the transverse axis using a second ^{1}H pulse, followed by a standard cross-polarization scheme to transfer the magnetization to ^{13}C by matching the resonant frequencies to the *Hartmann-Hahn* condition. Finally, the ^{13}C signal is detected while ^{1}H-^{13}C heteronuclear decoupling is applied. It is important to note that the ^{1}H chemical shift evolves under the FSLG decoupling, which scales

the chemical shift by approximately 0.58. This must be taken into account during the processing step.

Contact times were set to 50-150 μs to obtain proximal correlations, as much as possible, from only directly bonded ^{1}H atoms. π/2 pulses of 3.15-3.50 μs were employed with an effective FSLG ^{1}H decoupling field of ~85 kHz. The chemical shift and scaling in the ^{1}H dimension was referenced to tyrosine·HCl. Due to this sort of experiment's impracticality when relaxation delays are long, only the minimum number of increments required to resolve the peaks in the ^{1}H dimension were acquired. However, this resulted in a significantly depreciated resolution in the ^{1}H dimension compared to what would typically be obtained for samples with more reasonable relaxation properties. NMR spectra were processed and analyzed using the ssNake python application.[56]

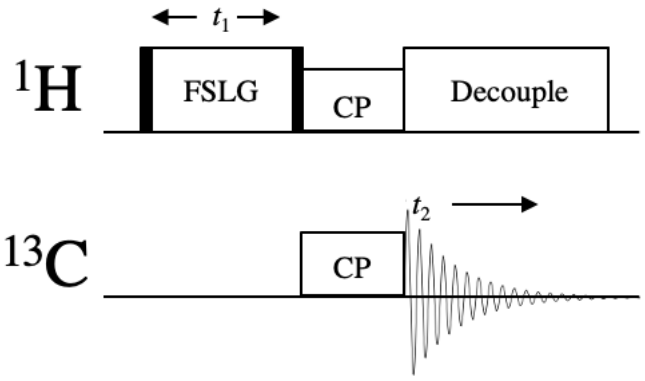

Figure 2-3. Pulse sequence for FSLG-HETCOR.[52] The ^{1}H pulses are not standard $\frac{\pi}{2}$ pulses and specifically set to achieve the LG condition (see main text).

It is well documented that a quadrupolar nucleus coupled to a spin-1/2 nucleus can indirectly result in a second-order frequency shift.[57-59] The dipolar coupling constant is calculated to be approximately 0.7 kHz in ^{14}N-^{13}CH$_3$ groups. We can then calculate the

absolute magnitude of the frequency shift resulting from the $m = \pm 1$ transitions to be on the order of 0.15 ppm or less for ^{14}N-$^{13}CH_3$ sites at 11.7 T. Therefore, the effects of the second-order frequency shifts are small relative to the observed ^{13}C line widths (~1 ppm).

2.2.5 Powder X-ray Diffraction

Data sets were collected on a Rigaku Ultima IV powder diffractometer equipped with an automatic sample changer and spinner at room temperature with Cuκα$_1$ radiation with a wavelength of 1.54056 Å. The measurements were carried out over a 2θ range of 5° to 65° using a continuous scanner with a step size of 0.02°. To confirm the cocrystals' successful recrystallizations, their experimental powder patterns are compared to diffraction patterns obtained from the published crystallographic information files (CIF) using Mercury software (see **Figure 2-4** for an example). Patterns were analyzed using Profex v4.2[60] and are shown in the Supporting Information.

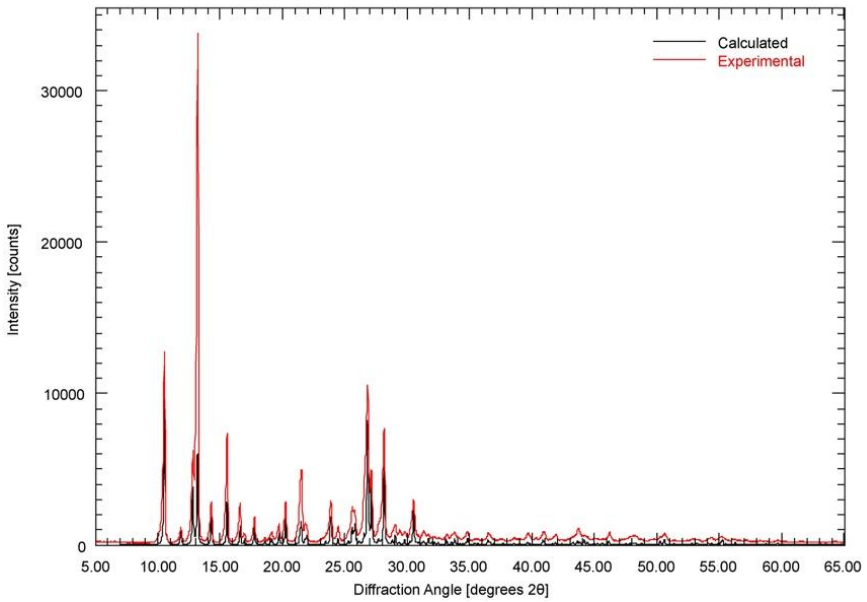

Figure 2-4. Experimental powder X-ray diffraction pattern of caffeine 4-nitroaniline (black) overlaid with the calculated pattern obtained from Mercury.

2.3 Results and Discussion

2.3.1 Tetrel Bonding

The goal of this study was to investigate a series of caffeine- and theophylline-based cocrystals by SSNMR spectroscopy in order to develop a greater understanding of the NMR response to tetrel bonds in the solid-state and what effects, if any, can be observed due to their competition with weak CH···O hydrogen bonds.

To this effect, ten compounds characterized previously by X-ray diffraction were chosen to be studied by solid-state NMR to explore the tetrel-bond induced effects upon cocrystallization. We selected a series of caffeine- and theophylline-based cocrystals following a Cambridge Crystal Database search (**Table 2-1**). These crystal structures are depicted in **Figure 2-5** and **Figure 2-6**.

Table 2-1. X-ray Structures of Caffeine and Theophylline Cocrystals Used in This Work

Number	CSD REFCODE	Space Group	Chemical Name
CA	CAFINE01	P21/c	caffeine monohydrate
1	VAWKOU	Pnma	caffeine acetic acid
2	LATGUK	P21/c	caffeine 4-nitroaniline
3	IJEZUT	P21/c	caffeine p-coumaric acid
4	VAWKEK	P21/c	caffeine formic acid
5	GANYEA	P21/n	caffeine maleic acid
6	KIGKAN	P21/c	theophylline citric acid hydrate
7	RABXOK	P1	theophylline acetamide
8	BAPLOT06	Pna21	theophylline (form II)
9	WOCHUT	P21/c	theophylline cinnamic acid

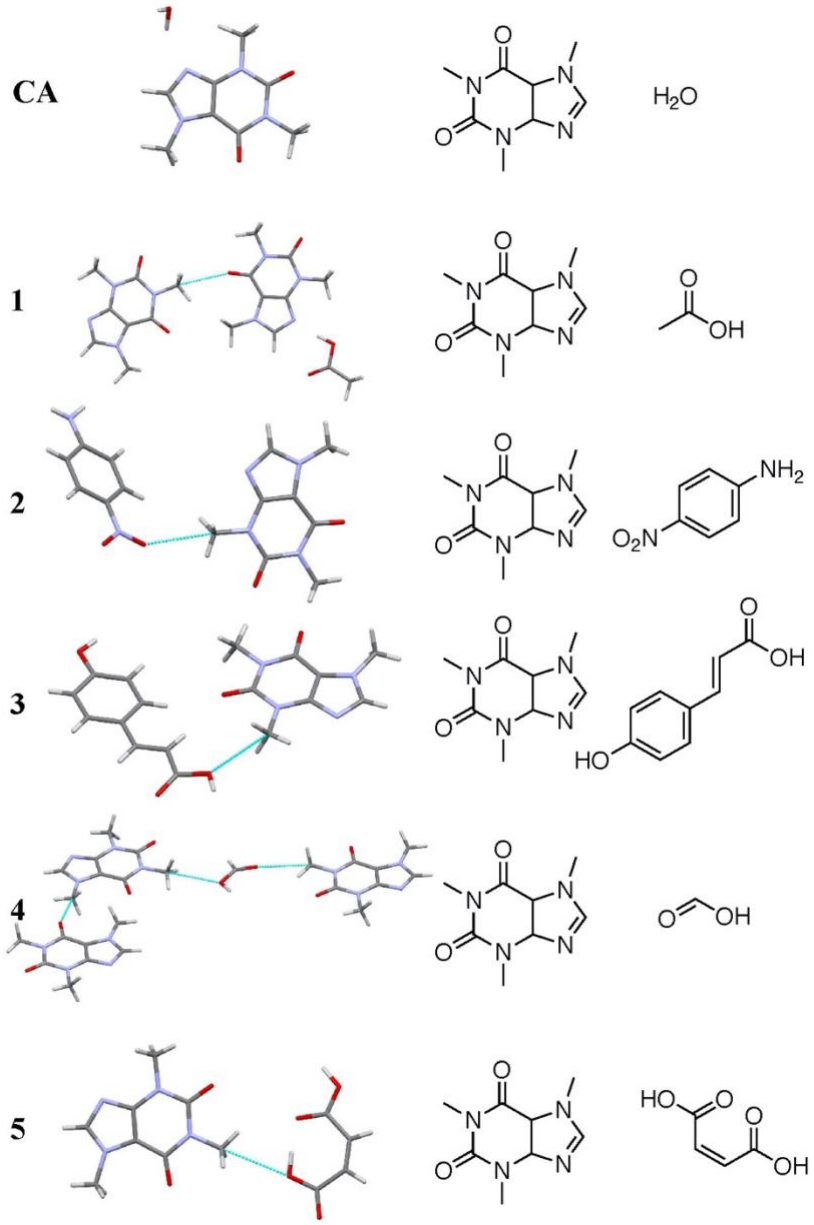

Figure 2-5. Excerpts from X-ray crystal structures of caffeine-based cocrystals used in this work (left) with their corresponding chemical structure diagrams (right). Tetrel bonding contacts are shown with turquoise dotted lines.

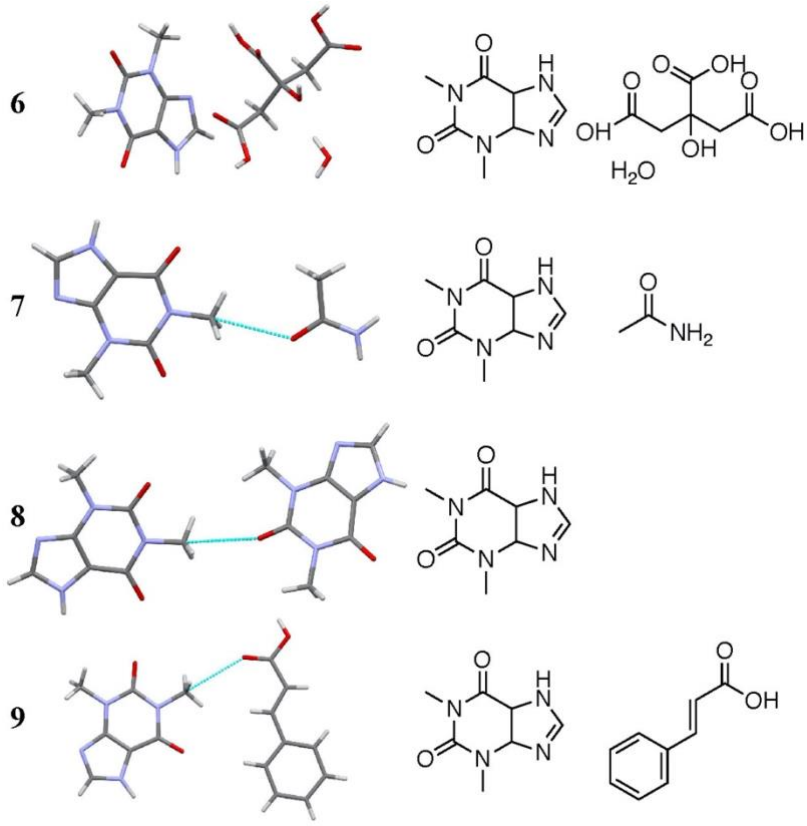

Figure 2-6. Excerpts from X-ray crystal structures of theophylline-based cocrystals used in this work (left) with their corresponding chemical structure diagrams (right). Tetrel bonding contacts are shown with turquoise dotted lines.

In most of the crystal structures presented here, the asymmetric unit contains one caffeine or theophylline molecule and one unit of the small molecule with which it cocrystallizes. The exceptions to this are the hydrates, and **4**, which crystallize with two caffeine units in the asymmetric unit. The cocrystals appear to have extensive networks of close contacts between hydrogens and electronegative atoms like oxygen and nitrogen. It is also clear that in each cocrystal, the hydrogen on C8 forms a close contact with oxygen, which suggests that this site is vital in the cocrystallization of these compounds.

Table 2-2 shows the tetrel bond geometries identified corresponding to carbon sites C10, C12, and C14 (see also **Figure 2-7**). As can be seen, most of these geometries are

characteristic of weak tetrel bonds. Although the bonds tend to be quite linear, the length of the TB determined by X-ray crystallography is often greater than 3 Å, corresponding to a standardized distance parameter of 0.932 with respect to the sum of the van der Waals radii (Eq. 2-3) between oxygen and carbon of 3.22 Å. Furthermore, some of these methyl groups also have close contacts between the methyl hydrogen and the oxygen to which the methyl carbon is bonded or an oxygen atom elsewhere.

$$R = \frac{d_{C-O}}{\sum d_{vdW}} \qquad \text{Eq. 2-3}$$

Table 2-2. Experimentally Measured and DFT Calculated Tetrel Bonding Geometries of Caffeine- and Theophylline-based Cocrystals.

Tetrel Bonded Carbon	Co-crystal	$d_{C\text{-}O}$ /Å (exp.)	$R_{C\text{-}O}$ (exp.)	Angle /degrees (exp.)	$d_{N\text{-}C}$ /Å (exp.)	$d_{C\text{-}O}$ /Å (calc.)	$R_{C\text{-}O}$ (calc.)	Angle /degrees (calc.)	$d_{N\text{-}C}$ /Å (calc.)
C10	4^{II}	3.05	0.947	150.67	1.47	3.07	0.953	149.63	1.458
	4^{I}	3.11	0.965	177.51	1.47	3.14	0.975	177.69	1.46
	9	3.12	0.970	178.90	1.47	3.15	0.978	179.79	1.46
	8	3.10	0.963	158.98	1.47	3.14	0.975	156.67	1.46
	7	3.00	0.932	172.44	1.47	3.01	0.935	172.91	1.46
	5	3.15	0.978	177.71	1.47	3.17	0.984	177.81	1.46
	1	3.09	0.960	172.05	1.45	3.18	0.988	147.60	1.45
C12	2	2.94	0.913	166.59	1.47	3.18	0.988	171.94	1.45
	3	3.18	0.988	145.82	1.47	3.18	0.988	147.60	1.45
C14	4^{I}	3.07	0.953	167.38	1.46	2.93	0.910	165.47	1.45

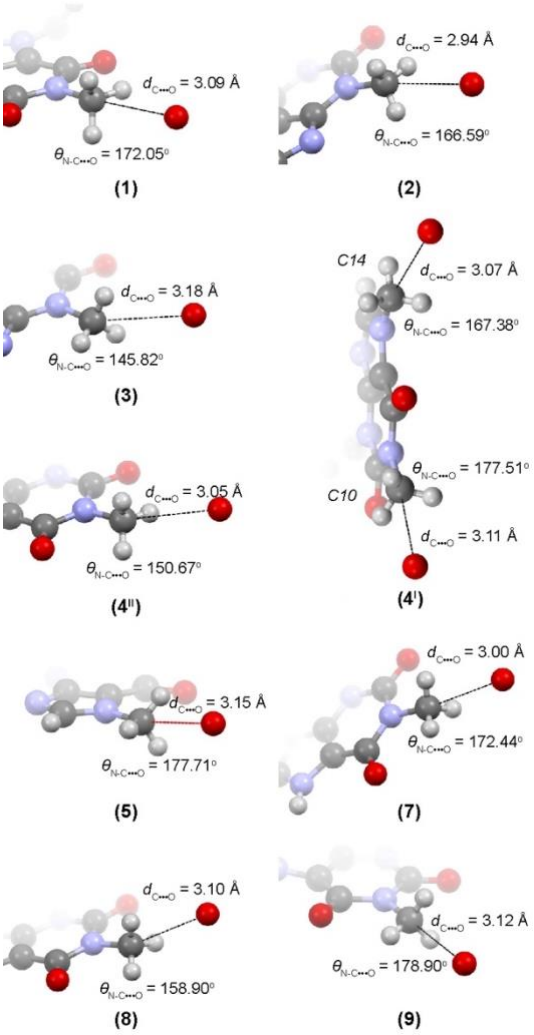

Figure 2-7. Tetrel bond geometries of the caffeine and theophylline cocrystals studied in this work. Tetrel bond distances and angles (as presented in **Table 2-2**) are shown at the tetrel bonding sites.

2.3.2 NMR Spectroscopy

To rationalize the methyl ^{13}C NMR chemical shift response upon TB-induced cocrystallization, the compounds selected for this study are compared to caffeine monohydrate, the results for which have been obtained previously by Enright and colleagues[62], and theophylline citric acid hydrate (**6**), which do not experience TBs. Pure theophylline is an obvious point of reference for theophylline-based compounds; however, it

experiences a TB at C10. Theophylline in its various polymorphic forms has been studied previously by DNP-enhanced cross-polarization solid-state NMR.[61] The most common of these polymorphs, which is typically obtained from commercial suppliers, is form II. Our commercially supplied form of theophylline is indeed form II, as indicated by the four distinct carbon signals within the ^{f}C CP/MAS spectrum's aromatic region. Pinon and colleagues[61] report that the carbon resonance of C10 is situated at a slightly higher frequency than that for C12. However, this distinction is difficult to observe in our work when the spectrum is acquired at room temperature and is exacerbated by small dipolar couplings to the nitrogen atoms to which they are bound. Nevertheless, we report the chemical shifts of C10 and C12 as 30.0 and 29.6 ppm, respectively.

^{13}C CP/MAS NMR spectra were obtained for each of the compounds (**Figure 2-8**). Signals in the methyl region (25-30 ppm) often overlap or are broadened by the effects of local disorder or dipolar coupling, which was described previously.[41,42] To be sure of our chemical shift assignments and to deconvolute overlapping peaks, two-dimensional ^{1}H-^{13}C FSLG-HETCOR experiments were performed for each system (see Appendix 1). The resulting spectra allow us to assign ^{13}C chemical shifts through their correlations with distinct ^{1}H environments and enable the measurement of ^{1}H chemical shifts. Combined with the magnetic resonance calculations conducted using CASTEP, complete assignments for all carbon atoms in each of the cocrystals were carried out either by direct observation or interpolation. We could not successfully isolate caffeine monohydrate, which has already proven to be challenging to obtain by other authors.[62] Consequently, methyl ^{1}H chemical shifts are qualitatively compared to each other.

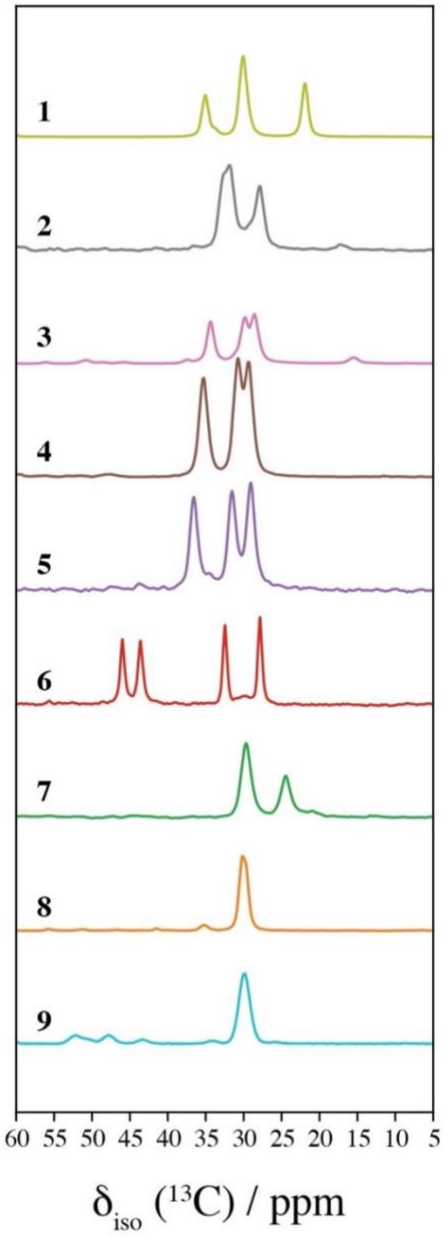

Figure 2-8. ^{13}C CP/MAS NMR spectra of caffeine- and theophylline-based cocrystals (11.7 T). The caffeine-based cocrystals are compared to the previously published[62] chemical shift of caffeine monohydrate. The theophylline-based cocrystals are compared to theophylline citric acid hydrate (**6**). The spectrum corresponding to caffeine *p*-coumaric acid (**3**) was obtained at a field strength of 9.4 T. In all cases, the spinning speed was set to 10 kHz. The measured ^{13}C chemical shifts are listed in **Table 2-3**.

It will be instructive to compare chemical shifts for methyl groups that are in similar chemical environments. C10 and C12 for each cocrystal are structurally similar enough to draw comparisons between their ^{13}C chemical shifts (see **Scheme 1**). Both of these methyl groups are situated on the pyrimidinedione ring, whereas C14 is on the imidazole ring in caffeine. The difference in chemical environments is taken into account when comparing chemical shifts. **Table 2-3** shows the experimental ^{13}C, and ^{1}H isotropic chemical shifts and the principal components of the DFT calculated magnetic shielding tensors for each cocrystal. In most cases, there is an increase in the ^{13}C chemical shift relative to caffeine monohydrate or **6**.

2.3.2.1 Caffeine cocrystals

Figure 2-9 shows a representative ^{1}H-^{13}C FSLG HETCOR spectrum for **1** for the assignment of ^{1}H and ^{13}C isotropic chemical shifts. There are a few things that are worth pointing out in this spectrum. First, an overlay of the calculated chemical shifts, obtained in MagresView[50], is shown side-by-side, both assuming motional-averaging of the methyl groups (**A**) or not (**B**). While we expect motional averaging of the methyl groups at ambient temperature in all of the structures, we observe some additional correlations for some of the methyl hydrogens; the exact nature of these signals remains unknown, though one possibility is that the signals result from longer range correlations elsewhere in the structure.[63]

Table 2-3. Calculated Magnetic Shielding and Experimental Chemical Shift Parameters.

Tetrel Bonded Carbon	Cocrystal	$d_{C\text{-}O}$ expt. /Å	$R_{C\text{-}O}$ (exp.)	δ_{iso} (^{13}C) expt. /ppm	σ_{iso} (^{13}C) calc. /ppm	Average δ_{iso} (^{1}H) expt. /ppm	Average σ_{iso} (^{1}H) calc. /ppm	Ω (^{13}C) calc. / ppm	κ (^{13}C) calc. / ppm	σ_{11} (^{13}C) calc. /ppm	σ_{22} (^{13}C) calc. /ppm	σ_{33} (^{13}C) calc. /ppm
C10	CA			29[62]	148.6		29.4	54.4	-0.02	121.2	149.1	175.6
	6			27.7	151.5	3.0	28.9	52.0	-0.18	123.9	154.7	175.9
	7	3.00	0.947	29.9	149.2	1.9	28.5	53.8	-0.21	120.4	152.9	174.2
	4[II]	3.05	0.965	28.3	149.7	1.4	28.4	53.2	-0.17	121.5	152.5	174.6
	8	3.10	0.963	30.0	147.5	3.0	28.1	50.9	-0.10	121.3	149.2	172.2
	4[I]	3.11	0.966	28.6	149.5	1.6	28.5	51.9	-0.11	122.8	151.6	174.7
	9	3.12	0.969	29.9	148.9	3.0	28.1	48.9	-0.24	122.5	152.8	171.4
	5	3.15	0.978	28.3	149.9	1.9	28.4	51.3	-0.22	122.4	153.6	173.7
	1	3.09	0.960	29.2	147.4	2.5	29.4	50.5	0.02	122.3	147.2	172.8
C12	CA			30.6	147.1		28.0	48.4	0.19	124.5	144.0	172.9
	6			32.4	146.0	4.1	27.9	50.0	0.36	140.1	174.0	146.0
	2	2.94	0.913	31.4	149.3	2.7	27.9	48.2	-0.29	123.0	153.9	171.2
	3	3.18	0.988	29.4	144.4	2.5	28.3	56.0	0.26	122.3	143.1	178.3
C14	CA			34.9	143.1		27.6	57.3	0.64	120.5	130.9	177.8
	4[I]	3.07	0.953	34.8	143.0	2.1	27.1	59.1	0.59	119.8	132.1	178.9

1. Caffeine formic acid (**4**) contains two molecules of caffeine in its asymmetric unit and these are labelled by I and II.

The peak corresponding to H10 has a ^{1}H isotropic chemical shift of 2.5 ppm. This is important because of the increase of the ^{1}H isotropic chemical shift compared to the others, which we would expect to see because of a hydrogen bond. However, on careful inspection of the crystal structure of **1**, H10c forms a cis-interaction with the nearby aromatic ketone, putting it nearby ($d_{\text{H-O, calc.}}$ = 2.22 Å) according to the geometry-optimized structure. C10 is also tetrel bonded ($d_{\text{C...O, expt.}}$ = 3.09 Å). Using the correlation at H10, we can measure the ^{13}C isotropic chemical shift of C10 as 29.2 ppm. As compared to the same methyl carbon on both caffeine monohydrate and **6**, there is an increase in the ^{13}C chemical shift of 0.2 and 2.5 ppm, respectively.

Caffeine:4-nitroaniline (**2**) cocrystallizes with one unit of caffeine and one unit of 4-nitroaniline. We note a TB ($d_{\text{C...O,expt.}}$ = 2.94 Å, θ = 166.59°, **Figure 2-6**) and a hydrogen bond occurring at C12, whereas no TB interactions occur at C10 or C14. In the methyl ^{13}C region of the HETCOR spectrum (**Figure S1-12**), we resolve three ^{13}C peaks: 27.9 ppm (C10), 31.4 ppm (C12) and 32.1 ppm (C14). Compared to C12 in CA, the ^{13}C chemical shift of **2** is higher (by 0.8 ppm), consistent with a tetrel bond.

Caffeine *p*-coumaric acid (**3**) features what appears to be a TB at C12. The TB angle is quite acute, and the length is relatively long ($d_{\text{C...O, expt.}}$ = 3.18 Å, θ = 145.82°; see **Figure 2-6**). Because these metrics barely qualify to be considered a TB, it is a structure that can provide helpful insight into the effects of hydrogen bonding on the ^{13}C chemical shift as the geometry moves away from a tetrel bond towards a weak CH···O hydrogen bond. C12 is found to have a ^{13}C chemical shift of 29.4 ppm, a decrease of 1.2 ppm compared with CA, and 3.0 ppm compared to **6**.

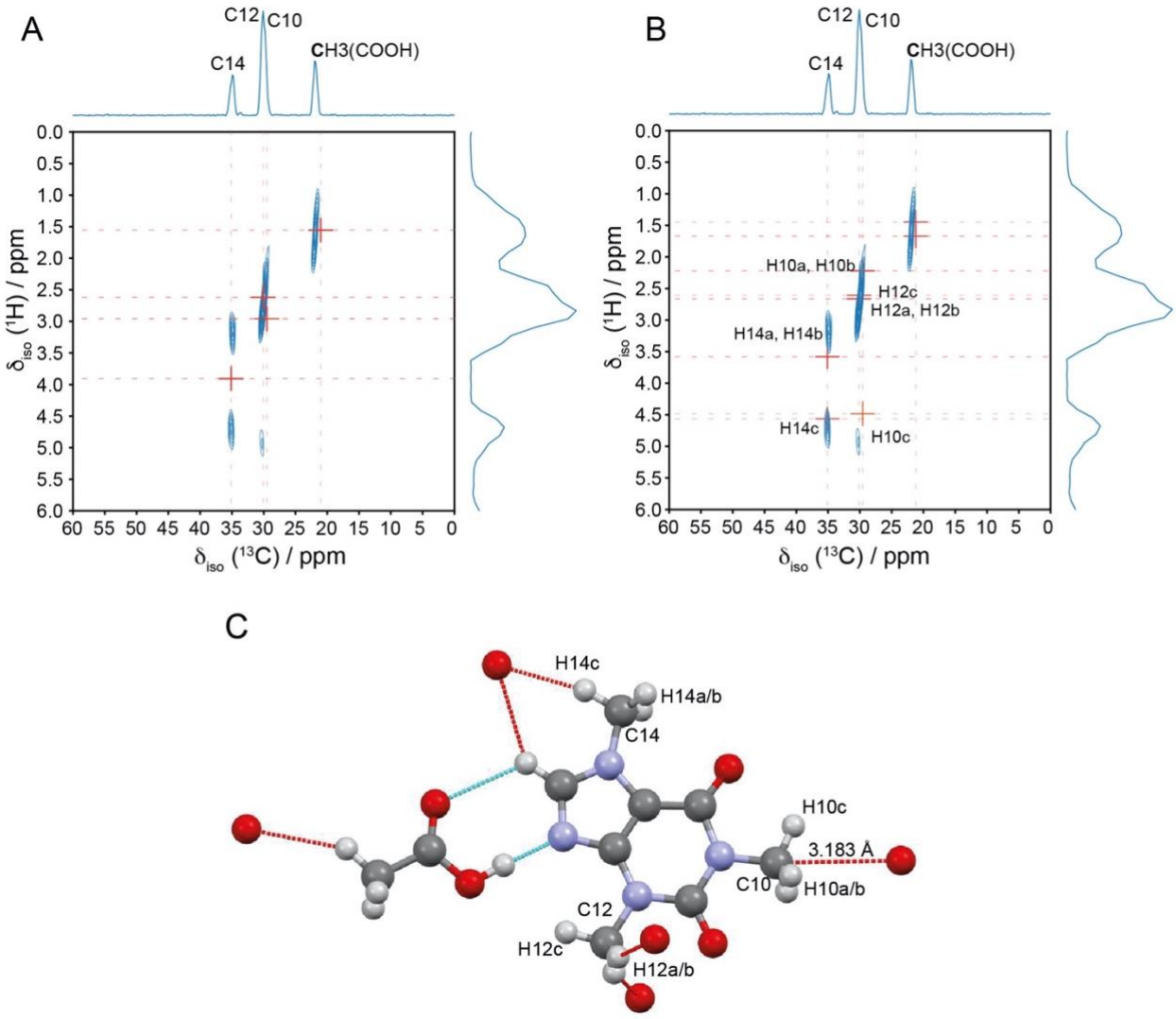

Figure 2-9. ^{1}H-^{13}C FSLG-HETCOR NMR spectra of the methyl-region of caffeine acetic acid (**1**) (CSD: VAWKOU) overlaid with correlations from ^{1}H atoms to the ^{13}C, obtained by DFT calculations, indicated by red horizontal and vertical dashed lines, which are labelled with the corresponding H and C atoms shown on the molecular scheme. The calculated ^{1}H chemical shift values for each methyl group are averaged to represent motional averaging (**A**) or are represented as calculated (**B**). A representation of the geometry-optimized asymmetric unit of the crystal structure (**C**) shows the selected close contacts between hydrogens and oxygens are shown, and the tetrel bond is shown as measured by the geometry optimization.

While the oxygen atom participating in the tetrel bond to C12 is close enough to fall within the sum of their van der Waals radii, it still lies far enough from the hydrogen atoms that a hydrogen bond would be weak. The average calculated ^{1}H chemical shift increases by 0.3 ppm and 0.4 ppm with respect to **CA** and **6,** respectively, which is consistent with the notion that the oxygen engages hydrogen in a weak HB rather than a TB.

Caffeine formic acid (**4**) has a somewhat more complicated crystal structure. It cocrystallizes in a 2:1 ratio of caffeine to formic acid. In **4^{I}**, there are two C-O contacts, one each at C^{I}10 ($d_{C\ldots O,\ expt.}$ = 3.11 Å, θ = 177.51°; see **Figure 2-6**) and C^{I}14 ($d_{C\ldots O,\ expt.}$ = 3.07 Å, θ = 167.08°). At the same time, C^{I}14 appears to experience a hydrogen bond above the plane of caffeine. On **4^{II}**, we only see one possible contact at C10 ($d_{C\ldots O,\ expt.}$ = 3.05 Å, θ = 150.67°), but the other two methyl carbons are engaged in hydrogen bonds above and below their planes, in very similar bonding environments. Upon inspection of the NMR data (**Figure S1-13**), we see several obvious signals in the methyl region of the ^{13}C dimension of the HETCOR spectrum. For C^{II}10, we see a signal at δ_{iso}(^{13}C) = 28.3 ppm.

The last caffeine-based cocrystal is caffeine-maleic acid (**5**), which cocrystallizes in a 1:1 ratio. This cocrystal features one unique caffeine molecule participating in a tetrel bond with maleic acid at C10 ($d_{C\ldots O,\ expt.}$ = 3.15 Å, $\theta_{NC\text{-}O}$ = 177.7°; see **Figure 2-6**). Given the long distance between C10 and oxygen, it is unlikely that the methyl hydrogen atoms are participating in a trifurcated hydrogen bond. The HETCOR spectrum (**Figure S1-10**) shows that tetrel-bonded C10 has a ^{13}C isotropic chemical shift of 28.3 ppm. Indeed, the TB is quite long, which explains such a slight change in the ^{13}C chemical shift relative to C10 of **CA** and **6**. Consequently, if a very weak tetrel bond is present, one may conclude that its effects on the chemical shift are likely to be masked by other crystallographic effects.

2.3.2.2 Theophylline cocrystals

The theophylline-based cocrystals are somewhat simpler to study in terms of their NMR parameters because there is one less methyl group attached to the molecule frame. We start with pure anhydrous theophylline (**8**). There are several known polymorphs of theophylline, but Form II is metastable at room temperature. A possible tetrel bond is present at C10 ($d_{C...O,\ expt.}$ = 3.10 Å, θ = 159.0°; see **Figure 2-6**). The methyl region of the HETCOR and CP/MAS spectra consists of two overlapping ^{13}C peaks. The peak at 30.0 ppm is assigned to C10 (*vide supra*). Thus an increase in the chemical shift is noted for tetrel-bonded C10 relative to CA and **6** (29 and 27.7 ppm, respectively).

Theophylline citric acid hydrate (**6**) is formed by the cocrystallization of theophylline and citric acid hydrate. Herein, **6** is used as a standard reference for comparing the C10 and C12 carbon sites in the theophylline and caffeine cocrystals because it does not appear to form tetrel bonds at either methyl group. Methyl carbons C10 and C12 resonate at 27.7 ppm and 32.4 ppm, respectively.

Theophylline acetamide (**7**) features a tetrel bond at C10 ($d_{C...O,\ expt.}$ = 3.00 Å, θ = 172.4°; see **Figure 2-6**) and possibly a weak hydrogen bond at C12 ($d_{C...O,\ expt.}$ = 3.62 Å). The HETCOR spectrum (**Figure S1-15**) shows two slightly overlapping peaks attributed to C10 ($\delta_{iso}(^{13}C)$ = 29.9 ppm) and C12 ($\delta_{iso}(^{13}C)$ = 29.7 ppm). The ^{13}C chemical shift at tetrel-bonded C10 is thus elevated compared to **CA** and **6** by 0.9 and 2.2 ppm, respectively.

Finally, theophylline cinnamic acid (**9**) cocrystallizes to form a highly linear tetrel bond at C10 ($d_{C...O,\ expt.}$ = 3.12 Å, θ = 178.9°; see **Figure 2-6**), and a possible CH···N hydrogen bond at C12 ($d_{C\text{-}N,\ expt.}$ = 3.45 Å). The HETCOR and CP/MAS spectra show that $\delta_{iso}(^{13}C)$ = 29.9 ppm for tetrel-bonded C10; this is elevated by 2.2 and 0.9 ppm relative to CA and **6**,

respectively. C10 is also correlated to a ^{1}H signal with a higher chemical shift, supporting the presence of an intramolecular HB occurring with the oxygen bonded to C6 ($d_{C..O,\ calc.}$ = 2.31 Å).

2.3.2.3 Observed Trends

A plot of the experimental ^{13}C data for all TBs is shown as a function of the experimentally measured tetrel bond length in **Figure 2-11A**. It must be noted that C14 of **4^{II}** is omitted from the plots in **Figure 2-11** as its chemical environment is too dissimilar to those of C10 and C12, resulting in an inherent increase in the carbon chemical shift, so it cannot be compared in this way without other examples experiencing tetrel bonds at C14. To demonstrate that the trend is consistent with data for other systems not studied herein, the experimental data from two other caffeine-based cocrystals are also included[41] (caffeine-malonic acid and caffeine-glutaric acid, as indicated by the blue circles). Generally speaking, there is an increase in the ^{13}C chemical shift as the TB length becomes shorter, particularly at C10, spanning from ~28 ppm for the longest TB to ~32 ppm for the shortest TB. Generally, the increase is observable but small (< 3 ppm). These experimental data agree with previous computational evidence presented by us[39] and Scheiner[35], whereby ^{13}C becomes less shielded as C and O are brought together.[35] Newly computed shielding constants have been plotted against $d_{C\cdots O}$ (**Figure S1-20**); these data are also consistent with the experimental trend shown in **Figure 2-11**. That being said, the correlation is not strong, and this is likely explained by the fact that there are other factors, including long-range effects, which may influence the ^{13}C chemical shift.

Analysis of the magnetic shielding tensor components provides a valuable way to understand the underlying causes for changes in the isotropic chemical shift. The magnitude

of the magnetic shielding tensor can be described by its three principal components (σ_{11}, σ_{22}, and σ_{33}, where $\sigma_{33} \geq \sigma_{22} \geq \sigma_{11}$).[64] The calculated isotropic magnetic shielding is given by $\sigma_{iso} = (\sigma_{11} + \sigma_{22} + \sigma_{11})/3$, the anisotropy of the tensor is described by the span and is given by $\Omega = \sigma_{33} - \sigma_{11}$, and the asymmetry is quantified by the skew, $\kappa = (2\sigma_{22} - \sigma_{11} + \sigma_{33})/\Omega$.

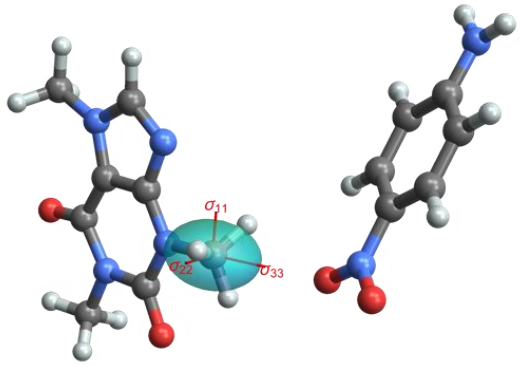

Figure 2-10. DFT-computed carbon magnetic shielding tensor orientation in cocrystal 2. For all compounds in this work, σ_{33} generally lies along the N-C bond and this orientation is only subtly perturbed by the formation of a tetrel bond.

Firstly, it is noted that the calculated value of $\Omega(^{13}C)$ increases as the TB gets shorter (**Figure 2-11B**). This trend is dominated by a change in σ_{33} (**Figure 2-11C**). $\sigma_{33, calc.}$ becomes more positive as the TB length gets shorter. The skew, κ, does not seem to correlate well with the TB length; however, there is a loose decrease of κ as the TB angle approaches linearity (**Figure 2-12**). The large degree of scattering in the observed correlations suggests that while the tetrel bond plays a role in the ^{13}C chemical shift response, other competing factors are likely, including weak hydrogen bonding and other crystal packing effects. The direction of the σ_{33} eigenvector does not change significantly upon tetrel bond formation (see **Figure 2-10**).

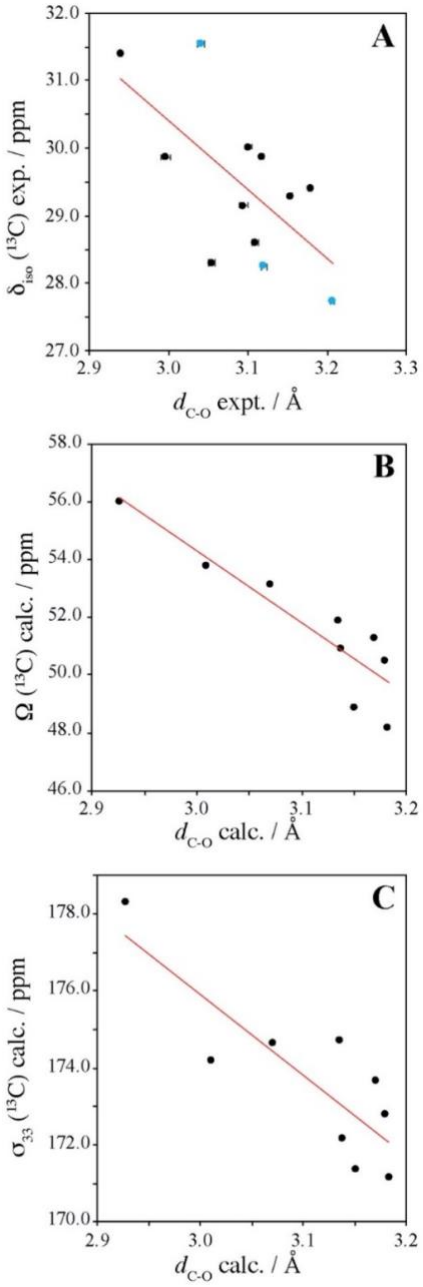

Figure 2-11. Comparison between (**A**) the experimental TB length and the experimental ^{13}C chemical shift (R^2 = 0.4276), (**B**) the calculated TB length and the calculated magnetic shielding tensor span (R^2 = 0.8225), and (**C**) the calculated TB length and σ_{33} (R^2 = 0.7040). The red lines are fits for all data corresponding to carbons C10 and C12. In panel **A** the blue circles correspond to the NMR data obtained by Vigilante and Mehta[41], where δ_{iso} (^{13}C) = 28.24 (C10) and 31.54 (C12) ppm for caffeine:malonic acid, and 27.73 ppm for caffeine:glutaric acid.[41]

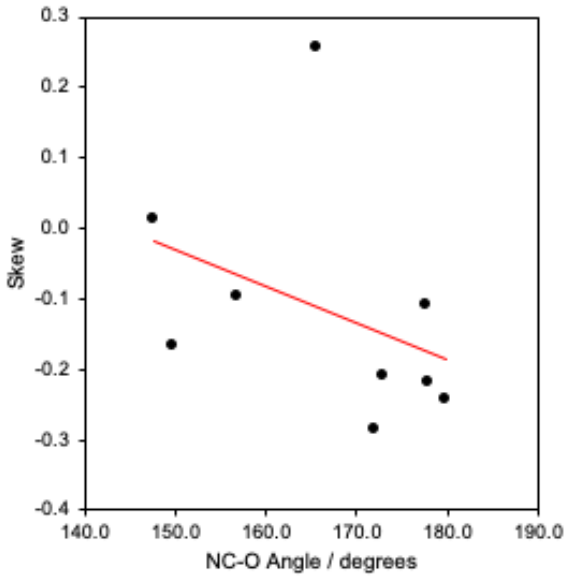

Figure 2-12. DFT calculated magnetic shielding tensor skew versus the calculated TB angle.

Figure 2-13 shows the general lack of correlation between isotropic ^{13}C and ^{1}H chemical shifts and the TB angle (see also **Figure S1-20**). There is also no clear trend between the average experimental ^{1}H chemical shifts and the TB length. At C10, in some cases, $\delta_{iso}(^{1}H)$ increases. In other cases, it decreases with respect to **6**. However, in comparing the calculated ^{1}H shieldings to similar methyl groups on **CA** and **6**, we see that the hydrogen shifts undergo a slight change in the negative direction in most cases. It is also important to recognize that for C10, the DFT calculations suggest that the methyl hydrogen tends to adopt a *cis* configuration with respect to the aromatic keto oxygen, which may influence the shielding at both the ^{13}C and ^{1}H sites of C10. Overall, as the TB approaches a geometry that prefers the HB, the ^{1}H response increases subtly, though apart from a few outliers, there is no significant change for most of the systems. Scheiner's results indicated a deshielding at the ^{1}H nucleus as the motif adopts more of a hydrogen bond geometry.[35]

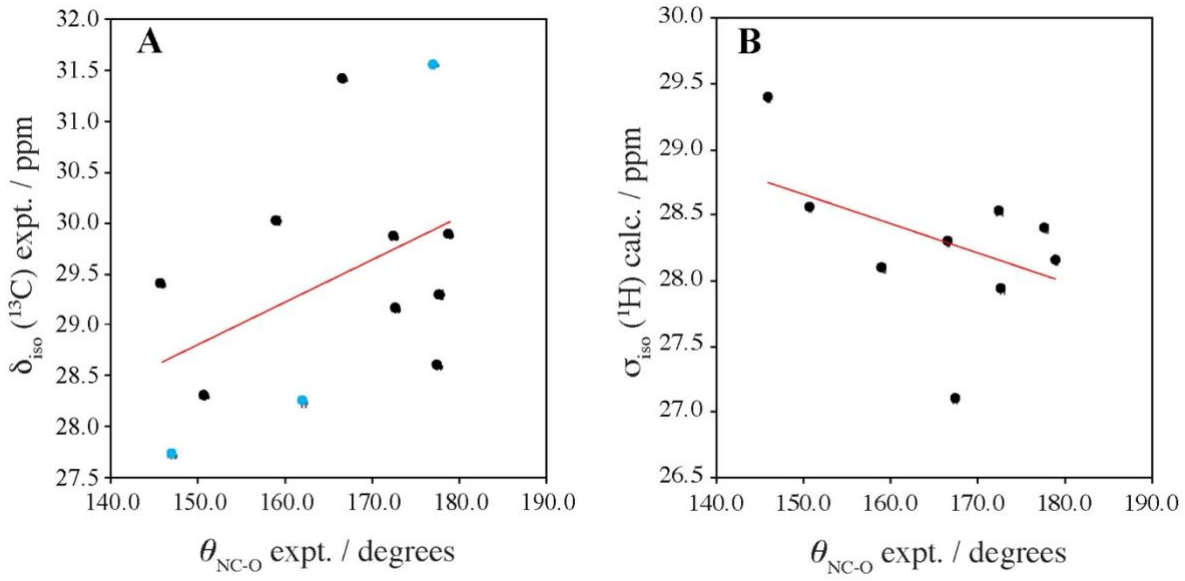

Figure 2-13. Lack of correlation between the experimental TB angles and (**A**) the experimental ^{13}C chemical shift (R^2 = 0.1912) and (**B**) the computed ^{1}H magnetic shieldings (R^2 = 0.1963). The red line is meant to guide the eye towards the generally observed trend and fit the data corresponding to carbons C10 and C12. In panel **A** the blue circles correspond to the NMR data obtained by Vigilante and Mehta[41], where δ_{iso} (^{13}C) = 28.24 (C10) and 31.54 (C12) ppm for caffeine:malonic acid, and 27.73 ppm for caffeine:glutaric acid.[41]

Two structures with close contacts at C12 are assessed (**2** and **3**), but the TB angle in **3** is low (slightly below 160°). Interestingly in these situations, the experimental ^{13}C chemical shifts decrease for both **2** and **3** relative to **6**.

The correlations presented here are generally not strong. The ^{13}C isotropic chemical shift is very sensitive to the changes in the nearby electronic environment; there are many variables at play within a crystal structure, such as strain, long-range noncovalent forces or ring currents, which could contribute to the imperfections noted in our correlations. However, the tetrel bond is important enough of an interaction that the preceding correlations can be understood with careful analysis and computation (*vide infra*).

2.3.3 Isolated Molecules

Complimentary quantum chemical calculations are required to understand how the 13C chemical shift response changes are attributable to the tetrel bond in the absence of other crystallographic effects. The magnetic shielding constants of the methyl carbons participating in the tetrel bonds were calculated for these systems using a "molecule-in-a-box" approach using CASTEP, a similar method to single-molecule cluster calculations. In other words, the optimized geometries of the two molecules (dimer) involved in the tetrel bond were retained while the unit cell was emptied of all other atoms and enlarged to the point that periodic effects would not affect the chemical shift. The calculation was repeated with the acceptor molecule removed (monomer). **Table 2-4** shows the results of these calculations. The trends are striking. In agreement with Scheiner,[35] upon cocrystallization, the calculated value of $\sigma_{iso}(^{13}C)$ decreases by an average of 2.9 ppm over all of the sampled cocrystals, which corresponds to a chemical shift increase. Notably, other methyl carbons in the system that do not engage in any type of bonding do not undergo any substantial shielding changes upon heterodimerization. These data indicate the chemical shift change observed in the absence of other crystallographic effects. An increase in the magnitude of Ω and κ upon dimerization is also noted. The positive change in Ω is consistent with the trend depicted in **Figure 2-11B**. The results of magnetic shielding calculations on the full crystal structures confirm that while the impact of a tetrel bond in isolation on the ^{13}C magnetic shielding constant is to decrease it consistently, further inclusion of the whole crystal lattice can obscure this effect (i.e., two out of nine data points for the full crystal calculation show that the impact of the lattice is to oppose the effect of the tetrel bond in isolation).

Table 2-4. ^{13}C Magnetic Shielding Calculations for Tetrel Bonded Heterodimers versus Their Corresponding Non-Tetrel Bonded Monomers.

Compound	TB location	TB Length calc. / Å	TB Angle calc. /degrees	σ_{iso} (^{13}C) calc. /ppm (monomer)	σ_{iso} (^{13}C) calc. /ppm (dimer)	σ_{iso} (^{13}C) calc. /ppm (crystal)	$\Delta\sigma_{iso}$ (^{13}C) /ppm (dimer-monomer)	Ω (^{13}C) calc. /ppm (monomer)	Ω (^{13}C) calc. /ppm (dimer)	κ (^{13}C) calc. /ppm (monomer)	κ (^{13}C) calc. /ppm (dimer)
1	C10	3.18	171.9	155.1	151.9	147.4	-3.2	51.27	53.28	-0.23	0.27
2	C12	2.93	165.5	152.5	149.4	149.3	-3.1	54.38	57.92	0.30	0.37
3	C12	3.18	147.6	152.4	149.5	144.4	-2.9	52.93	53.60	0.26	0.29
4^{II}	C10	3.07	149.6	152.5	149.8	149.7	-2.7	51.14	53.32	0.01	0.06
4^{I}	C10	3.13	177.7	152.7	151.0	149.5	-1.7	51.01	55.85	0.02	0.01
4^{I}	C14	3.10	166.5	145.0	142.3	143.0	-2.7	59.11	62.6	0.81	0.85
5	C10	3.17	177.8	152.8	150.8	149.9	-2.0	51.22	55.42	-0.04	0.05
7	C10	3.01	172.9	153.6	149.8	149.2	-3.8	51.53	57.58	-0.17	-0.05
9	C10	3.15	179.8	153.8	150.1	148.9	-3.7	51.23	54.22	-0.17	-0.04

2.4 Conclusions

The purpose of this contribution was to provide experimental insight into (*i*) the effect of weak methyl group tetrel bonding on the ^{13}C isotropic chemical shift, (*ii*) the dependence of these shifts on the TB geometry, and (*iii*) the potential competing influence of weak CH···O hydrogen bonds on these shifts. Although most correlations between experimental shifts and structural features are weak, close inspection of the data in concert with computational results allows the following conclusions to be drawn:

1. The tetrel bond influences the ^{13}C experimental chemical shift. As the tetrel bond length, measured by X-ray diffraction or optimized with DFT, gets shorter, the ^{13}C isotropic chemical shift increases. This increase more strongly correlates with TB distance in the absence of competing structural effects.

2. Generally, the ^{13}C chemical shift increases compared to the chemically similar methyl carbons in cocrystals that do not feature tetrel bonds. The magnitude of this effect (based on present and past experimental and computational work) is up to approximately 5 ppm but varies due to other crystallographic effects. Based on our assessment of the hydrogen bonding in these systems, one such effect is the NMR response to the other weak CH···O hydrogen bonds at most methyl sites resulting in a competing effect on the ^{13}C chemical shift. For systems featuring a competing hydrogen bond, the ^{13}C isotropic chemical shift's overall increase due to the tetrel bond is usually not as large as if there were no hydrogen bonds. However, there is

also evidence that a competing hydrogen bond can either reinforce or detract from the influence of the TB on the ^{13}C chemical shift.

3. While the ^{1}H chemical shift of the methyl hydrogens is also affected by tetrel bond formation, all experimentally observed correlations are weak and show a significant degree of scatter. This is consistent with the notion that a range of weak interactions influences the overall ^{1}H shift response.

To summarize, this work has provided experimental NMR data to address the question of how tetrel bonds influence chemical shifts. Given the low polarizability of carbon and the weakness of the TBs studied presently, the lack of strong experimental correlations with structural features is perhaps not surprising. This work could prove to be a valuable resource for future computational analyses to explore further the relationship between chemical shifts and various non-covalent interactions, particularly in the solid state. These results may also find utility in NMR crystallographic approaches to solve and refine structures that may feature tetrel bonds.

2.5 References

[1] Cavallo, G.; Metrangolo, P. Pilati, T.; Resnati, G; Terraneo, G. Naming Interactions from the Electrophilic Site. *Cryst. Growth Des*. **2014**, *14*, 2697-2702.

[2] Politzer, P.; Murray, J. S.; Clark, T. Halogen Bonding and Other σ-Hole Interactions: a Perspective. *Phys. Chem. Chem. Phys.* **2013**, *15*, 11178-11189.

[3] Metrangolo, P.; Neukirch, H.; Pilati, T.; Resnati, G. Halogen Bonding Based Recognition Processes: A World Parallel to Hydrogen Bonding. *Acc. Chem. Res.* **2005**, *38*, 386-395.

[4] Zahn, S.; Frank, R.; Hey-Hawkins, E.; Kirchner, B. Pnicogen Bonds: A New Molecular Linker? *Chem. -Eur. J.* **2011**, *17*, 6034-6038.

[5] Sarkar, S.; Pavan, M. S.; Guru Row, T. N. Experimental Validation of 'Pnicogen Bonding' in Nitrogen by Charge Density Analysis. *Phys. Chem. Chem. Phys.* **2015**, *17*, 2330-2334.

[6] Scheiner, S.; Adhikari, U. Abilities of Different Electron Donors (D) to Engage in a P···D Noncovalent Interaction. *J. Phys. Chem. A* **2011**, *115*, 11101-11110.

[7] Wang, W.; Ji, B.; Zhang, Y. Chalcogen Bond: A Sister Noncovalent Bond to Halogen Bond. *J. Phys. Chem. A* **2009**, *113*, 8132-8135.

[8] Scilabra, P.; Terraneo, G.; Resnati, G. The Chalcogen Bond in Crystalline Solids: A World Parallel to Halogen Bond. *Acc. Chem. Res*. **2019**, *52*, 1313-1324.

[9] Bauzá, A. Mooibroek, T. J.; Frontera, A. Tetrel-Bonding Interaction: Rediscovered Supramolecular Force? *Angew. Chem. Int. Ed.* **2013**, *125*, 12317-12321.

[10] Grabowski, S. J. Tetrel Bond-σ-Hole Bond as a Preliminary Stage of the S_N2 Reaction. *Phys. Chem. Chem. Phys.* **2014**, 16, *1824*-1834.

[11] Bauzá, A.; Frontera, A. Aerogen Bonding Interaction: A New Supramolecular Force? *Angew. Chem. Int. Ed.* **2015**, *54*, 7340-7343.

[12] Bauzá, A.; Frontera, A. σ/π-Hole Noble Gas Bonding Interactions: Insights from Theory and Experiment. *Coord. Chem. Rev.* **2020**, *404*, 213112.

[13] Del Bene, J. E.; Alkorta, J.; Elguero, J. Influence of Substituent Effects on the Formation of P···Cl Pnicogen Bonds or Halogen Bonds. *J. Phys. Chem. A* **2014**, *118*, 2360-2366.

[14] Li, Q.; Guo, X.; Yang, X.; Li, W.; Cheng, J.; Li, H.-B. A σ-Hole Interaction with radical species as Electron Donors: Does Single-Electron Tetrel Bonding Exist? *Phys. Chem. Chem. Phys.* **2014**, *16*, 11617-11625.

[15] Clark, T. Hennemann, M.; Murrary, J. S.; Politzer, P. Halogen Bonding: The σ-Hole. *J. Mol. Model.* **2007**, *13*, 291-296.

[16] Mani, D.; Arunan, E. The X-C···Y (X = O/F, Y = O/S/F/Cl/Br/N/P) 'Carbon Bond' and Hydrophobic Interactions. *Phys. Chem. Chem. Phys.* **2013**, *15*, 14377-14383.

[17] Murray, J. S.; Lane, P.; Politzer, P. Expansion of the σ-Hole Concept. *J. Mol. Model.* **2009**, *15*, 723-729.

[18] Thomas, S. P.; Pavan, M. S.; Guru Row, T. N. Experimental Evidence for Carbon Bonding' in the Solid State From Charge Density Analysis. *Chem. Commun.* **2014**, *50*, 49-51.

[19] Daolio, A.; Scilabra, P. Terraneo, G. Resnati, G. C(sp^3) Atoms as Tetrel Bond Donors: A Crystallographic Survey. *Coord. Chem. Rev.* **2020**, *413*, 213265.

[20] Breliere, C.; Carré, F.; Corriu, R. J. P.; Poirier, M.; Royo, G.; Zwecker, J. Hexacoordinated Silicon Species: A Possible Model for Reaction Intermediates. 1. X-ray Determination of the Geometry in the Solid State. *Organometallics* **1989**, *8*, 1831-1833.

[21] Belzner, J.; Schär, D.; Herbst-Irmer, R.; Kneisel, B. O.; Noltemeyer, M. Synthesis and Structure of Intramolecularly Coordinated Silicon Compounds Coordinated by Hydrazino Groups. *Tetrahedron* **1998**, *54*, 8481-8500.

[22] Carre, F.; Chuit, C.; Corriu, R. J. P.; Mehdi, A.; Reye, C. Synthesis, Structure and Fluxional Behaviour of a Dihydrosilane Bearing and Aryldiamine Pincer Ligand. *Organometallics* **1995**, *14*, 2754-2759.

[23] Berceanc, V.; Crainic, C.; Haiduc, I.; Mahon, M. F.; Molloy, K. C.; Venter, M. M.; Wilson, P. J. The Structural Chemistry of Organotin Derivatives of 5-Mercapto-3-phenyl-1,3,4-thiadiazoline-2-thione: Supramolecular Structures Involving Intermolecular Sn···S, N-H···S or S···S Interactions. *J. Chem. Soc. Dalton Trans.* **2002**, 1036-1045.

[24] Akkari-El Ahdab, A.-E.; Rima, G.; Gornitzka, H.; Barrau, J. Synthesis And Characterization Of 2,4,6-Tris((Dimethylamino)Methyl)Phenoxysilicon Compounds. *J. Organomet. Chem.* **2001**, 636, 96-107.

[25] Kost, D.; Gostevskii, B.; Kalikhman, I. Silicon Rehybridization and Molecular Rearrangements in Hypercoordinate Silicon Dichelates. *Pure Appl. Chem.* **2007**, *79*, 1125-1134.

[26] Frontera, A. Tetrel Bonding Interactions Involving Carbon at Work: Recent Advances in Crystal Engineering and Catalysis. *C* **2020**, *6*, 60.

[27] Kumar, V.; Rodrigue, C.; Bryce, D. L. Short and Linear Intermolecular Tetrel Bonds to Tin. Co-crystal Engineering with Triphenyltin Chloride. *Cryst. Growth. Des.* **2020**, 20, 2027-2034.

[28] Gargari, M. S.; Bauzá, A.; Frontera, A.; McArdle, P.; Van Derveer, D; Ng, S. W.; Mahmoudi, G. Design of Lead(II) Metal-Organic Frameworks Based on Covalent and Tetrel Bonding. *Chem. -Eur. J.* **2015**, *21*, 17591-17598.

[29] Afkhami, F. A.; Mahmoudi, G.; Qu, F.; Gupta, A.; Köse, M.; Zangrando, E.; Zubkov, F. I.; Alkorta, A.; Safin, D. A. Supramolecular Lead(II) Architectures Engineered By Tetrel Bonds. *CrystEngComm* **2020**, *22*, 2389-2396.

[30] Hou, M.; Zhu, Y.; Li, Q.; Scheiner, S. Tuning the Competition between Hydrogen and Tetrel Bonds by a Magnesium Bond. *ChemPhysChem*. **2020**, *21*, 212-219.

[31] Hou, M.; Li, Q.; Scheiner, S. The Ability of A Tetrel Bond to Transition a Neutral Amino Acid into a Zwitterion. *Chem. Phys. Lett.* **2019**, *731*, 136584.

[32] Michalczyk, M.; Zierkiewicz, W.; Wysokiński, R.; Scheiner, S. Theoretical Studies of IR And NMR Spectral Changes Induced By Sigma-Hole Hydrogen, Halogen, Chalcogen, Pnicogen, And Tetrel Bonds In A Model Protein Environment. *Molecules* **2019**, *24*, 3329.

[33] Del Bene, J.E.; Alkorta, I.; Elguero, J. Potential Energy Surfaces of HN(CH)SX:CO_2 for X = F, Cl, NC, CN, CCH, and H: N···C Tetrel Bonds and O···S Chalcogen Bonds. *J. Phys. Chem. A* **2019**, *123*, 7270-7277.

[34] Grabowski, S. J. Pnicogen And Tetrel Bonds—Tetrahedral Lewis Acid Centres. *Struct. Chem.* **2019**, *30*, 1141-1152.

[35] Scheiner, S. Ability of IR and NMR Spectral Data to Distinguish between a Tetrel Bond and a Hydrogen Bond. *J. Phys. Chem. A* **2018**, *122*, 7852-7862.

[36] Scheiner, S. Dependence Of NMR Chemical Shifts upon CH Bond Lengths of a Methyl Group Involved in a Tetrel Bond. *Chem. Phys. Lett.* **2019**, *714*, 61-64.

[37] Lu, J.; Scheiner, S. Relationships between Bond Strength and Spectroscopic Quantities in H-Bonds and Related Halogen, Chalcogen and Pnicogen Bonds. *J. Phys. Chem. A.* **2020**, *124*, 7716-7725.

[38] Lu, T.; Zhang, J.; Gou, Q.; Feng, G. Structure And C···N Tetrel-Bonding of the Isopropylamine-CO_2 Complex Studied by Microwave Spectroscopy and Theoretical Calculations. *Phys. Chem. Chem. Phys.* **2020**, *22*, 8467-8475.

[39] Southern, S. A.; Bryce, D. L. NMR Investigations of Noncovalent Carbon Tetrel Bonds. Computational Assessment and Initial Experimental Observation. *J. Phys. Chem. A* **2015**, *119*, 11891-11899.

[40] Southern, S. A.; Errulat, D.; Frost, J. M.; Gabidullin, B.; Bryce, D. L. Prospects for ^{207}Pb Solid-State NMR Studies of Lead Tetrel Bonds. *Faraday Discuss.* **2017**, *203*, 165-186.

[41] Vigilante, N. J.; Mehta, M. A. A ^{13}C Solid-State NMR Investigation of Four Co-Crystals of Caffeine and Theophylline. *Acta Cryst.* **2017**, *C73*, 234-243.

[42] Kerr, H. E.; Mason, H. E.; Sparkes, H. A.; Hodgkinson, P. Testing the Limits of NMR Crystallography: The Case of Caffeine-Citric Acid Hydrate. *CrystEngComm*, **2016**, *18*, 6700-6707.

[43] *ConQuest*; software for crystal structure database searches; Cambridge Crystallographic Data Centre: Cambridge, UK, 2020.

[44] *Mercury,* version 4.1.3; software for crystal structure database searches; Cambridge Crystallographic Data Centre: Cambridge, UK, 2020.

[45] Clark, S.J.; Segall, M.D.; Pickard, C.J.; Hasnip, P.J.; Probert, M.J.; Refson, K.; Payne, M. C. First Principles Methods Using CASTEP. *Z. Kristall*. **2005**, *220*, 567-570.

[46] Monkhorst, H. J.; Pack, J. D. Special Points for Brillouin-zone Integrations. *Phys. Rev. B.* **1976**, *13*, 5188-5192.

[47] Pfrommer, B. G.; Cote, M.; Louie, S. G.; Cohen, M. L. Relaxation Of Crystals With The Quasi-Newton Method. *J. Comput. Phys.* **1997**, *131*, 233-240.

[48] Holmes, S. T.; Schurko, R. W. Refining Crystal Structures With Quadrupolar NMR And Dispersion-Corrected Density Functional Theory. *J. Phys. Chem. C* **2018**, *122*, 1809-1820.

[49] Adiga, S.; Aebi, D.; Bryce, D. L. EFGShield - A Program For Parsing and Summarizing the Results of Electric Field Gradient and Nuclear Magnetic Shielding Tensor Calculations. *Can. J. Chem*. **2007**, *85*, 496-505.

[50] Sturniolo, S.; Green, T. F. G.; Hanson, R. M.; Zilka, M.; Refson, K.; Hodgkinson, P.; Brown, S. P.; Yates, J. R. Visualization and Processing of Computed Solid-State NMR Parameters: Magresview and Magrespython. *Solid State Nucl. Magn. Reson.* **2016**, *78*, 64-70.

[51] Morcombe, C. R.; Zilm, K. W. Chemical Shift Referencing in MAS Solid State NMR. *J. Magn. Reson*. **2003**, *162*, 479-486.

[52] van Rossum, B. J.; Förster, H; DeGroot, H. J. M. High-Field and High-Speed CP-MAS ^{13}C NMR Heteronuclear Dipolar-Correlation Spectroscopy of Solids with Frequency-Switched Lee-Goldburg Homonuclear Decoupling. *J. Magn. Reson.* **1997**, *120*, 516-519.

[53] van Rossum, B. J.; DeGroot, C. P.; Ladizhansky, V.; Vega, S.; DeGroot, H. J. M. A Method for Measuring Heteronuclear ($^{1}H-^{13}C$) Distances in High Speed MAS NMR. *J. Am. Chem. Soc.* **2000**, *112*, 3465-3472.

[54] Burum, D. P.; Bielecki, A. An Improved Experiment for Heteronuclear-Correlation 2D NMR in Solids. *J. Magn. Reson.* **1991**, *94*, 645-652.

[55] Lesage, A.; Emsley, L. Through-Bond Heteronuclear Single-Quantum Correlation Spectroscopy in Solid-State NMR, and Comparison to Other Through-Bond and Through-Space Experiments. *J. Magn. Reson.* **2001**, *148*, 449-454.

[56] van Meerten, S. G. J.; Franssen, W. M. J.; Kentgens, A. P. M. ssNake: A cross-Platform Open-Source NMR Data Processing and Fitting Application. *J. Magn. Reson.* **2019**, *301*, 56-66.

[57] Ashbrook, S. E.; Duer, M. J. Structural Information from Quadrupolar Nuclei In Solid State NMR. *Concepts Magn. Reson. Part A* **2005**, *28A*, 183-248.

[58] Freude, D.; Haase, J. Klinowski, J; Carpenter, T. A.; Roniker, G. NMR Line Shifts Caused by the Second-Order Quadrupolar Interaction. *Chem. Phys. Lett.* **1985**, *119*, 365-367.

[59] Engelhardt, G.; Koller, H. A Simple Procedure for the Determination of the Quadrupole Interaction Parameters and Isotropic Chemical Shifts from Magic Angle Spinning NMR Spectra of Half-Integer Spin Nuclei in Solids. *Magn. Reson. Chem.* **1991**, *29*, 941-945.

[60] Döbelin, N.; Kleeberg, R.; Profex: a Graphical User Interface For The Rietveld Refinement Program BGMN. *J. Appl. Cryst.* **2015,** *48*, 1573-1580.

[61] Pinon, A. C.; Rossini, A. J.; Widdifield, C. M.; Gajan, D.; Emsley, L. Polymorphs of Theophylline Characterized by DNP Enhanced Solid-State NMR. *Mol. Pharmaceutics* **2015**, *12*, 4146-4153.

[62] Enright, G. D.; Terskikh, V. V.; Brouwer, D. H.; Ripmeester, J. A. The Structure of Two Anhydrous Polymorphs of Caffeine from Single-Crystal Diffraction and Ultrahigh-Field Solid-State ^{13}C NMR Spectroscopy. *Cryst. Growth. Des.* **2007**, *7*, 1406-1410.

[63] Carignani, E.; Borsacchi, S.; Radley, J. P.; Brown, S. P.; Geppi, M. Strong Intermolecular Ring Current Influence on ^{1}H Chemical Shifts in Two Crystalline Forms of Naproxen: A Combined Solid-State NMR and DFT Study. *J. Phys. Chem. C* **2013**, *117*, 17731-17740.

[64] Herzfeld, J; Berger, A. E. Sideband Intensities in NMR Spectra Of Samples Spinning at the Magic Angle. *J. Chem. Phys.* **1980**, *73*, 6021-6030.

Chapter 3 Prospects for ^{207}Pb Solid-State NMR Studies of Lead Tetrel Bonds

In this chapter, the feasibility and value of ^{207}Pb solid-state NMR experiments on compounds featuring lead tetrel bonds are explored. Although the definition remains to be formalized, lead tetrel bonds may be qualitatively described as existing when there is evidence of a net attractive interaction between an electrophilic region associated with lead in a molecular entity and a nucleophilic region in another, or the same, molecular entity. Unambiguous identification of lead tetrel bonds can be challenging due to the hypervalent tendency of lead.

We report a series of ^{207}Pb solid-state NMR experiments on five metal-organic frameworks featuring lead coordinated to hydrazone-based ligands. Such frameworks may be held together in part by lead tetrel bonds. The acquisition of ^{207}Pb solid-state NMR spectra for such materials is feasible and is readily accomplished using a combination of magic-angle spinning and Carr-Purcell-Meiboom-Gill methods in moderate to low applied magnetic fields. The lead centres are characterized by ^{207}Pb isotropic chemical shifts ranging from -426 to -2591 ppm and chemical shift tensor spans ranging from 910 to 2681 ppm. Careful inspection of the compounds' structures and the literature ^{207}Pb NMR data may suggest that a tetrel bond to lead results in chemical shift parameters, which are intermediate to those characteristic of holodirected and hemidirected lead coordination geometries. Challenges associated with DFT computations of the ^{207}Pb NMR parameters are discussed. In summary, the ^{207}Pb data for the compounds studied herein show a marked response to the presence of non-coordinating

electron-rich moieties in close contact with the electrophilic surface of formally hemidirectionally coordinated lead compounds.

The work presented in this chapter was the subject of an oral presentation at the Faraday Discussion on Halogen Bonding in Supramolecular and Solid State Chemistry held in Ottawa on July 10-12th, 2017. The Faraday discussions are a series of conferences that began in 1907 by the Faraday Society, intending to promote the study of chemical physics, among other subjects.[1] Since then, a detailed account of each meeting, including the oral discussions held, has been published in various journals that have evolved to the modern publication *Faraday Discussions*. The journal provides a unique format for sharing scientific ideas, and this chapter is now included in its historical record. A record of the oral discussion held at the conference is included in **Appendix 3** for the reader's interest.

3.1 Introduction

Non-covalent interactions play critical roles in the structures, properties, and dynamics of broad classes of materials, biochemical systems, and simple chemical compounds and cocrystals. The most well-known of such interactions include, for example, hydrogen bonds, van der Waals' interactions, and π-stacking. In recent years, halogen bonds have also taken on increased prominence.[2,3] A halogen bond "occurs when there is evidence of a net attractive interaction between an electrophilic region associated with a halogen atom in a molecular entity and a nucleophilic region in another, or the same, molecular entity."[4] Cavallo et al. have proposed a generalization of this concept, whereby additional interactions are named per the electrophilic site's identity.[5] Thus, one may speak of pnictogen bonds, chalcogen bonds, tetrel bonds, and aerogen bonds, for example.[6-10] The precise definitions of some of these

non-covalent bonds are currently being assessed through a project of the International Union of Pure and Applied Chemistry (IUPAC) entitled "Categorizing Chalcogen, Pnictogen, And Tetrel Bonds, and Other Interactions Involving Groups 14-16 Elements".[11]

Solid-state NMR spectroscopy proves to be a valuable tool for characterizing various interactions mentioned above, rather in analogy to NMR's role in characterizing hydrogen bonds. In addition to a growing body of work on halogen bonds,[12-14] we have recently reported a computational study and initial experimental assessment of carbon tetrel bonding via NMR spectroscopy.[15] The tetrel elements include carbon, silicon, germanium, tin, and lead. Shown in **Table 3-1** are the NMR properties of the most abundant spin-active nuclides of this group. All of these except for germanium have spin-1/2 isotopes, which are quite amenable to study by NMR spectroscopy. The purpose of the current contribution is to discuss and explore the prospects of ^{207}Pb solid-state NMR spectroscopy for characterizing lead tetrel bonds.

^{207}Pb is a spin-1/2 nuclide with a natural abundance of 22.1% and an NMR receptivity relative to ^{13}C of 11.8. These characteristics suggest that ^{207}Pb NMR spectra should be relatively easy to obtain in reasonable amounts of time. Indeed, there is a substantial body of ^{207}Pb solid-state NMR literature.[16] Perhaps most interesting is its sizeable chemical shift range of about 17000 ppm. Such a large range suggests that ^{207}Pb NMR chemical shifts may be exquisitely sensitive to the lead atom's chemical environment and that perhaps weak tetrel bonding interactions may manifest themselves in relatively substantial chemical shift changes. Such changes could be much more significant than the modest shifts on the order of a few ppm that we have recently noted for carbon tetrel bonds using ^{13}C solid-state NMR spectroscopy.[15] In the solid-state, the full ^{207}Pb anisotropic chemical shift tensor is available through experiments carried out on magic-angle spinning (MAS) or stationary powdered

samples. The three principal components of this tensor (δ_{11}, δ_{22}, and δ_{33}) may offer further insight into the lead atom's molecular and electronic environment.

Table 3-1. NMR properties of the first five tetrel (group 14) elements.[17]

NMR-active isotope	*I*	natural abundance / %	magnetogyric ratio / 10^7 rad T^{-1} s^{-1}	relative receptivity[a]	chemical shift range / ppm
^{13}C	½	1.07	6.728284	1.00	250
^{29}Si	½	4.6832	-5.3190	2.16	900
^{73}Ge	9/2	7.73	-0.9360303	0.642	1200
^{115}Sn	½	0.34	-8.8013	0.711	2600
^{117}Sn	½	7.68	-9.58879	20.8	2600
^{119}Sn	½	8.59	-10.0317	26.6	2600
^{207}Pb	½	22.1	5.58046	11.8	17000

[a] The relative receptivity is an intrinsic measure of the intensity of an NMR signal obtained for a given nuclear spin at natural abundance relative to another to which it is being compared at a constant magnetic field. The relative receptivity has a $\gamma^3 I(I+1)$ dependence arising from the spin angular momentum.

Frontera and co-workers coined the term 'tetrel bonding'[18] in 2013 and provided an account of the field in 2016.[19] Their discussion was largely within the framework of σ-hole interactions, and they rightly noted that heavy elements like Pb are perhaps more prone to form hypervalent structures than to engage in σ-hole interactions. In this context, it is useful to recall that, as mentioned above, the IUPAC definition of the tetrel bond is only now being discussed.[11] For example, one may wonder whether the concept of the σ-hole must be used in defining the tetrel bond, or whether the more general concept advanced as part of the definition of the halogen bond (that the bonding occurs between 'an electrophilic region' of an atom) is apposite. In the case of lead, the situation may become particularly murky given this element's ability to have a coordination number of up to fifteen potentially[20] and readily engage in covalent and ionic bonding. In the absence of a highly localized σ-hole, how does one clearly differentiate between the lead tetrel bond and a weak covalent or ionic interaction?

Is this differentiation needed? This contribution does not aim to answer these questions, but it is important to be aware of these issues when attempting to ascribe a spectral shift to a particular interaction. In this light, the discussion of our results will thus proceed cautiously.

As a starting point, we have selected metal-organic frameworks featuring Pb(II) ions, which have been described previously in the literature as featuring lead tetrel bonds.[21] Nicotinoyl hydrazone species are ideal candidates for coordinating Pb(II) to become hemidirectional, with an open face available for non-covalent bonding. There have been several recent studies suggesting that supramolecular frameworks built from these classes of ligands are, in fact, a result of lead tetrel bonding interactions.[21-25] We have chosen these and related novel systems to assess the prospects for ^{207}Pb solid-state NMR studies of lead tetrel bonds.

3.2 Experimental

3.2.1 Synthetic details

*3.2.1.1 Synthesis of 2-pyridinecarbaldehyde isonicotinoyl hydrazone (**L1**) and 2-acetylpyridine isonicotinoyl hydrazone (**L3**)*

The ligand 2-pyridinecarbaldehyde isonicotinoyl hydrazone (**L1**; **Figure 3-1**) was prepared by condensation reaction following a known synthetic procedure.[26] A round bottom flask was charged with isoniazid (7.72 g, 52.7 mmol) along with 2-pyridine carboxaldehyde (2.5 mL, 52.7 mmol) and dissolved in 150 mL ethanol to which were added roughly 20 drops of acetic acid. The apparatus was equipped with a condenser and a stir bar, and the reaction was refluxed under a steady stream of N_2 gas for 12 h. The solution was allowed to cool to

room temperature, after which time a white precipitate formed. The solid was collected and washed with 200 mL of ethanol to give the product in quantitative yield.

The same general procedure was followed to synthesize 2-acetylpyridine isonicotinoyl hydrazone (**L3**;**Figure 3-1**), following a known recipe.[26,27] However, 1-(2-pyridinyl)-ethanone was used as a reagent in place of 2-pyridine carboxaldehyde to form the product.

*3.2.1.2 Preparation of Pb(**L1**)$(NO_3)_2$ (**1**) and Pb(**L1**)Cl_2 (**2**)*

A 5 mL solution of 2-pyridinecarbaldehyde isonicotinoyl hydrazone (0.0227 g, 0.1 mmol) was filtered and slowly added to a 10 mL filtered solution of $Pb(NO_3)_2$ (0.0331 g, 0.1 mmol) in methanol. The solvent was allowed to evaporate slowly over a few days, after which time off-white microcrystals of Pb(**L1**)$(NO_3)_2$ (**1**) were collected and air-dried. Pb(**L1**)Cl_2 (**2**) was prepared as per the same procedure by replacing lead nitrate with $PbCl_2$ (0.0278g, 0.1 mmol).

*3.2.1.3 Preparation of Pb(**L3**)$(SCN)_2$ (polymorph A) (**3**), Pb(**L3**)$(SCN)_2$ (polymorph B) (**4**), and Pb(**L3**)$(SCN)_2 \cdot CH_3OH$ (**5**)*

$Pb(SCN)_2$ (0.323g, 1 mmol) and **L3** (0.227 g, 1 mmol) were mixed in 100 mL of methanol (**5**), ethanol (**4**), or acetonitrile (**3**) and stirred at 60°C for 2 h. Each solution was cooled to room temperature, filtered, and the solvent allowed to evaporate over several days. Yellow crystals of all three samples were collected and air-dried. **5** is a methanol solvate and is a different polymorph than that reported previously.[21]

3.2.2 X-ray Crystallography

3.2.2.1 Single crystal X-ray diffraction

Single crystals of **1**, **2**, and **5** were each individually mounted on thin glass fibres using paraffin oil. Prior to data collection, the crystals were cooled to 200(2) K. The data were collected on a Bruker AXS single-crystal diffractometer equipped with a sealed Mo tube (wavelength 0.71073 Å) and APEX II CCD detector. The raw data collection and reduction were made with the Bruker APEXII software package.[28] Semi-empirical absorption corrections based on equivalent reflections were applied.[29] Systematic absences in the diffraction dataset and unit cell parameters were consistent with monoclinic $P2_1/c$ (#14) for **5** and **1** (the latter was solved in the alternative setting $P2_1/n$), and orthorhombic *Pbca* (#61) for **2**. The structures were solved by direct methods and refined with full-matrix least-squares procedures based on F^2, using SHELXL[30] and WinGX.[31] All non-H atoms were refined anisotropically. No constraints or restraints were applied to the displacement parameters, bond lengths, or non-H atoms' angles. The hydrogen atoms bonded to the nitrogen (H(9) in **1,** H(9) in **2**) and oxygen atoms (H(23) in **5**) were located in a difference Fourier map and refined freely while the remaining hydrogen atoms were placed in idealized positions. Uncertainties were estimated using PLATON.[32]

3.2.2.2 Powder X-ray diffraction

Sample phase purity was assessed by X-ray powder diffraction (see **Appendix 2**) using a Rigaku Ultima IV Diffractometer operating at room temperature (298 ± 1 K) with a copper source and a diffracted beam monochromator and with 2θ ranging from 5º to 60º in increments

of 0.02º at a rate of 1º per minute. Simulations were generated using Mercury 3.6 software from the Crystallographic Data Center.

3.2.3 Solid-State NMR Spectroscopy

^{207}Pb solid-state NMR experiments were conducted on a Bruker AVANCE III spectrometer in a magnetic field strength of 4.7 T (ν_L (^{207}Pb) = 41.747 MHz) using a Bruker 7 mm triple resonance probe. Spectra were referenced to solid spinning $Pb(NO_3)_2$ powder at -3490 ppm with respect to the primary reference, tetramethyl lead (0 ppm). Experiments were carried out at room temperature. The magic angle of 54.74º was verified by maximizing the number of spinning sidebands in the ^{79}Br NMR spectrum of powdered KBr. Conventional Bloch decay MAS NMR spectra were collected at 4000, 4500, or 5000 Hz spinning frequencies. These experiments were conducted using 5.5 μs radiofrequency pulses and continuous wave proton decoupling. Due to probe ringing problems, spectral distortions were corrected for using a pre-scan delay of at least 30 μs and linear backwards prediction throughout the processing. MAS sidebands were analysed by the *Herzfeld-Berger* methodology[33] using HBA ver. 1.7.5[34] to provide a starting point for more precise fitting of static line shapes. Due to the wide chemical shift range associated with ^{207}Pb, static Carr-Purcell-Meiboom-Gill (CPMG) NMR spectra were acquired using variable transmitter offsets. The complete powder patterns were produced by either the co-addition of CPMG sub-spectra or by overlaying CPMG sub-spectra using the sky-line method. All spectra were simulated using WSolids1 ver. 1.21.3.[35]

3.2.4 Computational details

Calculation of molecular electrostatic potential (MESP) isosurfaces was done with the Amsterdam Density Functional package (ADF)[36] ver. 2016 running at the Centre for Advanced Computing (http://cac.queensu.ca/). Cluster models were built using the atomic coordinates available from the single-crystal X-ray structures to contain one lead centre coordinated by the ligand and two counterions above and below the ligand's plane. The calculations were initiated using the BP86 functional and an all-electron doubly polarized triple-ζ basis set for all atoms except Pb, on which a quadruply polarized quadruple-ζ basis set was employed. ESPs were generated at the 0.001 au surface density for all compounds.

Cluster model calculations of the lead magnetic shielding tensors were conducted on dimers of the compounds using ADF. All coordinates were obtained from the corresponding crystal structures. In all cases, the fifth or higher coordination shell around the Pb(II) centre of interest was included, as long-range effects are known to play essential roles in the calculation of lead NMR parameters.[37,38] As much as possible, whole ligand molecules were used, and in some cases, when the crystal structure was missing hydrogen atoms on the hydrazine group, one was added to ensure charge balance for converging the self-consistent field. The BP86 or the B3LYP exchange-correlation functionals were used as indicated, and doubly polarized triple-ζ all-electron basis sets were used on all atoms. DFT calculations, including MESPs, were run using the relativistic zeroth-order regular approximation (ZORA)[39] and Grimme's dispersion correction[40] as indicated. The calculated NMR parameters were extracted from the ADF output files using EFGShield ver. 4.2.[41]

3.3 Results and Discussion

3.3.1 Structures

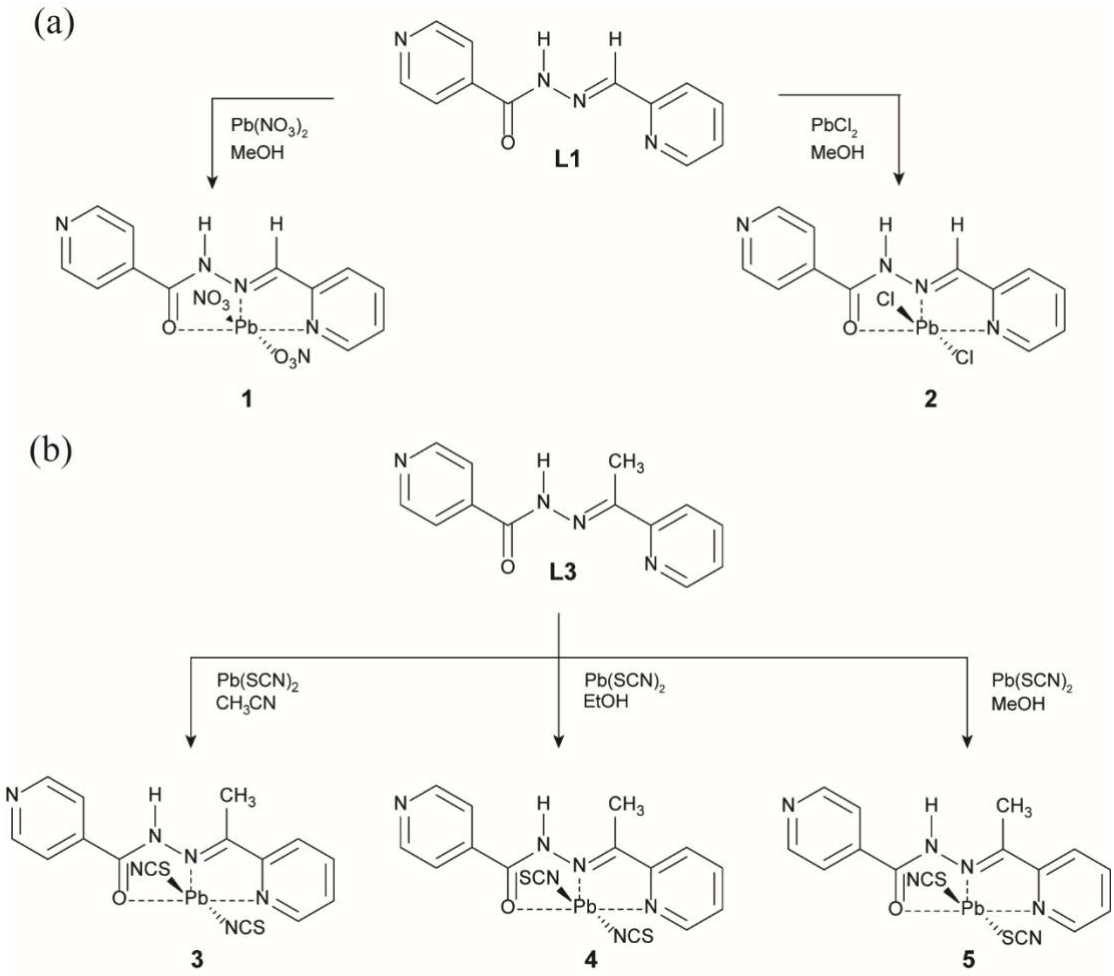

Figure 3-1. Synthetic routes and compound numbering. (a) Lead frameworks formed with ligand **L1**. (b) Lead frameworks formed with ligand **L3**. Purported tetrel bond acceptors, as seen in the X-ray crystal structures of compounds **1** to **5**, are not shown here. **3** and **4** are polymorphs, and **5** is a methanol solvate.

Samples of each compound were prepared as described above and as depicted in **Figure 3-1**. The single-crystal X-ray structures were solved, and relevant crystallographic data are summarized in **Table 3-2**. The local lead environments are depicted in **Figure 3-2**

and crystal packing diagrams are shown in **Figure 3-3**. Powder X-ray diffraction was used to confirm the identity of the powdered samples being analyzed (**Figure S2-1** to **Figure S2-5**), and to ensure that the compounds maintained their structures after grinding them into fine powders for solid-state NMR experiments. Good agreement is observed in each of the cases. Exceptionally, **1** and **3** show additional peaks, indicating perhaps the starting material or a second polymorph of the compound of interest. The origins of these additional peaks are elucidated using the corresponding ^{207}Pb solid-state NMR spectra (*vide infra*).

In all five compounds, a consistent pattern of five bonds to lead is preserved. Pb(II) is coordinated by the hydrazone group's nitrogen, the keto-oxygen, and a nitrogen atom from the adjacent pyridine ring of the same ligand (**Figure 3-2**). These atoms form three in-plane bonds to lead. In each compound, there are also two further bonds, roughly orthogonal to the plane of the three bonds to the ligand: to two nitrate oxygens in **1**, to two chloride anions in **2**, and the nitrogen or sulphur atoms of thiocyanate ions in **3**, **4**, and **5**. By this geometry, the Pb(II) atom is hemidirectionally coordinated, leaving an area of the Pb(II) surface directly opposite the in-plane bonds to the hydrazone group available for interactions with other moieties.

Table 3-3 presents some geometrical features associated with the nearest atoms that may be engaged in tetrel bonding with the lead centre (see also dotted lines in **Figure 3-2**). The contacts noted in the table are those for which the distance between the two atoms is smaller than the sum of their van der Waals (vdW) radii (Pb-N: 3.57 Å; Pb-Cl: 3.77 Å; Pb-O: 3.54 Å; Pb-S: 3.82 Å).[42] The reduced distance parameter, $R_{Pb\text{-}X}$, may be used for comparing the non-covalent interaction distances between species with different vdW radii (where X is the tetrel bond acceptor) (see Eq. 2-3).

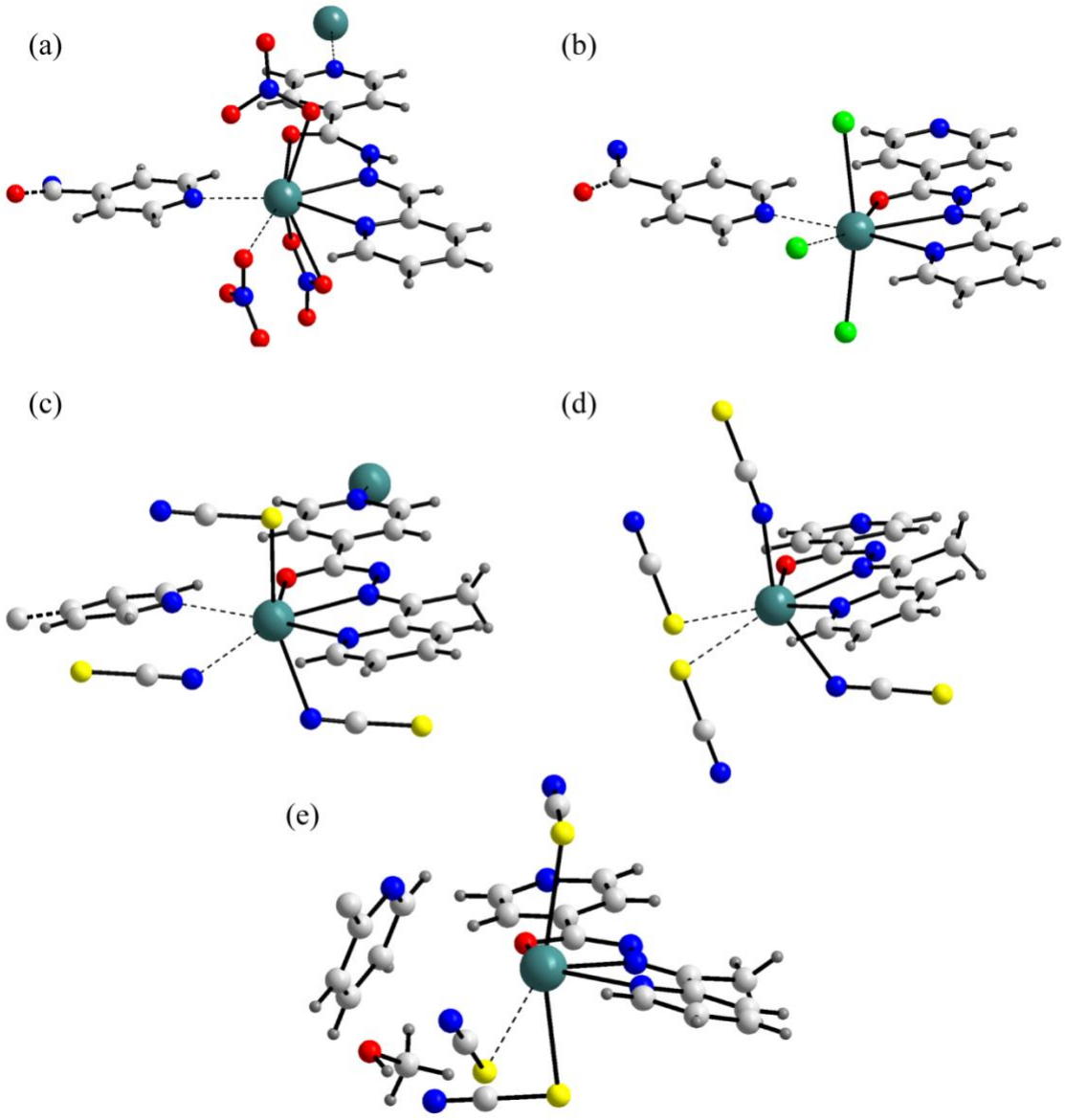

Figure 3-2. Diagrams of the compounds studied in this work, in coordination with their ligands and showing the closest molecules to the open face of the hemidirected Pb(II) centres. (a) **1** (b) **2** (c) **3** (d) **4** (e) **5**. Only pyridyl fragments of some of the ligands on adjacent lead centres are shown in (a), (b), (c), and (e). Atoms are coloured according to the following scheme: carbon (white); hydrogen (grey); oxygen (red); sulphur (yellow); nitrogen (blue); lead (teal).

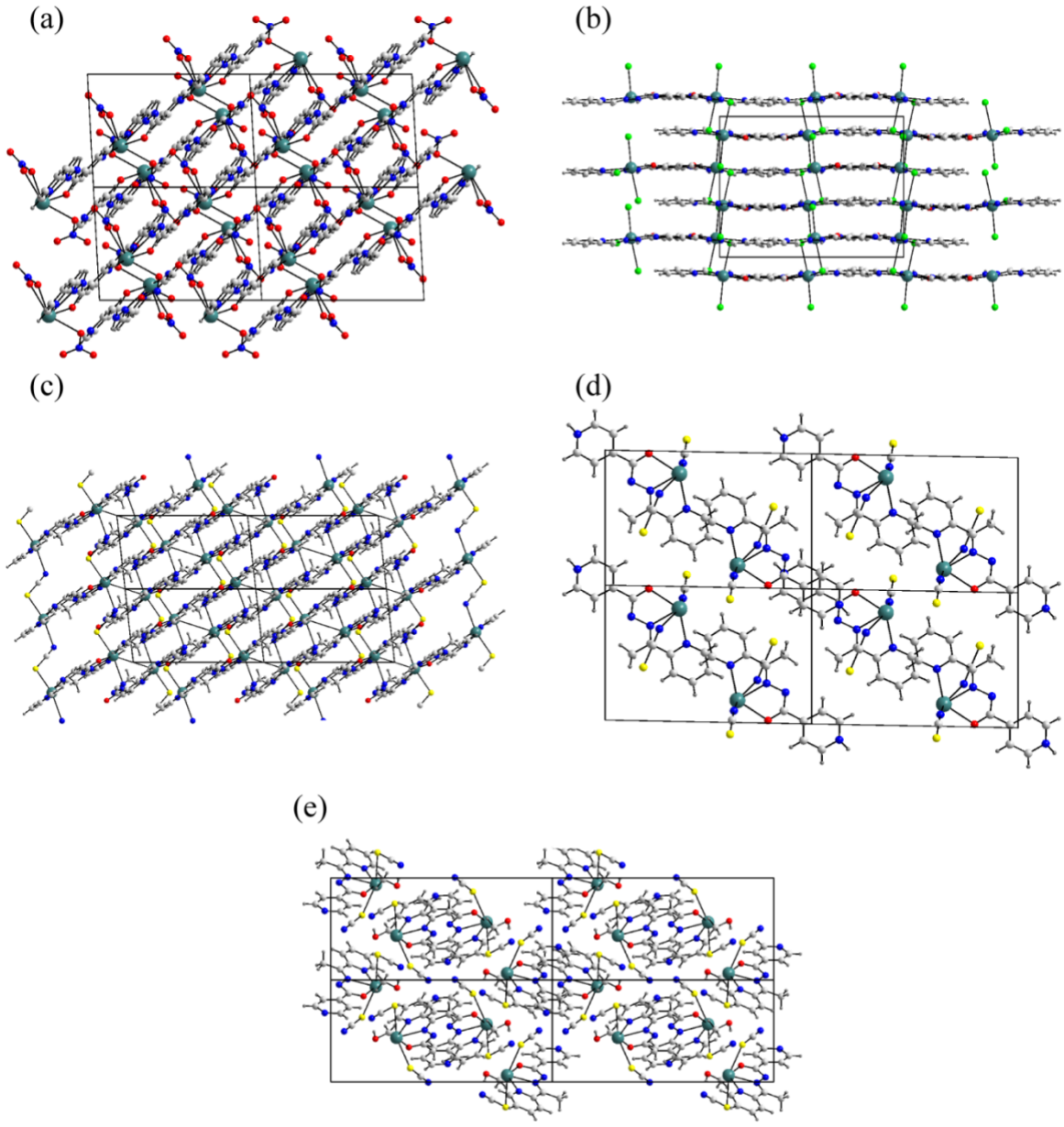

Figure 3-3. Crystal packing diagrams of (a) **1** (b) **2** (c) **3** (d) **4** (e) **5**.

The $R_{Pb\text{-}X}$ values listed in **Table 3-3** are less than unity in all cases, providing an additional indication that they are all candidates for a tetrel bonding interaction. As mentioned in the introduction, the definition of a tetrel bond involving lead, in particular, may not be so clear-cut for a variety of reasons. In addition to questions about how to differentiate between various possible classes of weak interactions, the van der Waals' radius of lead (2.02 Å) may also not be particularly reliable.[42] Nevertheless, it appears that tetrel bonds are formed along the extensions of one (in **5**) or two (in **1**, **2**, **3,** and **4**) of the five preserved bonds described above (see **Table 3-3**). For example, in all five metal-organic frameworks, an anion is positioned opposite the carbonyl oxygen. The C=O···Pb···X angles (where X is the interacting electron donor) range from 133.89° for the C=O···Pb···SCN^- interaction in **5** to 162.94° for the C=O···Pb···ONO_2^- angle in **1**. In addition, in **1**, **2**, and **3**, a pyridyl nitrogen atom (from the next lead centre) is positioned opposite the pyridyl nitrogen atom of the directly-bonded ligand, with N···Pb···N angles of roughly 160° in each case. Compound **4** features the sulphur of a thiocyanate anion opposite the pyridyl nitrogen atom of the directly-bonded ligand with an N···Pb···SCN angle of 148.33°.

Table 3-2. Selected crystallographic data for the lead compounds studied herein.

	1	2	3[a]	4[a]	5
formula	$C_{12}H_{10}N_6O_7Pb$	$C_{12}H_{10}Cl_2N_4OPb$	$C_{13}H_{12}N_7S_2OPb$	$C_{13}H_{12}N_7S_2OPb$	$C_{13}H_{12}N_7S_2OPb$
crystal system	monoclinic	orthorhombic	monoclinic	triclinic	monoclinic
space group	$P2_1/n$	*Pbca*	$P2_1/n$	*P*1	$P2_1/c$
a, Å	7.9846(2)	14.0154(6)	7.0449(7)	7.2730(7)	12.964(4)
b, Å	17.4996(4)	12.5288(5)	17.2171(19)	8.9632(9)	8.401(3)
c, Å	11.4514(3)	16.4104(6)	12.4641(14)	13.6742(13)	18.917(6)
α, deg	90	90	90	88.354(2	90
β, deg	93.0640(10)	90	96.364(3)	84.972(2)	105.216(3)
γ, deg	90	90	90	83.215(2)	90
cell volume, $Å^3$	1597.79	2881.6	1502.49	881.611	1987.9(11)
Z	4	8	0	0	4

a. Compounds **3** and **4** are reported in reference 21.

Table 3-3. Geometries of possible tetrel bonds to lead in each compound. They are indicated by dashed lines in **Figure 3-2**.

Compound	Pb-X distances		Reduced Distance Parameter		Y···Pb···X angles	
1	Pb-N (pyr)	2.774	Pb-N (pyr)	0.78	N···Pb···N	162.76°
	Pb-O (NO_3)	3.010	Pb-O (NO_3)	0.85	CO···Pb···O	162.94°
2	Pb-N (pyr)	2.715	Pb-N (pyr)	0.76	N···Pb···N	166.65°
	Pb-Cl	2.834	Pb-Cl	0.75	CO···Pb···Cl	158.99°
3	Pb-N (pyr)	2.813	Pb-N (pyr)	0.79	N···Pb···N	159.58°
	Pb-N (SCN)	3.540	Pb-N (SCN)	0.99	CO···Pb···N	152.97°
4	Pb-S (SCN)	3.403	Pb-S (SCN)	0.89	CO···Pb···S	135.99°
	Pb-S (SCN)	3.472	Pb-S (SCN)	0.91	N···Pb···S	148.33°
5	Pb-S (SCN)	3.362	Pb-S (SCN)	0.88	CO···Pb···S	133.89°

A non-covalent interaction may involve σ-hole bonding, whereby an area of relatively depleted electrostatic charge forms opposite of a covalent bond between the donor atom and the acceptor atom. A suitable probe for the presence of the σ-hole is the calculated electrostatic surface potential. Previously, our group showed that σ-holes could form on carbon atoms[15] while others have shown these areas to exist on Pb(II) centres.[21-24] **Figure 3-4** shows similarly that an area of positive potential appears on the open face of the Pb atom hemidirectionally coordinated to the ligands. In each case, this area corresponds to a surface potential of *ca*. 0.04 to 0.08 au, comparable to hydrogen atoms situated on the ligands. The magnitude of this surface potential seems to depend, in part, on species' identity and geometries above and below the ligand plane, also in coordination with the Pb(II) centre.

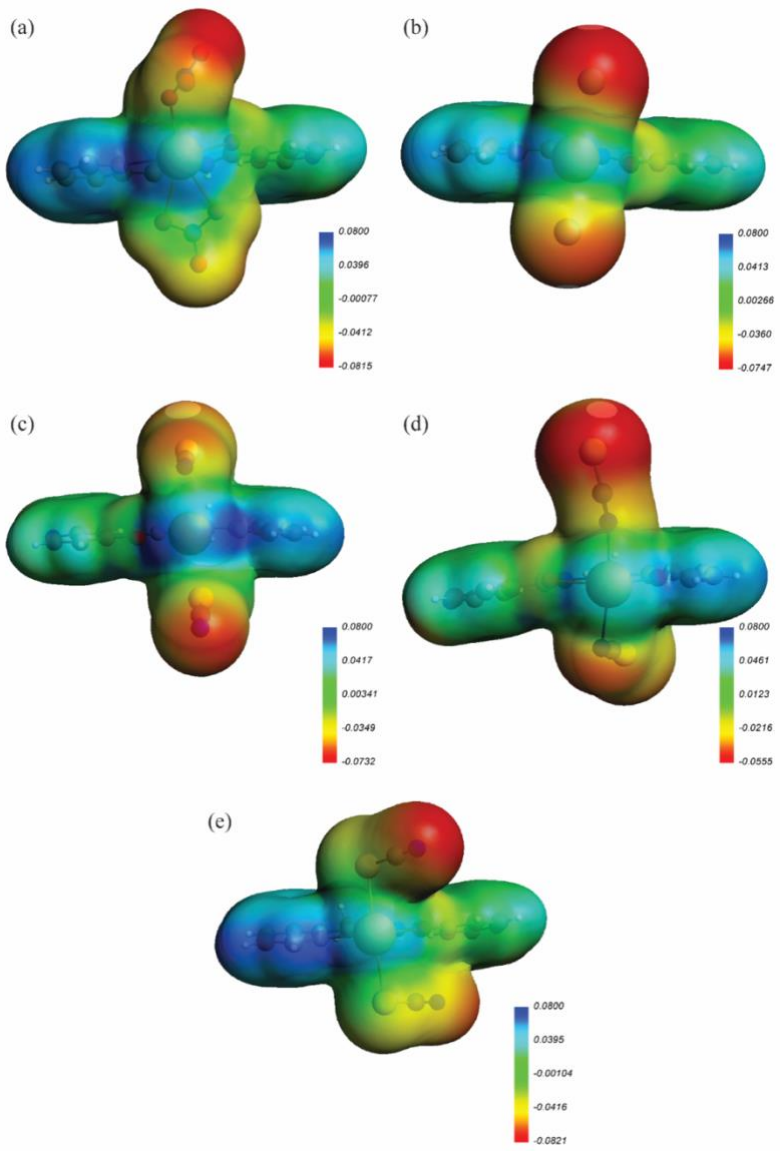

Figure 3-4. Electrostatic potential at the 0.001 au surface of (a) **1** (b) **2** (c) **3** (d) **4** (e) **5**. Each surface has been computed by VWN-BP86 with a doubly-polarized triple-zeta basis set on all atoms, including spin-orbit relativistic effects. The maximum and minimum electrostatic potential values are listed in **Table S2-1**, and all scales have been modified so that the deepest blue represents 0.0800 a.u. to emphasize the colours around the Pb atom.

Interestingly, two areas of relatively high electrostatic potential are clearly visible on the open surface of **3** and, to a lesser extent, **1** (**Figure 3-4**). While not immediately visible in the rest of the figures, similar areas of slightly elevated electrostatic potential as each of the

compounds feature ligands with the same basic framework. These regions' presence could suggest that a tetrel bonding interaction does play a role in constructing the supramolecular structures of these species without the formation of a well-defined σ-hole. Murray et al. provide a timely discussion of such diffuse areas of positive electrostatic potential, consistent with what is shown in **Figure 3-4**.[43]

3.3.2 Solid-State ^{207}Pb NMR Spectroscopy

Solid-state NMR has been a useful tool for probing non-covalent interaction involving halogen bonds[44-50]and, recently, tetrel bonds.[15] The chemical shift is an NMR parameter that is highly sensitive to changes in a particular nucleus's electronic environment and is therefore expected to change as it participates in a non-covalent interaction with another species. ^{207}Pb line widths in the solid-state are usually very broad (often several thousand ppm), leading to some challenges in acquiring undistorted spectra. However, some success has been observed in the literature for obtaining solid-state NMR spectra of Pb(II) coordination polymers.[51,52] In particular, it has been shown that the CPMG methodology of obtaining wide line shapes corresponding to ^{207}Pb(II) provides the most accurate information.[16,53-55]

For this work, conventional Bloch decay magic-angle spinning spectra were generally recorded at two spinning frequencies to obtain the isotropic chemical shift of the ^{207}Pb(II) centre and obtain the principal components of the chemical shift tensor using a *Herzfeld-Berger* analysis[33] of the spinning sideband intensities. Static CPMG spectra were also obtained, and these data were also fit to improve the accuracy and precision of the reported lead chemical shift tensors. All the experimental data are reported in **Table 3-4**.

A moderately low magnetic field of 4.7 T was used in these studies; this proved highly useful. Since chemical shift anisotropy is the dominant source of spectral broadening for

^{207}Pb, and since this broadening increases in Hz with the strength of the applied magnetic field, narrower lines are obtained in lower magnetic fields. A field of 4.7 T (^{1}H resonance frequency of 200 MHz) offers an excellent compromise between sensitivity and line width.

Table 3-4. Experimentally measured ^{207}Pb chemical shift tensors parameters for each of the compounds.[a,b]

compound	δ_{iso} / ppm	Ω / ppm	κ	δ_{11} /ppm	δ_{22} /ppm	δ_{33} /ppm
1[c]	-2591	910	0.21	-2168	-2527	-3078
2	-1732	1071	0.18	-1228	-1670	-2299
3[d]	-426	2681	0.48	700	3	-1981
4	-1036	2259	0.53	-106	-638	-2365
5	-556	2192	0.72	277	-30	-1915

a. The data are presented using the *Herzfeld-Berger* convention, where $\delta_{iso} = \frac{\delta_{11}+\delta_{22}+\delta_{33}}{3}$ and $\delta_{11} \geq \delta_{22} \geq \delta_{33}$. The span is calculated by $\Omega = \delta_{11} - \delta_{33}$ and the skew is given by $\kappa = \frac{3(\delta_{22}-\delta_{iso})}{\Omega}$.

b. Errors in δ_{iso} are estimated at ±1 ppm, and errors in each of the principal components are estimated at ±10 ppm.

c. Impurity (or different polymorph) characterized by the following principal components: -2563, -2790, -3492 ppm.

d. Line shape fitting also included a contribution from $Pb(SCN)_2$ with principal components -832, -1845, -2100 ppm.

The first series of compounds was made by coordinating the **L1** ligand with $PbCl_2$ or $Pb(NO_3)_2$. The ^{207}Pb NMR spectra for **1** are shown in **Figure 3-5**. While not visible at a spinning speed of 5 kHz, an impurity becomes apparent at 4 kHz. The isotropic chemical shifts of each of these compounds are separated by a frequency of 15 kHz (at 4.7 T), meaning that at a MAS spinning frequency of 5 kHz, the sidebands overlap perfectly. The impurity has a ^{207}Pb chemical shift of -2948 ppm, a span (Ω) of 929 ppm, and a skew (κ) of 0.51 (see footnote to **Table 3-4** for parameter definitions). The signal is due to an unknown polymorph of **1** and not residual $Pb(NO_3)_2$; shown in **Figure 3-5a** is the spectrum for pure $Pb(NO_3)_2$ (δ_{iso} = -3471 ppm[56]). Using the results of DFT calculations described in a later section, it is possible to attribute the known polymorph of **1** to the NMR powder pattern described by a ^{207}Pb chemical shift of -2591 ppm, with Ω = 910 ppm and κ = 0.21. The powder X-ray diffractogram supports

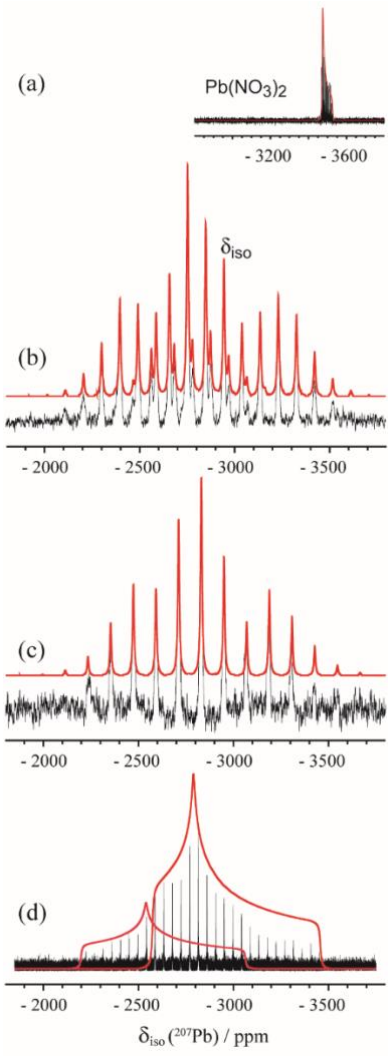

Figure 3-5. (a) ^{207}Pb CPMG NMR spectrum of $Pb(NO_3)_2$. (b), (c) ^{207}Pb MAS and (d) stationary CPMG spectra of **1**. Two MAS spectra are shown to demonstrate a second powder pattern that is clearly resolved at slower spinning frequencies. The MAS spinning speeds are (b) 4500 Hz and (c) 5000 Hz. In all cases, the experimental spectrum is shown in black. Simulated spectra are shown in red. The co-addition of individual sub spectra formed the CPMG spectrum with the transmitter frequency separated by 6 kHz offsets.

this assignment for this sample (**Figure S2-1**). In summary, the ^{207}Pb NMR spectra of **1**, in addition to being much broader than those for $Pb(NO_3)_2$, are characterized by a larger (less negative) isotropic chemical shift.

2 is the second compound prepared using the **L1** ligand. It features a crystallographically unique Pb(II) centre in complex with the ligand and two distinct chlorine atoms; one in the plane of the ligand and one perpendicular (**Figure 3-2**). The distance between the in-plane Cl atom and the Pb(II) centre is 2.834 Å, and the distance from the pyridyl nitrogen from an opposing ligand molecule is 2.715 Å, resulting in $R_{Pb\text{-}X}$ parameters of 0.76 and 0.75, respectively. The ^{207}Pb NMR spectra of **2** (**Figure 3-6**) show an axially asymmetric chemical shift tensor characterized by a skew of 0.18. The line shape is broad, spanning 1071 ppm, and the isotropic lead chemical shift is -1732 ppm. In comparison, the spectrum corresponding to the precursor, $PbCl_2$ (**Figure 3-6a**), has a chemical shift of -1716 ppm, spans 543 ppm, and has a skew of $\kappa = 0.5$. Like **1**, this material experiences an increase in its chemical shift and its span relative to the starting material.

The second family of compounds was formed from the complex of $Pb(SCN)_2$ with **L3** in three different solvents, forming two polymorphs and a methanol solvate. Each species' unit cell varies significantly (**Table 3-2**); however, each contains a single unique Pb(II) centre in coordination with the ligand. While **3** and **4** have been reported in the literature, to the best of our knowledge, **5** is a newly reported solvate. In **3**, made in acetonitrile, the Pb(II) centre is coordinated by **L3** and is close in proximity to two SCN^- molecules above and below the ligand's plane. Opposite the open face of the Pb(II) centre are the pyridyl nitrogen (2.813 Å) and the nitrogen of a third SCN^- anion coordinated with the next Pb(II) centre (3.540 Å). The $R_{Pb\text{-}X}$ parameters are 0.79 and 0.99. Qualitatively, it is unlikely that the SCN^- nitrogen is close enough to the Pb(II) centre to play any real role in tetrel bonding.

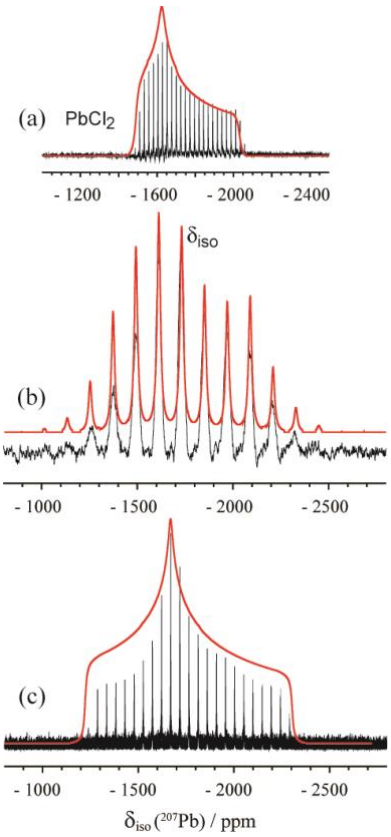

Figure 3-6. (a) ^{207}Pb CPMG NMR spectrum of $PbCl_2$. (b) ^{207}Pb MAS and (c) stationary CPMG spectra of **2**. The CPMG spectrum was formed by the overlay (sky-line) of individual subspectra with the transmitter frequency separated by 10 kHz offsets. In all cases, the experimental spectrum is shown in black. Simulated spectra are shown in red.

Figure 3-7 shows the ^{207}Pb MAS and CPMG NMR spectra for **3**. From the MAS NMR spectrum, two crystallographically distinct lead sites exist in this sample. One of the sites corresponds to a residual amount of starting material, which is evident when compared to the spectrum of pure $Pb(SCN)_2$ (**Figure 3-7a**). This was confirmed by simulating the spinning sidebands of the impurity in the MAS spectrum. The chemical shift parameters correspond precisely to $Pb(SCN)_2$, with δ_{iso} = -1592 ppm, Ω = 1268, and κ = -0.60. The starting material exists in the sample in a quantity of roughly 10%. This can also be observed

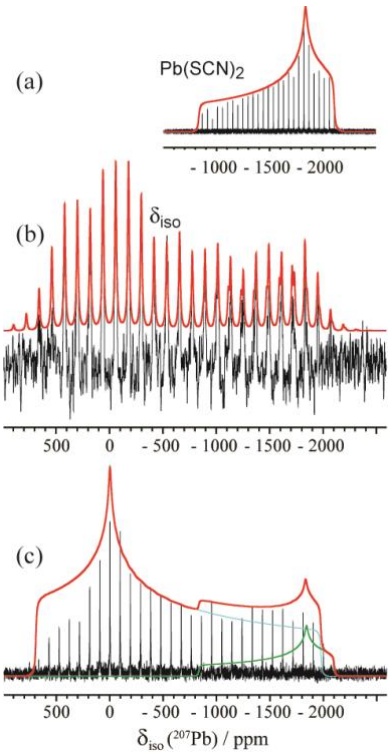

Figure 3-7. (a) ^{207}Pb static CPMG spectrum of $Pb(SCN)_2$. (b) ^{207}Pb MAS and (c) stationary CPMG spectra of **3.** The MAS spinning frequency is 5000 Hz. The CPMG spectrum of **3** is constructed by the coaddition of individual sub-spectra with transmitter offsets of 28 kHz. The spikelet separation was set to 4000 Hz.

in the corresponding powder X-ray diffraction pattern in the form of a few additional reflections (**Figure S2-3**). However, the site of interest for **3** has a chemical shift of -426 ppm, a span, Ω, of 2681 ppm, and a skew, κ, of 0.48, characteristic of a relatively asymmetric and anisotropic ^{207}Pb chemical shift tensor. **4**, made in ethanol (**Figure 3-8**), shows similar ^{207}Pb chemical shift tensors parameters, though the excitation appears deficient due to a lower sample volume available: Ω = 2259 ppm and κ = 0.53.

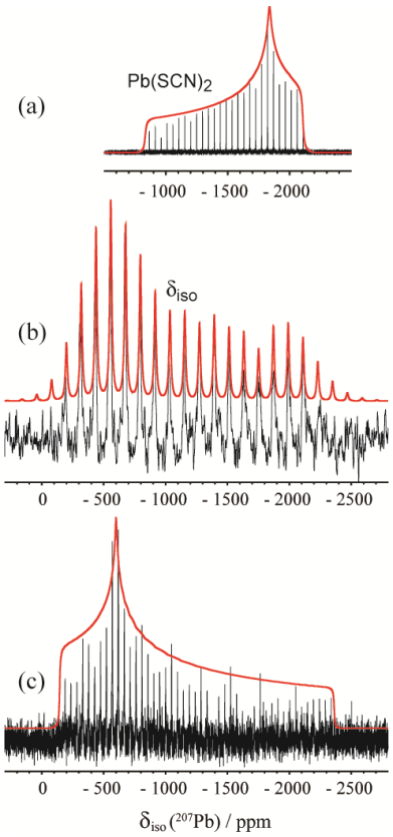

Figure 3-8. (a) ^{207}Pb static CPMG spectrum of $Pb(SCN)_2$. (b) ^{207}Pb MAS and (c) stationary CPMG spectra of **4.** The MAS spinning frequency is 5000 Hz. The CPMG spectrum of **4** is constructed by the coaddition of several sub-spectra acquired with transmitter offsets of 10 kHz. The spikelet separation was set to 2000 Hz.

The key difference between **3** and **4** is that δ_{iso} = -1036 ppm for the latter, which is almost 500 ppm more shielded than **3**. The polymorph **4** is similar to **3** except that the Pb(II) centre is near two sulphur atoms from SCN^- anions in coordination with the next nearest Pb(II) centres (3.403 Å, 3.472 Å; $R_{Pb\text{-}X}$ = 0.88, 0.91). The last compound, the methanol solvate **5**, features a Pb(II) centre, which is only near one sulphur atom (3.362 Å; $R_{Pb\text{-}X}$ = 0.88) from an opposing SCN^- anion. The ^{207}Pb NMR spectra of **5** (**Figure 3-9**) are characterized by chemical shift tensor parameters similar to those for **3** (δ_{iso} = -556 ppm and Ω = 2192 ppm).

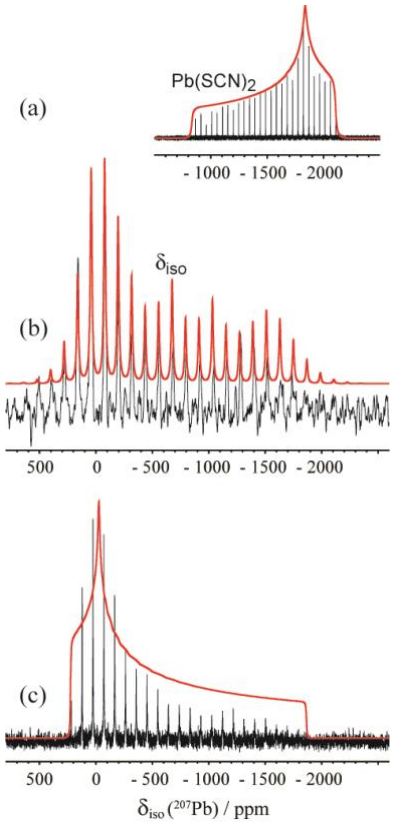

Figure 3-9. (a) ^{207}Pb static CPMG spectrum of $Pb(SCN)_2$. (b) ^{207}Pb MAS and (c) stationary CPMG spectra of **5.** The MAS spinning frequency is 5000 Hz. The CPMG spectrum of **5** is constructed by the coaddition of individual sub-spectra with transmitter offsets of 10 kHz. The spikelet separation was set to 2000 Hz.

We can generate a full picture of the local environments surrounding the lead (II) centres using the ^{207}Pb NMR parameters. Based on the measurements of the ^{207}Pb chemical shift tensor spans, two groups can be established. The lead centres in compounds **1** and **2** each have spans of roughly 1000 ppm. The lead centres in the other three compounds each have spans of over 2000 ppm. These values are characteristic of holodirected and hemidirected geometries around Pb(II) centres, respectively.[57] The skews for **1** and **3** are each below 0.5, with **4** falling slightly higher. These values are within the range recently observed for

holodirected Pb species (<0.55).[37,57] On the other hand, **5** experiences a skew of 0.72, which falls close to the range observed previously for hemidirected Pb(II) centres (>0.6). Therefore, the ^{207}Pb chemical shift tensor spans and skews are consistent with holodirected geometries for **1** and **2**, and hemidirected for **5**. Interestingly, compounds **3** and **4** have spans consistent with hemidirected geometries even though their skews imply holodirected Pb species. Finally, the measured isotropic chemical shifts of **1** and **2** are < -1500 ppm, which are consistent with a more holodirected geometry, while the remaining compounds have chemical shifts > -1100 ppm, suggestive of hemidirected coordination.[57]

Taken together, these data suggest that the lead centres in **1** and **2** are indeed engaged in non-covalent interactions opposite the **L1** ligand (causing the NMR parameters to report a more holodirected geometry). In contrast, the lead centres in **3** and **5** are perhaps engaged in weaker non-covalent interactions opposite **L3** (as reflected in the NMR parameters largely characteristic of hemidirected coordination). Based on the NMR data, the intermediate case is for the lead centre in **4** because its isotropic chemical shift (as well as the δ_{11} and δ_{22} principal components) is intermediate between those typical of holodirected and hemidirected lead centres. The observed data are consistent with the trends observed for other lead compounds whereby more holodirected geometry invariably leads to more negative chemical shifts than hemidirected Pb(II) structures.[37,57] The chemical shift of **4**, in particular, may provide evidence for the tetrel bonding interaction introducing partial holodirectional character to the Pb(II) centre.

3.3.3 DFT Calculations of ^{207}Pb Magnetic Shielding Tensors

DFT calculations of ^{207}Pb NMR parameters can provide useful insights into experimental trends.[37,38] One of the significant challenges associated with ^{207}Pb is that it is a

relatively heavy nucleus and is therefore affected by relativistic effects. In this work, a series of DFT calculations were done on cluster models of **1** to **5**. Two different functionals were tested (BP86 and B3LYP), the role of spin-orbit relativistic effects on the computed NMR parameters was assessed, and the importance of *Grimme's* dispersion correction was also checked.[40]

In general, this series of compounds is difficult to work with due to the heavy Pb(II) centre coordinated with the ligand and because these systems are very difficult to converge. One of the problems is that the separation between the HOMO and the LUMO of each compound is calculated to be very small, and consequently, the self-consistent field (SCF) either does not converge easily or converges with partially occupied molecular orbitals. By varying the size of the cluster model employed and ensuring that the charges were balanced correctly, proper convergence could be reached (see *Experimental Section*). This is important because the NMR parameters depend heavily on the SCF being converged and orbitals being appropriately filled.

The calculated NMR parameters are shown in **Table 3-5** in comparison with experimental values. Data for $Pb(CH_3)_4$ were calculated at each level of theory to serve as a reference in converting the calculated magnetic shielding tensors to chemical shift tensors. The magnetic shielding parameters are presented using the *Herzfeld-Berger* convention.[33] The calculated σ_{iso} values were converted to δ_{iso} by the following formula:

$$\delta_{iso} = \frac{\sigma_{ref} - \sigma_{iso}}{1 - \sigma_{ref}} \qquad \text{Eq. 3-1}$$

where σ_{ref} is the calculated isotropic shielding value of $Pb(CH_3)_4$ (δ_{iso} = 0 ppm) using the same computational methodology.

From the calculations, it is clear, as observed previously,[55] that the omission of relativistic effects results in a complete failure to obtain reliable NMR parameters for ^{207}Pb. However, upon the inclusion of scalar or spin-orbit relativistic effects, the calculated data become more correlated with the experimental values. The correlation between isotropic components is shown in **Figure 3-10**. The best correlation occurs using the B3LYP functional with spin-orbit relativistic and Grimme's dispersion correction. The correlation can be attributed in part to the exchange-correlation component of the B3LYP functional for dealing with the Pb(II) centre.[37] The correlation results in a fit with an R^2 value of only 0.8. Despite this, the general trend follows that of the measured experimental chemical shifts, so the calculations provide some value compared to experimental parameters.

Concerning the span, the experimental values are not well reproduced by the B3LYP functional. None of the methods seem to reproduce experimental values reliably. A similar result is observed for the skew. This results from the magnetic shielding tensor's principal components being overestimated or underestimated in the calculations by several hundred to a thousand ppm in some cases. Further improvements to the computational methods could be made by incorporating the valence model's strategies[58], involving an increase of the coordination shell around the Pb(II) centre by at least five, and accounting for dangling bonds by altering atomic charges. While we ensured that the cluster models' geometry extended to five shells, it is perhaps possible that the full extent of the effects of the supramolecular framework has not been modelled sufficiently, and even larger cluster models are required to obtain reliable results. The downside is that this can rapidly exceed reasonable computational resources. Many of these observations are not new for ^{207}Pb and not specific to tetrel bonded species.

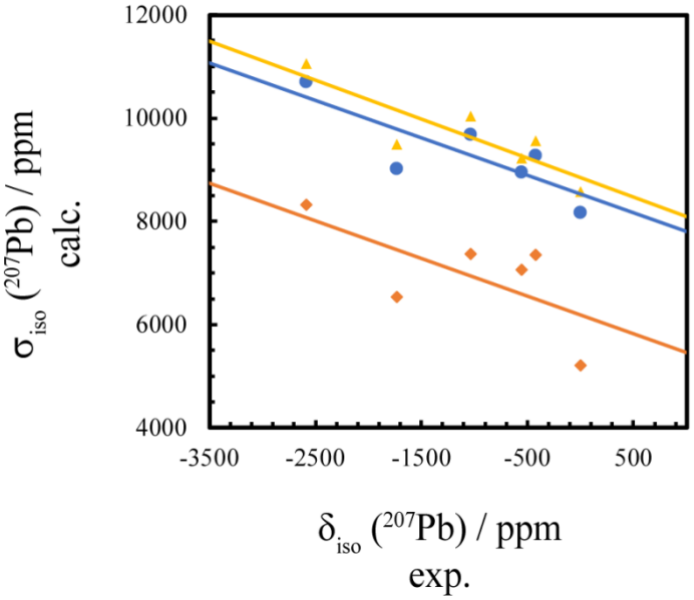

Figure 3-10. Comparison between the DFT calculated ^{207}Pb isotropic shielding constants and the experimentally measured isotropic ^{207}Pb chemical shifts. Yellow diamonds: ZORA/B3LYP/Grimme/Spin-orbit; blue circles: ZORA/BP86/Grimme/Spin-orbit; orange diamonds: ZORA/BP86/Grimme/Scalar.

(Intentionally blank)

Table 3-5. DFT calculated ^{207}Pb magnetic shielding parameters of the compounds studied in this work.

		σ_{iso}/ppm	δ_{iso} /ppm	Ω /ppm	κ	δ_{11} /ppm	δ_{22} /ppm	δ_{33} /ppm
1	ZORA/BP86/Grimme/Spin Orbit	10691.9	-2545.5	1822.0	-0.37	-1515.0	-2769.5	-3352.0
	ZORA/BP86/Grimme/Scalar	8306.7	-3128.0	559.8	-0.54	-2796.0	-3229.2	-3358.8
	BP86	8090.8	-2592.7	537.5	-0.13	-2310.6	-2616.5	-2851.1
	ZORA/B3LYP/Spin Orbit	11058.7	-2504.1	1441.0	-0.04	-1766.9	-2525.1	-3220.3
	Experimental	-	-2591	910	0.21	-2168	-2527	-3078
2	ZORA/BP86/Grimme/Spin Orbit	9011.8	-851.6	2877.5	0.59	313.6	-280.8	-2587.5
	ZORA/BP86/Scalar	6526.2	-1338.2	1709.6	-0.42	-359.6	-1576.7	-2078.1
	BP86	6726.6	-1221.0	1311.5	-0.10	-540.8	-1262.8	-1859.5
	ZORA/B3LYP/Spin Orbit	9486.4	-918.2	2763.4	0.58	208.5	-384.3	-2578.8
	Experimental	-	-1732	1071	0.18	-1228	-1670	-2299
3	ZORA/BP86/Grimme/Spin Orbit	9273.8	-1115.7	2670.9	0.14	169.7	-993.6	-2523.2
	ZORA/BP86/Grimme/Scalar	7343.6	-2159.9	1305.7	0.00	-1502.7	-2161.6	-2815.3
	BP86	7351.1	-1848.9	961.3	-0.22	-1330.6	-1918.9	-2297.2
	ZORA/B3LYP/Spin Orbit	9557.2	-989.6	2706.9	0.18	292.0	-822.5	-2438.3
	Experimental	-	-426	2681	0.48	700	3	-1981
4	ZORA/BP86/Grimme/Spin Orbit	9667.0	-1512.2	636.0	0.88	-1285.7	-1324.0	-1926.9
	ZORA/BP86/Grimme/Scalar	7361.1	-2177.4	847.8	-0.23	-1718.5	-2242.9	-2570.8
	BP86[a]	7107.6	-1604.1	-	-	-	-	-
	ZORA/B3LYP/Spin Orbit	10026.8	-1463.2	848.1	0.86	-1157.5	-1219.4	-2012.9
	Experimental	-	-1036	2259	0.53	-106	-638	-2365
5	ZORA/BP86/Grimme/Spin Orbit	8943.6	-782.8	1397.3	0.89	-288.3	-363.0	-1697.1
	ZORA/BP86/Grimme/Scalar	7058.9	-1873.7	807.8	0.90	-1590.0	-1628.9	-2402.0
	BP86	7107.6	-1604.1	822.6	-0.58	-1110.2	-1764.7	-1937.4
	ZORA/B3LYP/Spin Orbit	9215.6	-645.0	1550.3	0.45	20.7	-412.7	-1543.0
	Experimental	-	-556	2192	0.72	277	-30	-1915
$Pb(CH_3)_4$	ZORA/BP86/Grimme/Spin Orbit	8167.2	0	21.3	1.0	7.2	7.1	-14.3
	ZORA/BP86/Grimme/Scalar	5195.0	0	4.9	1.0	3.3	-1.6	-1.7
	BP86	5512.3	0	5.0	-0.98	3.3	-1.6	-1.7
	ZORA/B3LYP/Spin Orbit	8576.1	0	18.3	0.99	6.2	6.1	-12.3
	Experimental	-	0	-	-	-	-	-

a. A computation using BP86 for this compound provided unphysical results for the anisotropic of the tensor.

3.4 Concluding Remarks

We have presented ^{207}Pb solid-state NMR spectra of framework materials featuring putative lead tetrel bonds. The acquisition of ^{207}Pb solid-state NMR spectra for such materials is feasible and is readily accomplished using a combination of magic-angle spinning and CPMG methods in moderate to low applied magnetic fields. The lead centres are characterized by ^{207}Pb isotropic chemical shifts ranging from -426 to -2591 ppm and chemical shift tensor spans ranging from 910 to 2681 ppm. Careful examination of the compounds' structures and the literature ^{207}Pb NMR data may suggest that a tetrel bond to lead results in NMR parameters intermediate between those that are characteristic of holodirected and hemidirected lead coordination geometries. The computation via DFT methodologies of ^{207}Pb NMR parameters is challenging due to the simultaneously important roles of relativity, dispersion, and the influence of the extended crystal lattice.

This work has clearly shown that ^{207}Pb NMR spectroscopy can be a valuable tool in studying compounds featuring lead tetrel bonds. One of the outstanding challenges is distinguishing between the effects (both in terms of structures and in terms of NMR data) of various classes of weak interactions. We expect progress to be made as the definitions for the pnictogen, chalcogen, and tetrel bonds are formalized. In the meantime, the ^{207}Pb data for the compounds studied herein do show a clear response to the presence of non-coordinating electron-rich moieties in close contact with the electrophilic surface of formally hemidirectionally coordinated lead compounds.

3.5 References

[1] Weatherby, S.; Seddon, J.; Vallance, C. *Faraday Discuss.* **2019**, *214*, 9-12.

[2] Metrangolo, P.; Resnati, G. Eds. Halogen Bonding: Fundamentals and Applications; Springer: Berlin, **2008**.

[3] Metrangolo, P.; and Resnati, G. Eds. Halogen Bonding I: Impact on Materials Chemistry and Life Sciences; Springer International Publishing: Cham, **2015**.

[4] Desiraju, G. R.; Ho, P. S.; Kloo, L.; Legon, A. C.; Marquardt, R.; Metrangolo, P.; Politzer, P.; Resnati, G.; Rissanen, K. *Pure Appl. Chem.* **2013**, *85*, 1711-1713.

[5] Cavallo, G.; Metrangolo, P.; Pilati, T.; Resnati, G.; Terraneo, G. Naming Interactions from the Electrophilic Site. *Cryst. Growth Des.* **2014**, *14*, 2697-2702.

[6] Murray, J. S.; Lane, P.; Politzer, P. A. A predicted new type of directional noncovalent interaction *Int. J. Quantum Chem*. **2007**, *107*, 2286-2292.

[7] Kapecki, J. A.; and Baldwin, J. E.; Cycloaddition chemistry. XXI. Extended Hueckel calculations on two heterocyclic systems containing 2.41- and 2.64-A. sulfur-oxygen distances *J. Am. Chem. Soc.* **1969**, *91*, 1120-1123.

[8] Murray, J. S.; Lane, P.; Clark, T.; Politzer, P. σ-hole bonding: molecules containing group VI atoms. *J. Mol. Model.* **2007**, *13*, 1033-1038.

[9] Ramasubbu, N.; Parthasarathy, R. Stereochemistry of Incipient Electrophilic and Nucleophilic Reactions at Divalent Selenium Center: Electrophilic-Nucleophilic Pairing and Anisotropic Shape of Se in Se…Se Interactions. *Phosphorus Sulfur Relat. Elem*. **1987**, *31*, 221-229.

[10] Bauzá, A.; Frontera, A. Aerogen Bonding Interaction: A New Supramolecular Force? *Angew. Chem. Int. Ed.* **2015**, *54*, 7340-7343.

[11] IUPAC Project 2016-001-2-300: Categorizing Chalcogen, Pnictogen, And Tetrel Bonds, And Other Interactions Involving Groups 14-16 Elements. https://iupac.org/projects/project-details/?project_nr=2016-001-2-300

[12] Szell, P. M. J.; Bryce, D. L. Solid-State NMR Studies of Halogen Bonding. *Modern Magn. Reson.* **2016**, 1-18

[13] Bryce, D. L.; Viger-Gravel, J. Solid-State NMR Study of Halogen-Bonded Adducts. *Top. Curr. Chem.* **2015**, *358*, 183-203.

[14] Cerreia Vioglio, P.; Chierotti, M. R.; Gobetto, R. Solid-state nuclear magnetic resonance as a tool for investigating the halogen bond *CrystEngComm* **2016**, *18*, 9173-9184.

[15] Southern, S. A.; Bryce, D. L. NMR Investigations of Noncovalent Carbon Tetrel Bonds. Computational Assessment and Initial Experimental Observation *J. Phys. Chem. A* **2015**, *119*, 11891-11899.

[16] Dybowski C.; Neue, G. Solid state ^{207}Pb NMR spectroscopy. *Prog. Nucl. Magn. Reson. Spectrosc.* **2002**, *41*, 153-170.

[17] Harris, R. K.; Becker, E. D.; Cabral de Menezes, S. M.; Goodfellow R.; Granger, P. NMR nomenclature. Nuclear spin properties and conventions for chemical shifts(IUPAC Recommendations 2001). *Pure Appl. Chem.* **2001**, *73*, 1795-1818.

[18] Bauzá, A.; Mooibroek T. J.; Frontera, A.; Tetrel-bonding interaction: rediscovered supramolecular force? *Angew. Chem. Int. Ed.* **2013**, *52*, 12317-12321.

[19] Bauzá, A.; Mooibroek T. J.; Frontera, A. Tetrel Bonding Interactions. *Chem. Rec.* **2016**, *16*, 473-487.

[20] Hermann, A.; Lein M.; Schwerdtfeger, P. The search for the species with the highest coordination number. *Angew. Chem. Int. Ed*. **2007**, *46*, 2444-2447.

[21] Gargari, M. S.; Stilinović, V.; Bauzá, A.; Frontera, A.; McArdle, P.; Van Derveer, D.; Ng S. W.; Mahmoudi, G. Design of Lead(II) Metal-Organic Frameworks Based on Covalent and Tetrel Bonding. *Chem. -Eur. J.* **2015**, *21*, 17951-17958.

[22] Mahmoudi, G.; Bauzá, A.; Frontera, A.; Garczarek, P.; Stilinović, V.; Kirillov, A. M.; Kennedy A.; Ruiz-Pérez, C.; Metal-organic and supramolecular lead(II) networks assembled from isomeric nicotinoylhydrazone blocks: the effects of ligand geometry and counter-ion on topology and supramolecular assembly. *CrystEngComm*, **2016**, *18*, 5375-5385.

[23] Mahmoudi, G.; Bauzá, A.; Amini, M.; Molins, E.; Mague J. T.; Frontera, A. On the importance of tetrel bonding interactions in lead(II) complexes with (iso)nicotinohydrazide based ligands and several anions. *Dalton Trans.* **2016**, *45*, 10708.

[24] Mahmoudi, G.; Safin, D. A.; Mitoraj, M. P.; Amini, M.; Kubicki, M.; Doert, T.; Locherer, F.; Fleck, M. Anion-driven tetrel bond-induced engineering of lead(II) architectures with *N*′-(1-(2-pyridyl)ethylidene)nicotinohydrazide: experimental and theoretical findings. *Inorg. Chem. Front.* **2017**, *4*, 171.

[25] Mahmoudi, G.; Bauzá A.; Frontera, A. Concurrent agostic and tetrel bonding interactions in lead(II) complexes with an isonicotinohydrazide based ligand and several anions *Dalton Trans.* **2016**, *45*, 4965-4969.

[26] Moksharagni, B.; Kumar, K. D.; Chandrasekhar S.; Reddy, K. H. Synthesis, spectral characterization and evaluation of in vitro antibacterial activity of isonicotinoyl hydrazones bearing pyridine moiety. *Int. J. Pharm. Bio. Sci.* **2015**, ***6***, 11-18.

[27] Yi-Min F.; Xi-Shi T. *N*′-[1-(2-Pyrid-yl)ethyl-idene]nicotino-hydrazide. *Acta Cryst.* **2008**, *E64*, o65.

[28] Bruker, APEX2, Bruker AXS Inc. 2012, Madison, Wisconsin, USA.

[29] Bruker, SADABS, Bruker AXS Inc. 2003, Madison, Wisconsin, USA.

[30] Sheldrick, G. M. Crystal structure refinement with SHELXL. *Acta Cryst*. **2015**, *C71*, 3-8.

[31] Farrugia, L. J. WinGX suite for small-molecule single-crystal crystallograph. *J. Appl. Cryst*. **1999**, *32*, 837-838.

[32] Spek, A. L. Structure validation in chemical crystallography. *Acta Cryst*. **2009**, *D65*, 148-155.

[33] Herzfeld J.; Berger A. E. Sideband intensities in NMR spectra of samples spinning at the magic angle. *J. Chem. Phys.* **1980**, ***73***, 6021-6030.

[34] Eichele, K. HBA ver. 1.7.5, Universität Tübingen, **2015**.

[35] Eichele, K. WSolids1 ver. 1.21.3, Universität Tübingen, **2015**.

[36] Te Velde, G.; Bickelhaupt, F. M.; Baerends, E. J.; Fonseca Guerra, C.; van Gisbergen, S. J.; A.; Snijders J. G.; Ziegler, T. Chemistry with ADF *J. Comput. Chem.* **2001**, *22*, 931-967.

[37] Alkan F.; Dybowski, C. Effect of Co-Ordination Chemistry and Oxidation State on the (207)Pb Magnetic-Shielding Tensor: A DFT/ZORA Investigation. *J. Phys. Chem. A* **2016**, *120*, 161-168.

[38] Alkan F.; Dybowski, C. Chemical-shift tensors of heavy nuclei in network solids: a DFT/ZORA investigation of ^{207}Pb chemical-shift tensors using the bond-valence method *Phys. Chem. Chem. Phys.* **2015**, *17*, 25014-25026.

[39] Van Lenthe, E.; Baerends E. J.; Snijders, J. G. Relativistic regular two-component Hamiltonians. *Chem. Phys.* **1993**, *99*, 4597-4610.

[40] Grimme, S.; Antony, J.; Ehrlich S.; Krieg, H. A consistent and accurate ab initio parametrization of density functional dispersion correction (DFT-D) for the 94 elements H-Pu. *J. Chem. Phys.* **2010**, *132*, 154104.

[41] Adiga, S.; Aebi D.; Bryce, D. L. EFGShield A program for parsing and summarizing the results of electric field gradient and nuclear magnetic shielding tensor calculations. *Can. J. Chem.* **2007**, *85*, 496-505.

[42] Bondi, A. van der Waals Volumes and Radii. *J. Phys. Chem.* **1964**, *68*, 441-451.

[43] Murray, J. S.; Resnati, G.; Politzer, P. Close contacts and noncovalent interactions in crystals, *Faraday Disc.* **2017**, *203*, 113-130.

[44] Viger-Gravel, J.; Leclerc, S.; Korobkov I.; Bryce, D. L. Direct investigation of halogen bonds by solid-state multinuclear magnetic resonance spectroscopy and molecular orbital analysis. *J. Am. Chem. Soc*. **2014**, *136*, 6929-6942.

[45] Viger-Gravel, J.; Leclerc, S.; Korobkov I.; Bryce, D. L. Correlation between ^{13}C chemical shifts and the halogen bonding environment in a series of solid para-diiodotetrafluorobenzene complexes. *CrystEngComm*, **2013**, *15*, 3168-3177.

[46] Bouchmella, K.; Dutremez, S. G.; Alonso, B.; Mauri F.; Gervais, C. ^{1}H, ^{13}C, and ^{15}N Solid-State NMR Studies of Imidazole- and Morpholine-Based Model Compounds Possessing Halogen and Hydrogen Bonding Capabilities. *Cryst. Growth Des*. **2008**, *8*, 3941-3950.

[47] Szell, P. M. J.; Bryce, D. L. ^{35}Cl solid-state NMR and computational study of chlorine halogen bond donors in single-component crystalline chloronitriles. *J. Phys. Chem. C* **2016**, *120*, 11121-11130.

[48] Xu, Y.; Viger-Gravel, J.; Korobkov I.; Bryce, D. L.; Mechanochemical Production of Halogen-Bonded Solids Featuring P═O···I-C Motifs and Characterization via X-ray Diffraction, Solid-State Multinuclear Magnetic Resonance, and Density Functional Theory. *J. Phys. Chem. C* **2015**, *119*, 27104-27117.

[49] Cerreia Vioglio, P.; Catalano, L.; Vasylyeva, V.; Nervi, C.; Chierotti, M. R.; Resnati, G.; Gobetto, R.; Metrangolo, P. Natural Abundance ^{15}N and ^{13}C Solid-State NMR Chemical Shifts: High Sensitivity Probes of the Halogen Bond Geometry. *Chem. -Eur. J.* **2016**, *22*, 16819.-16928

[50] Baldrighi, M.; Cavallo, G.; Chierotti, M. R.; Gobetto, R.; Metrangolo, P.; Pilati, T.; Resnati G.; Terraneo, G. Halogen Bonding and Pharmaceutical Cocrystals: The Case of a Widely Used Preservative. *Mol. Pharmaceutics* **2013**, *10*, 1760-1772.

[51] Katz, M. J.; Michaelis, V. K.; Aguiar, P. M.; Yson, R.; Lu, H.; Kaluarachchi, H.; Batchelor, R. J.; Schreckenbach, G.; Kroeker, S.; Patterson, H. H.; Leznoff, D. B. Structural and Spectroscopic Impact of Tuning the Stereochemical Activity of the Lone Pair in Lead(II) Cyanoaurate Coordination Polymers via Ancillary Ligands. *Inorg. Chem.* **2008**, *47*, 6353-6363.

[52] Greer, B. J.; Michaelis, V. K.; Katz, M. J.; Leznoff, D. B.; Schreckenbach G.; Kroeker, S. Characterising Lone-Pair Activity of Lead(II) by ^{207}Pb Solid-State NMR Spectroscopy: Coordination Polymers of $[N(CN)_2]^-$ and $[Au(CN)_2]^-$ with Terpyridine Ancillary Ligands. *Chem. -Eur. J.* 2011, **17**, 3609-3618.

[53] Siegel, R.; Nakashima T.; Wasylishen, R. E. Application of Multiple-Pulse Experiments to Characterize Broad NMR Chemical-Shift Powder Patterns from Spin-1/2 Nuclei in the Solid State. *J. Phys. Chem. B* **2004**, *108*, 2218-2226.

[54] Rossini, A. J.; Macgregor, A.; Smith, A. S.; Schatte, G.; Schurko R. W.; Briand, G. G. Structural variation in ethylenediamine and -diphosphine adducts of $(2,6\text{-}Me_2C_6H_3S)_2Pb$: a single crystal X-ray diffraction and ^{207}Pb solid-state NMR spectroscopy study. *Dalton Trans.* **2013**, *42*, 9533-9546.

[55] Briand, G. G.; Smith, A. D.; Schatte, G.; Rossini A. J.; Schurko, R. W. Probing Lead(II) Bonding Environments in 4-Substituted Pyridine Adducts of $(2,6\text{-}Me_2C_6H_3S)_2Pb$: An X-ray Structural and Solid-State ^{207}Pb NMR Study. *Inorg. Chem.* **2007***, 46*, 8625-8637.

[56] Neue, G.; Dybowski, C.; Smith, M. L.; Hepp, M. A.; Perry, D. L. Determination of $^{207}Pb^{2+}$ chemical shift tensors from precise powder lineshape analysis. *Solid State Nucl. Mag. Reson.* **1996**, *6*, 241-250.

[57] Catalano, J.; Murphy, A.; Yao, Y.; Yap, G. P. A.; Zumbulyadis, N.; Centeno, S. A.; Dybowski, C. Coordination geometry of lead carboxylates - spectroscopic and crystallographic evidence, *Dalton Trans.* **2015**, *44*, 2340-2347.

[58] Brown, I. D.; Recent Developments in the Methods and Applications of the Bond Valence Model. *Chem. Rev.* **2009**, *109*, 6858-6919.

Chapter 4 Tin Tetrel Bonds

4.1 Introduction

Before this chapter, this thesis addresses directly addresses tetrel bonded complexes featuring both ^{13}C and ^{207}Pb electrophilic donor sites. Coupled with previous experimentation, it is clear that the tetrel bond can be detected by solid-state NMR and that the chemical shift is diagnostic in the assessment of tetrel bonds in NMR crystallography. To date, however, there has been no experimentation work done to assess the effect of tetrel bonds on the other NMR parameters, including direct dipolar coupling, indirect spin-spin coupling and an assessment of the quadrupolar and EFG tensor information of quadrupolar nuclei directly bonded to tetrel bond donors as an indirect probe. The purpose of this chapter is to assess and discuss observations of *J*-coupling across Sn-Cl covalent bonds in response to the strength of tetrel bonds in a series of organotin complexes.

Like the other tetrel elements studied herein, both ^{119}Sn and ^{117}Sn are spin-1/2 nuclides with a natural abundance of 8.59% and 7.68%, respectively. Due to the slightly higher natural abundance of ^{119}Sn, it is commonly the observed nucleus in tin NMR. Like ^{207}Pb, ^{119}Sn has a wide chemical shift range, and its NMR response is particularly sensitive to its bonding environment and oxidation state.[1] ^{119}Sn spectra can be acquired in a reasonable amount of time. However, this depends significantly on the concentration of ^{119}Sn in the sample. In situations where larger molecular structures flank the tin, significantly more extended periods of time are required to acquire a good signal-to-noise ratio. Furthermore, ^{119}Sn coordinated in organotin complexes require excessively long relaxation times, even up to several minutes,

leading to long experimental times due to the need for more extended periods between each scan.

Early on, it was made clear that the ^{1}H-^{119}Sn CP/MAS center band line shapes for organotin chloride compounds exhibit substantial influences resulting from the coupling between ^{119}Sn and $^{35/37}$Cl,[2,3] suggesting that ^{119}Sn is highly sensitive to its immediate structural environment[4], particularly when a quadrupolar nucleus directly bonded. Indeed, the effect arises from the fact that MAS does not entirely suppress the effects of dipolar coupling between a spin-1/2 and a quadrupolar nucleus ($I > ½$) in situations where the quadrupolar interaction is considerable in comparison to the *Zeeman* interaction.[2,5-8] *J*-coupling is of interest in solid-state NMR spectroscopy because of the relatively few examples noted in comparison to solution NMR. In the liquid state, *J*-couplings between spin-1/2 and quadrupolar nuclei are seldom observed due to the rapid relaxation of the quadrupolar nuclei in solution. Consequently, solid-state NMR affords an ideal opportunity to observe these relatively rare *J*-couplings.

For spin-1/2 nuclei coupled to quadrupolar nuclei, the isotropic signals often appear as doublets or triplets, giving rise to helpful information about the dipolar coupling and $^{1}J(^{119}\text{Sn-}^{35/37}\text{Cl})$ coupling. Analysis of the line shapes can also determine the anisotropy of the *J*-coupling tensor, $\mathbf{\Delta J}$.[9] To date, there have been numerous observations of $^{1}J(^{119}\text{Sn-}^{35/37}\text{Cl})$ coupling in organic compounds[10-15] in addition to $^{1}J(^{119}\text{Sn-}^{13}\text{C})$.[16] Furthermore, the NMR parameters measured from coupled spin-1/2 quadrupolar spin pairs have been used to gain insights about the CS and *J*-tensors' orientations at nuclei undergoing halogen bonds in single-crystal solid-state NMR studies.[17] The ^{119}Sn anisotropic chemical shift tensor can be measured by carrying out experiments on magic-angle spinning (MAS) samples. The three principal

components of this tensor (δ_{11}, δ_{22}, and δ_{33}) offer some information about the local environment at the ^{119}Sn site.

Kumar and coworkers recently presented a series of 10 new tetrel bonded cocrystals between organotin chloride donor molecules and various N-oxide, carbonyl, and pyridyl acceptor molecules.[18] These structures feature strong and linear tetrel bonds on the extension of the Sn-Cl covalent bond. In an extension to that work, this study fully characterizes some of the tetrel bonded complexes presented and attempts to relate the solid-state NMR observables to the structural elements of the tetrel bond to tin.

4.2 Experimental Methods

4.2.1 Synthetic Details and Characterization by X-ray Diffraction

For this follow-up study, all compounds studied were prepared for a recent manuscript where their crystal structures were studied in detail.[18] The following is a brief overview of the synthetic procedure carried out by the authors.

Triphenyl tin chloride was obtained commercially and used as the tetrel bond donor molecule. Under argon, the triphenyl tin chloride was refluxed in ethanol in the presence of a stoichiometric amount of the tetrel bond acceptor molecule. After some time, the solution was cooled to room temperature, and the solvent was removed. The resulting materials were then cleaned and filtered, and finally recrystallized for single crystal and powder X-ray diffraction analysis.

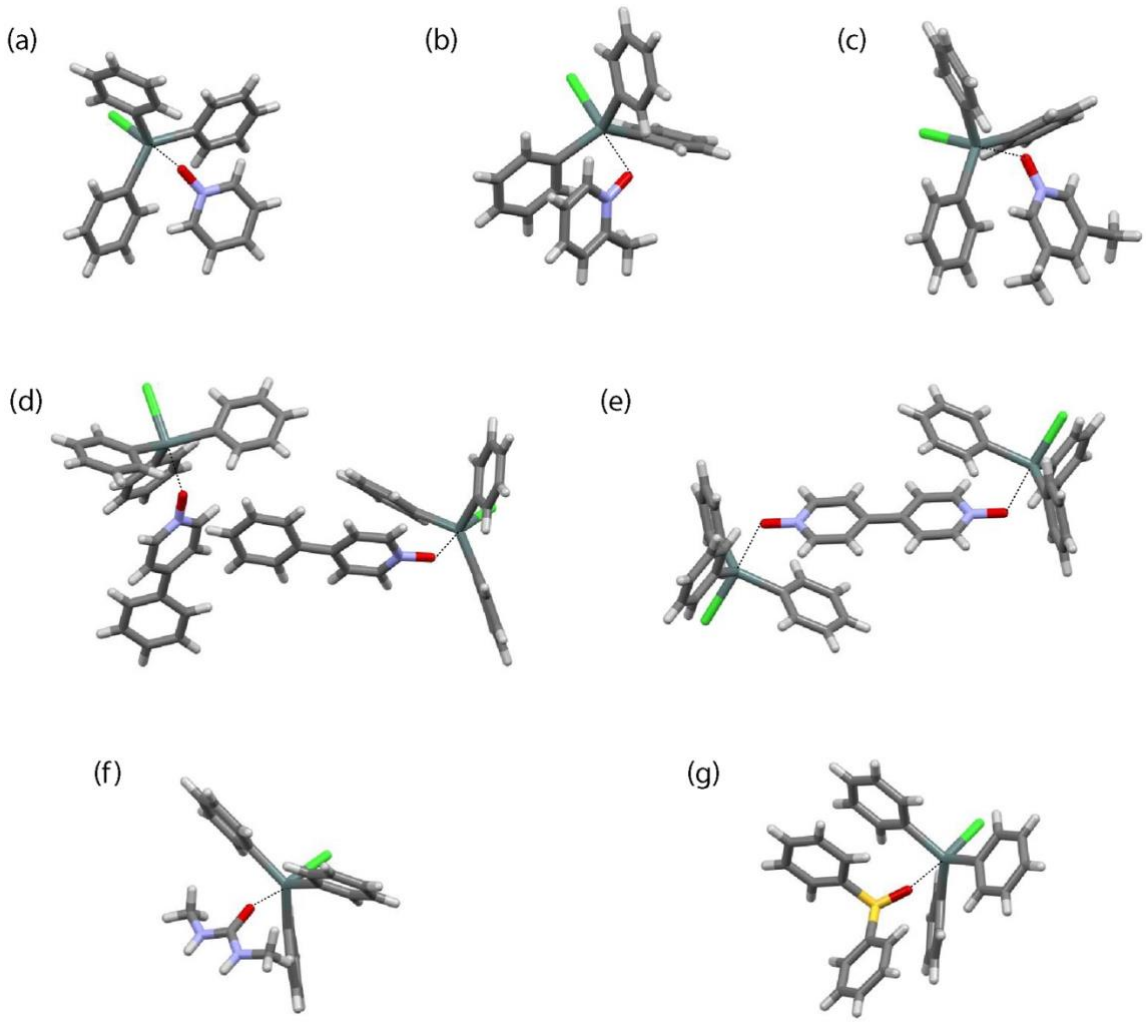

Figure 4-1. Representation of the cocrystal structures[18] of organotin chloride structures studied herein. The cocrystals are denoted using alphanumeric reference codes, and include triphenyl tin, **1**, and (a) pyridine *N*-oxide, **PNO**; (b) 2-methylpyridine *N*-oxide, **2MPNO**; (c) 3,5-dimethylpyridine *N*-oxide, **35DMPNO**; (d) 4-phenyl pyridine *N*-oxide, **PPNO**; (e) 4'4-dipyridyl *N*,*N*'-oxide, **DPNO**; (f) dimethylurea, **DMU**; and, (g) diphenyl sulfoxide, **DPSO**.

4.2.2 Solid-State NMR Spectroscopy

^{119}Sn solid-state NMR experiments were carried out at room temperature on a Bruker AVANCE III spectrometer and in a magnetic field strength of 4.7 T (ν_L (^{119}Sn) = 74.61 MHz)

or 9.4 T (ν_L (^{119}Sn) = 149.28 MHz). At 4.7 T, the samples were packed in a 7 mm (outer diameter, O.D.) zirconia rotor and measurements were carried out in a Bruker 7 mm triple resonance probe. At 9.4 T, samples were packed into 4 mm O.D. zirconia rotors and data were acquired using a Bruker 4 mm triple resonance probe for both magic angle spinning and static experiments. In each case, where there was not enough sample to fill the rotors, spacers made from either Teflon or KelF were used to centre the powder in the middle of the coil. Spectra were referenced to an external standard of a spinning sample of trimethyl tin chloride ($SnClCH_3$) at -97.35 ppm with respect to the primary reference, tetramethyl lead (0 ppm).[4,19] The magic angle of 54.74° was verified by maximizing the number of spinning sidebands in the ^{79}Br NMR spectrum of powdered KBr. Cross-polarization magic angle spinning (CP/MAS) experiments were carried out at both fields by subjecting the samples to a rotational frequency of 2.35 kHz and 4.5 kHz at 4.7 T and 4.5 kHz and 10 kHz at 9.4 T. This was done to identify the isotropic chemical shift for each compound and minimize the error in measuring other NMR parameters discussed herein. The CP parameters used for each compound were obtained by optimization on a sample of triphenyl tin chloride. At 4.7 T, the experiments were conducted using 4.0 μs radiofrequency pulses using proton decoupling, while at 9.4 T, the experiments were conducted using 4.0 μs radiofrequency pulses using SPINAL64 proton decoupling and polarization transfer times of 2,500 μs. Recycle delays were set to between 30 s and 260 s depending on the sample and the signal-to-noise acquired after ~64 scans. The number of scans acquired was maximized over reasonable experimental times for each spectrum, so between 256 and 1024 scans were typically collected depending on the recycle delay. In each MAS spectrum, the isotropic peak used for the simulation analysis was obtained *via* a summation of all spinning sidebands. An iterative procedure was performed to extract

the isotropic chemical shift, the ^{119}Sn-$^{35/37}$Cl *J*-coupling and the ^{119}Sn-$^{35/37}$Cl dipolar coupling. ^{35}Cl quadrupolar coupling constants were obtained from periodic GIPAW DFT calculations and used as a starting point for the simulations. The ^{37}Cl coupling constants were inputted by scaling the ^{35}Cl coupling constant by a factor of their quadrupolar moments, *Q*. All isotropic signal patterns were simulated using WSolids1 ver. 1.21.3.[20]

The integrals of the MAS sidebands were measured and analyzed by the *Herzfeld-Berger* methodology[21] using HBA ver. 1.7.5[22] to provide an estimate of the static line shapes (to be referred to herein as *HBA analysis*). The chemical shift tensor parameters were obtained by performing HBA analysis at each magnetic field and spinning speed. The average CS tensor parameters obtained from each of the data sets acquired at multiple fields are reported herein.

4.2.3 Computational details

Periodic DFT calculations were performed using CASTEP v19.11.[23] In all cases, the revised Perdew-Burke-Ernzerhof (revPBE) functional was used with on-the-fly-generated scalar ZORA pseudopotentials (OTFG). ZORA has been identified previously as being useful for the calculation of coupling constants involving ^{119}Sn.[24] The convergence of the computed parameters was tested such that 600 eV was determined to be an adequate cut-off energy for both geometry optimizations and magnetic resonance calculations, and the minimum *k*-point spacing of 0.07 Å^{-1} over the Brillouin zone was observed to be sufficient for convergence.[25] Geometry optimizations were carried out on hydrogen atoms only using the minimization approach of Broyden, Fletcher, Goldfarb, and Shanno (BFGS) with experimental unit cell dimensions fixed.[26] During geometry optimizations, the dispersion was accounted for using the two-body force-field method of Grimme (D2) with a re-parameterized the damping

function (s_6=1.0; d=5.0).[27] Calculations of magnetic shielding tensors were carried out on the geometry-optimized crystal structures using the gauge including projector augmented wave (GIPAW) approach. The calculated NMR parameters were extracted from the output files using EFGShield ver. 4.5[28]

4.3 Results and Discussion

4.3.1 ^{119}Sn Solid-State NMR

Tetrel bonded complexes featuring triphenyltin chloride bond donors were subjected to CP/MAS experiments at two magnetic field strengths (4.7 T and 9.4 T) to extract accurate chemical shifts and *J*-coupling constants. For the sake of comparison, the tetrel bond donor remains the same across all complexes (triphenyl tin chloride) and engages an Sn-O tetrel bond with the acceptor molecules. All of the acceptor molecules are N-oxides, except for two, which feature carbonyl or sulfoxide acceptor atoms.

The isotropic peaks for each of the compounds are presented herein. In most cases, the signal features an asymmetric triplet. The chlorine isotopes are indistinguishable because they overlap; however, a small shoulder can often be identified on the right side of the higher-frequency singularity resulting from the $^1J(^{119}\text{Sn}\text{-}^{37}\text{Cl})$ coupling being scaled from $^1J(^{119}\text{Sn}\text{-}^{35}\text{Cl})$ by a factor of $\gamma(^{37}\text{Cl})/\gamma(^{35}\text{Cl})$. For this manuscript, only $^1J(^{119}\text{Sn}\text{-}^{35}\text{Cl})$ is reported and discussed. The isotropic chemical shift can be obtained by measuring the centre of gravity at each signal, but the *J*-coupling constant is obtained from iterative analysis as described in the *Experimental Methods*.

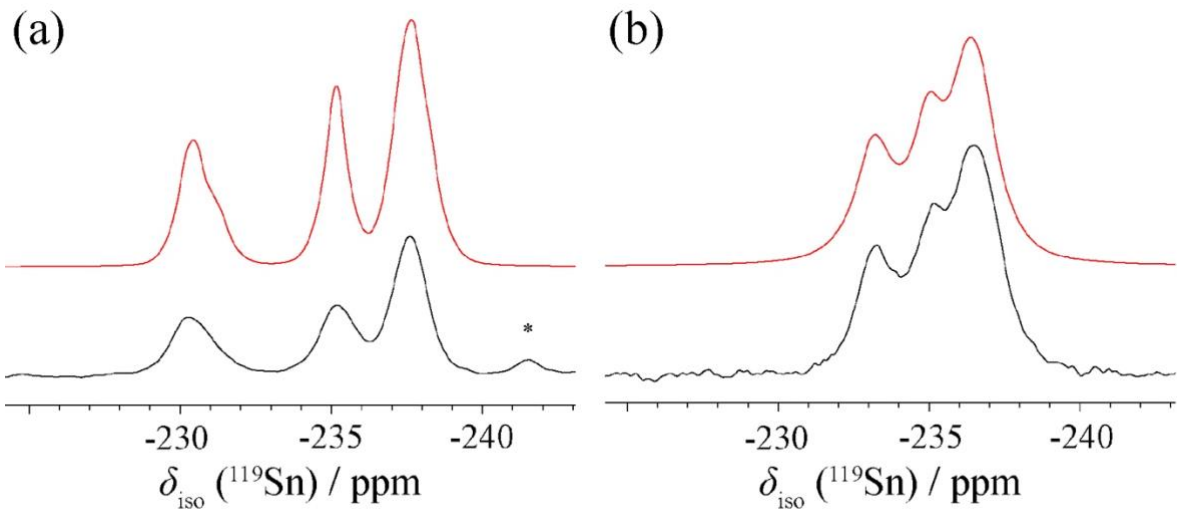

Figure 4-2. ^{1}H-^{119}Sn CP/MAS spectra of the isotropic signal for triphenyl tin pyridine N-oxide. The magnetic field strengths and MAS spinning frequencies were (a) 4.7 T, 4.5 kHz; (b) 9.4 T, 10.0 kHz. The asterisk corresponds to an artifact.

1·PNO features a classic representation of an asymmetric triplet at δ_{iso} (^{119}Sn) = -235.3 ppm dominated by a relatively large *J*-coupling (**Figure 4-2**). The crystal structure features a linear Cl-Sn···O tetrel bond length of 2.37 Å, with an angle of 177.7 degrees resulting in a dipolar coupling constant, R_{DD} = 282 Hz. The Cl-Sn covalent bond's measured length is 2.51 Å, associated with a measured ^{1}J(^{119}Sn-^{35}Cl) of 185 Hz. HBA analysis over the combination of MAS spinning frequencies indicates a span of 424 ppm and a skew of -0.59. **Figure 4-10** shows the complete spinning sideband manifold acquired for **1-PNO** and serves to demonstrate the spans of the other spectra, which are not shown here.

The addition of one or more methyl groups, either *meta*- or *ortho*- to the oxygen acceptor atom, introduces some steric effects[29] which seem to tilt the molecule from **1** in comparison with **1-PNO**. In **1·2MPNO**, there are two distinct tetrel bonds, with Cl-Sn···O tetrel bond lengths of 2.37 and 2.39 Å, with angles of 175.4 and 175.9 degrees. However, these two contacts are too similar to be distinguished in the ^{119}Sn CP/MAS spectra (**Figure**

4-3) and are considered identical to fit the NMR spectra. At lower field (B_0 = 4.7 T), the asymmetric triplet pattern of the isotropic peak (δ_{iso} (^{119}Sn) = -231.0 ppm) is less well defined than the last structure. It completely collapses into a broad peak at 9.4 T, likely resulting from the combined effects of four overlapping ^{119}Sn signals resulting from the presence of two sites, and a change in the degeneracy resulting from the interaction between the *Zeeman* term of ^{119}Sn and the $^{35/37}$Cl quadrupolar interactions. The $^{1}J(^{119}\text{Sn-}^{35}\text{Cl})$ was measured from the spectra acquired at two spinning speeds at 4.7 T (**Figure 4-3a**) and was 185 Hz, which is similar to **1-PNO** given the Sn-Cl bond lengths in these structures are 2.51 Å. The simulation of the spectrum acquired at 9.4 T (**Figure 4-3b**) was carried out using the same parameters as those found at the lower field, with a significant amount of line broadening applied. **1-3,5DMPNO** features only one tetrel bond with a Cl-Sn···O bond length of 2.47 Å and an angle of 178.9 degrees. The measured Cl-Sn bond length 2.48 Å. Coupled with a shorter tetrel bond length, not surprisingly, the isotropic signal (δ_{iso} (^{119}Sn) = -203.6 ppm, **Figure 4-4**) exhibits a $^{1}J(^{119}\text{Sn-}^{35}\text{Cl})$ which is relatively higher than the last three complexes at 194 Hz.

1·PPNO features two tetrel bonds; this time, differing substantially enough in their geometries that two distinguishable ^{119}Sn sites with significantly different chemical shifts at 4.7 T (δ_{iso} (^{119}Sn) =-234.5 and -247.1ppm) can be discerned (**Figure 4-5a**). Site 1 features a linear tetrel bond with a length of 2.33 Å and an angle of 176.6 degrees. Conversely, site 2 features a tetrel bond that deviates more from linearity with an angle of 171.5 degrees (2.34 Å) as opposed to the other complexes studied herein, which all feature angles close to 175-176 degrees. With the help of periodic DFT calculations, $^{1}J(^{119}\text{Sn-}^{35}\text{Cl})$ was measured to be 178 Hz for the site with the shorter tetrel bond and 184 Hz for the other. The difference between the combinations of tetrel bond lengths and angles results in a chemical shift

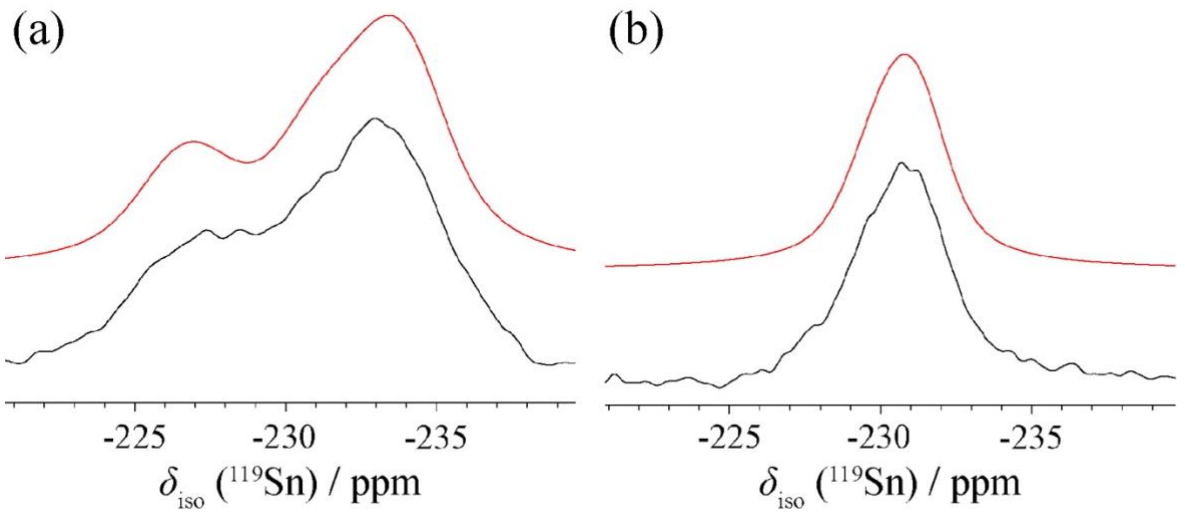

Figure 4-3. ^{1}H-^{119}Sn CP/MAS spectra of the isotropic signal for triphenyl tin 2-methylpyridine *N*-oxide. The magnetic field strengths and MAS spinning frequencies were (a) 4.7 T, 4.5 kHz; (b) 9.4 T, 10.0 kHz.

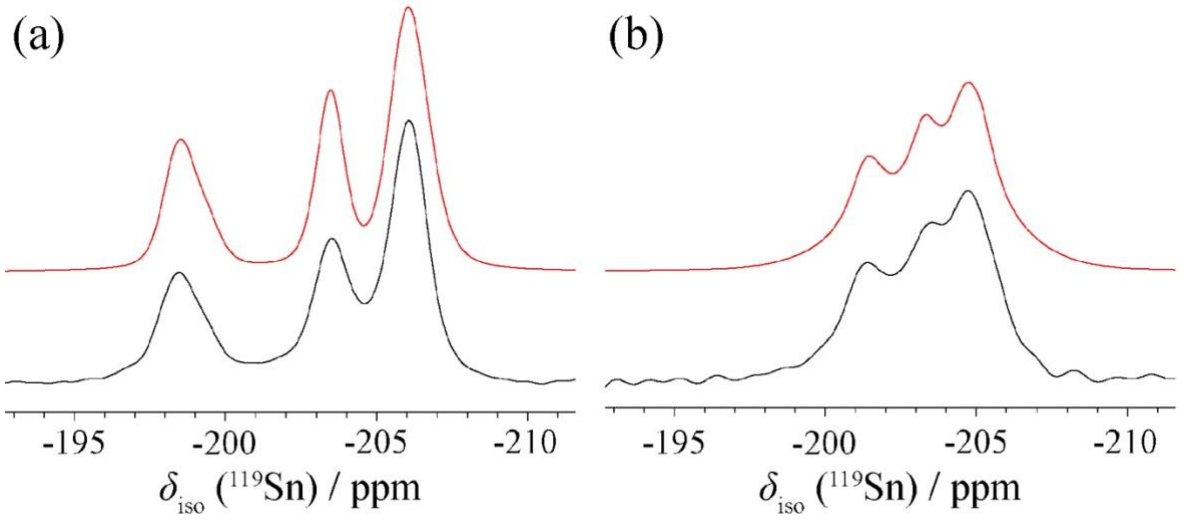

Figure 4-4. ^{1}H-^{119}Sn CP/MAS spectra of the isotropic signal for triphenyl tin 3,5-dimethylpyridine *N*-oxide. The magnetic field strengths and MAS spinning frequencies were (a) 4.7 T, 4.5 kHz; (b) 9.4 T, 10.0 kHz.

difference of 12.6 ppm. The results contrast with **1·2MPNO** where both sites have the same angle (*ca.* 175.5 degrees) and bond lengths (2.37 and 2.39 Å). The data suggest that the tetrel

bond angle's magnitude has a noticeable influence on the ^{119}Sn chemical shift. However, when the spectrum acquired at 4.7 T is compared to those acquired at 9.4 T (**Figure 4-5b and c**), a significant change in the lower frequency ^{119}Sn signal's chemical shift is observed. This site's chemical shift changes from -251.5 ppm to -244.9 ppm when subjected to the stronger magnetic field, while the higher frequency signal remains mostly unaffected (< 2 ppm). Thie data suggests that the site experiences a substantial second-order quadrupolar frequency shift due to its coupling to $^{35/37}$Cl. Based on a structural analysis of the two tetrel bonded complexes, there should be no reason for the NMR properties to differ substantially from the other tetrel bonded cocrystals, so a further look into this phenomenon is required. Consequently, this site is excluded from any comparison of its CS tensor to the other tetrel bonds.

Finally, the remaining *N*-oxide **1·DPNO,** features a bridging dipyridine acceptor forming two crystallographically equivalent tetrel bonds with lengths of 2.39 Å and almost perfectly linear angles of 178.2 degrees. This tetrel bonded complex experiences the least negative chemical shift observed from all of the compounds (δ_{iso} (^{119}Sn) = -193.1 ppm). Notably, it also features the longest tetrel bond, suggesting in comparison to the other cocrystals that the geometry of the tetrel bond highly influences the ^{119}Sn chemical shift. Again, this system features an asymmetric triplet reflecting a *J*-coupling value of 189 Hz (**Figure 4-6**).

The remaining two tetrel bonded complexes involve carbonyl acceptors rather than *N*-oxides. **1·DMU** is similar to the remaining five compounds in that it features an oxygen atom as the tetrel bond acceptor, along with an over structure containing only carbons, nitrogens and hydrogens. The chemical shift outside of the same range as the others (δ_{iso} (^{119}Sn) = -260.5 ppm, **Figure 4-7**), and the measured $^{1}J(^{119}\text{Sn}\text{-}^{35}\text{Cl})$ is 272 Hz. **1·DPSO** features a

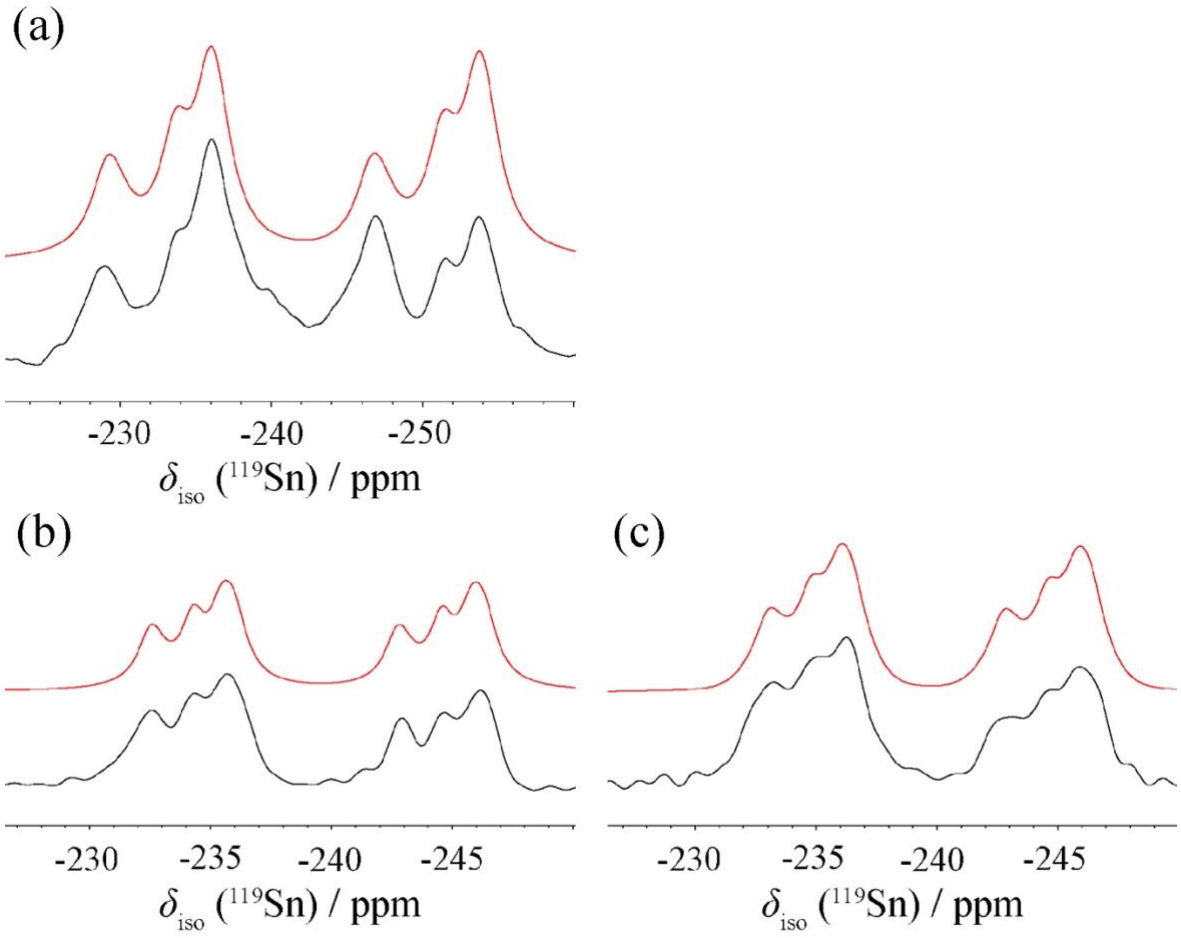

Figure 4-5. ^{1}H-^{119}Sn CP/MAS spectra of the isotropic signal for triphenyl tin 4-phenyl pyridine *N*-oxide, showing a second-order quadrupolar frequency shift of the lower frequency ^{119}Sn site. The magnetic field strengths and MAS spinning frequencies were (a) 4.7 T, 4.5 kHz; (b) 9.4 T, 4.5 kHz; and (c) 9.4 T, 10.0 kHz.

sulfoxide, which seems to result in a significantly longer tetrel bond than the other cocrystals. The TB length is 2.48 Å, resulting in a chemical shift of δ_{iso} (^{119}Sn) = -209.7 ppm (**Figure 4-8**). Given that this crystal structure is the only sulfoxide assessed in this study, it must b e treated separately from the N-oxides and the carbonyl due to the difference in its

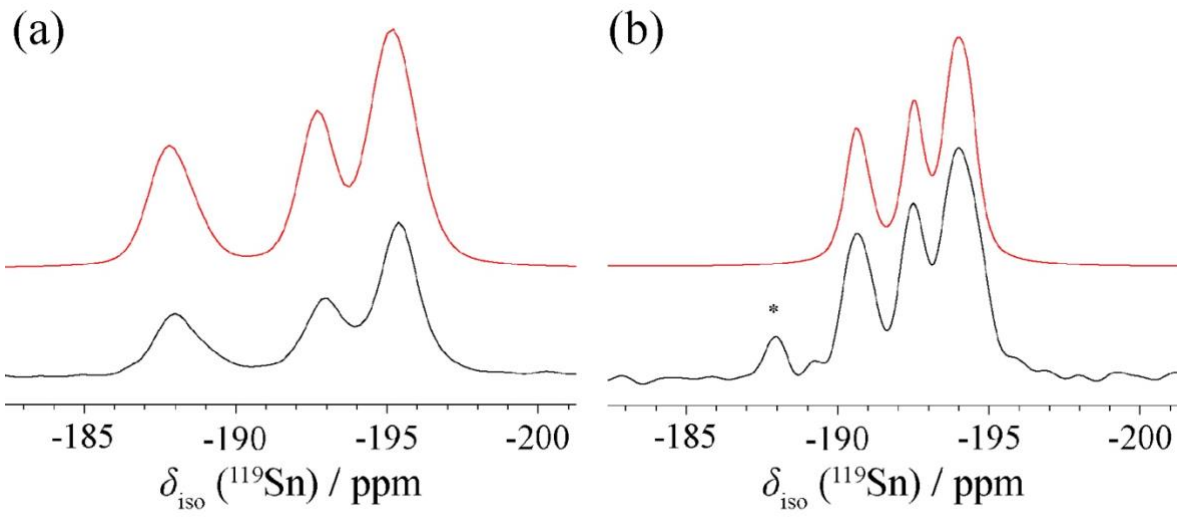

Figure 4-6. ^{1}H-^{119}Sn CP/MAS spectra of the isotropic signal for triphenyl tin 4'4-dipyridyl *N*,*N*'-oxide. The magnetic field strengths and MAS spinning frequencies were (a) 4.7 T, 4.5 kHz; (b) 9.4 T, 10.0 kHz.

chemical composition. Therefore, it is excluded from direct comparison to the other compounds, except for $^{1}J(^{119}\text{Sn-}^{35}\text{Cl})$ which should follow a similar trend resulting from the change in the Sn centre's bonding environment.

4.3.2 ^{119}Sn-^{35}Cl Spin-Spin (J) Coupling

The NMR data used to simulate each spectrum are summarized in **Table 4-1**. The tetrel bonded complexes are listed in order of their tetrel bond lengths. In general, some key trends are noticeable. First, as the tetrel bond length decreases, the $^{1}J(^{119}\text{Sn-}^{35}\text{Cl})$ trends downward. There also seems to be a loose correlation between the tetrel bond length and the

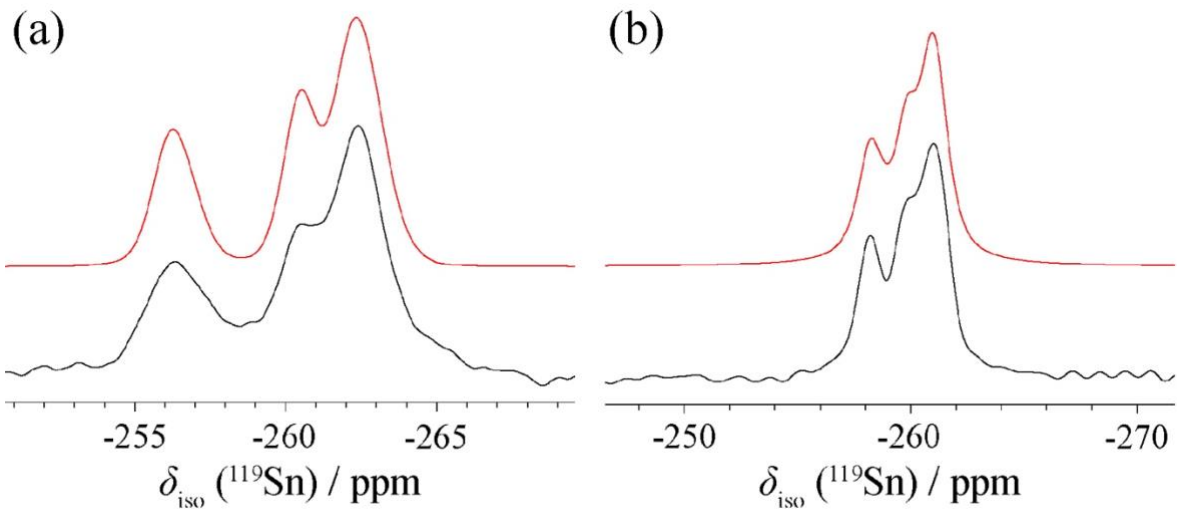

Figure 4-7. ^{1}H-^{119}Sn CP/MAS spectra of the isotropic signal for triphenyl tin dimethylurea. The magnetic field strengths and MAS spinning frequencies were (a) 4.7 T, 4.5 kHz; (b) 9.4 T, 10.0 kHz.

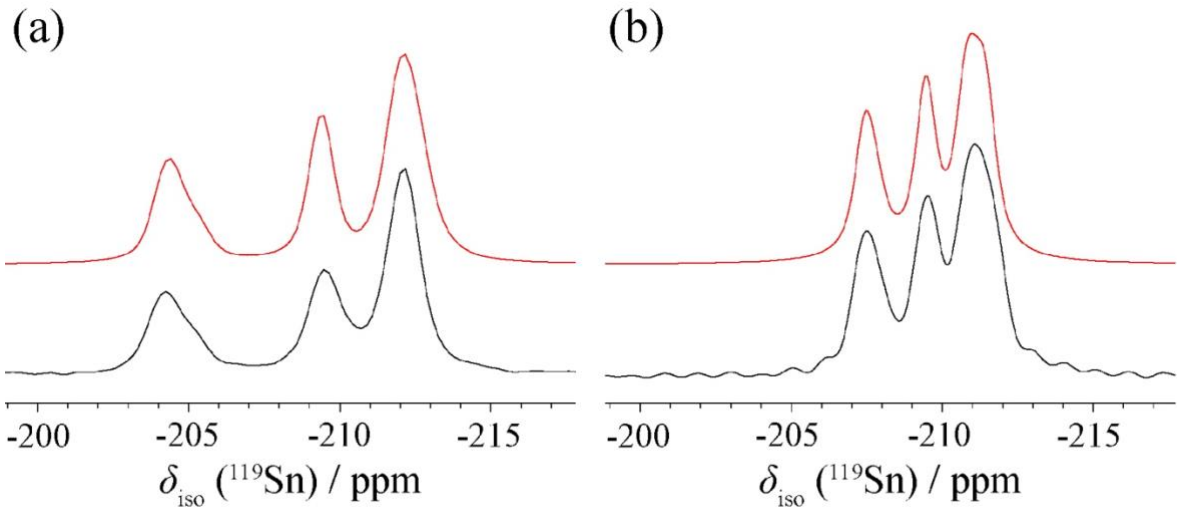

Figure 4-8. ^{1}H-^{119}Sn CP/MAS spectra of the isotropic signal for triphenyl tin diphenyl sulfoxide. The magnetic field strengths and MAS spinning frequencies were (a) 4.7 T, 4.5 kHz; (b) 9.4 T, 10.0 kHz.

length of the Sn-Cl covalent bond. When these two sets of data are considered together, it becomes clear that the tetrel bond affects the Sn-Cl covalent bond and the associated *J*-coupling.

J-coupling arises from the coupling of two nuclei mediated by electrons, implying a direct contact either *via* a covalent or non-covalent bond. In the case of triphenyl tin chloride, which features two crystallographically distinct Sn sites, $^{1}J(^{119}\text{Sn-}^{35}\text{Cl})$ is reported to be 280 and 275 Hz.[15] Previous studies have shown that *J*-couplings can give rise to a quantitative measurement of bond strengths.[30,31]

Table 4-1. NMR parameters used to simulate the experimental isotropic peaks obtained from $^{1}\text{H-}^{119}\text{Sn}$ CP/MAS spectra for each tetrel bonded complex

Sample	Cl-Sn···O TB length / Å	Cl-Sn···O TB angle / degrees	Sn-Cl length / Å	R_{DD} / Hz	C_Q (^{35}Cl) / MHz	$^{1}J(^{119}\text{Sn-}^{35}\text{Cl})$ / Hz	$\Delta J\,^{119}\text{Sn-}^{35}\text{Cl})$ / Hz	*B* / *deg*
1·DMU	2.31	175.90	2.53	272.0	-24.5	154	30	0
1·PPNO (Site 1)	2.33	176.56	2.51	278.0	-23.0	178	40	2
1·PPNO (Site 1)	2.35	171.50	2.51	279.0	-23.0	184	40	2
1·2 MPNO	2.37	175.41	2.51	279.0	-23.0	185	40	0
3,5 DMPNO	2.37	178.94	2.48	290.0	-24.6	194	20	3
1·PNO	2.37	177.66	2.51	282.0	-24.7	185	40	2
1·DPNO	2.39	178.20	2.50	294.0	-25.0	189	60	2
1·DPSO	2.48	175.82	2.48	294.0	-25.8	202	20	12

The *J*-coupling values can be measured by careful analysis of the splitting of the isotropic peak in experimental spectra. The isotropic peaks all exhibit asymmetric triplets, which are, in reality, quartets under the influence of strong quadrupolar couplings to $^{35/37}$Cl.[11] The result is a frequency shift of each of the peaks in the quartet, so the lower frequency peaks collapse onto one another resulting in the triplet. The frequency shift on ^{119}Sn (*I*) resulting from $^{35/37}$Cl (*S*) is given by:

$$\Delta v_m = -m_s J_{IS} + \frac{3C_Q D'}{10 v_L}\left(\frac{5}{4} - m_s^2\right) \quad \text{Eq. 4-1}$$

where m_s is the magnetic quantum number, v_L is the Larmor frequency of the quadrupolar nucleus, *S*, and C_Q is the quadrupolar coupling constant. The nuclear quadrupole moments, Q, for ^{35}Cl and ^{37}Cl are 2.264 x 10^7 and 2.184 x 10^7 rad s^{-1} T^{-1}, respectively. D' is the effective dipolar coupling constant, which is dependent upon the direct dipolar coupling constant, R_{DD}, and the anisotropy of the *J*-coupling tensor, **ΔJ**, given by:

$$D' = R_{DD} - \frac{\mathbf{\Delta J}}{3} \quad \text{Eq. 4-2}$$

It becomes immediately clear that no matter the value of m_s this frequency shift is heavily dependent on the J_{IS}, R_{DD} and **ΔJ**. However, it is important to note that Eq. 4-1 is only valid in the limit of $\frac{C_Q}{4S(2S-1)v_L} \ll 1$ under MAS.[32] It must also be noted that only the effective dipolar coupling, D', is measurable from the NMR spectra due to the codependence of R_{DD} and **ΔJ**.

In order to properly extract the *J*-coupling using iterative fitting routines, one must first consider the dipolar coupling. As mentioned previously, the dipolar coupling can be calculated directly from the crystal structure and used for the simulations. Also, the calculated quadrupolar coupling constant, C_Q, is used for the fitting procedure, while the asymmetry, η_Q, did not have a noticeable effect on the spectra and is assumed to be zero in all cases. These calculated parameters provide useful starting points for the fitting because they are otherwise difficult to measure experimentally.

The angle between the largest principal component of the EFG tensor and the Sn-Cl bond, β, was observed to affect the spectra and was therefore optimized. In most cases, the magnitude of β was small, landing at 1-3 degrees. The exception was **1·DPSO** likely resulting

from a substantial change of the EFG tensor orientation compared to the other structures. Finally, $^{1}J(^{119}\text{Sn-}^{35}\text{Cl})$ and ΔJ were accounted for in the simulations, with the latter remaining relatively similar between each of the tetrel bonded complexes.

A plot of the experimental $^{1}J(^{119}\text{Sn-}^{35}\text{Cl})$ coupling constants *versus* the experimentally measured tetrel bond distances is shown in **Figure 4-9**. This plot includes the *J*-coupling measured for all compounds. The magnitude of $^{1}J(^{119}\text{Sn-}^{35}\text{Cl})$ increases as the tetrel bonds to Sn get longer. The data are fit with both using an asymptotic regression model, which within the limits of a TB, predicts that $^{1}J(^{119}\text{Sn-}^{35}\text{Cl})$ adopts a value more reflective of the absence of a tetrel bond when the TB lengthens. The results can be rationalized by similar effects seen resulting from P=Se···I halogen bond formation.[33] A natural localized molecular orbital (NLMO) analysis of the halogen bonded complexes suggests that the Se lone-pair orbital contributes the most to the *J*-coupling trends, while the P=Se bonding orbital accounts for the

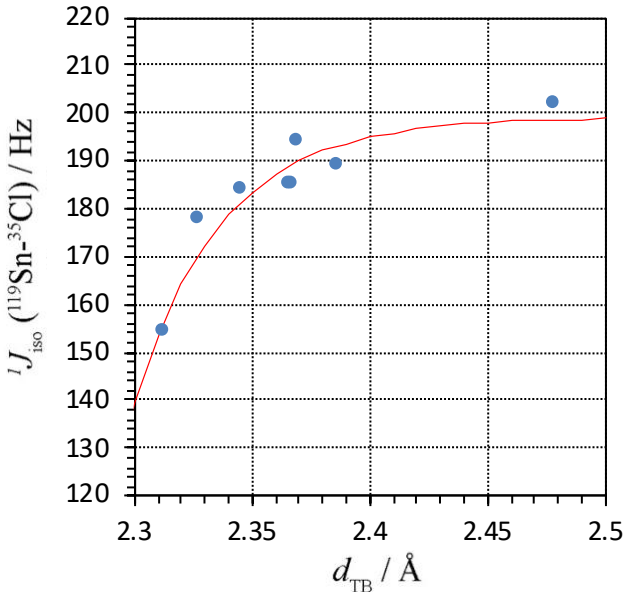

Figure 4-9. A plot of the experimental $^{1}J(^{119}\text{Sn-}^{35}\text{Cl})$ values corresponding to the tetrel bonded complexes. The plot is modelled with an asymptotic regression fit ($y = a - (a - b)e^{-cx}$) where $a = 199.08$, $b = -2.83 \times 10^{28}$ and $c = 26.71$. $R^2 = 0.8966$.

second-largest contribution to the *J*-couplings, and the iodine lone pair orbital does not contribute much to the *J*-coupling at all. In our structures, the magnitude of *J*-coupling changes as the TB shortens, while the calculated C_Q decreases in magnitude. The data suggests that Lewis bases' contribution to the TB results in a systematic weakening of the Sn-Cl covalent bond, resulting in chlorine that adopts a slightly elevated ionic character.

Further computational studies will need to be carried out on the organotin chloride complexes discussed herein to understand the relationship between the tetrel bond and $^1J(^{119}\text{Sn-}^{35}\text{Cl})$. However, this work establishes that the $^1J(^{119}\text{Sn-}^{35}\text{Cl})$ coupling constant is a valuable indicator of the presence of a Cl-Sn···O/S tetrel bond.

4.3.3 Chemical Shift Tensors

^{119}Sn CP/MAS experiments of the tetrel bonded complexes were carried out at multiple fields and multiple spinning frequencies to identify the isotropic peaks amongst the spinning sidebands. An example of spectra acquired at multiple fields is shown in **Figure 4-10**. A Herzfeld-Berger analysis was carried out on the spinning sidebands' integrals on spectra acquired at 9.4 T for each spectrum. The CS tensor components are shown in **Table 4-2**. It is important to note that while the HBA analysis can provide useful information about the CS tensor, it can only provide accurate data when other effects such as the dipolar coupling interaction are absent. In cases where a very significant influence on the CS from a large dipolar coupling, the HBA method cannot be used. For example, when the dipolar coupling magnitude is comparable to the CS tensor span, the HBA method can only provide weak estimates of the CS tensor parameters. For the compounds studied here, the largest dipolar coupling constant calculated over all $^{119}\text{Sn-}^{35/37}\text{Cl}$ spin pairs at 9.4 T corresponds to a bond length of 2.49 Å and is 290 and 241 Hz for ^{35}Cl and ^{37}Cl, respectively. Therefore, the dipolar

coupling constants are on the order of less than 2 ppm, meaning that for all of the compounds, which have CS spans of >400 ppm, the dipolar coupling effects on the ^{119}Sn CS tensor from $^{35/37}$Cl are minimized. The HBA analysis is, however, still imperfect. The spectral integrals are adversely affected by the relatively low signal-to-noise ratio of all of the obtained spectra, the presence of the two overlapping signals resulting from the tin-chlorine isotopologues, and complications arising from the splitting due to *J*-coupling. Therefore, the HBA analysis discussed herein must be accepted as providing only an estimate of the ^{119}Sn CS tensor data to obtain only general insight into the tetrel bond's effects. The measured CS tensor data must therefore be interpreted with caution.

Over the series of tetrel bonded complexes, there are a few critical observations made. First, the experimental ^{119}Sn chemical shift is observed to decrease as the tetrel bond length decreases (**Figure 4-11a**). This trend is reproduced by the DFT calculations, showing an increase in the isotropic magnetic shielding constant (**Figure 4-11d**). A change in the negative direction is also reflected in the experimental skews (**Figure 4-11c** and **f**), whereas a lack of correlation is observed in the experimental or calculated spans (**Figure 4-11b** and **e**).

When broken down into the individual tensor components, clearer experimental trends are observed and reproduced by GIPAW DFT calculations. δ_{11} and δ_{22} are observed to decrease in response to a shortened tetrel bond (**Figure 4-12**). Overall, δ_{11} experiences a decrease from 42 ppm to -5 ppm, while δ_{22} decreases from -385 ppm to -227 ppm. While δ_{33} is also observed to change, the trend is influenced by a higher degree of scatter. Both δ_{11} and δ_{22} lead to an overall decrease in the isotropic chemical shift in response to a shorter tetrel bond length. Similar trends have been observed in chalcogen bonded complexes.[34] Periodic DFT calculations of the ^{119}Sn magnetic shielding tensors corroborate the experimental trends,

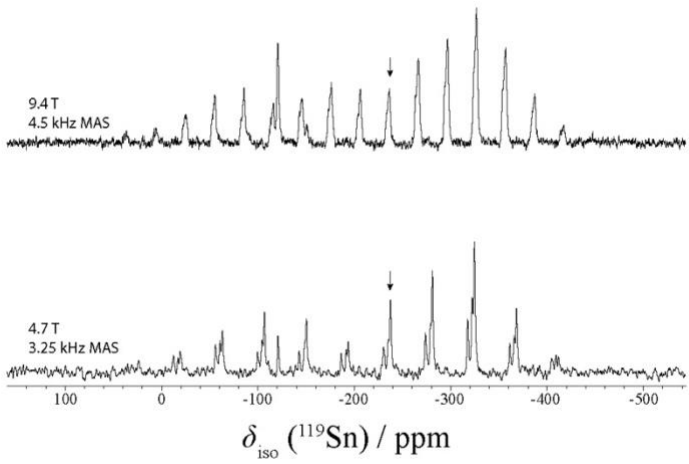

Figure 4-10. Experimental ^{119}Sn CP/MAS spectra of triphenyl tin pyridine N-oxide acquired at 4.7 and 9.4 T at spinning frequencies as indicated. A downward-pointing arrow labels the isotropic chemical shift.

with the magnetic shielding tensor's principal components, σ_{33} and σ_{22}, increasing as the tetrel bond length gets shorter.

Table 4-2. Estimated CS Tensor data for the tetrel bonded complexes obtained at 9.4 T[a]

	1·PPNO (Site 1)[b]	**1·PPNO** (Site 2)[b]	**1·2MPNO**	**3,5DMPNO**	**1·DMU**	**1·DPNO**[b]	**1·PNO**	**1·DPSO**
δ_{iso} /ppm	-234.9(3)	-245.0(1)	-231.0(0)	-203.6(0)	-260.4(3)	-193.1	-235.3(0)	-209.8(1)
Ω /ppm	433(11)	418(10)	444(5)	412(0)	407(6)	427	425(3)	405(1)
κ	-0.57(8)	-0.45(3)	-0.64(5)	-0.58(2)	-0.92(6)	-0.24	-0.61(4)	-0.29(2)
δ_{11} /ppm	23(16)	-5(3)	38(0)	42(2)	5(1)	37	20(1)	12(2)
δ_{22} /ppm	-317(10)	-307(4)	-325(5)	-283(3)	-385(6)	-227	-322(5)	-248(3)
δ_{33} /ppm	-410(11)	-423(7)	-405(5)	-369(2)	-402(7)	-389	-405(4)	-393(1)

a. Data were obtained by an HBA analysis of the integrals of the spinning sidebands obtained from 1H-119Sn CP/MAS acquired at 9.4 T, with MAS frequencies of 4.5 kHz and 10 kHz. Standard deviations for the averages are reported. All CS data are given in units of ppm.

b. A spectrum was not obtained at 9.4 T and a MAS frequency of 4.5 kHz. The error is estimated to be 5%.

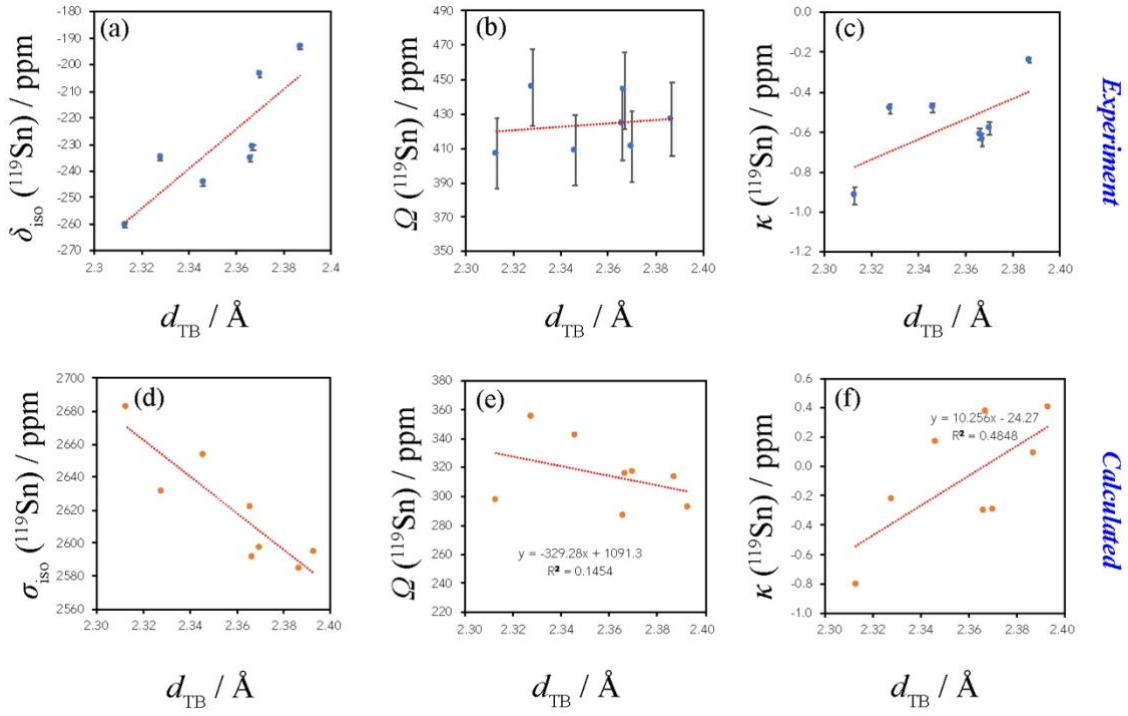

Figure 4-11. Linear comparisons between the correlations between the tetrel bond length and the experimental ^{119}Sn (a) isotropic chemical shift (R^2 = 0.7084), (b) span (R^2 = 0.0269), and (c) skew ((R^2 = 0.4146) and the GIPAW DFT calculated (d) magnetic shielding constant (R^2 = 0.7880), (e) span (R^2 = 0.1454), and (f) skew (R^2 = 0.4848).

4.4 Conclusions

This contribution presents experimental ^{119}Sn solid-state NMR spectra of some tetrel bonded tin complexes featuring short and linear tetrel bonds. This work's primary goal is to provide experimental insights into the dependence of the ^{119}Sn NMR parameters on the geometric features of the tetrel bonds. Insights into the tetrel bonding mechanism's nature are revealed by close observations of the $^{1}J(^{119}\text{Sn-}^{35}\text{Cl})$ coupling constants, clearly shown to correlate with the tetrel bond length. The estimated ^{119}Sn CS tensor parameters are also observed to correlate with the tetrel bond's length, whereby as the tetrel bond length between

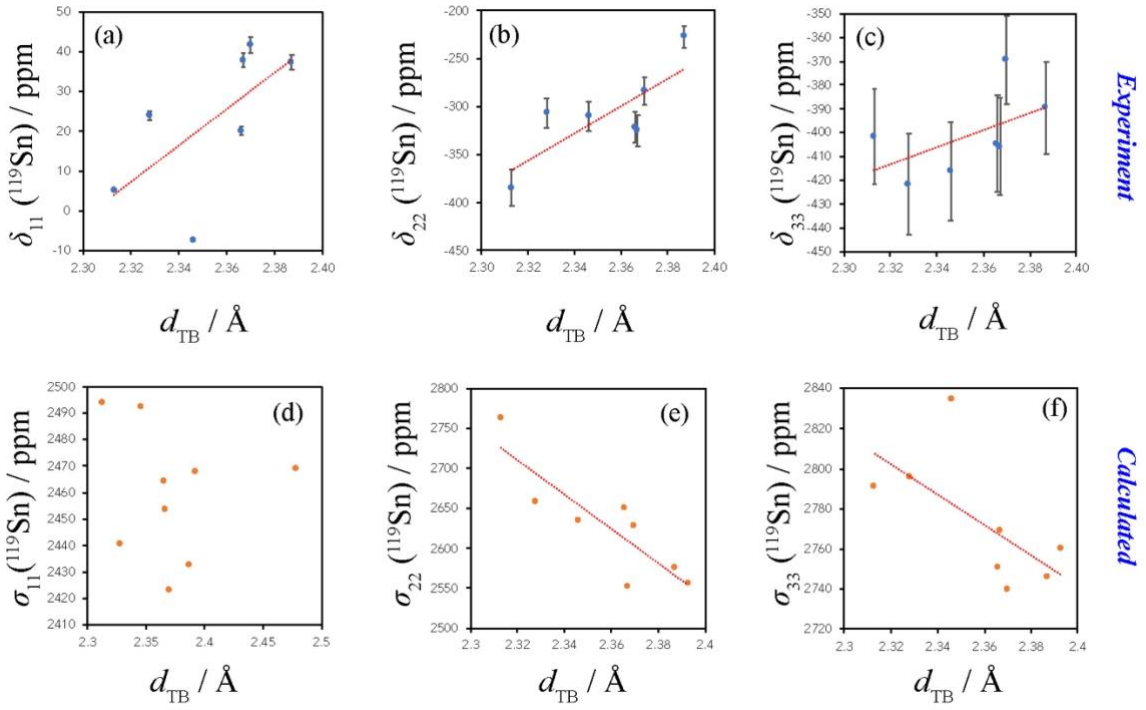

Figure 4-12. Correlation between (a, b and c) the experimentally measured values of δ_{11} (R^2 = 0.4272), δ_{22} (R^2 = 0.6089) δ_{33} (R^2 = 0.2901) and the tetrel bond lengths. The corresponding correlations to the GIPAW DFT computed values of σ_{22} (R^2 = 0.7441) and σ_{33} (R^2 = 0.4319), and a lack of correlation to σ_{11} are shown (e, f and d, respectively).

Sn and N-oxides gets shorter, the magnitude of the ^{119}Sn chemical shift increases in the negative direction. This trend arises primarily from changes in δ_{11} and δ_{22}. However, it is essential to note that more work will need to be done to finalize the comparisons between the experimental and calculated CS data and confirm the trends observed in this preliminary data. Further analysis of static ^{119}Sn spectra may afford more precise CS tensor data. However, the results show clear correlations between the chemical shift and the Cl-Sn···O tetrel bonds.

This work provides more experimental NMR data to support our previous studies showing how NMR parameters are influenced by tetrel bonds (see chapters 3 and 4 of this thesis). This work will augment how σ-hole interactions influence NMR spectra and how the

data may be incorporated into NMR crystallographic approaches for crystal structure refinement.

4.5 References

[1] Lucier, B. E. G.; Terskikh, V. V.; Guo, J.; Bourque, J. L; McOnie, S. L.; Ripmeester, J. A.; Huang, Y. *Inorg. Chem.* **2020**, *59,* 13651-13670.

[2] Harris, R. K. *J. Magn. Reson.* **1988**, *78*, 389-393.

[3] Harris, R. K; Sebald, A.; Furlani, D.; Tagliavini, G. *Organometallics*, **1988**, *7*, 388-394.

[4] Lippmaa, E. T.; Alla, M. A.; Pehk, T. J.; Engelhardt, G. *J. Am. Chem. Soc.* **1978**, *6*, 1929-1931.

[5] Olivieri, A. C. *Solid State Nucl. Magnet. Reson.* **1992**, *1*, 345-353.

[6] Apperley, D. C.; Haiping, B.; Harris, R. K. *Mol. Phys.* **1989**, *68*, 1277-1286.

[7] Naito, A.; Ganapathy, S.; McDowell, C. A. *J. Chem. Phys.* **1981**, *74*, 5393-

[8] Zumbulyadis, N.; Henrichs, R. M.; Young, R. H. *J. Chem. Phys.* **1981**, *75*, 1603-

[9] Harris, K. J.; Bryce, D. L.; Wasylishen, R. E.; *Can. J. Chem.* **2009**, *87*, 1338-1351.

[10] Komoroski, R. A.; Parker, R. G.; Mazany, A. M.; Early, T. A. *J. Magn. Reson.* **1987**, *3*, 389-398.

[11] Geller, J. M.; Butler, I. A.; Gilson, D. F. R.; Morin, F. G.; Wharf, I. *Can. J. Chem.* **2003**, *11*, 1187-1195.

12 Alarcón, S. H.; Olivieri, A. C.; Harris, R. K. Solid State Nucl. Magn. Reson. **1993**, 6, 325-334.

[13] Mundus, C. Taillades, G. Pradel, A. Ribes, M. *Solid State Nucl. Magn. Reson.* **1996**, *2*, 141-146.

[14] Lyčka, A.; Holeček, J.; Sebald, A.; Tkáč, I. *J. Organomet. Chem.* **1991**, *409*, 331-339.

[15] Willans, M. J.; Demko, B. A.; Wasylishen, R. E. *Phys. Chem. Chem. Phys.* **2006**, *23*, 2733-2743.

[16] Lockhart, T. P.; Manders, W. F.; Zuckerman, J. J. *J. Am. Chem. Soc.* **1985**, *107*, 4546-4547.

[17] Xu, Y.; Gabidullin, B.; Bryce, D. L. *J. Phys. Chem. A*, **2019**, *123*, 6194-6209.

[18] Kumar, V.; Rodrigue, C. Bryce, D. L.; *Cryst. Growth. Des.* **2020**, *3*, 2027-2034.

[19] Harris, R. K.; Sebald, A. *Magn. Reson. Chem.* **1987**, *25*, 1058-1062.

[20] WSolids1 ver. 1.21.3, K. Eichele, Universität Tübingen, **2015**.

[21] J. Herzfeld and A. E. Berger, *J. Chem. Phys.* **1980**, **73**, 6021.

[22] HBA 1.7.5, K. Eichele, Universität Tübingen, **2015**.

[23] Clark, S.J.; Segall, M.D.; Pickard, C.J.; Hasnip, P.J.; Probert, M.J.; Refson, K.; Payne, M. C. First Principles Methods Using CASTEP. *Z. Kristall*. **2005**, *220*, 567-570.

[24] Bagno, A.; Casella, G.; Saielli, G. *J. Chem. Theory Comput.* **2006**, *2*, 37-46.

[25] Monkhorst, H. J.; Pack, J. D. Special Points for Brillouin-zone Integrations. *Phys. Rev. B.* **1976**, *13*, 5188-5192.

[26] Pfrommer, B. G.; Cote, M.; Louie, S. G.; Cohen, M. L. Relaxation Of Crystals With The Quasi-Newton Method. *J. Comput. Phys.* **1997**, *131*, 233-240.

[27] Holmes, S. T.; Schurko, R. W. Refining Crystal Structures With Quadrupolar NMR And Dispersion-Corrected Density Functional Theory. *J. Phys. Chem. C* **2018**, *122*, 1809-1820.

[28] S. Adiga, D. Aebi and D. L. Bryce, *Can. J. Chem.* 2007, **85**, 496.

[29] Scheiner, S. Steric Crowding in Tetrel Bonds. *J. Phys. Chem. A*, **2018**, *122*, 2550-2562.

[30] Brown, S. P.; Pérez-Torralba, M.; Sanz, D.; Claramunt R. M.; Emsley, L. Determining Hydrogen-bond Strengths in the Solid State by NMR: The Quantitative Measurement of Homonuclear *J* Couplings, *Chem. Commun.* **2002**, 1852-1853.

[31] Maiti, N. C.; Zhu, Y.; Carmichael, I.; Serianni, A. S.; Anderson, V. E. $^{1}J_{CH}$ Correlates with Alcohol Hydrogen Bond Strength, *J. Org. Chem.* **2006**, *71*, 2878-2880.

[32] Olivieri, A. C. Quadrupolar effects in the CPMAS NMR spectra of spin-1/2 nuclei. *J. Magnet. Reson.* **1989**, *81*, 201-205.

[33] Viger-Gravel, J.; Meyer, J. E.; Korobkov, I.; Bryce, D. L. Probing Halogen Bonds with Solid-State NMR Spectroscopy: Observation and Interpretation of $J(^{77}Se, ^{31}P)$ Coupling in Halogen-Bonded P=Se···I Motifs, *CrystEngComm*, **2014**, *16*, 7285-7297.

[34] Kumar, V.; Xu, Y.; Leroy, C.; Bryce, D. L. Direct investigation of chalcogen bonds by multinuclear solid-state magnetic resonance and vibrational spectroscopy, *Phys. Chem. Chem. Phys.* **2020**, *22*, 3817-3824.

Chapter 5 General Conclusions

5.1 Summary

In this thesis, considerable efforts have been made to demonstrate the effect that the tetrel bond has on the solid-state NMR response. A systematic study of group 14 elements began with carbon in Chapter 2. An analysis of organic cocrystals featuring either caffeine or theophylline tetrel bond donors revealed the weak nature of carbon tetrel bonding at methyl centres. Indeed, the tetrel bond's weakness resulted in very loose correlations between experimental shifts and structural features. However, this work showed that one must be cautious when assigning chemical shifts to specific structural elements. It became clear that computational chemistry must be used alongside the experimental NMR data to interpret the NMR spectrum when tetrel bonding is suspected correctly. For example, regarding the tetrel bond's influence on the ^{13}C experimental chemical shift, it was demonstrated that as the tetrel bond's length gets shorter, the ^{13}C isotropic chemical shift increases, albeit only slightly. The ^{13}C chemical shift increases compared to similar methyl carbons in cocrystals that do not feature tetrel bonds. The computational study showed that, in fact, the increase more strongly correlates with TB distance in the absence of competing structural effects. One must carefully consider that other crystallographic effects can significantly alter the chemical shift change due to tetrel bonds. One such example is the competition of weak CH…O hydrogen bonds observed in many of the complexes studied. These hydrogen bonds may either amplify or decrease the tetrel bond's effect on the ^{13}C chemical shift.

Next, ^{207}Pb solid-state NMR spectra of supramolecular structures that feature lead tetrel bonds were presented. This work focused on relating the ^{207}Pb solid-state NMR spectra,

acquired by static and magic angle spinning techniques, to structural features at the Pb(II) centre in hemidirectionally coordinated tetrel bond donors. Interestingly, Pb(II) features unique NMR parameters if it is in hemidirectional *versus* holodirectional geometry. For each of the five compounds assessed, the ^{207}Pb isotropic chemical shifts range from -426 to -2591 ppm and chemical shift tensor spans ranging from 910 to 2681 ppm. The data suggest that a tetrel bond to lead results in NMR parameters intermediate between those characteristic of holodirected and hemidirected lead coordination geometries. The work demonstrated that ^{207}Pb NMR spectroscopy is beneficial not only for studying tetrel bonds between non-coordinating electrophiles and Pb(II) centres and understanding how a tetrel bond may affect an NMR response.

The final stop on the periodic table is tin. The work's focus was not only to assess the ^{119}Sn chemical shift response to short and linear tetrel bonds in organotin chloride complexes but also to relate the observable $^{1}J(^{119}\text{Sn-}^{35}\text{Cl})$ coupling to either the tetrel bond lengths. Indeed, the ^{119}Sn CS tensor parameters appear to correlate well with the tetrel bond's length: as the Sn…O tetrel bond's length gets shorter, the ^{119}Sn chemical shift becomes more negative, resulting from changes primarily in δ_{11} and δ_{22}. More convincingly, a clear logistic correlation is observed between the tetrel bond length and $^{1}J(^{119}\text{Sn-}^{35}\text{Cl})$, showing *J*-coupling to be a sensitive probe to tetrel bonding.

5.2 Impact and Future Directions

The results of this work will be helpful in NMR crystallographic approaches to solve and refine structures that may feature tetrel bonds. This thesis's work comprises the first attempts to detect the tetrel bond by solid-state NMR and understand its effects on the NMR spectrum. However, the work is far from over: this author only considers this to be the

beginning of what might prove to be a long but fruitful project. There is still much left to be done to explore the tetrel bond by solid-state NMR, and several proposals for future directions are outlined in the following few paragraphs.

Briefly, there is a real opportunity to investigate the indirect coupling between ^{17}O and ^{207}Pb centres using enriched tetrel bond acceptor molecules. More work also needs to be done to investigate the effects of tetrel bond formation on other atoms within the donor and acceptor molecules. A systematic study of the effects of electron-withdrawing substituents on the tetrel bond and the subsequent effect on NMR observables must be investigated.

In an extension of this thesis's theme, other tetrel bond donors must be explored, not examined here. For example, silicon-based tetrel bonded complexes show promise for the study of solid-state NMR. ^{29}Si is a spin-1/2 nucleus easily detected by MAS NMR and is already used extensively to study materials[1] such as zeolites[2] and other inorganic solids.[3] There are already some examples of simple systems[4] having been identified and studied by rotational spectroscopy.[5,6] However, Si-based tetrel bonded systems seem to be generally underexplored. However, Si tetrel bonds have been identified to form intramolecular tetrel bonds in systems applicable to solid-state NMR.[7-10] While the intramolecular tetrel bonds can certainly be studied by solid-state NMR, the identification of other complexes featuring tetrel bonded heteromolecules would be a good starting point to demonstrate the applicability of Si tetrel bonds in crystal engineering.

In addition to Si, the remaining nuclide of interest for solid-state NMR studies is ^{73}Ge. This isotope is a spin-9/2 quadrupolar nuclide which has a very large quadrupole moment (Q = -19.2 fm^2) and a low gyromagnetic ratio (γ = -0.936 x 10^7 rad T^{-1} s^{-1}), making it very difficult to study by solid-state NMR due to the significant broadening observed for systems whereby

an EFG is present at a non-symmetric ^{73}Ge site. As a result, very few studies have traditionally used ^{73}Ge solid-state NMR, though, in more recent years, some works have demonstrated the applicability of ^{73}Ge solid-state NMR at higher magnetic field strengths (B_0 = 21.1 T) where the effects of quadrupolar broadening are reduced.[11-13] Consequently, structures featuring Ge tetrel bonds[14] could be potentially studied by solid-state NMR.

Beyond the tetrel elements, there is a need to study nuclei directly or indirectly involved in the tetrel bond but are structurally close to the site of interest. Sometimes, atoms such as those covalently bound to the donor atom also display effects induced by noncovalent bonds' formation. For example, ^{17}O NMR has been used to probe iodine-based halogen bond P=O···I-C) motifs.[15] Similar experiments for most of the compounds studied in this thesis would provide useful insights into the tetrel bond's role in the acceptor atom's solid-state NMR response. Complimentary NLMO calculations could provide insights about the orbital contributions to either the EFG tensors of the ^{17}O acceptor nucleus or *J*-coupling across the tetrel bond if it is observed.

While it is weak, the tetrel bond can significantly impact the fields of chemistry and biochemistry. It is anticipated that tetrel bonding will be recognized as an important force in developing pharmaceutical solids and their polymorphs to improve drug design to increase their affinity to biological molecules such as proteins or enzymes. Perhaps harnessing the cumulative strength of multiple CH_3 or CF_3[16] tetrel bonds to oxygen or other electronegative atoms in biological active sites can be used to minimize the overall binding energies at the site of protein-ligand interactions. While these are perhaps very early suppositions, in the immediate term, it is foreseen that tetrel bonding will be more applicable to the field of crystal engineering.

In conclusion, this thesis provides new experimental insights into the tetrel bond. It has demonstrated experimental solid-state NMR responses to the formation of a tetrel bond and its geometry. Careful analysis of both experimental and computation data has paved the way towards understanding how the tetrel bond may manifest itself in NMR data from an NMR crystallographic point of view. It is important to stress that tetrel elements, compared to their cousins, the chalcogens, pnictogens and halogens, are the least polarizable, and indeed, in the case of carbon, give rise to the weakest trends between structural and NMR data.

There can be no mistake about the importance of this work, however. The International Union of Pure and Applied Chemistry (IUPAC) has projects underway to define the various sigma hole interactions.[17] In both chalcogen[18] bonding and halogen[19] bonding, one of the critical elements of their definitions is that they usually affect NMR observables of nuclei in both the donor and acceptor molecules. This work is fundamental and provides the data to support such a claim in the upcoming IUPAC definition of tetrel bonding.

5.3 References

[1] Lipmaa, E.; Mägi, M.; Samoson, A.; Engelhardt, G.; Grimmer, A. -R. Structural Studies of Silicates by Solid-State High-Resolution ^{29}Si NMR, I. *J. Am. Chem. Soc.* **1980**, *102*, 4889-4893.

[2] Brouwer, S. H.; Brouwer, C. C.; Mesa, S.; Semelhago, C. A.; Steckley, E. E.; Sun, M. P. Y.; Mikolajewski, J. G.; Baerlocher, C. Solid-state ^{29}Si NMR spectra of pure silica zeolites for the International Zeolite Association Database of Zeolite Structures. *Microporous and Mesoporous Materials*, **2020**, *297*, 110000.

[3] Engelhardt, G.; Koller, H. ^{29}Si NMR of Inorganic Solids, **1994**, In: Blümich B. (eds) Solid-State NMR II. NMR Basic Principles and Progress, vol 31. Springer, Berlin, Heidelberg.

[4] Alkorta, I.; Rozas, I.; Elguero, J. Molecular Complexes between Silicon Derivatives and Electron-Rich Groups. *J. Phys. Chem. A.* **2001**, *105*, 743-749.

[5] Ruoff, R. S. Rotational spectra, dipole moment, and structure of the SiF_4-NH_3 dimer. *J. Chem. Phys.* **1992**, *96*, 3441-3446.

[6] Urban, R. -D.; Rouillé, G.; Takami, M. Free-jet IR spectroscopy of SiF4-N2 and SiF4-CO complexes in the 10 μm region. *J. Molec. Struct.* **1997**, *413-414*, 511-519.

[7] Wei, Y.; Li, Q.; Yang, X.; McDowell, S. A. C. Intramolecular Si···O Tetrel Bonding: Tuning of Substituents and Cooperativity. *ChemistrySelect*, **2017**, *2*, 11104-11112.

[8] Mitzel, N. W.; Blake, A. J.; Rankin, D. W. H. β-Donor Bonds in SiON Units: An Inherent Structure- Determining Property Leading to (4 + 4)-Coordination in Tetrakis-(*N*,*N*-dimethylhydroxylamido)silane. *J. Am. Chem. Soc.* **1997**, *119*, 4143-4148.

[9] Vojinović, K.; McLachlan, L. J.; Hinchley S. L.; Rankin, D. W. H.; Mitzel, N. W. Strong Intramolecular Secondary Si···N Bonds in Trifluorosilylhydrazines. *Chem. -Eur. J.* **2004**, *10*, 3033-3042.

[10] Pestunovich, V. A.; Albanov, A. I.; Larin, M. F.; Voronkov, M. G.; Kramarova, E. P.; Baukov, Y. I. Intramolecular Si←O coordination in molecules of 1-(chlorosilylmethyl)lactams. *Izv. Akad. Nauk. Ser. Khim.* **1980**, *29*, 2178-2179.

[11] Michaelis, V. K.; Kroeker, S. ^{73}Ge Solid-State NMR of Germanium Oxide Materials: Experimental and Theoretical Studies. *J. Phys. Chem. C*, **2010**, *114*, 21736-21744.

[12] Sustrisno, A.; Hanson, M. A.; Rupar, P. A.; Terskikh, V. V.; Baines, K. M.; Huang, Y. Exploring the limits of ^{73}Ge solid-state NMR spectroscopy at ultrahigh magnetic field. *Chem. Comm.* **2010**, *46*, 2817-2819.

[13] Hanson, M. A.; Schnepf, A.; Terskikh, V. V.; Huang, Y.; Baines, K. M. Characterisation of Germanium Monohalides by Solid-State NMR Spectroscopy and First Principles Quantum Chemical Calculations. *Austral. J. Chem.* **2013**, *66*, 1202-1210.

[14] Scilabra, P.; Kumar, V.; Ursini, M.; Resnati, G. Close contacts involving germanium and tin in crystal structures: experimental evidence of tetrel bonds. *J. Molec. Model.* **2018**, *24*, 37.

[15] Xu, Y.; Viger-Gravel, J.; Korobkov, I.; Bryce, D. L. Mechanochemical Production of Halogen-Bonded Solids Featuring P═O···I-C Motifs and Characterization via X-ray Diffraction, Solid-State Multinuclear Magnetic Resonance, and Density Functional Theory. *J. Phys. Chem. C*, **2015**, *119*, 27104-27117.

[16] García-LLinás, X.; Bauzá, A.; Seth, S. K.; Frontera, A. Importance of R-CF_3···O Tetrel Bonding Interactions in Biological Systems. *J. Phys. Chem. A.* **2017**, *121*, 5371-5376.

[17] IUPAC Project No. 2016-001-2-300. Categorizing Chalcogen, Pnictogen, and Tetrel Bonds, and other Interactions Involving Groups 14-16 Elements. https://iupac.org/project/2016-001-2-300 (Accessed December, 2020).

[18] Aakeroy, C. B.; Bryce, D. L.; Desiraju, G. R.; Frontera, A.; Legon, A. C.; Nicotra, F.; Rissanen, K.; Scheiner, S.; Terraneo, G.; Metrangolo, P.; Resnati, G. Definition of the chalcogen bond (IUPAC Recommendations 2019). *Pure Appl. Chem.* **2019**, *91*, 1890-1892.

[19] Desiraju, G. R.; Shing Ho, P.; Kloo, L.; Legon, A. C.; Marquardt, R.; Metrangolo, P.; Politzer, P.; Resnati, G.; Rissanen, K. Definition of the halogen bond (IUPAC Recommendations 2013). *Pure Appl. Chem.* **2013**, *85*, 1711-1713.

Appendix 1 Supplementary Information for Chapter 2

A1.1 Synthesis

A1.1.1 Ball-Milling

Cocrystallization of certain products was carried out by liquid assisted grinding (LAG) using a Retsch ball mill and minimal amounts of organic solvent, as indicated in **Table S1-1**. Each milling jar was charged with two steel balls, and the experiments were run with a milling frequency of 30 Hz for 30 minutes.

A1.1.2 Slow-evaporation

Theophylline citric acid hydrate (CSD KIGKAN) was produced by slow evaporation, as described previously.[1]

Theophylline *p*-coumaric acid (CSD IJEZUT) was obtained by dissolving 194.0 mg of *p*-coumaric acid in 4.0 mL of acetone and stirring 600 uL of the resulting solution with a solution of 32.7 mg theophylline dissolved in 5.0 mL of methanol.[2] The resulting mixture was left in a small vial to evaporate, producing the product's resulting crystals.

(Intentionally left blank)

Table S1-1. Details for the cocrystallization by ball-milling.

Number	Chemical Name	CSD REFCODE	Reagents	Comments	Product melting point
1	Caffeine acetic acid	VAWKOU	146.2 mg caffeine 43 ul acetic acid 4 drops of heptane	The resulting product was a fine, white powder.	110 °C
2	Caffeine 4-nitroaniline	LATGUK	193.5 mg caffeine 139.5 mg 4-nitroaniline 5 drops of methanol	A yellow powder was extracted.	162 °C
4	Caffeine formic acid (2:1)	VAWKEK	195.5 mg caffeine 50 ul formic acid	A white, flaky powder was extracted.	238 °C
5	Caffeine maleic acid	GANYEA	204.7 mg theophylline 129.8 mg maleic acid 6 drops of methanol	A grey powder was extracted and left overnight to evaporate residual solvent.	95 °C
7	Theophylline acetamide	RABXOK	200 mg theophylline 80 mg acetamide 6 drops of ethanol	A grey-white chunky powder was extracted and left to dry at ambient conditions for 1 hour.	270 °C
9	Theophylline cinnamic acid	WOCHUT	205.6 mg theophylline 163.7 mg cinnamic acid 5 drops of acetone	A white powder was extracted.	194 °C

(Intentionally left blank)

A1.2 Powder X-ray Diffraction Patterns

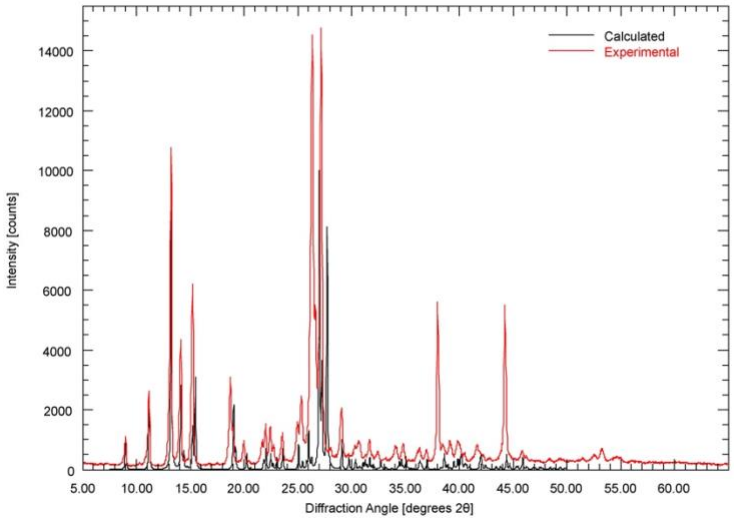

Figure S1-1. Powder X-ray diffraction pattern of caffeine maleic acid (CCDC refcode GANYEA).

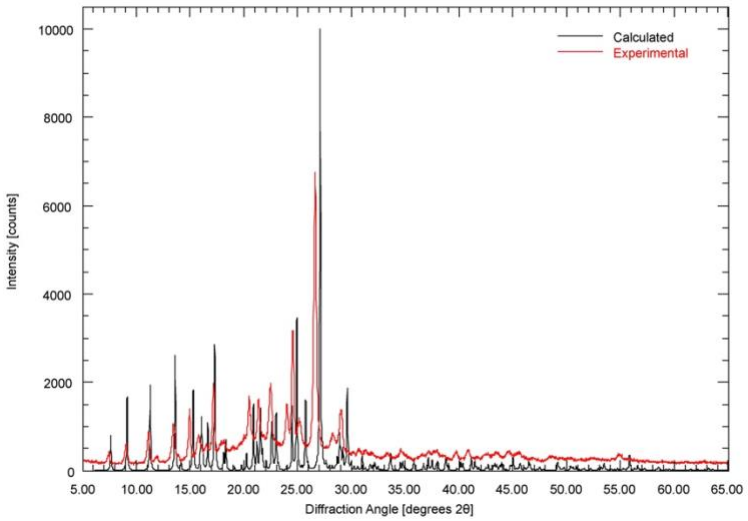

Figure S1-2. Powder X-ray diffraction pattern of caffeine.*p*-coumeric acid (CCDC refcode IJEZUT).

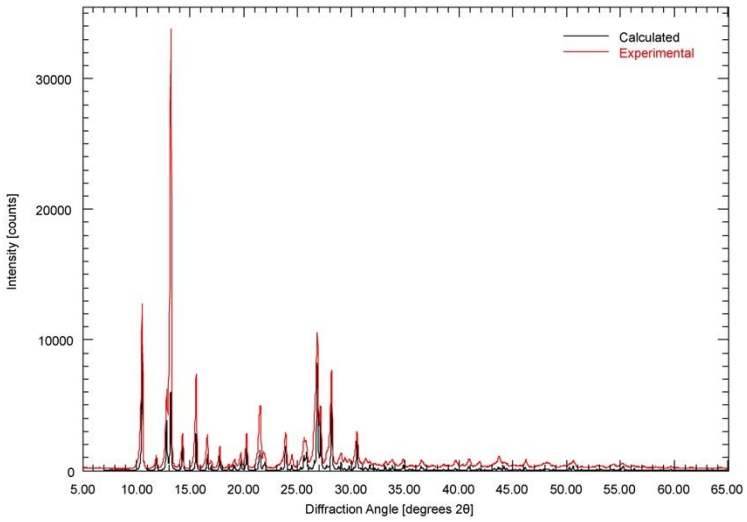

Figure S1-3. Powder X-ray diffraction pattern of caffeine 4-nitroanaline (CCDC refcode LATGUK).

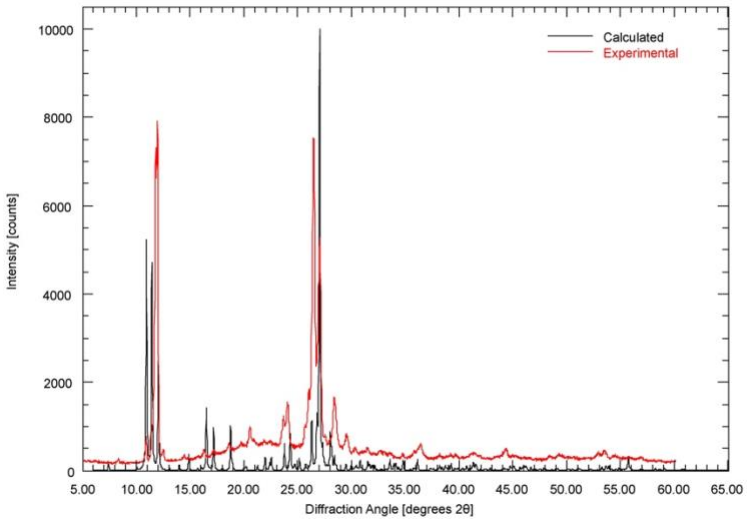

Figure S1-4. Powder X-ray diffraction pattern of caffeine acetic acid (CCDC refcode VAWKEK).

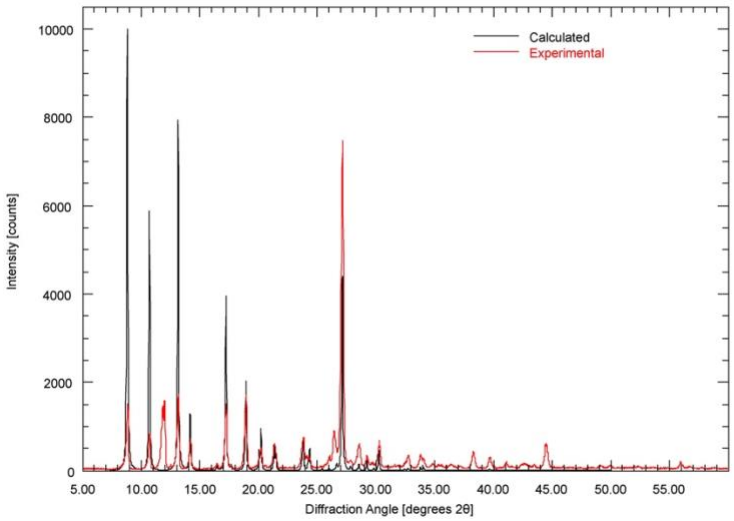

Figure S1-5. Powder X-ray diffraction pattern of caffeine formic Acid (CCDC refcode VAWKOU).

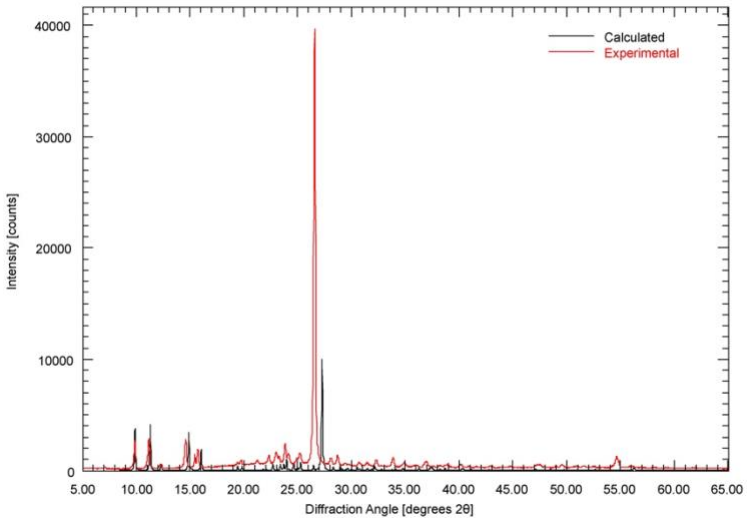

Figure S1-6. Powder X-ray diffraction pattern of theophylline acetamide (CCDC refcode RABXOK).

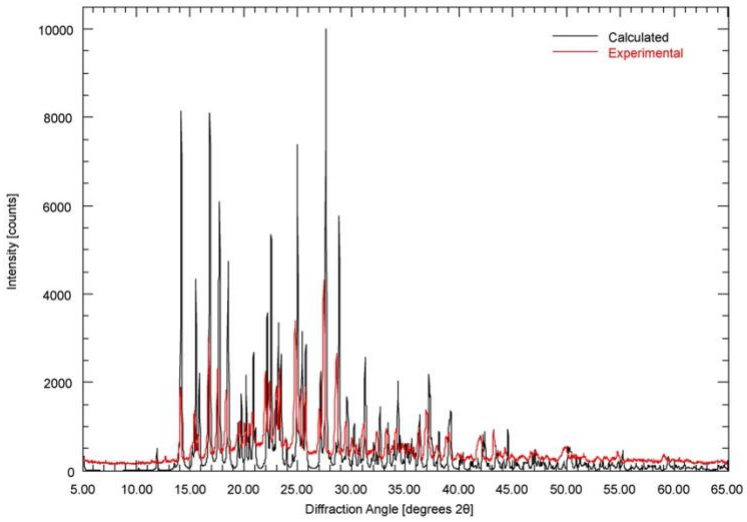

Figure S1-7. Powder X-ray diffraction pattern of theophylline citric acid hydrate (CCDC refcode KIGKAN).

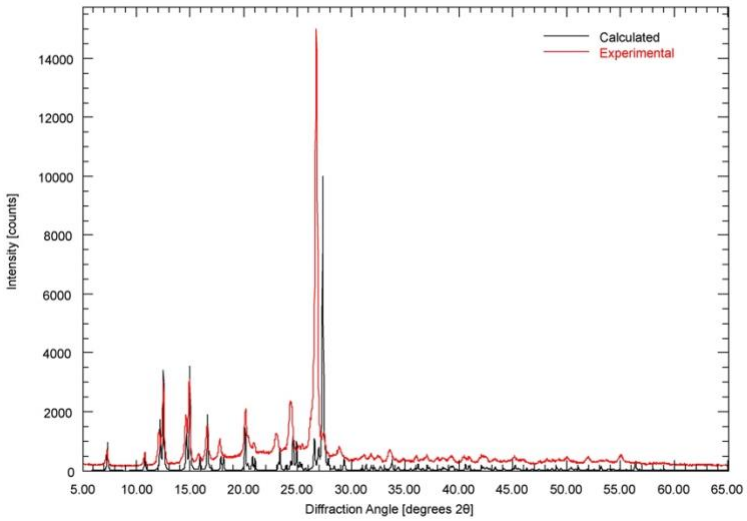

Figure S1-8. Powder X-ray diffraction pattern of theophylline cinnamic acid (CCDC refcode WOCHUT).

A1.3 CASTEP Convergence

CASTEP convergence was tested on theophylline's crystal structure by running single-point energy calculations with increasing energy cutoffs and numbers of *k*-points using the revPBE functional. The convergence was tested to a maximum force of 0.05 eV/Å. The CASTEPConv

python script was used to set up input files and extract and compile each calculation's results (see **Table S1-2**). Gnuplot was used to generate the resulting convergence graphs.

For all calculations, an energy cutoff of 700 eV was selected coupled with a minimum *k*-point spacing of 0.07 Å to balance a suitable level of convergence with computational resources.

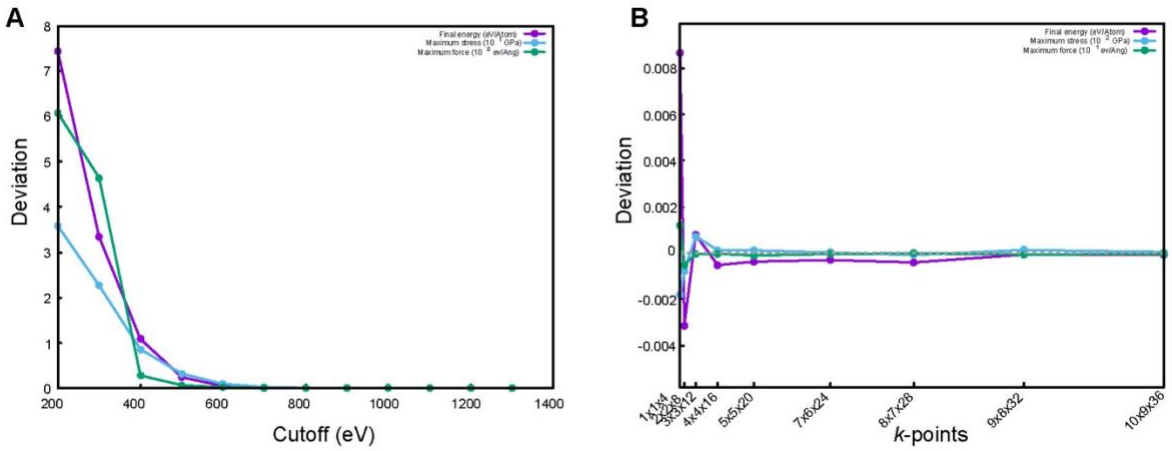

Figure S1-9. Plot of convergence of CASTEP calculation parameters for theophylline.

(space intentionally blank)

Table S1-2. Raw CASTEP energy and *k*-point cutoff calculation results obtained by CASTEPConv.

		Energy (eV)	Energy/Atom (eV)	Forces (eV/A)	Total stresses (GPa)
Cutoff (eV)	200	-12222.597	-145.50711	14.688032	59.086376
	300	-12567.177	-149.60925	13.2561639	45.923727
	400	-12756.387	-151.86174	8.89261538	31.837262
	500	-12827.161	-152.70429	8.6782444	26.495088
	600	-12843.813	-152.90254	8.63232232	24.233578
	700	-12846.955	-152.93994	8.61958311	23.546167
	800	-12847.438	-152.94569	8.61445735	23.336696
	900	-12847.517	-152.94663	8.61309148	23.276061
	1000	-12847.545	-152.94696	8.61386164	23.271949
	1100	-12847.555	-152.94709	8.61296104	23.267422
	1200	-12847.559	-152.94713	8.61302893	23.267173
	1300	-12847.562	-152.94717	8.61264444	23.266745
k-points	4	-12222.597	-145.50711	14.688032	59.086376
	32	-12223.589	-145.51891	14.670804	59.190628
	108	-12223.259	-145.51499	14.6757276	59.34062
	256	-12223.369	-145.5163	14.6757726	59.279774
	500	-12223.356	-145.51615	14.6750248	59.279928
	1008	-12223.351	-145.51608	14.6756721	59.270006
	1568	-12223.359	-145.51618	14.6759192	59.259179
	2304	-12223.331	-145.51584	14.6754774	59.28133
	3240	-12223.332	-145.51585	14.6755924	59.272879
	4400	-12223.325	-145.51578	14.6761112	59.268132

A1.4 NMR Experimental Parameters

A1.4.1 CP/MAS

Table S1-3. Key experimental solid-state CP/MAS NMR parameters used for each cocrystal (B_0 = 11.7 T)

Number	Chemical Name	CSD REFCODE	Number of Scans	90° ^{1}H Pulse Duration (μs)	Contact Pulse Duration (μs)	Recycle Delay (s)
1	Caffeine Acetic Acid	VAWKOU	512	3.35	2500	25
2	Caffeine 4-nitroaniline	LATGUK	4380	3.2	2000	5
3	Caffeine *p*-coumeric acid	IJEZUT	16	3.15	2000	3
4	Caffeine Formic Acid (2:1)	VAWKEK	828	3.2	2000	20
5	Caffeine Maleic Acid	GANYEA	1024	3.2	2000	15
6	Theophylline Citric Acid Hydrate	KIGKAN	1024	3.42	2500	20
7	Theophylline Acetamide	RABXOK	1024	3.2	2000	5
8	Theophylline (Form II)	BAPLOT06	1024	3.4	2500	25
9	Theophylline Cinnamic Acid	WOCHUT	5120	3.2	2000	20

Table S1-4. Key experimental solid-state CP/MAS NMR parameters used for each cocrystal (B_0 = 9.4 T)

Number	Chemical Name	CSD REFCODE	Number of Scans	90° ^{1}H Pulse Duration (μs)	Contact Pulse Duration (μs)	Recycle Delay (s)
1	caffeine acetic acid	VAWKOU	3072	3.0	2000	5
2	caffeine 4-nitroaniline	LATGUK	4096	3.5	2000	15
3	caffeine *p*-coumeric acid	IJEZUT	4096	3.5	2000	15
4	caffeine formic acid (2:1)	VAWKEK	4096	3.0	2000	15
5	caffeine maleic acid	GANYEA	400	3.0	2000	60
6	theophylline citric acid hydrate	KIGKAN	1080	3.5	2000	10
7	theophylline acetamide	RABXOK	1024	3.0	2000	60
8	theophylline (form ii)	BAPLOT06	256	2.75	2000	60
9	theophylline cinnamic acid	WOCHUT	300	3.0	2000	60

A1.4.2 ^{1}H-^{13}C FSLG-HETCOR

Table S1-5. Experimental solid-state FSLG-HETCOR NMR parameters used for each cocrystal.

Number	Chemical Name	CSD REFCODE	Number of Scans	Slices	Proton spin nutation frequency / Hz	90° ^{1}H Pulse Duration / µs	Contact Pulse Duration / µs	Recycle Delay / s
1	caffeine acetic acid	VAWKOU	64	42	74074	3.35	50	20
2	caffeine 4-nitroaniline	LATGUK	1024	32	119048	3.15	150	15
3	caffeine *p*-coumeric acid	IJEXUT	256	32	119048	3.15	50	5
4	caffeine formic acid (2:1)	VAWKEK	64	64	119048	3.15	150	15
5	caffeine maleic acid	GANYEA	64	128	119048	3.15	150	30
6	theophylline citric acid hydrate	KIGKAN	256	64	119048	3.15	150	4
7	theophylline acetamide	RABXOK	64	42	74074	3.43	50	20
8	theophylline (form ii)	BAPLOT06	64	42	74074	3.4	50	20
9	theophylline cinnamic acid	WOCHUT	64	42	74074	3.5	50	25

A1.4.3 Two-dimensional ^{1}H-^{13}C FSLG heteronuclear correlation (HETCOR) spectra.

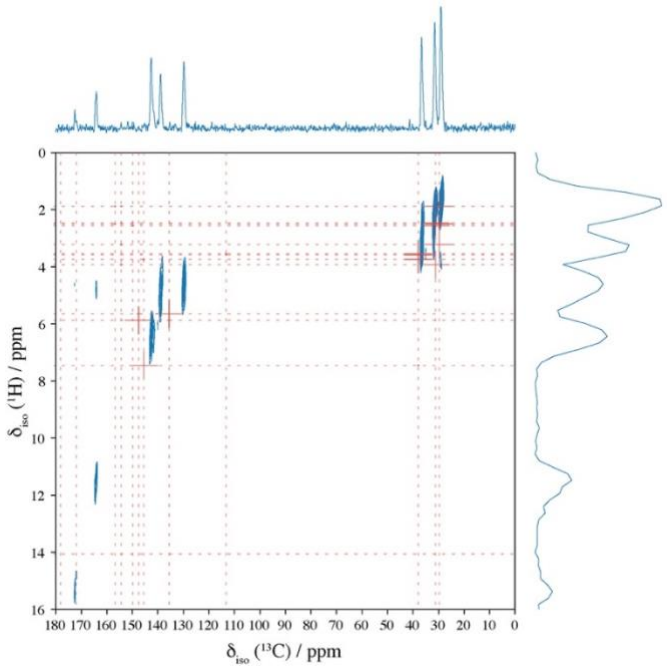

Figure S1-10. Caffeine maleic acid (CCDC refcode GANYEA).

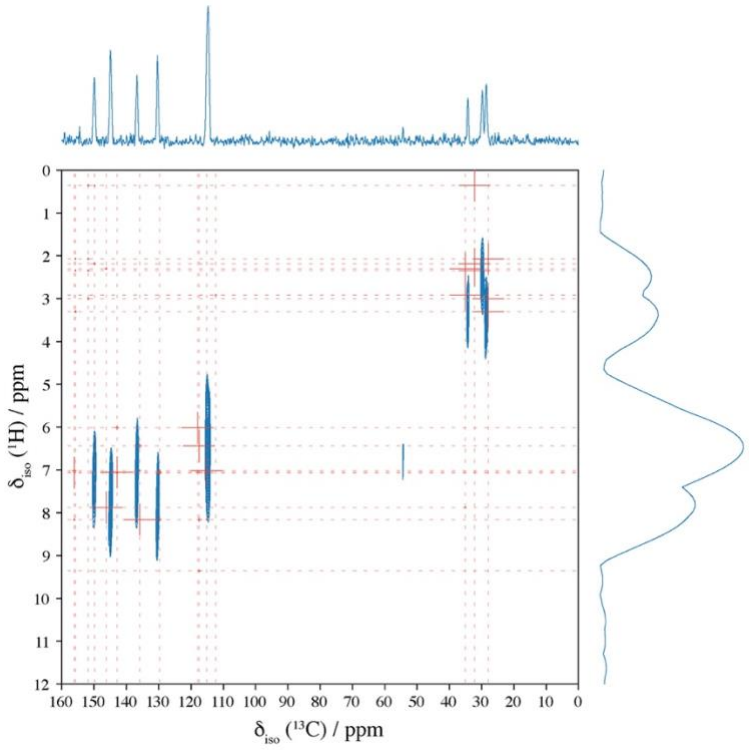

Figure S1-11. Caffeine.*p*-coumeric acid (CCDC refcode IJEZUT).

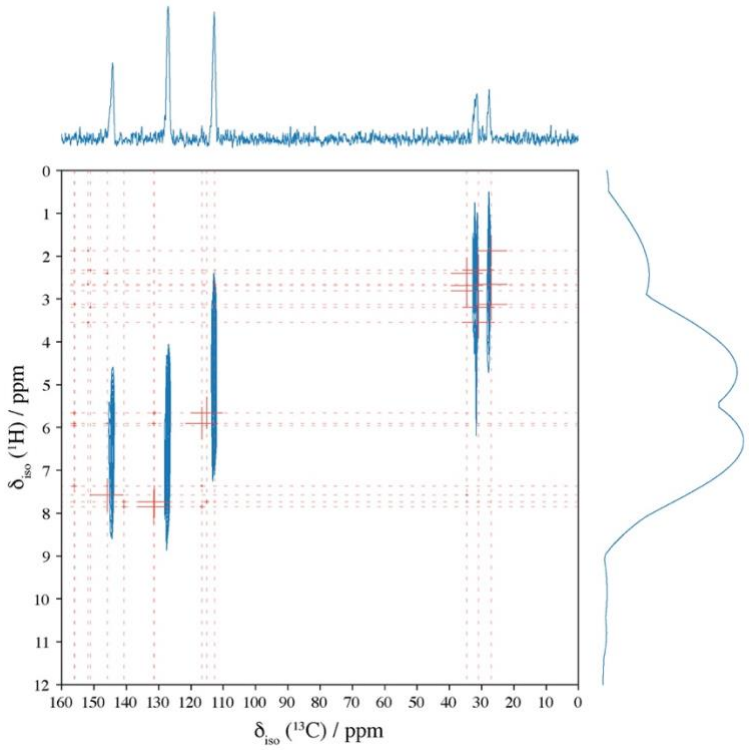

Figure S1-12. Caffeine 4-nitroanaline (CCDC refcode LATGUK).

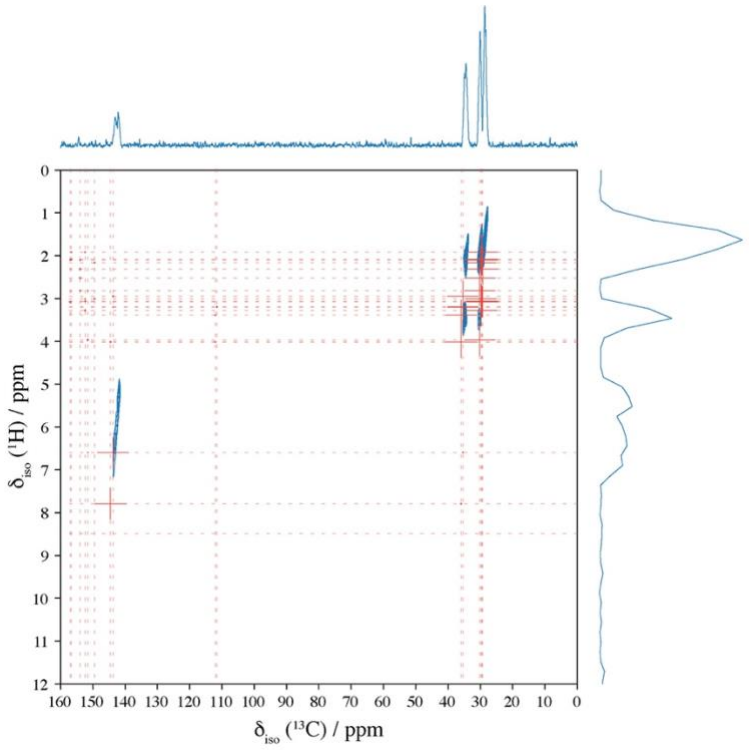

Figure S1-13. Caffeine formic acid (CCDC refcode VAWKEK).

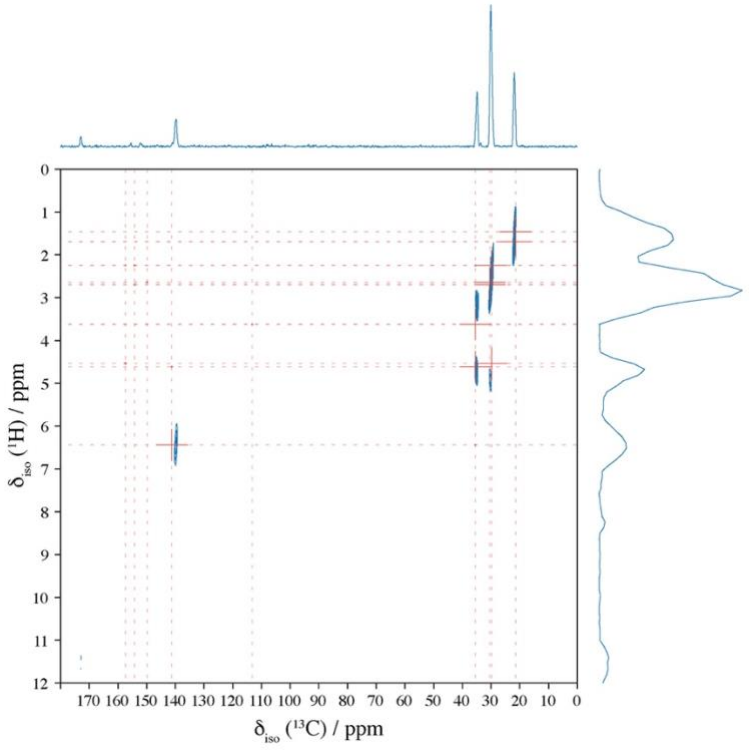

Figure S1-14. Caffeine formic acid (CCDC refcode VAWKOU).

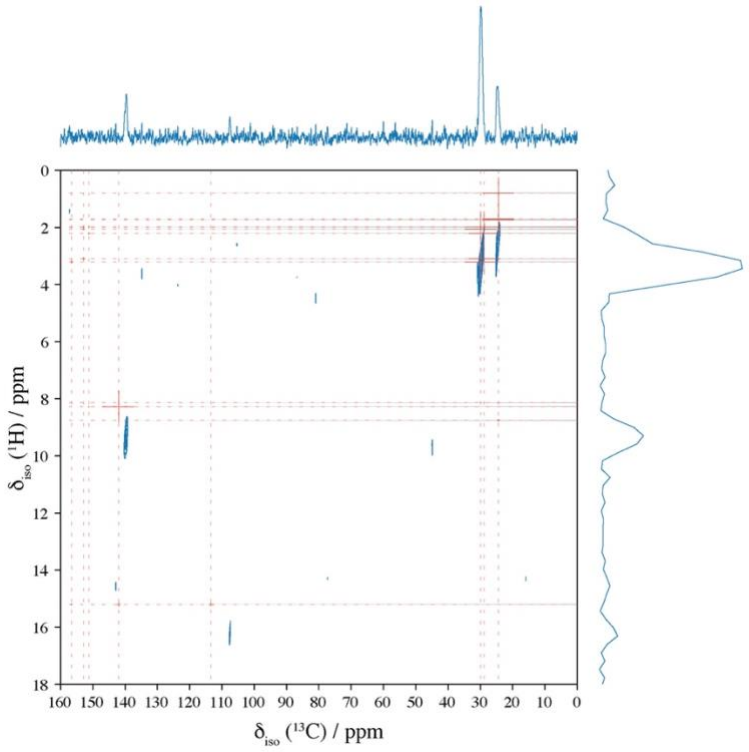

Figure S1-15. Theophylline acetamide (CCDC refcode RABXOK).

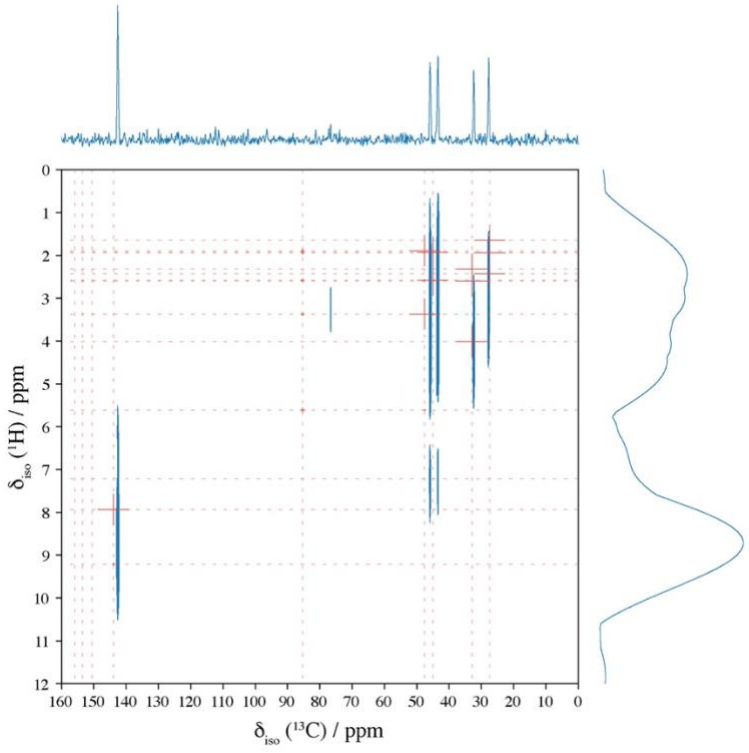

Figure S1-16. Theophylline citric acid hydrate (CCDC refcode KIGKAN).

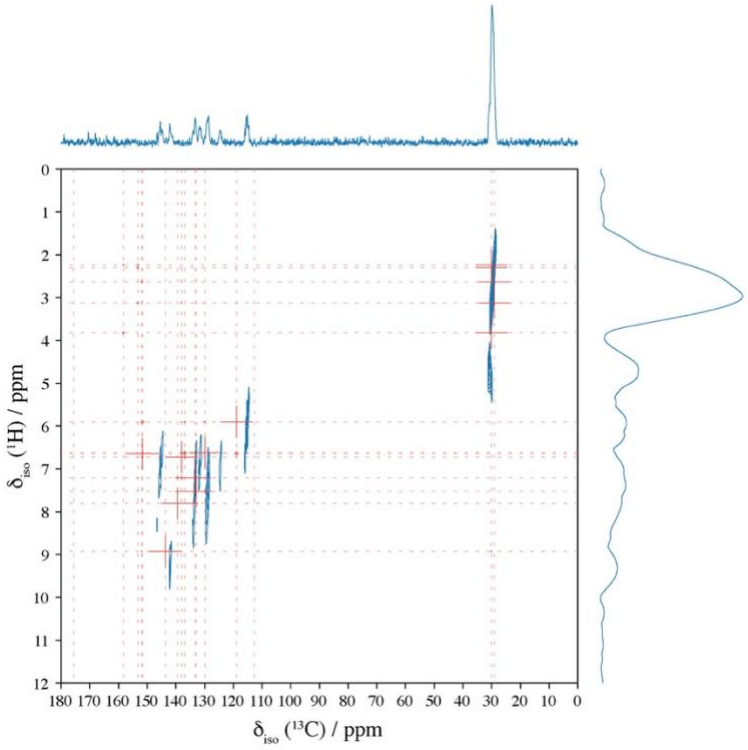

Figure S1-17. Theophylline cinnamic acid (CCDC refcode WOCHUT).

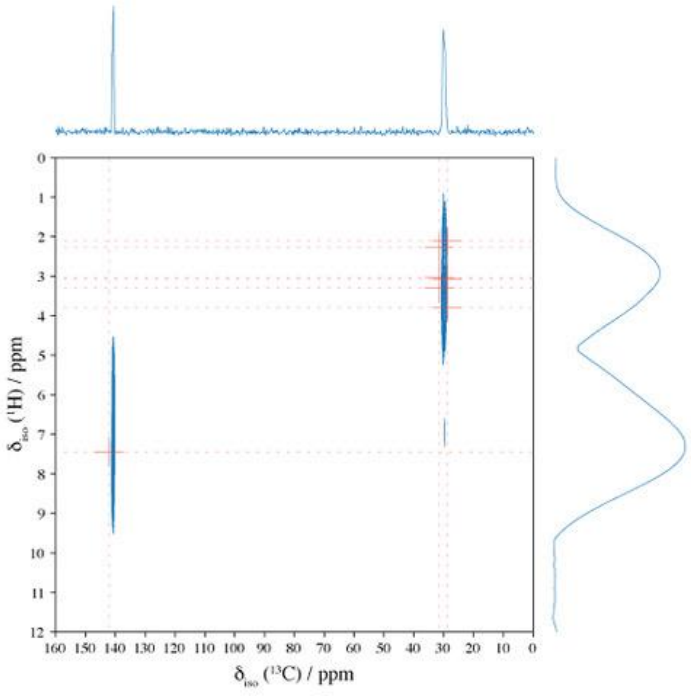

Figure S1-18. Theophylline (CCDC refcode BAPLOT06).

A1.5 Supplemental Data Figures for Chapter 2.

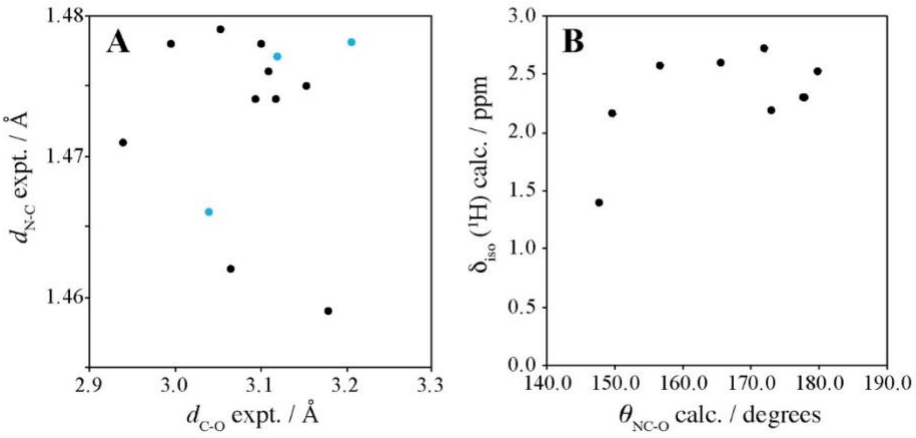

Figure S1-19. Comparison between the experimental TB length and (**A**) the NC-O amine bond length, and (**B**) comparison between the experimental ^{1}H chemical shifts and calculated TB angles. In panel **A** the blue circles correspond to the data for caffeine malonic acid and caffeine glutaric acid.

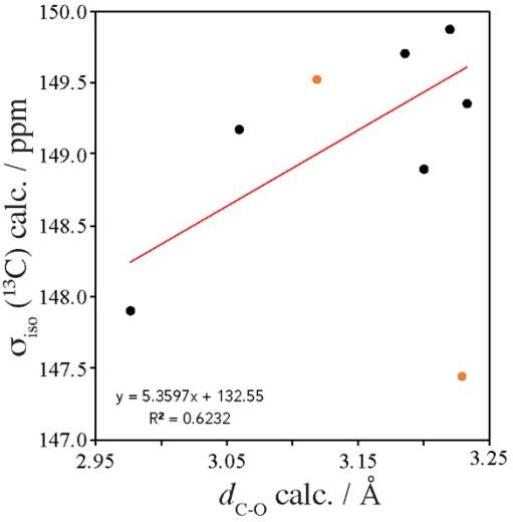

Figure S1-20. Plot of the calculated isotropic shielding constant versus the tetrel bond length from geometry optimized crystal structures. The orange circles represent structures where the tetrel bond angle lies below 160°. The fitting is based solely on tetrel bonds where the angle is between 160° and 180° (black circles).

A1.6 References

[1] Karki, S.; Friščić, T.; Jones, W.; Motherwell, W.D.S. Screening for Pharmaceutical Cocrystal Hydrates via Neat and Liquid-Assisted Grinding. *Mol. Pharmaceutics*, **2007**, *4*, 347-354.

[2] Schultheiss, N.; Roe, M.; Boerrigter, S. X. M. Cocrystals Of Nutraceutical p-Coumaric Acid With Caffeine And Theophylline: Polymorphism And Solid-State Stability Explored In Detail Using Their Crystal Graphs. *CrystEngComm*, **2011**, *13*, 611-619.

Appendix 2 Supplementary Information for Chapter 3

Table S2-1. Minimum and maximum computed electrostatic potential values (a.u.)

compound	minimum electrostatic potential	maximum electrostatic potential
1	-0.0814	0.130
2	-0.0746	0.129
3	-0.0732	0.117
4	-0.0555	0.120
5	-0.0821	0.122

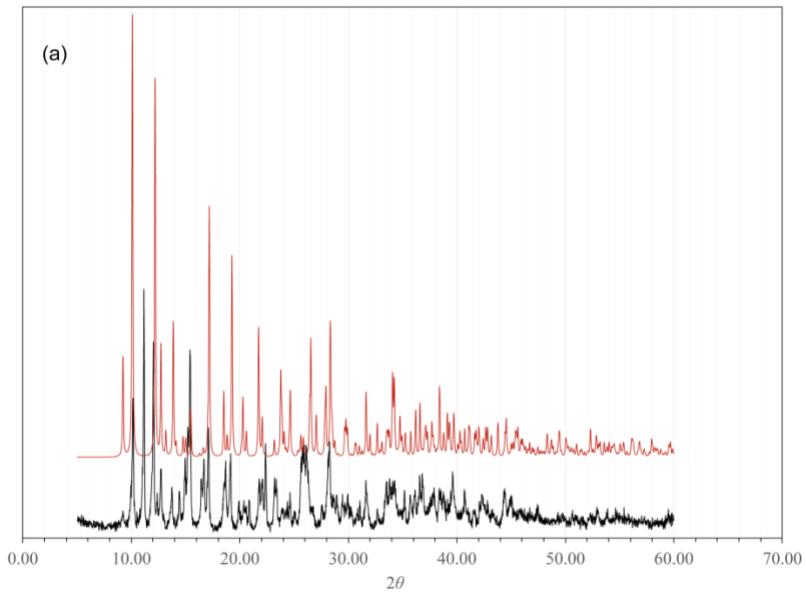

Figure S2-1. Powder X-Ray diffractogram for **1**. The calculated pattern (red) obtained from Mercury is offset above the experimental data (black). The origins of additional reflections are addressed in Chapter 3.

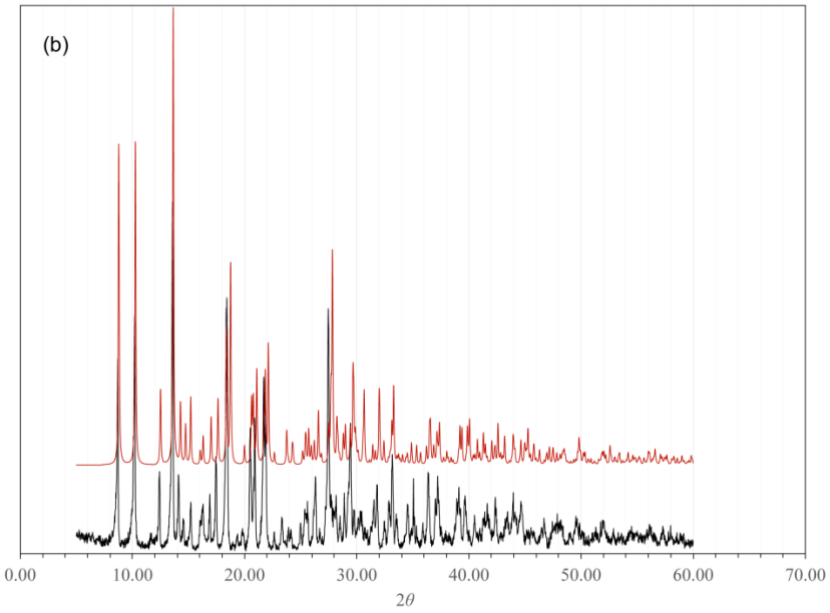

Figure S2-2. Powder X-Ray diffractogram for **3**. The calculated pattern (red) obtained from Mercury is offset above the experimental data (black). The presence of additional peaks of low intensity is attributed to residual lead thiocyanate.

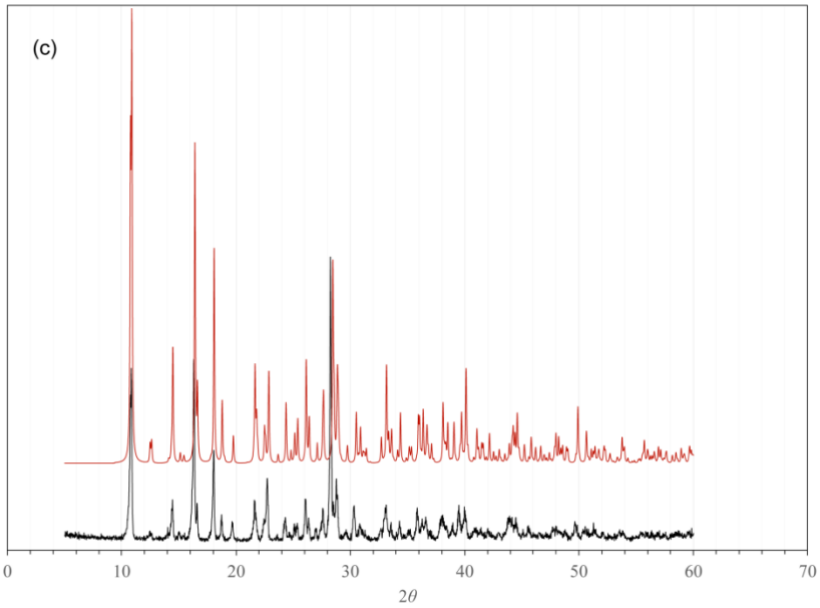

Figure S2-3. Powder X-Ray diffractogram for **2**. The calculated pattern (red) obtained from Mercury is offset above the experimental data (black).

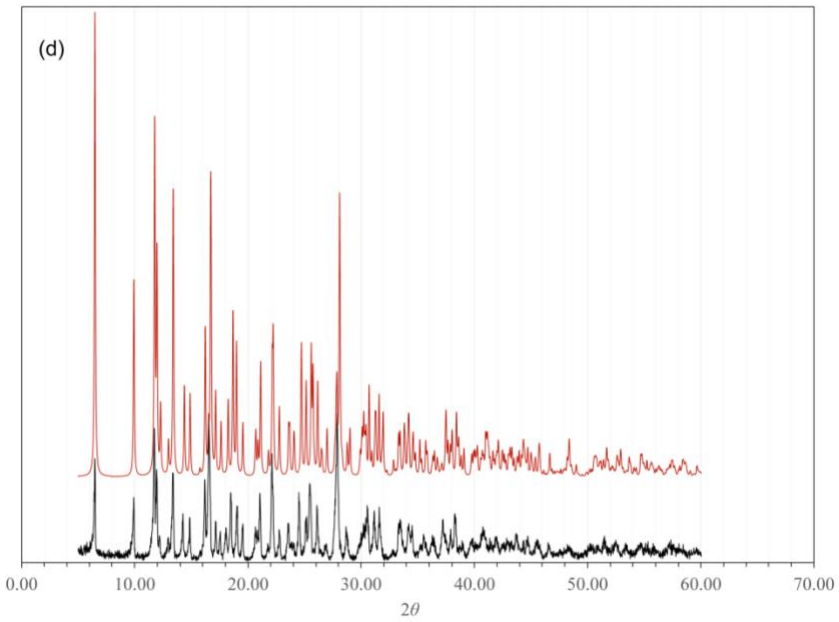

Figure S2-4. Powder X-Ray diffractogram for **4**. The calculated pattern (red) obtained from Mercury is offset above the experimental data (black).

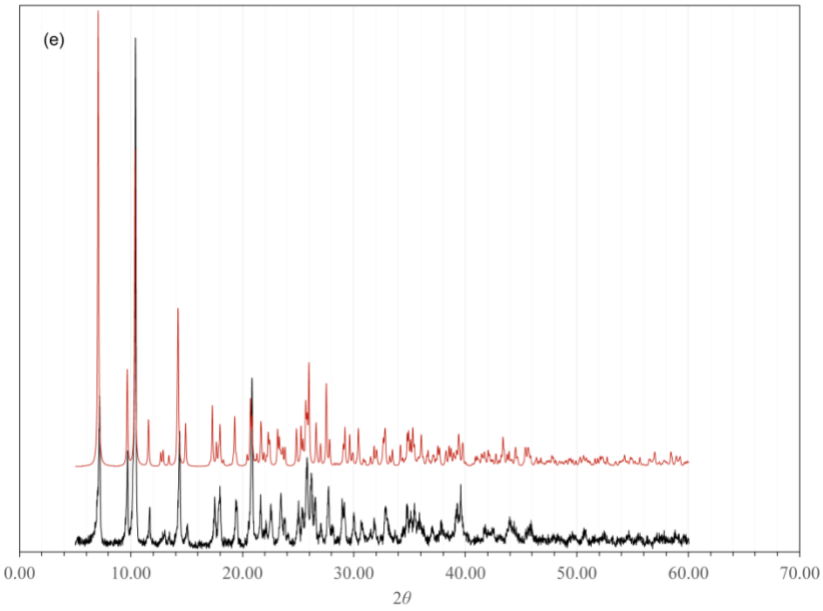

Figure S2-5. Powder X-Ray diffractogram for **5**. The calculated pattern (red) obtained from Mercury is offset above the experimental data (black).

Appendix 3 An Excerpt from the Published Record of the Oral Discussion held on the Subject of Chapter 3 at the Faraday Discussion on Halogen Bonding in Supramolecular Chemistry, 2017

A3.1 Permissions

C. B. Aakeröy, S. Alavi, P. D. Beer, N. K. Beyeh, L. Brammer, D. L. Bryce, T. Clark, S. J. Cottrell, J. E. Del Bene, A. J. Edwards, C. Esterhuysen, T. Friščić, T. N. Guru Row, P. Kennepohl, G. O. Lloyd, A. Roy Choudhury, S. Scheiner, S. A. Southern, M. S. Taylor, S. Tsuzuki and I. Vargas-Baca, *Faraday Discuss.*, **2017**, *203*, 227-244. **DOI:** 10.1039/C7FD90062G

Faraday Discussions

Cite this: *Faraday Discuss.*, 2017, **203**, 227

DISCUSSIONS

View Article Online
View Journal | View Issue

Beyond the halogen bond: general discussion

Christer B. Aakeröy, Saman Alavi, Paul D. Beer, Ngong Kodiah Beyeh, Lee Brammer, David L. Bryce, Timothy Clark, Simon J. Cottrell, Janet E. Del Bene, Alison J. Edwards, Catharine Esterhuysen, Tomislav Friščić, Tayur N. Guru Row, Pierre Kennepohl, Gareth O. Lloyd, Angshuman Roy Choudhury, Steve Scheiner, Scott A. Southern, Mark S. Taylor, Seiji Tsuzuki and Ignacio Vargas-Baca

DOI: 10.1039/C7FD90062G

Alison Edwards opened a general discussion of the paper by Scott Southern: Do you observe a variation in the resolution of the spectra depending on the extent of crystallinity of your materials? Is amorphous material less well resolved? Do peaks in the pattern resolve as a function of MAS spinning speed and/or temperature?

Scott Southern and **David Bryce** answered: To date we have only investigated the crystalline materials described in our paper. More generally, amorphous materials give broader NMR peaks than do crystalline materials. With regards to resolving different peaks, yes, as noted in our paper, in one case (compound **1**) multiple spinning rates were required to clearly identify the presence of an impurity phase.

Alison Edwards addressed Scott Southern and David Bryce: Do you see significant variation in the chemical shift anisotropy envelope as a function of temperature? Is the envelope well averaged *via* magic angle spinning?

Scott Southern and **David Bryce** answered: Our experiments were conducted at room temperature and we have not explored the temperature dependence of the chemical shift tensors for these particular compounds. Generally, ^{207}Pb NMR frequencies are known to be temperature dependent. The powder patterns are averaged by magic angle spinning as shown in our paper.

Alison Edwards addressed Scott Southern and David Bryce: I wish to suggest a different approach to the temperature selection for your experiments. Where you have a highly crystalline sample, different peaks in the solid state NMR are fully averaged/sharpened (chemical shift anisotropic is suppressed), for a particular speed of magic angle spinning, at different temperatures. How have you chosen the

temperature for your measurements? Have you considered choosing the temperature at which the peaks of interest are sharpest? If you wish to use a fixed temperature would varying the magic angle spinning speed offer improvement in the data? I acknowledge the difficulty in using the chemical shift anisotropy data (unsuppressed), but there is potentially information in the tensors, have you considered whether this may be useful?

Scott Southern and **David Bryce** responded: The temperature of the experiment was ambient room temperature, with some heat added due to the friction with air caused by magic angle spinning. The temperature-dependent chemical shift scale was calibrated using the resonance of lead nitrate. The line width of the static powder pattern may be slightly affected if experiments were carried out at different temperatures, due to the temperature-dependence of the principal components of the lead chemical shift tensor. The line width of the individual spinning sidebands depends more on the sample crystallinity and the proton decoupling efficiency. With regards to using the information available from the complete chemical shift tensors, this is actually central to our paper, where we have used the span and skew, along with the isotropic chemical shift, to differentiate between hemidirected and holodirected species, and to detect the influence of the tetrel bond.

Steve Scheiner remarked: The whole hemidirectional thing is interesting. Why do the groups all cluster on one side? Is this unique to lead or does it happen for other elements too?

Scott Southern replied: The reason the ligands prefer to adopt the hemidirected form is because the lone pair on the Pb(II) atom is stereochemically active. The holodirected geometry tends to occur as the number of ligands increases, and results from steric crowding around the Pb(II) atom. At this point, the lone pair is no longer sterically active and is delocalized about the Pb(II) atom. This behaviour is unique to Pb(II), and not Pb(IV). Similar bonding environments have been observed for Zn(II) cations.[1] This is discussed further in response to Saman Alavi's question related to the positioning of the lone pair and its effect on the positioning of the two ligands, and in the references therein.

1 G. Vanthomme, S. Jiang and J.-M. Lehn, *J. Am. Chem. Soc.*, 2014, **136**, 9509–9518.

Lee Brammer commented: Related to Steve Scheiner's question – for Pb(II), is not the hemidirectional coordination due to the lone pair on Pb? What role does the lone pair play? Can the lead centre act as a Lewis base? Are the interactions you are looking at actually sigma-hole interactions?

Scott Southern replied: The hemidirected coordination is indeed due to the steric activity of the lone pair of electrons. The lead centre can indeed act as a hydrogen bond acceptor.[1] In our frameworks, however, while the lone pair has steric activity, the tetrel bonds form around this area of electron density. As these tetrel bonds form, the lone pair begins to adopt a more delocalized behaviour around the Pb(II) atom and is no longer sterically active.

The sigma-hole is a good model for conceptualizing these weak non-covalent interactions. That being said, it is possible that a localized sigma-hole is not

necessarily present; rather, a broader area of depleted electrostatic potential relative to the surrounding areas exists, which may not be best described as a localized sigma-hole. At this area, on the surface of the molecule, interactions may still occur, but "sigma-hole" may not be for the most precise term for describing the region of interaction.

1 G. Vanthomme, S. Jiang and J.-M. Lehn, *J. Am. Chem. Soc.*, 2014, **136**, 9509–9518.

Lee Brammer asked: Can you learn anything about the lone pair, do you get any information related to the electrons, such as coupling information, from your NMR data? You may learn more about the interactions with lead centre *via* the proposed experiments that you mentioned involving ^{15}N–^{203}Pb coupling. Have you thought about looking at a more conventional Pb(IV) tetracoordinated species rather than Pb(II)?

Scott Southern replied: Our NMR data has been obtained in the solid state. We performed each experiment at natural abundance of the NMR observable isotope of ^{207}Pb (n.a. ^{207}Pb = 22.1%). We did not observe *J* coupling because the tetrel bonded ligands were also at natural abundance (n.a. ^{15}N = 0.4%; ^{17}O = 0.04%). In order to observe coupling, isotopically enriched samples would likely need to be used. We have not looked at Pb(IV) species, as they are not known to exhibit hemidirected coordination geometry, which suggests that tetrel bonds in such species are not possible.

Tomislav Friščić added: Following up from Lee Brammer's comment – is there any chance you could make the oxidised materials with Pb(IV)? Sigma-holes should be more significant for compounds such as tetraphenyl lead – is there any evidence of tetrel bonding in that system?

Scott Southern answered: We have not explored oxidizing these materials into Pb(IV) to this date. Tetrel bonding of Pb(IV) has not been explored because Pb(IV) is not known to adopt the hemidirected coordination like Pb(II), typically necessary for tetrel bonding. In the case of tetraphenyl lead, a quick search of the Cambridge Crystallographic Database did not yield any structures with short contacts at the Pb(IV) centre which would predict tetrel bonding. However, it is perhaps possible that if one of the phenyl rings is either loaded with or replaced by good electron withdrawing groups, perhaps a sigma-hole could form on Pb(IV) in a similar way that it forms on a methyl carbon. One structure in particular (trimethyl-lead-diazo-ethylacetate; CCDC REFCODE MEPBAZ)[1] was found to exhibit a close contact between lead and oxygen at an angle of 175° and a distance of 3.05 Å. This could be good starting point for us to investigate lead tetrel bonding in systems featuring tetrahedral geometries using solid state NMR, similar to our previous work on ^{13}C tetrel bonding.[2]

1 M. Birkhahn, E. Glozbach, W. Massa and J. Lorberth, *J. Organomet. Chem.*, 1980, **192**, 171–176.
2 S. A. Southern and D. L Bryce, *J. Phys. Chem. A*, 2015, **119**, 11891–11899.

Pierre Kennepohl commented: With respect to the large chemical shift anisotropies that are observed, is there any information regarding the direction of

the tensor and whether this can provide any additional information regarding the bonding in these systems?

Scott Southern responded: To date, we have not yet examined the orientation of the chemical shift (CS) tensor and its relation to the Pb(II) bonding environment. While we can in some cases use symmetry elements to predict the orientations of the CS tensor components, first principles calculations are more generally used to provide the orientations with respect to the molecular frame, but for the reasons discussed in our paper, more reliable DFT data would greatly improve the quality of these predictions. Time-consuming single-crystal NMR experiments can also provide the experimental tensor orientations. When available, the orientation of the CS tensor components will indeed be useful for interpreting the NMR spectra in the context of the bonding environment around the Pb(II) centres, as well as the nature of the lone pair, as studied in comparable Pb(II) species.[1–4]

1 G. G. Briand, A. D. Smith, G. Schatte, A. J. Rossini and R. W. Schurko, *Inorg. Chem.*, 2007, **46**, 8625–8637.
2 A. J. Rossini, A. W. Macgregor, A. S. Smith, G. Schatte, R. W. Schurko and G. G. Briand, *Dalton Trans.*, 2013, **42**, 9533–9546.
3 M. J. Katz, V. K. Michaelis, P. M. Aguiar, R. Yson, H. Lu, H. Kaluarachchi, R. J. Batchelor, G. Schreckenbach, S. Kroeker, H. H. Patterson and D. B. Leznoff, *Inorg. Chem.*, 2008, **47**, 6353–6363.
4 B. J. Greer, V. K. Michaelis, M. J. Katz, D. B. Leznoff, G. Schreckenbach and S. Kroeker, *Chem. Eur. J.*, 2011, **17**, 3609–3618.

Saman Alavi asked: In the Pb(**L1**)$(X)_2$ complexes, taking the label "hemidirected" somewhat literally, are the X ligands distributed within a range of angles? How do their thermal ellipsoids look? How do the distribution of the X ligands differ among the different Pb(**L1**)$(X)_2$ complexes?

Scott Southern responded: The angles of the tetrel bonded ligands are described in the paper. In each case, the angles are similar to one another. Furthermore, the thermal ellipsoids produced by the crystallography are quite restrained, indicating that the determined locations of the ligands are quite precise. For further information we invite the reader to refer to our paper.

Saman Alavi asked: Within the structure and the placement of the ligands in the Pb(**L1**)$(X)_2$ complexes, can you estimate where the lone pair would be and how it affects the positioning of the two X ligands?

Scott Southern answered: This question can be answered by delving into the literature about the nature of the 6s6p lone pair on Pb(II). Interestingly, there exists three geometries around Pb(II): hemidirected, holodirected, and bisdirected, and in each case, the versatile lone pair adopts a different arrangement. In the hemidirected case, the ligands assemble themselves on only one side of the Pb(II) atom, whilst the lone pair forms a sterically active orbital directly opposite the ligand on the other hemisphere.[1] In the case of holodirected coordination, the ligands tend to form a spherical arrangement, while the Pb(II) 6s6p lone pair loses its stereoactivity due to steric effects resulting from the ligands. Finally, in the

bisdirected case, the lone pair is split between both hemispheres of the Pb(II) centre due to the ligands adopting an annular arrangement.[2,3]

In our paper, five species exist whereby a Pb(II) atom is coordinated five-fold by a planar nicotynyl hydrazine ligand, and by two molecules above and below the plane of the ligand (NO_3^-, SCN^-, Cl^-). Each of these cases represents a hemi-directed Pb(II) environment where the lone pair of electrons is predicted to be sterically active, and directly opposite the ligand, and sharing its plane. As a result, the lone pair is placed directly in between the two areas where a tetrel bond may occur on the extension of the N–Pb(II) or O–Pb(II) coordination bonds.

1 E. D. Hancock, J. H. Reibenspies and H. Maumela, *Inorg. Chem.*, 2004, **43**, 2981–2987.
2 M.-C. van Severen, J.-P. Piquemal and O. Parisel, *Chem. Phys. Lett.*, 2009, **478**, 17–19.
3 M.-C. van Severen, Y. Ryde, O. Parisel and J.-P. Piquemal, *J. Chem. Theor. Comput.*, 2013, **9**, 2416–2424.

David Bryce opened a general discussion of the paper by Ignacio Vargas-Baca: In the first session, there was a lot of discussion about the terminology used in describing halogen bonds and related interactions. In your paper you stated that "sigma-hole bonding is a particular case of the Lewis acid–base concept". Can you expand on this statement? What are the similarities and differences, if any, between these two concepts?

Ignacio Vargas-Baca replied: In the Lewis acid–base concept, two chemical species have affinity for each other due to the attractive interaction of a pair of electrons with an electrophilic centre, just as in the interactions we have been discussing here. In the simple case of a very strong Lewis acid–base interaction such as the addition of F^- to BF_3, the result is a significant structural distortion and the formation of a B–F bond that is indistinguishable from the other three. In cases of halogen bonding and the related interactions centred on p-block elements, the interactions are so much weaker that the constituting molecular units display small structural distortions and, consequently, are readily identified. In truth, there is a continuum between the two extremes for which there are well-characterized examples (see for instance the paper by M. Fourmigué *et al.*).[1] In the case presented in our article, the adducts of Lewis bases with **1**-BF_3 display a wide range of Te–N distances. There are cases, such as the adduct of the N-heterocyclic carbene, in which the roles of the Te–N bond in the heterocycle and the Te–B_{Lewis} are swapped.

1 E. Aubert, E. Espinosa, I. Nicolas, O. Jeannin and M. Fourmigué, *Faraday Discuss.*, 2017, DOI: 10.1039/C7FD00067G.

Paul Beer asked: Do you have solution Te NMR evidence for the cyclic oligomers?

Ignacio Vargas-Baca replied: We do use ^{125}Te NMR to characterise these systems. However, their spectra are not always observable due to low solubility. In the case of compound **1**, the VT experiments permitted monitoring the equilibrium $\mathbf{1}_4 \rightleftharpoons \mathbf{1}_6$. The details are described in ref. 1.

1 P. C. Ho, P. Szydlowski, J. Sinclair, P. J. W. Elder, J. Kübel, C. Gendy, L. M. Lee, H. Jenkins, J. F. Britten, D. R. Morim and I. Vargas-Baca, *Nat. Commun.*, 2016, **7**, 11299.

Appendix 4 Sample Input Files for Quantum Chemical Calculations

A4.1 Gaussian 09 input file for geometry optimization with the generation of a *Formcheck* file to obtain MESP diagrams

```
%nprocshared=4
%mem=200MB
%chk=silicon.chk
# opt freq b3lyp/6-31g(d,p) geom=connectivity formcheck

Tetrahedral Silicon Tetrel Bond

1 1
 N                  0.47176187   -0.09171326   -1.20048906
 H                  0.13694817    0.85057064   -1.20140399
 H                  1.47176022   -0.09014192   -1.19957546
 H                  0.13991633   -0.56416833   -2.01698446
 Si                -0.15158225   -0.97323159    0.32635983
 H                  0.33623136   -0.27872264    1.52660781
 H                 -1.62157982   -0.97554108    0.32501653
 H                  0.34059347   -2.35838907    0.32770483

 1 2 1.0 3 1.0 4 1.0 5 1.0
 2
 3
 4
 5 6 1.0 7 1.0 8 1.0
 6
 7
 8
```

A4.2 ADF input script for a geometry optimization for a molecular model of a tetrel-bonded Pb(II) isonicotinoyl hydrazone structure

```
#!/bin/bash
#$ -N AA00006.run
#$ -S /bin/bash
#$ -q abaqus.q
#$ -l qname=abaqus.q
#$ -M (intentionally removed)

#$ -m be
#$ -o AA00006.out
#$ -e AA00006.err
#$ -cwd
#$ -V
#$ -pe shm.pe 8

$ADFBIN/adf -n $NSLOTS << eor
Title AA000023

Basis
 Core None
 Pb $ADFRESOURCES/ZORA/TZ2P/Pb
 N $ADFRESOURCES/ZORA/TZ2P/N
 O $ADFRESOURCES/ZORA/TZ2P/O
 H $ADFRESOURCES/ZORA/TZ2P/H
 C $ADFRESOURCES/ZORA/TZ2P/C
 S $ADFRESOURCES/ZORA/TZ2P/S
End

SAVE TAPE10

relativistic spinorbit zora

ATOMS
1 S      -7.473300000000       8.607000000000       9.330000000000
2 O      -4.716800000000      11.075800000000       9.463900000000
3 C      -3.663600000000       7.477400000000      10.601000000000
4 C      -4.011600000000       6.342800000000       9.710400000000
5 C      -3.767400000000       5.034300000000      10.098100000000
6 H      -3.314900000000       4.841400000000      10.910700000000
7 C      -4.203800000000       4.011600000000       9.260700000000
8 H      -4.060500000000       3.104200000000       9.504800000000
9 C      -4.839000000000       4.311200000000       8.090100000000
10 H      -5.156600000000       3.625900000000       7.514100000000
11 C      -5.004100000000       5.643800000000       7.770500000000
12 H      -5.426500000000       5.855500000000       6.946800000000
13 C      -4.161499998000      10.853700000000      10.593600000000
14 C      -3.913000000000      12.021000000000      11.485500000000
15 C      -3.225400000000      11.881500000000      12.679600000000
16 H      -2.945600000000      11.024100000000      12.981900000000
```

17	C	-2.955800000000	13.016100000000	13.420400000000
18	H	-2.486500000000	12.912800000000	14.240400000000
19	C	-4.000200000000	14.365900000000	11.914100000000
20	H	-4.292500000000	15.230200000000	11.647800000000
21	C	-4.307600000000	13.289900000000	11.095300000000
22	H	-4.781200000000	13.420700000000	10.281500000000
23	C	-2.925800000000	7.250100000000	11.869500000000
24	H	-2.809500000000	8.104100000000	12.336500000000
25	H	-2.047200000000	6.864500000000	11.672500000000
26	H	-3.434400000000	6.633700000000	12.436800000000
27	C	-8.540200000000	9.101000000000	8.158300000000
28	N	-3.770300000000	9.689800000000	11.078000000000
29	N	-4.060200000000	8.655000000000	10.215800000000
30	N	-4.605400000000	6.657900000000	8.553400000000
31	N	-3.315900000000	14.255800000000	13.055000000000
32	N	-9.307100000000	9.428100000000	7.371700000000
33	N	-6.147600000000	11.569900000000	6.861300000000
34	O	-7.548400000000	14.749900000000	3.270200000000
35	C	-6.495200000000	18.348300000000	4.407400000000
36	C	-6.843200000000	19.482900000000	3.516800000000
37	C	-6.599100000000	20.791400000000	3.904500000000
38	H	-6.146500000000	20.984200000000	4.717100000000
39	C	-7.035400000000	21.814100000000	3.067100000000
40	H	-6.892200000000	22.721400000000	3.311100000000
41	C	-7.670700000000	21.514500000000	1.896500000000
42	H	-7.988200000000	22.199700000000	1.320500000000
43	C	-7.835800000000	20.181900000000	1.576900000000
44	H	-8.258200000000	19.970100000000	0.753100000000
45	C	-6.993200000000	14.972000000000	4.400000000000
46	C	-6.744600000000	13.804700000000	5.291900000000
47	C	-6.057100000000	13.944100000000	6.486000000000
48	H	-5.777300000000	14.801500000000	6.788200000000
49	C	-5.787500000000	12.809500000000	7.226700000000
50	H	-5.318100000000	12.912800000000	8.046800000000
51	C	-6.831900000000	11.459700000000	5.720500000000
52	H	-7.124100000000	10.595400000000	5.454100000000
53	C	-7.139300000000	12.535800000000	4.901700000000
54	H	-7.612800000000	12.404900000000	4.087800000000
55	C	-5.757500000000	18.575500000000	5.675900000000
56	H	-5.641200000000	17.721600000000	6.142900000000
57	H	-4.878900000000	18.961200000000	5.478900000000
58	H	-6.266000000000	19.191900000000	6.243200000000
59	N	-6.602000000000	16.135900000000	4.884300000000
60	N	-6.891900000000	17.170600000000	4.022200000000
61	N	-7.437000000000	19.167800000000	2.359800000000
62	H	-9.321000000000	0.964700000000	6.618400000000
63	S	-7.998100000000	8.610100000000	3.057300000000
64	O	-10.754600000000	6.141300000000	2.923400000000
65	C	-11.807800000000	9.739700000000	1.786200000000
66	C	-11.459800000000	10.874300000000	2.676900000000
67	C	-11.704000000000	12.182800000000	2.289200000000
68	H	-12.156500000000	12.375700000000	1.476600000000
69	C	-11.267600000000	13.205500000000	3.126600000000
70	H	-11.410900000000	14.112900000000	2.882500000000
71	C	-10.632400000000	12.905900000000	4.297200000000

72	H	-10.314800000000	13.591200000000	4.873200000000
73	C	-10.467200000000	11.573300000000	4.616700000000
74	H	-10.044800000000	11.361600000000	5.440500000000
75	C	-11.309900000000	6.363400000000	1.793700000000
76	C	-11.558400000000	5.196100000000	0.901800000000
77	C	-12.246000000000	5.335600000000	-0.292300000000
78	H	-12.525700000000	6.193000000000	-0.594600000000
79	C	-12.515600000000	4.201000000000	-1.033100000000
80	H	-12.984900000000	4.304300000000	-1.853100000000
81	C	-11.471200000000	2.851200000000	0.473200000000
82	H	-11.178900000000	1.986900000000	0.739500000000
83	C	-11.163700000000	3.927200000000	1.292000000000
84	H	-10.690200000000	3.796400000000	2.105800000000
85	C	-12.545500000000	9.967000000000	0.517800000000
86	H	-12.661800000000	9.113000000000	0.050800000000
87	H	-13.424200000000	10.352600000000	0.714700000000
88	H	-12.037000000000	10.583400000000	-0.049500000000
89	C	-6.931100000000	8.116100000000	4.229000000000
90	N	-11.701100000000	7.527300000000	1.309300000000
91	N	-11.411200000000	8.562100000000	2.171500000000
92	N	-10.866000000000	10.559200000000	3.833900000000
93	N	-12.155500000000	2.961300000000	-0.667700000000
94	N	-6.164300000000	7.789000000000	5.015600000000
95	O	-7.923000000000	2.467200000000	9.117000000000
96	C	-8.976100000000	-1.131200000000	7.979900000000
97	C	-8.628100000000	-2.265800000000	8.870500000000
98	C	-8.872300000000	-3.574300000000	8.482800000000
99	H	-9.324900000000	-3.767100000000	7.670200000000
100	C	-8.435900000000	-4.597000000000	9.320200000000
101	H	-8.579200000000	-5.504300000000	9.076200000000
102	C	-7.800700000000	-4.297400000000	10.490800000000
103	H	-7.483100000000	-4.982600000000	11.066800000000
104	C	-7.635600000000	-2.964800000000	10.810400000000
105	H	-7.213200000000	-2.753000000000	11.634100000000
106	C	-8.478200000000	2.245100000000	7.987300000000
107	C	-8.726700000000	3.412400000000	7.095400000000
108	C	-9.414300000000	3.273000000000	5.901300000000
109	H	-9.694100000000	2.415600000000	5.599100000000
110	C	-9.683900000000	4.407600000000	5.160500000000
111	H	-10.153200000000	4.304300000000	4.340500000000
112	C	-8.639500000000	5.757400000000	6.666800000000
113	H	-8.347200000000	6.621700000000	6.933200000000
114	C	-8.332100000000	4.681300000000	7.485600000000
115	H	-7.858500000000	4.812200000000	8.299500000000
116	C	-9.713900000000	-1.358400000000	6.711400000000
117	H	-9.830200000000	-0.504500000000	6.244400000000
118	H	-10.592500000000	-1.744100000000	6.908400000000
119	H	-9.205400000000	-1.974800000000	6.144100000000
120	N	-8.869400000000	1.081200000000	7.503000000000
121	N	-8.579500000000	0.046500000000	8.365100000000
122	N	-8.034400000000	-1.950700000000	10.027500000000
123	N	-9.323800000000	5.647200000000	5.526000000000
124	S	-0.428400000000	8.607000000000	9.330000000000
125	C	-1.495300000000	9.101000000000	8.158300000000
126	N	-2.262200000000	9.428100000000	7.371700000000

```
127 Pb      -5.036199998000       9.264100000000       8.029000000000
128 S     -15.043000000000       8.610100000000       3.057300000000
129 C     -13.976000000000       8.116100000000       4.229000000000
130 N     -13.209200000000       7.789000000000       5.015600000000
131 Pb     -10.435200000000       7.953000000000       4.358300000000
132 H     -12.152700000000       7.643700000000       0.424700000000
133 H      -6.150400000000      16.252400000000       5.768900000000
134 H      -3.318700000000       9.573400000000      11.962600000000
END

GUIBONDS
1 1 27 1.0
2 1 127 1.0
3 2 13 1.0
4 2 127 1.0
5 3 29 1.0
6 3 4 1.0
7 3 23 1.0
8 4 30 1.0
9 4 5 1.5
10 5 6 1.0
11 5 7 1.5
12 7 8 1.0
13 7 9 1.5
14 9 10 1.0
15 9 11 1.5
16 11 12 1.0
17 11 30 1.0
18 13 28 1.0
19 13 14 1.0
20 124 125 2.0
21 14 21 1.5
22 14 15 1.5
23 15 16 1.0
24 15 17 1.5
25 17 18 1.0
26 17 31 1.5
27 19 20 1.0
28 19 31 1.5
29 19 21 1.5
30 21 22 1.0
31 23 25 1.0
32 23 26 1.0
33 23 24 1.0
34 27 32 3.0
35 28 134 1.0
36 28 29 1.0
37 29 127 1.0
38 30 127 1.0
39 130 131 1.0
40 33 51 1.0
41 33 49 1.0
42 126 127 1.0
43 34 45 2.0
44 35 60 2.0
```

```
45 35 36 1.0
46 35 55 1.0
47 36 61 1.5
48 36 37 1.5
49 37 38 1.0
50 37 39 1.5
51 39 40 1.0
52 39 41 1.5
53 41 42 1.0
54 41 43 1.5
55 43 44 1.0
56 43 61 1.5
57 45 59 1.0
58 45 46 1.0
59 46 47 1.5
60 46 53 1.5
61 47 48 1.0
62 47 49 1.0
63 49 50 1.0
64 129 130 2.0
65 51 52 1.0
66 125 126 2.0
67 51 53 1.0
68 53 54 1.0
69 55 57 1.0
70 55 58 1.0
71 55 56 1.0
72 59 133 1.0
73 59 60 1.0
74 128 129 2.0
75 63 89 1.0
76 63 131 1.0
77 64 75 1.0
78 64 131 1.0
79 65 91 1.0
80 65 66 1.0
81 65 85 1.0
82 66 92 1.0
83 66 67 1.5
84 67 68 1.0
85 67 69 1.5
86 69 70 1.0
87 69 71 1.5
88 71 72 1.0
89 71 73 1.5
90 73 74 1.0
91 73 92 1.0
92 75 90 1.0
93 75 76 1.0
94 75 131 1.0
95 76 77 1.5
96 76 83 1.5
97 77 78 1.0
98 77 79 1.5
99 79 80 1.0
```

```
100 79 93 1.5
101 81 82 1.0
102 81 93 1.5
103 81 83 1.5
104 83 84 1.0
105 85 87 1.0
106 85 88 1.0
107 85 86 1.0
108 89 94 3.0
109 90 132 1.0
110 90 91 1.0
111 91 131 1.0
112 92 131 1.0
113 95 106 2.0
114 96 121 2.0
115 96 97 1.0
116 96 116 1.0
117 97 122 1.5
118 97 98 1.5
119 98 99 1.0
120 98 100 1.5
121 100 101 1.0
122 100 102 1.5
123 102 103 1.0
124 102 104 1.5
125 104 105 1.0
126 104 122 1.5
127 106 120 1.0
128 106 107 1.0
129 107 114 1.5
130 107 108 1.5
131 108 109 1.0
132 108 110 1.5
133 110 111 1.0
134 110 123 1.0
135 112 113 1.0
136 112 123 1.0
137 112 114 1.5
138 114 115 1.0
139 116 118 1.0
140 116 119 1.0
141 116 117 1.0
142 120 62 1.0
143 120 121 1.0
END

CONSTRAINTS
ATOM   3
ATOM   4
ATOM   5
ATOM   7
ATOM   9
ATOM   11
ATOM   13
ATOM   14
```

```
ATOM   15
ATOM   17
ATOM   19
ATOM   21
ATOM   23
ATOM   27
ATOM   35
ATOM   36
ATOM   37
ATOM   39
ATOM   41
ATOM   43
ATOM   45
ATOM   46
ATOM   47
ATOM   49
ATOM   51
ATOM   53
ATOM   55
ATOM   65
ATOM   66
ATOM   67
ATOM   69
ATOM   71
ATOM   73
ATOM   75
ATOM   76
ATOM   77
ATOM   79
ATOM   81
ATOM   83
ATOM   85
ATOM   89
ATOM   96
ATOM   97
ATOM   98
ATOM   100
ATOM   102
ATOM   104
ATOM   106
ATOM   107
ATOM   108
ATOM   110
ATOM   112
ATOM   114
ATOM   116
ATOM   125
ATOM   129
ATOM   28
ATOM   29
ATOM   30
ATOM   31
ATOM   32
ATOM   33
ATOM   59
```

```
ATOM   60
ATOM   61
ATOM   90
ATOM   91
ATOM   92
ATOM   93
ATOM   94
ATOM   120
ATOM   121
ATOM   122
ATOM   123
ATOM   126
ATOM   130
ATOM   2
ATOM   34
ATOM   64
ATOM   95
ATOM   127
ATOM   131
ATOM   1
ATOM   63
ATOM   124
ATOM   128
END

Integration 6.0

qtens

XC
   LDA VWN
   GGA BP86
   DISPERSION Grimme3
End

Geometry
Optim Cartesian
Contraints FullConverge
Iterations 500
Converge 1e-5
End

End Input
Eor
```

A4.3 CASTEP v19.11 input files (.cell and .param) for a geometry optimization of a caffeine-based cocrystal

A4.3.1 Example of .cell file

```
#*******************************************************************************
#*                  Generated by cif2cell 1.2.11 2020-01-13 14:12                *
#*  T. Bjorkman, Comp. Phys. Commun. 182, 1183-1186 (2011). Please cite generously. *
#*                                                                               *
#*                                      ()                                       *
#*             Failed to get author information, No journal information          *
#*******************************************************************************

%BLOCK LATTICE_CART
ang    # angstrom units
   6.522500000000000   0.000000000000000   0.000000000000000
   0.000000000000000  10.647399999999999   0.000000000000000
  -1.614567354854244   0.000000000000000  23.188257882312737
%ENDBLOCK LATTICE_CART

%BLOCK POSITIONS_FRAC
O    0.043580000000000   0.180820000000000   0.976840000000000
O    0.956420000000000   0.819180000000000   0.023160000000000
O    0.043580000000000   0.319180000000000   0.476840000000000
O    0.956420000000000   0.680820000000000   0.523160000000000
O    0.566770000000000   0.242900000000000   0.107910000000000
O    0.433230000000000   0.757100000000000   0.892090000000000
O    0.566770000000000   0.257100000000000   0.607910000000000
O    0.433230000000000   0.742900000000000   0.392090000000000
O    0.298770000000000   0.280840000000000   0.189560000000000
O    0.701230000000000   0.719160000000000   0.810440000000000
O    0.298770000000000   0.219160000000000   0.689560000000000
O    0.701230000000000   0.780840000000000   0.310440000000000
O    0.425630000000000   0.678600000000000   0.090270000000000
O    0.574370000000000   0.321400000000000   0.909730000000000
O    0.425630000000000   0.821400000000000   0.590270000000000
O    0.574370000000000   0.178600000000000   0.409730000000000
O    0.326100000000000   0.757860000000000   0.172900000000000
O    0.673900000000000   0.242140000000000   0.827100000000000
O    0.326100000000000   0.742140000000000   0.672900000000000
O    0.673900000000000   0.257860000000000   0.327100000000000
N    0.806180000000000   0.214390000000000   0.042390000000000
N    0.193820000000000   0.785610000000000   0.957610000000000
N    0.806180000000000   0.285610000000000   0.542390000000000
N    0.193820000000000   0.714390000000000   0.457610000000000
N    0.088880000000000   0.350200000000000   0.034930000000000
N    0.911120000000000   0.649800000000000   0.965070000000000
N    0.088880000000000   0.149800000000000   0.534930000000000
N    0.911120000000000   0.850200000000000   0.465070000000000
N    0.821860000000000   0.475170000000000   0.146830000000000
```

```
N    0.178140000000000   0.524830000000000   0.853170000000000
N    0.821860000000000   0.024830000000000   0.646830000000000
N    0.178140000000000   0.975170000000000   0.353170000000000
N    0.100110000000000   0.525750000000000   0.101480000000000
N    0.899890000000000   0.474250000000000   0.898520000000000
N    0.100110000000000   0.974250000000000   0.601480000000000
N    0.899890000000000   0.025750000000000   0.398520000000000
C    0.697720000000000   0.101920000000000   0.020590000000000
C    0.302280000000000   0.898080000000000   0.979410000000000
C    0.697720000000000   0.398080000000000   0.520590000000000
C    0.302280000000000   0.601920000000000   0.479410000000000
C    0.984620000000000   0.244470000000000   0.015620000000000
C    0.015380000000000   0.755530000000000   0.984380000000000
C    0.984620000000000   0.255530000000000   0.515620000000000
C    0.015380000000000   0.744470000000000   0.484380000000000
C    0.275790000000000   0.384890000000000   0.008210000000000
C    0.724210000000000   0.615110000000000   0.991790000000000
C    0.275790000000000   0.115110000000000   0.508210000000000
C    0.724210000000000   0.884890000000000   0.491790000000000
C    0.018110000000000   0.418350000000000   0.078920000000000
C    0.981890000000000   0.581650000000000   0.921080000000000
C    0.018110000000000   0.081650000000000   0.578920000000000
C    0.981890000000000   0.918350000000000   0.421080000000000
C    0.845640000000000   0.384440000000000   0.105450000000000
C    0.154360000000000   0.615560000000000   0.894550000000000
C    0.845640000000000   0.115560000000000   0.605450000000000
C    0.154360000000000   0.884440000000000   0.394550000000000
C    0.726300000000000   0.278210000000000   0.088000000000000
C    0.273700000000000   0.721790000000000   0.912000000000000
C    0.726300000000000   0.221790000000000   0.588000000000000
C    0.273700000000000   0.778210000000000   0.412000000000000
C    0.666910000000000   0.479870000000000   0.189020000000000
C    0.333090000000000   0.520130000000000   0.810980000000000
C    0.666910000000000   0.020130000000000   0.689020000000000
C    0.333090000000000   0.979870000000000   0.310980000000000
C    0.976400000000000   0.556230000000000   0.142530000000000
C    0.023600000000000   0.443770000000000   0.857470000000000
C    0.976400000000000   0.943770000000000   0.642530000000000
C    0.023600000000000   0.056230000000000   0.357470000000000
C    0.840840000000000   0.010630000000000   0.178490000000000
C    0.159160000000000   0.989370000000000   0.821510000000000
C    0.840840000000000   0.489370000000000   0.678490000000000
C    0.159160000000000   0.510630000000000   0.321510000000000
C    0.007540000000000   0.000470000000000   0.144300000000000
C    0.992460000000000   0.999530000000000   0.855700000000000
C    0.007540000000000   0.499530000000000   0.644300000000000
C    0.992460000000000   0.500470000000000   0.355700000000000
C    0.162580000000000   0.089340000000000   0.147560000000000
C    0.837420000000000   0.910660000000000   0.852440000000000
C    0.162580000000000   0.410660000000000   0.647560000000000
C    0.837420000000000   0.589340000000000   0.352440000000000
C    0.153120000000000   0.190300000000000   0.185080000000000
C    0.846880000000000   0.809700000000000   0.814920000000000
C    0.153120000000000   0.309700000000000   0.685080000000000
C    0.846880000000000   0.690300000000000   0.314920000000000
```

```
C    0.989860000000000   0.200870000000000   0.220100000000000
C    0.010140000000000   0.799130000000000   0.779900000000000
C    0.989860000000000   0.299130000000000   0.720100000000000
C    0.010140000000000   0.700870000000000   0.279900000000000
C    0.836320000000000   0.111670000000000   0.216650000000000
C    0.163680000000000   0.888330000000000   0.783350000000000
C    0.836320000000000   0.388330000000000   0.716650000000000
C    0.163680000000000   0.611670000000000   0.283350000000000
C    0.669590000000000   0.922810000000000   0.174610000000000
C    0.330410000000000   0.077190000000000   0.825390000000000
C    0.669590000000000   0.577190000000000   0.674610000000000
C    0.330410000000000   0.422810000000000   0.325390000000000
C    0.629940000000000   0.835660000000000   0.134120000000000
C    0.370060000000000   0.164340000000000   0.866025403784439
C    0.629940000000000   0.664340000000000   0.634120000000000
C    0.370060000000000   0.335660000000000   0.365880000000000
C    0.446730000000000   0.755900000000000   0.135660000000000
C    0.553270000000000   0.244100000000000   0.864340000000000
C    0.446730000000000   0.744100000000000   0.635660000000000
C    0.553270000000000   0.255900000000000   0.364340000000000
H    0.591100000000000   0.079500000000000   0.046500000000000
H    0.408900000000000   0.920500000000000   0.953500000000000
H    0.591100000000000   0.420500000000000   0.546500000000000
H    0.408900000000000   0.579500000000000   0.453500000000000
H    0.795400000000000   0.032300000000000   0.018800000000000
H    0.204600000000000   0.967700000000000   0.981200000000000
H    0.795400000000000   0.467700000000000   0.518800000000000
H    0.204600000000000   0.532300000000000   0.481200000000000
H    0.634100000000000   0.118600000000000   0.981900000000000
H    0.365900000000000   0.881400000000000   0.018100000000000
H    0.634100000000000   0.381400000000000   0.481900000000000
H    0.365900000000000   0.618600000000000   0.518100000000000
H    0.342100000000000   0.455200000000000   0.029400000000000
H    0.657900000000000   0.544800000000000   0.970600000000000
H    0.342100000000000   0.044800000000000   0.529400000000000
H    0.657900000000000   0.955200000000000   0.470600000000000
H    0.241600000000000   0.409900000000000   0.968100000000000
H    0.758400000000000   0.590100000000000   0.031900000000000
H    0.241600000000000   0.090100000000000   0.468100000000000
H    0.758400000000000   0.909900000000000   0.531900000000000
H    0.369600000000000   0.312900000000000   0.009100000000000
H    0.630400000000000   0.687100000000000   0.990900000000000
H    0.369600000000000   0.187100000000000   0.509100000000000
H    0.630400000000000   0.812900000000000   0.490900000000000
H    0.689400000000000   0.554400000000000   0.213400000000000
H    0.310600000000000   0.445600000000000   0.786600000000000
H    0.689400000000000   0.945600000000000   0.713400000000000
H    0.310600000000000   0.054400000000000   0.286600000000000
H    0.677200000000000   0.404300000000000   0.213100000000000
H    0.322800000000000   0.595700000000000   0.786900000000000
H    0.677200000000000   0.095700000000000   0.713100000000000
H    0.322800000000000   0.904300000000000   0.286900000000000
H    0.529900000000000   0.484000000000000   0.169000000000000
H    0.470100000000000   0.516000000000000   0.831000000000000
H    0.529900000000000   0.016000000000000   0.669000000000000
```

```
H    0.470100000000000   0.984000000000000   0.331000000000000
H    0.996100000000000   0.628300000000000   0.166400000000000
H    0.003900000000000   0.371700000000000   0.833600000000000
H    0.996100000000000   0.871700000000000   0.666400000000000
H    0.003900000000000   0.128300000000000   0.333600000000000
H    0.014700000000000   0.931700000000000   0.118500000000000
H    0.985300000000000   0.068300000000000   0.881500000000000
H    0.014700000000000   0.568300000000000   0.618500000000000
H    0.985300000000000   0.431700000000000   0.381500000000000
H    0.275500000000000   0.081300000000000   0.124100000000000
H    0.724500000000000   0.918700000000000   0.875900000000000
H    0.275500000000000   0.418700000000000   0.624100000000000
H    0.724500000000000   0.581300000000000   0.375900000000000
H    0.389000000000000   0.264300000000000   0.164300000000000
H    0.611000000000000   0.735700000000000   0.835700000000000
H    0.389000000000000   0.235700000000000   0.664300000000000
H    0.611000000000000   0.764300000000000   0.335700000000000
H    0.984100000000000   0.269100000000000   0.246300000000000
H    0.015900000000000   0.730900000000000   0.753700000000000
H    0.984100000000000   0.230900000000000   0.746300000000000
H    0.015900000000000   0.769100000000000   0.253700000000000
H    0.725100000000000   0.119100000000000   0.240700000000000
H    0.274900000000000   0.880900000000000   0.759300000000000
H    0.725100000000000   0.380900000000000   0.740700000000000
H    0.274900000000000   0.619100000000000   0.259300000000000
H    0.576000000000000   0.928100000000000   0.204100000000000
H    0.424000000000000   0.071900000000000   0.795900000000000
H    0.576000000000000   0.571900000000000   0.704100000000000
H    0.424000000000000   0.428100000000000   0.295900000000000
H    0.720500000000000   0.825200000000000   0.104200000000000
H    0.279500000000000   0.174800000000000   0.895800000000000
H    0.720500000000000   0.674800000000000   0.604200000000000
H    0.279500000000000   0.325200000000000   0.395800000000000
H    0.307000000000000   0.632200000000000   0.093000000000000
H    0.693000000000000   0.367800000000000   0.907000000000000
H    0.307000000000000   0.867800000000000   0.593000000000000
H    0.693000000000000   0.132200000000000   0.407000000000000
%ENDBLOCK POSITIONS_FRAC

# Commented out pseudopotential block for easy editing
#%BLOCK SPECIES_POT
# H   H_00.usp
# C   C_00.usp
# O   O_00.usp
# N   N_00.usp
#%ENDBLOCK SPECIES_POT

%BLOCK SYMMETRY_OPS
# Symm. op. 1
  1.000000000000000   0.000000000000000   0.000000000000000
  0.000000000000000   1.000000000000000   0.000000000000000
  0.000000000000000  -0.000000000000000   1.000000000000000
  0.000000000000000   0.000000000000000   0.000000000000000
# Symm. op. 2
 -1.000000000000000   0.000000000000000   0.000000000000000
```

```
  0.000000000000000  -1.000000000000000   0.000000000000000
  0.000000000000000   0.000000000000000  -1.000000000000000
  0.000000000000000   0.000000000000000   0.000000000000000
# Symm. op. 3
  1.000000000000000   0.000000000000000   0.000000000000000
 -0.000000000000000  -1.000000000000000   0.000000000000000
  0.000000000000000   0.000000000000000   1.000000000000000
  0.000000000000000   0.500000000000000   0.500000000000000
# Symm. op. 4
 -1.000000000000000   0.000000000000000   0.000000000000000
  0.000000000000000   1.000000000000000   0.000000000000000
  0.000000000000000  -0.000000000000000  -1.000000000000000
  0.000000000000000   0.500000000000000   0.500000000000000
%ENDBLOCK SYMMETRY_OPS

# Commented out pseudopotential block for easy editing
%BLOCK SPECIES_POT
C19
%ENDBLOCK SPECIES_POT

FIX_ALL_CELL  : TRUE
KPOINTS_MP_SPACING 0.07 1/ang
```

A4.3.2 Example of .param file

```
TASK                        :   geometryoptimization
COMMENT                     :   Holmes et al., JPCA, 2020
XC_FUNCTIONAL               :   rpbe
CUT_OFF_ENERGY              :   700 eV
SEDC_APPLY                  :   true
SEDC_SCHEME                 :   G06
SEDC_S6_G06                 :   1.0
SEDC_D_G06                  :   5.0

FINE_GRID_SCALE             :   1.927248223
ELEC_ENERGY_TOL             :   5.0e-7
SPIN_POLARIZED              :   false
MAX_SCF_CYCLES              :   100

RELATIVISTIC_TREATMENT      :   zora

GEOM_METHOD                 :   bfgs
GEOM_MAX_ITER               :   200
GEOM_FORCE_TOL              :   0.01 eV/ANG
GEOM_DISP_TOL               :   5.0e-4 ANG
GEOM_STRESS_TOL             :   0.02 GPa
GEOM_ENERGY_TOL             :   5.0e-6 eV
#GEOM_PRECONDITIONER        :   exp

CALCULATE_STRESS            :   true

OPT_STRATEGY                :   speed
IPRINT                      :   1
PAGE_WVFNS                  :   0

WRITE_CELL_STRUCTURE        :   true
WRITE_CIF_STRUCTURE         :   true
```

A4.4 CASTEP v19.11 input files for the calculation of magnetic resonance shieldings and *J*-couplings

A4.4.1 Example of .param for shielding tensors

```
TASK                          :   magres
XC_FUNCTIONAL                 :   RPBE
CUT_OFF_ENERGY                :   700 eV
MAGRES_TASK                   :   NMR
ELEC_ENERGY_TOL               :   0.000005
ELEC_FORCE_TOL                :   0.01 eV/ANG
```

A4.4.2 Example of .param for J-couplings

```
TASK                          :   magres
XC_FUNCTIONAL                 :   RPBE
CUT_OFF_ENERGY                :   700 eV
MAGRES_TASK                   :   jcoupling
ELEC_ENERGY_TOL               :   0.000005
ELEC_FORCE_TOL                :   0.01 eV/ANG
```

Appendix 5 Conference Presentations

Southern, S. A.; West, M.; Bradshaw, M.; Bryce, D. L. Understanding the Nature of the ^{13}C and ^{1}H Chemical Shift Response to Tetrel and Hydrogen Bonds. Virtual poster presentation at the 4th International Symposium on Halogen Bonding, Hosted in Stellenbosch, South Africa, November 2nd to 5th, **2020**.

Southern, S. A.; Kumar, V.; Brinkmann, A.; Bryce, D. L. Solid-State NMR Crystallographic Investigations of Pharmaceutical Hydrochloride Salts: The Cases of Chlorpromazine HCl and Clenbuterol HCl. Virtual oral presentation at the 2020 Ottawa-Carleton Chemistry Institute Research Day, Ottawa, ON, June 4th, **2020**.

Southern, S. A.; Brinkmann, A.; Bryce, D. L. Solid-State NMR Crystallographic Investigations of Pharmaceutical Compounds: The Cases of Chlorpromazine and Clenbuterol. Accepted for oral presentation at the 103rd Canadian Chemistry Conference and Exhibition in Winnipeg, MB, May 24th to 28th, **2020**.

**This conference was cancelled due to the SARS-COVID-19 pandemic; however, the contribution was published in a virtual program: https://www.xcdsystem.com/cic/program/DeXjh0C/index.cfm

Southern, S. A.; West, M.; Bradshaw, M.; Bryce, D. L. NMR Crystallographic Investigations of a Series of Organic Cocrystals Exhibiting Tetrel Bonds. Oral presentation at the International Conference on Noncovalent Interactions, Lisbon, Portugal, September 2nd to 6th, **2019**.

Southern, S. A.; West, M.; Bradshaw, M.; Bryce, D. L. NMR Crystallographic Investigations of a Series of Organic Cocrystals Exhibiting Tetrel Bonds. Poster Presentation at the ISMAR EUROMAR Joint Conference, Berlin, Germany, August 25th to 30th, **2019**.

Southern, S. A.; Errulat, D.; Frost, J. M.; Gabidullin, B.; Bryce, D. L. Prospects for ^{207}Pb solid-state NMR studies of lead tetrel bonds. Oral Presentation and discussion at the Faraday Discussion on Halogen Bonding in Supramolecular and Solid-State Chemistry, Ottawa, ON, July 10th, **2017**.

Southern, S. A.; Errulat, D. Frost, J. M.; Bryce, D. L. ^{207}Pb Solid-state NMR Studies of Lead Tetrel Bonds. Oral Presentation at the 100th Canadian Chemistry Conference and Exhibition, Toronto, ON, May 30th, **2017**.

Southern, S. A.; Errulat, D.; Frost, J.; Bryce, D. L. Solid-State NMR Investigations of Tetrel Bonds. Poster Presentation at the 2016 CASTEP Training Workshop, Department of Materials, University of Oxford, United Kingdom, August 16th, **2016**.

Southern, S. A.; Errulat, D.; Frost, J.; Bryce, D. L. Solid-State NMR Investigations of Tetrel Bonds. Poster Presentation at the 2nd International Symposium on Halogen Bonding, Gothenburg, Sweden, June 10th, **2016**.

Deshkar, A.; Southern S.; Kobera, L.; Bryce, D. L.; McCloy, J.; Marcial, J.; Goel, A. Crystallization Behavior of Nepheline ($Na_2O•Al_2O_3•2SiO_2$) Based Glasses Designed in

Na_2O - CaO - Al_2O_3 - SiO_2 System. Poster Presentation at the WM2016 Conference (Contributing Author), March 6th, **2016**.

Southern, S. A.; Bryce, D. L. Computational Assessment and Initial Investigations of NMR Trends in Carbon Tetrel Bonds. Poster presentation at the 28th Annual MOOT NMR Conference, McMaster University, ON, October 24th, **2015**.

Southern, S. A.; Bryce, D. L. Solid-State NMR and Computational Investigations of Non-Covalent Tetrel Bonds. Poster presentation at the 98th Canadian Chemistry Conference and Exhibition, Ottawa, ON, June 16th, **2015**.

Southern, S. A.; Bryce, D. L. Solid-State NMR and Computational Investigations of Non-Covalent Tetrel Bonds. Oral and poster presentation at the 2nd Crystal Engineering and Emerging Materials Workshop of Ontario and Quebec, University of Guelph, ON, June 11th, **2015**.

Southern, S. A.; Bryce, D. L. Carbon-13 Solid-State NMR and Computational Investigations of Non-Covalent Tetrel Bonds. Oral presentation at the 27th MOOT NMR Symposium, University de Québec à Montréal, QC, October 18th, **2014**.